NASA Reference Publication 1037

Collisionless Galaxy Simulations

Frank Hohl, Thomas A. Zang,
and John B. Miller

APRIL 1979

NASA

NASA Reference Publication 1037

Collisionless Galaxy Simulations

Frank Hohl
Langley Research Center
Hampton, Virginia

Thomas A. Zang
The College of William and Mary
Williamsburg, Virginia

John B. Miller
Old Dominion University
Norfolk, Virginia

National Aeronautics
and Space Administration

**Scientific and Technical
Information Office**

1979

PREFACE

Three-dimensional fully self-consistent computer models were used to determine the evolution of galaxies consisting of 100 000 simulation stars. One series of computer experiments used initially balanced flattened galaxies with an exponential radial density variation. Comparison of two-dimensional (infinitesimally thin disk) simulations with three-dimensional (disk with finite thickness) simulations showed only a very slight stabilizing effect due to the additional degree of freedom. The addition of a fully self-consistent, nonrotating, exponential core/halo component resulted in considerable stabilization. The most pronounced instabilities present were those due to the Jeans' instability in the outer regions of the disk, while at the same time a relatively slowly growing bar instability appeared. A second series of computer experiments was performed to determine the collapse and relaxation of initially spherical, uniform density and uniform velocity dispersion stellar systems. The evolution of the system was followed for various amounts of angular momentum in solid body rotation. For initially low values of the angular momentum satisfying the Ostriker-Peebles stability criterion, the systems quickly relax to an axisymmetric shape and resemble elliptical galaxies in appearance. The maximum flattening for these systems is equivalent only to an E2 system. For larger values of the initial angular momentum, bars develop and the systems undergo a much more drastic evolution. The apparent rotational and random velocities of the bar systems are very sensitive to the viewing direction. An additional complication is the frequent misalignment of the apparent major axis with the direction that reflects the maximum rotation.

INTRODUCTION

In recent years, large-scale N-body computer simulations (refs. 1 and 2) have become an important tool in investigating the structure of spiral galaxies, especially in determining the development of large-scale instabilities resulting in spiral and bar formation. Until recently, most of these simulations used essentially two-dimensional models with the "stars" confined to the plane of the galactic disk (refs. 3 and 4). These simulations have shown that the disks of stars tend to develop fast-growing nonaxisymmetric instabilities resulting in bar formation. The bar instabilities occur even for velocity dispersions that are considerably larger than those found in the solar neighborhood or those predicted by Toomre (ref. 5) as being locally stabilizing. Global stability studies of disks of stars have been primarily numerical large-scale N-body simulations. Some limited analytical work has been done primarily for uniformly rotating disks (refs. 6 and 7), but generally linear stability analyses were used in these analytical studies of disks of stars.

Any spiral structure in computer-generated galaxies is generally short lived and the final state is a rotating bar. The bar thus obtained rotates more slowly than the stars. For a typical case investigated by Hohl (ref. 4), the bar rotates at 2.25τ and the stars rotate at 1.5τ where τ is the rotational period of the initial disk.

It has been argued by Ostriker and Peebles (ref. 8) that core/halo components have a stabilizing effect on galaxies and result in longer lived spiral structures. However, numerical experiments with large fixed stellar components representing the core/halo component (refs. 9 and 10) show that a multiarmed spiral structure develops and persists for many rotations but only in an evolving manner. That is, the spiral structure is either wound up into a tight pattern or it is wound up and then reappears again. A recent study of the effect of fixed core/halo components using two-dimensional N-body simulations (ref. 11) does show that the bar instability is indeed inhibited by a sufficiently large fixed component.

The purpose of the present study of initially balanced flattened galaxies is twofold. First, we want to determine the effect of a self-consistent (rather than a fixed nonresponding) core/halo component. This will show whether there are any instabilities (such as "two-stream") or other important interactions present that may be suppressed with a fixed nonresponding core. Second, we want to determine the effects of finite thickness of the disk and of three-dimensional essentially spherical core/halo components.

The second part of the present study, using initially spherical collapsing galaxies, is aimed at resolving the dynamics of the formation of galaxies. It is likely that galaxies arise directly from the gravitational collapse and subsequent relaxation of portions of the expanding universe. After initially collapsing, the system expands and undergoes additional oscillations with amplitudes and damping depending on the dissipative mechanisms operating. According

to this script, elliptical galaxies result if the gaseous component is largely exhausted by the end of the first collapse. The various physical processes involved in this simple collapse picture, as well as some nonconventional alternatives, have been discussed in the reviews by Larson, by Jones, and by Gott (refs. 12 to 14). For situations in which very little gas is left by the time of first collapse, a collisionless system of stars appears to be an appropriate model. Numerical experiments studying the effect of dynamical mixing in such systems with spherical symmetry were carried out by Bouvier and Janin (ref. 15) and by Hénon (ref. 16).

Less restricted simulations aimed specifically at modeling the formation of elliptical galaxies by collisionless stellar dynamics were performed by Gott (refs. 17 and 18), who included rotation and relaxed the imposed symmetry conditions from spherical to axial. These uniformly rotating models produced flattened, oblate systems. In later work, Gott (ref. 18) added the effects of cosmological infall and tidal interactions and obtained good agreement with the ellipticity profile and light distributions of ellipticals. However, Gott's calculations have remained somewhat suspect since his method did not permit the development of the fierce bar instabilities and the associated large-scale momentum transfer that have been so common in simulations of disk galaxies (refs. 4, 8, and 11).

Recently Miller (ref. 19) and Miller and Smith (ref. 20) have produced some fully three-dimensional simulations of the collapse of stellar systems. Their earlier examples produced prolate bars rather than oblate systems like those obtained by Gott. This striking difference, however, seems attributable more to the colder initial conditions used by Miller and by Miller and Smith than to their removal of the constraint of axial symmetry.

But even leaving aside this concern about possible suppressed nonaxisymmetric instabilities, the merits of the oblate models of ellipticals have been called into question by the recent observations of the rotational and random velocities of elliptical systems by Illingworth (ref. 21) and by Peterson (ref. 22). As discussed by Illingworth, data for numerous elliptical galaxies seem to indicate that the ratios of rotational to random velocities are typically a factor of 2 or 3 smaller than those predicted by the oblate models.

It may well be that more exotic models of the formation of elliptical galaxies are required. Nevertheless, it seems a pity to give up too soon on the simple collapse model, especially since the range of initial conditions covered by the fully three-dimensional calculations of Miller and of Miller and Smith is limited. We report here some extensive results of three-dimensional models of the collisionless collapse and relaxation of rotating stellar systems with initial random velocities patterned after those of Gott (ref. 17). This permits an assessment of the importance of his requirement of axial symmetry. At the same time, these initial conditions cover a markedly different range from those of other three-dimensional experiments.

SYMBOLS

C	constant, $3M_g/(4\pi r^2\,\rho(0,0))$
c	velocity, defined in equation (5)
G	gravitational constant
H	Green's function
h	defines z-dimension of $n \times n \times h$ active array
I	moment of inertia
K	gravitational field
M_g	mass of galaxy
$M_\odot$	mass of Sun
m	mass of simulation star
N	dimension of array used in potential calculation
n	defines $n \times n \times h$ active array, $N/2$
P	angular momentum
Q	$= \sigma_r/\sigma_{r,min}$
R	radius of galaxy
r,ϕ,θ	spherical coordinates
T	random kinetic energy
T_{cir}	kinetic energy in rotation
T_{rand}	random kinetic energy
t	time
U	$= V_m/\sigma_v(0)$
V	velocity
V_m	peak rotational velocity

W	total potential energy
x,y,z	Cartesian coordinates
ϵ	ellipticity
ζ	radius, $x^2 + y^2 + (7z/5)^2$
κ	epicylic frequency
μ	surface mass density
ρ	volume mass density
$\rho(0)$	mass density at center of galaxy
σ	velocity dispersion
$\sigma_{r,min}$	velocity dispersion defined by equation (3)
σ_v	line-of-sight velocity dispersion
ϕ	gravitational potential
Ω	angular velocity of spherical model
Ω_o	$= \sqrt{GM_g/R^3}$
ω	angular velocity of disk model
ω_o	angular velocity of cold balanced disk

Subscripts:

i,j,k	summation indices
r,ϕ,θ	radial, azimuthal, and colatitudinal component
x,y,z	x-, y-, and z-component
ξ,η,ζ	summation indices

Notation:

$\tilde{}$	Fourier transformed quantity

MODEL

The model used for the present galaxy simulations consists of 100 000 representative stars of equal mass that move inside an active 64 × 64 × 16 (or 33 × 33 × 33) three-dimensional array of cells. For the disk simulations the

stars are confined to the plane of the disk represented by a 64 × 64 active array. The number of stars inside a particular cell defines the mass density at the center of each cell. Fast Fourier transform methods are used to obtain the gravitational potential at the center of each cell for a given mass density distribution. Thus the potential calculation actually requires an array larger than the 33 × 33 × 33 active array so that the periodicity associated with the Fourier transform can be eliminated. The force acting on a particular star is determined by trilinear interpolation from the gravitational field at the surrounding eight cell centers. After the force acting on a star is determined, its position and velocity are advanced by a small time step using the time-centered leap-frog method. Details of the two-dimensional model are given by Hohl and Hockney (ref. 2) and by Hohl (ref. 23). The extension of the model to three dimensions is described in the appendix. Collisional effects in this model become important only after hundreds of rotations (ref. 24).

DISK-CORE SIMULATIONS

Observational evidence (refs. 25 to 27) indicates that the luminosity (and presumably the density) in the outer regions of many spiral and S0 galaxies decreases exponentially with radius. Also, previous simulations (ref. 4) showed that initially unstable stellar disks evolved into stable systems with radial density variations that closely approximated the sum of two exponentials. The inner exponential with a scale length of about 1 kpc describes the nonrotating or slowly rotating spheroidal, or core, component and the remaining exponential with a scale length of about 8 kpc describes the extended disk population. Thus, it seems reasonable to use an exponential density variation for the disk in the present computer simulations. Similarly, the central core used is described by an exponential density variation.

Figure 1 illustrates the evolution of a disk of 100 000 stars with an initially exponential surface mass density distribution $\mu(r) = \mu(0)\, e^{-r/2}$ with a cutoff at $r = 10$ kpc. The initial angular velocity of the disk was obtained from

$$\omega^2 = \omega_o^2 + \frac{1}{r\,\mu(r)} \frac{\partial}{\partial r}\left[\mu(r)\ \sigma_r^2(r)\right] + \frac{1}{r^2}\left[\sigma_r^2(r) - \sigma_\phi^2(r)\right] \tag{1}$$

with

$$\sigma_\phi(r) = \frac{\kappa(r)}{2\ \omega_o(r)}\ \sigma_r(r) \tag{2}$$

Here, $\omega_o(r)$ is the angular velocity required to balance the cold (zero velocity dispersion) disk, $\omega(r)$ is the actual angular velocity, and $\kappa(r)$ is the epicyclic frequency. The initial value of the radial velocity dispersion σ_r

was taken to be that determined by Toomre (ref. 5) as the minimum required to stabilize all local axisymmetric instabilities,

$$\sigma_r(r) = \sigma_{r,min} = 3.36G\ \mu(r)/\kappa(r) \tag{3}$$

The time t is given in rotational periods $(2\pi/\omega_o)$ of the cold disk at a radius of 5 kpc, that is, halfway to the edge of the initial disk.

As expected (refs. 4 and 9), only the small-scale instabilities are prevented by $\sigma_r = \sigma_{r,min}$ and the system quickly forms a two-arm spiral which eventually tends to evolve into a rotating bar. The evolution of the azimuthally averaged radial density variation for this system is shown in figure 2. As previously observed (refs. 4 and 9), the eventual density variation approaches one which can be closely approximated by the sum of two exponentials. One exponential describes the central core component and the other describes the extended disk. The evolution of the radial and azimuthal velocity distributions as a function of radius is shown in figure 3. It is obvious that the system has not reached an equilibrium condition. Note that there are still large outward velocities in the outer regions of the system. This can be seen more clearly in figure 4 where the evolution of the azimuthally averaged, mean radial velocity is plotted as a function of radius. This figure displays considerable systematic radial flows. The radial and azimuthal velocity dispersions displayed in figure 5 show that there is some heating near the center and that the velocity dispersion for stars expanding into the extended disk component increases considerably. The increases in the central mass density and heating near the center result in large changes in the rotation curve. Figure 6 shows the evolution of the rotation curve,

$$V_{\phi_o} = r\ \omega_o(r) = \sqrt{rK_r}$$

and the corresponding mean rotation of the stars $\langle V_\phi \rangle$. In the central region of the system the galaxy is now balanced to a large extent by increased pressure due to the higher velocity dispersion. The mean rotation has been reduced in this region by transferring momentum to larger radii. This is illustrated in figure 7 which shows that as the bar instability develops (compare with fig. 1), much of the angular momentum is transferred to larger radii.

Various other diagnostics have been performed on the system. For example, figure 8 shows the evolution of the moment of inertia I and the angular momentum P divided by their values at $t = 0$. As can be seen, P is conserved in the simulation, but I is still increasing at a nearly linear rate after three rotations. The evolution of various components of the total kinetic energy divided by the total potential energy is shown in figure 9. The components T_r and T_ϕ represent the random kinetic energies due to the velocity dispersions in the r- and ϕ-directions, respectively, while T_{cir} is the kinetic energy of rotation. Note that the ratio of the kinetic energy in rotation to the absolute value of the total gravitational energy of the system is approach-

ing the value 0.14 predicted by Ostriker and Peebles (ref. 8) for stability. This indicates that considerable heating of the system occurs.

One of the aims of the present study is to determine the effect of adding the third degree of freedom by allowing the exponential disk to have a finite thickness. Using again an exponential projected surface mass density variation $\mu(r) = \mu(0)\ e^{-r/2}$, the stars are now distributed in the z-direction according to the one-dimensional distribution $\operatorname{sech}^2 (z/C)$. The parameter C is determined from $\rho(0) = 3M_g/4\pi R^2 C$ (ref. 28) where M_g is the total mass of the galaxy and $R = 10$ kpc is the radius of the disk. The central thickness of the disk is 2 kpc and the density is cut off at z_1 given by

$$\sqrt{1 - \left(\frac{r}{R}\right)^2}\ \operatorname{sech}^2 \left(\frac{z_1}{C}\right) = 0.1 \tag{4}$$

The radial and azimuthal velocity components are determined in a manner similar to that for the infinitesimally thin disk and the z-component of the velocity dispersion is determined by a force balance in the z-direction. Note also that all initial velocities are truncated so that stars have kinetic energies no greater than those which would allow them to reach the boundary of the system in the gravitational potential at $t = 0$.

Figure 10 shows two side views of the initial disk and the evolution for up to 3 rotations. The differences in the projections as the evolution proceeds are due to the bar formation. Note also the rapid expansion in the plane of the disk. This is the result of the bar instability, as shown in figure 11 which gives the evolution of the disk projected in the x-y plane. Note that the evolution is very similar to that shown in figure 1 for the thin disk. The similarities in the evolution of the two systems are even more accentuated by comparing the evolution of the surface mass density distribution and the velocity distribution in figures 12 and 13 with those in figure 2 and 3. For completeness figures 14 to 19 show the evolution of the various other parameters for comparison with figures 4 to 9. For the finite thickness system, the additional variable of z-component velocity or kinetic energy remains small compared with the r- or ϕ-components. Thus, one would expect little difference in the evolution of the finite thickness disk when compared with the infinitesimally thin disk.

As shown in figures 1 and 11, exponential disks with velocity dispersion ($Q \approx 1$) are violently unstable to the bar-forming mode. Previous work (ref. 11) with a superimposed fixed (non-self-consistent) central mass distribution indicated a stabilizing effect toward the bar-forming instability. A more realistic simulation is to allow core-disk interaction; thus, we are presently interested in the stabilizing effects of a completely self-consistent core, or spheroid, component. Again, the effect is investigated for both the infinitesimally thin disk (two-dimensional) and for the three-dimensional disk.

For the core-disk system, 50 percent of the mass (50 000 stars) is contained in the nonrotating core and the remaining mass (50 000 stars) is con-

tained in the disk. The disk component is again given the surface density variation $\mu_{disk}(r) = \mu_{disk}(0)\ e^{-r/2}$, whereas the initial nonrotating core component is given a density variation $\mu_{core}(r) = \mu_{core}(0)\ e^{-2r}$. Note that the disk and core densities are cut off at $r = 10$ kpc and $r = 3.5$ kpc, respectively. The initial velocity dispersion and rotation of the disk are obtained by again using equations (1), (2), and (3) with $\mu = \mu_{disk}$. Similarly, as before, the z-dimensions of the disk are determined from equation (4). The initial velocity dispersion of the nonrotating core component was obtained by taking $\sigma_\phi = \sigma_r$ and simply balancing the core in the presence of the disk. In order to ensure that the core component was in a stable equilibrium state at the start of the core-disk simulation, the core was allowed to evolve for several rotational periods ($2\pi/\omega_o$ at 5 kpc) with the disk stars held fixed. Starting from these initial conditions, the system evolved as shown in figure 20. Note that even though a two-arm spiral structure still forms, the system as a a whole evolves in a much less violent manner than that displayed in figure 1. This can also be seen in figure 21 which shows the evolution of the surface mass density for both the core and the disk components. Nevertheless, the spiral instability in figure 20 is leading toward the formation of a bar structure. Note also that with the exception of a slow outward diffusion of stars near the edge, the core remains essentially stationary, while the disk component displays the outward shift of mass generally associated with bar formation. Figure 22 shows the evolution of the radial and azimuthal velocity distributions as a function of radius. When comparing the results with figure 3, two features stand out. One feature is, of course, the large-velocity stars in the core near the center and the other is the much more violent instability at larger radii in figure 3. The mean radial velocity shown in figure 23 also displays a considerable reduction in the net radial flow when compared with figure 4. Similar information is contained in figure 24 which displays the evolution of the radial and azimuthal velocity dispersions for the core and disk components. Note the sharp increase in the radial velocity dispersion at $r \approx 3$ kpc which is associated with a marked reduction in the angular momentum of the disk in this region. This outward shift of the angular momentum is displayed in figure 25 which shows the evolution of the angular momentum distribution. In general, the simulations show that the formation of bars or two-armed spirals results in moving angular momentum outward to larger radii. The evolution of the rotation curve displayed in figure 26 shows that for up to 3 rotations the disk component continues to have a high rotational velocity in the central region of the system.

As shown in figure 27, the addition of the core component markedly reduced the rate of increase in the moment of inertia. Similarly, the ratios of kinetic energy to potential energy shown in figure 28 change considerably less than those of the disk without a central core component. This reflects the sizable differences in the initial values of these ratios.

The final system investigated in this series is a three-dimensional exponential disk with a three-dimensional core, or spheroid, component. The spatial distribution of the stars for the disk component is obtained as was done for the disk shown in figures 10 and 11 except that now the disk contains only 50 000 stars. For the nonrotating central core, the density is given by $\rho(\zeta) = \rho(0)\ e^{-2\zeta}$, where $\zeta^2 = x^2 + y^2 + (7z/5)^2$. The density is cut off at $\zeta = 7$. Thus, the central core or spheroid has an axis ratio of 7:5. Again

the Gaussian velocity dispersion for the core is obtained by a simple balance of the self-gravity of the total system. The velocity dispersion for the disk component is generated as was done for the system shown in figure 11. Before initiating the simulation of the combined core-disk system, the core was allowed to evolve for several rotations (with fixed disk stars) to ensure that no instabilities or other problems associated with the core component were present.

Figure 29 shows the evolution of the system perpendicular to the equatorial plane. Note the remarkable stability of the system when compared with the disk without the central core in figure 10. Figure 29 does show a slight bulging of the disk at $t = 3.0$ indicative of spiral-type instabilities. The evolution of the system in the equatorial plane is shown in figure 30 and displays the development of a comparatively weak spiral structure initiated by Jeans' type instabilities in the outer region of the disk. Although it is not apparent from figure 30, an analysis of the azimuthal density variation for the disk stars at $t = 3.0$ shows that a bar structure is forming. For example, in the region from 2 to 5 kpc, which is near the center away from the visible spiral structure displayed in figure 30, the peak density along the bar is 2.5 times the density 90° away from the major bar axis. It should be noted that because of the allowed initial relaxation, the core components of the two core-disk systems investigated here are expected to closely satisfy the collisionless Boltzmann equation. The same is not necessarily true for the disk component since satisfying equation (1) only ensures a balance of forces at $t = 0$. Also, for a stellar disk, $\sigma_r = \sigma_{r,min}$ does not ensure stabilization of global nonaxisymmetric instabilities (refs. 29 and 30). However, since one would hardly expect nature to generate a galaxy initially in an exact stable stationary state and since we are interested in the future development of instabilities and the final state toward which the system evolves, an exact stationary and stable initial state is not necessary.

The evolution of the radial, azimuthal, and axial velocity distributions as a function of radius is shown in figure 31. Note that now there is even less change visible than for the two-dimensional system shown in figure 22. This is illustrated more clearly in figure 32 which shows very little net mass motion in the radial direction.

The evolution of the azimuthally averaged projected surface mass density for the three-dimensional disk-core system is shown in figure 33 and is nearly identical to that of the two-dimensional disk-core system shown in figure 21. Note that there is very little change in the density for the core with the exception of a slight outward diffusion near the edge. Azimuthally averaged values of the total density variation in the z-direction are shown in figure 34 for various values of r. Note that the density follows an essentially exponential variation. Some of the fluctuations shown may be due to the relatively small sampling volume used. The evolution of the radial velocity dispersion shown in figure 35 indicates that (as expected) the velocity dispersion for the two-dimensional core (shown in fig. 24) is higher. Also, the large increase in the velocity dispersion of the thin disk near $r = 3$ kpc does not occur for the three-dimensional disk. Associated with this is the fact that there is very little change in the radial angular momentum distribution (fig. 36) during the evolution of the three-dimensional disk-core system, whereas considerable outward shift of angular momentum occurs for the two-dimensional disk-core system

(fig. 25). These results indicated that the global bar instability is much weaker for the three-dimensional system than for the two-dimensional system, as is obvious by comparing figures 20 and 30.

The evolution of the moment of inertia and of the kinetic energy ratios for the three-dimensional disk-core system is shown in figures 37 and 38. As can be seen, there is little change in the value of the various components during the evolution. Note that the ratio of the kinetic energy in rotation to the total potential energy of the system is slightly higher than the value of the 0.14 predicted for stability by Ostriker and Peebles (ref. 8). Also, the moment of inertia increases by only about one-third of that shown in figure 27 for the two-dimensional system. As was the case for all four systems investigated, the angular momentum was conserved to a high degree of accuracy.

SPHERICAL COLLAPSE SIMULATIONS

The initial locations of the stars for this series of simulations were obtained by distributing them at random inside a sphere of radius $R = 10$ kpc to produce a uniform mass density. The total mass of the system was taken to be $M_g = 2 \times 10^{11} M_\odot$. Solid body rotation about the vertical axis with angular velocity

$$\Omega_o = \sqrt{\frac{GM_g}{R^3}} = 29.3 \text{ km-sec}^{-1}\text{-kpc}^{-1}$$

balances the cold (zero velocity dispersion) system in the equatorial plane. The initial velocities of the stars were selected from an isotropic Maxwellian distribution superimposed upon solid body rotation with angular velocity $\Omega = \omega\Omega_o$. The amounts of rotation and the radial velocity dispersion σ_r used for each of the five models are listed in table I. Also given are the initial

TABLE I.- INITIAL CONDITIONS

	Model				
	I	II	III	IV	V
Ω/Ω_o	0	0.500	0.707	0.866	1.159
σ_r, km/sec . . .	92.8	92.8	92.8	65.7	41.5
$T_{rand}/\lvert W \rvert$ . . .	1/4	1/4	1/4	1/8	1/20
$T_{cir}/\lvert W \rvert$ . . .	0	1/12	1/6	1/4	4/9

ratios of the random kinetic energy T_{rand} and the rotational kinetic energy T_{cir} to the total gravitational energy W. The random kinetic energy is given by

$$T_{rand} \approx \frac{1}{2} m \sum_{i=1}^{10^5} \left(c_{r,i}^2 + c_{\theta,i}^2 + c_{\phi,i}^2 \right)$$

where m is the mass of a star and

$$\left.\begin{aligned} c_r^2 &= (V_r - \langle V_r \rangle)^2 \\ c_\theta^2 &= (V_\theta - \langle V_\theta \rangle)^2 \\ c_\phi^2 &= (V_\phi - \langle V_\phi \rangle)^2 \end{aligned}\right\} \qquad (5)$$

Note that initially (at t = 0)

$$\langle V_r \rangle = \langle V_\theta \rangle = 0 \qquad \langle V_\phi \rangle = (r \sin \theta)\Omega$$

The rotational kinetic energy is given by

$$T_{cir} = \frac{1}{2} m \sum_{i=1}^{10^5} \langle V_{\phi,i} \rangle$$

The first four models in table I have precisely the initial conditions used by Gott (ref. 17).

Main Features

The collapse and relaxation of the five models are illustrated in figures 39 through 43. For reasons of computational efficiency, the snapshots of the three orthogonal projections shown at each time in these figures were actually taken a time step apart. This accounts for the apparent lack of symmetry at certain stages. Since the initial configurations of each of these

models were far from equilibrium, the initial evolution is characterized by the collisionless violent relaxation process described by Lynden-Bell (ref. 31). In this process the distribution function tends, albeit incompletely, toward a Maxwellian form through the influences of the rapidly fluctuating gravitational field. The effectiveness of this process is expected to decrease with radial distance from the center since the duration of the rapidly fluctuating field is a decreasing fraction of the orbital time scales.

For models I, II, and III (the hotter and less rapidly rotating ones), this violent relaxation is the principal effect which determines the final, equilibrium configuration. On the other hand, in models IV and V an additional effect occurs, the development of a pronounced bar-shaped structure. For this reason, model IV is selected for special attention; not only is its evolution followed through 5 rotations rather than 3, but also the full time development of its properties is displayed rather than just the final properties, as for the remaining models. Because of difficulties in preserving the resolution of the nonaxisymmetric structure during the photographic processing, models IV and V in figures 42 and 43 are actually shown twice. Figure 42(a) shows model IV in three projections of 100 000 stars, each. For figure 42(b), the projections are printed much lighter and the x-y projection contains only 50 000 stars with 100 000 stars for the x-z and y-z projections. The same procedure is used for the two displays of model V in figures 43(a) and 43(b).

From the final frames of figures 42 and 43, it is apparent that a bar system appears quite flattened for certain viewing angles. The degree of flattening can be estimated from projected isodensity contours (see the discussion of fig. 66 subsequently). The eccentricities of the contours in the bar models decrease with increasing radius. The axial ratios of 1.0 to 0.39 to 0.54 and 1.0 to 0.19 to 0.28 for models IV and V were obtained from the innermost isodensity contours. The vertical axis is the last item listed for each model. Thus, even an apparent E8 system can be obtained from a collisionless model without invoking any dissipation. Notice also that the shortest of the three axes for the bar models lies in the equatorial plane rather than along the axis of rotation. These are thin bars rather than flat ones, as indeed is evident from figures 42 and 43. On the other hand, the isodensity contours for the axisymmetric models II and III are noticeably more eccentric in the outer regions than in the center. The maximum eccentricities found are 0.18 for model II and 0.25 for model III.

Figures 44 through 47 are useful in describing the general features of the collapse of the models. Both the moment of inertia and the various kinetic energy ratios reflect the oscillations occurring during the collapse phase. Although the moment of inertia oscillates only near its initial value for model I, for models II to IV it displays a steady increase after undergoing one or more oscillations reflecting the initial collapse in the horizontal direction, that is, in the direction perpendicular to the rotation axis. Model V, of course, initially expands in the horizontal direction since the centrifugal forces alone are sufficient to overcome the gravitational attraction. The eventual steady increase in the moment of inertia is due to a comparatively small number of escaping stars rather than to any failure to achieve equilibrium. The constancy of the total angular momentum, which is shown in figures 44 and 45, is reassuring evidence of the accuracy of the numerical simulation.

For models IV and V (shown in figs. 42 and 43), the first indications of the developing bar occur at $t = 1.5$ and $t = 0.75$, respectively, in the form of vertical "flares" at both ends of the two side projections. In subsequent frames the nonaxisymmetric structure is clearest in the equatorial (top) projection. With the exception of the vertical flares, the transitory development of the bar is similar to the bar formation process in the three-dimensional simulations of equilibrium, but unstable, flattened galaxies discussed earlier. Bar formation appears to become significant during or after the second collapse. For example, in figure 43, the peak of the second collapse, as indicated by the maximum of the z-component of the kinetic energy, occurs shortly before $t = 0.75$. At that time, large-scale axisymmetric structures have appeared. Prior to the emergence of this instability it is evident that the evolution is dominated by simple, axially symmetric collapse dynamics.

The amount of time taken by the initial collapse may be compared with that required for the collapse of the corresponding pressure-free, uniformly rotating Maclaurin spheroid. This simple model was described by Lynden-Bell (ref. 32) and has been used for comparison with stellar dynamic results by Gott and Thuan (ref. 33) and by Miller and Smith (ref. 20). It predicts that the end of the first collapse in the vertical direction is reached at $t = 0.18$, 0.19, 0.20, 0.20, and 0.21 for models I, II, III, IV, and V, respectively. The location of the first peak in the vertical kinetic energy ratios (figs. 46 and 47) suggests that the initial collapse is completed near $t = 0.25$ for models I to III and near $t = 0.20$ for models IV and V. Notice that in the four rotating models the horizontal components of the kinetic energy reach their first maximum distinctly later than the vertical components, as expected. Di Fazio and Occhionero (ref. 34) add pressure and relaxation effects to the Maclaurin spheroid model. Both of these effects increase the estimated collapse time, a result which appears needed for the three hottest models. However, a detailed comparison seems unwarranted in view of the uncertain relation between stellar velocity dispersion and the specific form of pressure employed by them.

The kinetic energy ratios suggest that models I to III have fairly well relaxed by $t \approx 1$. They also suggest that the collapse phase of model IV is largely completed by then. There appears to be a distinct interval between the end of the collapse process and the onset of the bar formation. For model V, however, it is more difficult to tell when the collapse stops and the bar formation begins. The duration of the collapse in models I to IV conforms to Gott's result showing that the violent relaxation occurs in roughly 3 collapse times. In the present units, the reference collapse times used by Gott are 0.27, 0.32, 0.40, and 0.36 for models I to IV and 0.49 for model V. A further comparison is available of the total maximum kinetic energy achieved during the collapse: for models I to IV, the maximum values of $T/|W|$ are 0.65, 0.61, 0.57, and 0.58 compared with 0.66, 0.62, 0.58, and 0.60 obtained in the axially symmetric calculation by Gott.

A more detailed critique of the axially symmetric simulations can be made by comparing the distribution of the stars with respect to their energy. The results for the three-dimensional simulations are shown in figures 48 and 49. The final distributions of non-bar-forming models I to III are essentially the same as those obtained previously by Gott. The basic feature of a separation into a low energy core and a high energy halo is apparent. Even the locations

and strengths of these two components correspond closely to those found by Gott. As might be expected from the rapid equilibration of the kinetic energy ratios, the energy distributions of the first three models at $t = 3$ differ only marginally from those at $t = 2$. Although the similarity of the present energy distributions to those obtained by Gott does not preclude a redistribution of angular momentum, there is no evidence that any redistribution occurs. Indeed, for each of these three axisymmetric models, the initial and final angular momentum distributions are virtually indistinguishable.

The occurrence of a bar in models IV and V has a marked effect upon the energy distributions. Although there do appear to be separate core and halo components in model IV at $t = 1$ and $t = 2$, this distinction disappears as the bar develops. By $t = 5$ the energy distribution is nearly uniform over a substantial range. The similarity between the energy distributions at $t = 4$ and $t = 5$ indicates that the latter distribution has essentially reached an equilibrium state. Such is not the case for the energy distribution of model V shown in figure 48. It is clear from the kinetic energy ratios that this example has not yet reached equilibrium at $t = 3$. Indeed the energy distribution at $t = 2$ is substantially different from the one at $t = 3$. Although the bar is well developed, several more rotations appear to be needed to achieve equilibrium.

From figures 39 through 43 it is sometimes difficult to determine whether a bar is forming in the central region of the system. A convenient method for obtaining more quantitative information on nonaxisymmetric behavior is to plot the projected surface mass density for a number of cylindrical shells with different radii as a function of longitude. This is done in figure 50 for models I to V. It can be seen that at $t = 3$ no barlike nonaxisymmetry is present for models I to III, whereas for models IV and V a pronounced bar structure is observed.

N-body calculations and other data used by Ostriker and Peebles (ref. 8) indicate that galaxies with $T_{cir}/|W| > 0.14$ are unstable to the bar-forming mode. The empirical evidence for this criterion has been gathered for systems near equilibrium. For the present calculations it makes more sense to inquire about the value of $T_{cir}/|W|$ after the collapse phase rather than at $t = 0$, especially since the first evidence of bar formation seems to appear during the second collapse. The ratios $T_{cir}/|W|$ for models I, II, IV, and V (figs. 46 and 47) are either well below or well above the value 0.14 and they behave accordingly. The ratio for model III reaches a low of 0.13 at $t = 0.75$, and subsequently oscillates between 0.14 and 0.15. Nevertheless, this system remains axially symmetric as indicated most convincingly by figure 50. This apparent disagreement could easily be due to the crudeness of the empirical criterion or to slight numerical errors in the computation of the ratio. The most likely cause of such numerical errors is an underestimate of the potential energy. This occurs because the interaction potential used in these calculations is cut off (and thus much lower than the actual Newtonian interaction potential) for distances less than one cell dimension (ref. 24). This effect becomes more pronounced for systems with high central mass concentrations. Such an effect may also be responsible for the slightly high ratio obtained in the three-dimensional disk-core case.

Detailed Features

We now turn to the more detailed diagnostics of these simulations. The volume density ρ is shown in figure 51 as a function of the spherical radius r for three values of the colatitude θ. This density represents an azimuthal average for a ring with radial thickness of 1 kpc and angular width of 10° in colatitude. The data points at $r = 10$ kpc for $t = 0$ appear to be a factor of 2 too small because the initial uniform density configuration fills only half of the ring centered at 10 kpc.

For models I to III, the final density plots display the same separation into a core and a halo that was evident in the energy distributions. In the density plots, this property manifests itself as a change in slope between 6 and 8 kpc. As before, this distinction becomes less sharp in the more rapidly rotating example. In the case of model I, and to a lesser extent for model II, it is tempting to describe the density as the sum of two exponentials. This feature is displayed more clearly in plots of the density projected onto the equatorial plane as shown in figures 52 and 53.

In the two bar models, the azimuthally averaged density in the equatorial plane maintains an exponential form up to at least 12 kpc. At higher inclinations, model V departs sooner from the exponential shape. This model, however, has not yet equilibrated. The exponential density profiles observed here have also habitually resulted from the evolution of flat galaxies into bars (ref. 4).

A different perspective of the densities is offered by figures 54 and 55, which show the variation in the vertical direction. Here, too, are the signs of a core-halo structure in the first three models and of a well-developed exponential profile in the last two.

The rotation curves in the equatorial plane $V_{\phi_o} = r\omega_o = \sqrt{rK_r}$ and the mean circular velocity are displayed in figures 56 and 57. The mean circular velocity represents the mean velocity in a cylindrical shell covering all z. Note that heating, transfer of angular momentum to larger radii, and the increasing central density result in large reduction of the mean circular velocity when compared with the rotation curve $r\omega_o$.

The mean rotation curves for various colatitudes are displayed in figures 58 and 59. The azimuthal velocities shown there were averaged in the same manner as the densities given in figure 51. Model I, of course, has no net rotation. Models II and III have rotation curves which are linear for the inner 4 or 5 kpc and which turn over near 8 kpc. The location, shape, and magnitude of the peak in these two sets of rotation curves resemble closely those obtained by Gott (ref. 17). At both $\theta = 90^{\circ}$ and $\theta = 45^{\circ}$, the present peak rotational velocities are within 10 km-sec^{-1} of those obtained by Gott. The reader who wishes to make his own comparison with figure 4 of Gott (ref. 17) should note that the virial velocity to be used there is 227 km-sec^{-1} and recall that the initial radius is 10 kpc.

The final rotation curve for model IV is substantially different from the earlier axisymmetric work. The region of solid body rotation here extends for

only 1 or 2 kpc from the center rather than for a half dozen. Moreover, the peak in the rotational velocity occurs near 11 kpc rather than 6, and it is at least 20 km-sec^{-1} lower. None of this is at all surprising, considering the vastly different shape assumed by this model when the nonaxisymmetric forces are unleashed. On the other hand, the $t = 2$ version of the model IV rotation curve is quite similar to Gott's result. After only 2 rotations the bar is still in its infancy while the collapse phase is nearly completed. As Gott noted, the violent relaxation of the axially symmetric collapse does tend to produce an extended region of solid body rotation. A comparison between the model IV rotation curves at $t = 2$ and $t = 5$ illustrates that the violent relaxation of the bar-forming stage produces quite a different result. The other bar system, model V, appears to be tending toward a rotation curve with properties similar to that of model IV. Given the additional integrals of motion that are likely to be present in a bar system, the theoretical interpretation of the last two rotation curves in terms of violent relaxation presents more difficulties. Note here that the rotation rates of the bars in models IV and V are 16 km-sec^{-1}-kpc^{-1} and 14 km-sec^{-1}-kpc^{-1}, respectively.

Some of the data obtained for the velocity dispersions are presented in figures 60 to 65. The radial velocity dispersions for models I to III are again similar to those of Gott. They indicate a small isothermal region in the center and larger dispersions perpendicular to the equatorial plane than in it. Curiously, the present velocity dispersions have the same local maxima, for example, near $r = 7$ for model I, that were exhibited by Gott's results.

These local maxima also appear in the vertically averaged velocity dispersions, which are a cruder but more statistically reliable measure than the one presented here. For model IV, a comparison of the various velocity dispersions at $t = 2$ and at $t = 5$ gives some indication of the difference between the velocities produced by the collapse itself and those that result from the bar formation. At least in the azimuthally averaged sense displayed here, the bar is seen to have relatively little effect upon the velocity dispersions in the vertical direction while increasing those in the horizontal direction by 30 to 40 percent near the center.

We conclude this section with a discussion of some crucial observable quantities. Recent measurements of rotational velocities in ellipticals by Illingworth (ref. 21), Peterson (ref. 22), and others suggest a substantial disagreement between the relatively high rotational velocities that arise in the collisionless models which remain oblate, that is the models of Gott (refs. 17 and 18) and Wilson (ref. 35), and the surprisingly low rotational velocities which have actually been observed. Models I to III, which behave just like the corresponding models of Gott, share this deficiency.

The bar models, on the other hand, offer some hope, as has been noted by Miller and Smith (ref. 20) and by Illingworth (ref. 21). We provide here some pertinent data on model IV, a case for which the bar is nearly equilibrated. The projected isodensity contours shown in figure 66 are especially illuminating. There we have established a coordinate system relative to the rotating bar which retains the z-axis as the rotation axis but which aligns the y-axis with the largest axis of the bar (and, accordingly, places the x-axis along the shortest axis). The line-of-sight direction is thus specified by the usual

spherical angles. For instance, a viewing direction along the rotation axis has $\theta = 0^{\circ}$ while a line of sight in the equatorial plane is specified by $\theta = 90^{\circ}$. Moreover, a viewing direction which sees the bar broadside is specified by $\phi = 0^{\circ}$ and one which sees the bar along the long axis is $\phi = 90^{\circ}$. As noted earlier, if the long axis of the bar is taken to have unit length, then the vertical axis has length 0.54 while the short axis in the equatorial plane has length 0.39.

The six views shown in figure 66 certainly give the impression of an elliptical of high eccentricity. The apparent ellipticity for these and a number of other viewing directions is listed in table II. The definition $\varepsilon = 1 - b/a$,

TABLE II.- ELLIPTICITY AND VELOCITY RATIO AS A FUNCTION OF VIEWING ANGLE FOR MODEL IV

θ, deg	ϕ, deg	ε	$V_m/\sigma_v(0)$ for slit along major axis	$V_m/\sigma_v(0)$ for slit in equatorial plane
30	0	0.71	0.61	0.61
	30	.70	.54	.63
	45	.70	.47	.64
	60	.70	.35	.66
	90	.71	.10	.65
45	0	.68	.92	.92
	30	.67	.80	.91
	45	.66	.67	.89
	60	.64	.49	.87
	90	.65	.10	.83
60	0	.65	1.20	1.20
	30	.62	1.07	1.11
	45	.58	.89	1.07
	60	.57	.71	1.01
	90	.54	.10	.97
90	0	.61	1.48	1.48
	30	.56	1.29	1.29
	45	.51	1.15	1.15
	60	.28	1.07	1.07
	90	.29	.10	1.03

where a and b are the measured long and short axes, is used. The values of ε listed in table II are the average of the ellipticities for the two innermost isodensity contours. For viewing directions near the rotation axis, the ellip-

ticity is rather insensitive to the azimuthal orientation. When viewed from the equatorial plane, however, there is a substantial dependence on ϕ. This effect is more dramatic for the thin bar which arose in model IV than it would be for a flat bar, one for which the vertical axis is the smallest. In the present case the projection effects also include a sudden switch of the apparent long axis.

An important consequence of the triaxial nature of this bar is that the projected long axis of the bar can be quite misaligned with the equatorial plane. Figure 66 provides several vivid examples. All but the $\phi = 90^{\circ}$ and $\phi = 0^{\circ}$ cases have the apparent major axis substantially misaligned with the equatorial plane. This can have a sizable effect upon the observed velocities if the measurements are made only with the slit aligned along the apparent major axis. We have imposed a rectangular slit upon many projected views of model IV. This slit was 6 kpc wide and 32 kpc long and was centered upon the center of the system. The average line-of-sight velocities were computed in 1 kpc × 6 kpc portions along the slit. The peak rotational velocity V_m and the central line-of-sight velocity dispersion $\sigma_v(0)$ were then computed. These measurements were performed for slits oriented both along the apparent major axis and perpendicular to the rotation axis. The results for the ratio $U = V_m/\sigma_v(0)$ are given in table II. The slit oriented perpendicular to the rotation axis picks up the maximum rotation. As the viewing direction varies, the changes in the average line-of-sight velocities reflect not only the geometric effects which occur even in oblate models, but also the noncircular streaming motions along the bar. When just these two effects are considered, the ratio U still seems to be fairly high for most orientations. But when the shifted orientation of the apparent major axis is also taken into account, the ratio U seems much closer to observed values. Note that the ellipticities for these orientations of model IV are all on the high side so that a $U \approx 0.50$ to 0.70 appears consistent with reported measurements. Nevertheless, a rough estimate suggests that a randomly chosen viewing direction will have $U < \epsilon$ about 40 percent of the time.

The same six projections are shown for model V in figure 67. Weak spiral features are still evident at $t = 3$, indicating that the bar has not yet reached equilibrium. Note again how thin the bar is.

Figure 68 displays polar and equatorial projections for models I to III. These show both the increased flattening and the decreased central concentration caused by increasing amounts of initial rotation.

DISCUSSION AND CONCLUSIONS

Comparison of the evolution of an infinitesimally thin stellar disk with a three-dimensional stellar disk for an initially exponential radial density variation shows that the primary effect of finite thickness is a reduction in the initial growth rate of the spiral or bar instability. Vandervoort's (ref. 36) formula for the thickness correction to the dispersion relation for an infinitesimally thin disk suggests that the effective Q for the three-dimensional system is the range 1.3 to 1.4 compared with roughly 1.0 for the infinitesimally thin disk. Nevertheless, after a time of three rotational

periods the systems have evolved to essentially the same general structure. Thus, two-dimensional disk models of galaxies are appropriate for the investigation of various global, spiral structure, or instability problems associated with flat galaxies. Adding a fully self-consistent central, nonrotating, exponential core/halo component has a considerable stabilizing effect on the system. The effective Q for this second three-dimensional system is in the range 1.5 to 1.6 from $r = 5$ kpc outward and considerably higher inward. While for the two-dimensional system an outer spiral and central bar structure quickly forms, the three-dimensional system's most apparent instability is a weak spiral structure evolving from Jeans' type instabilities in the outer regions of the disk. The spiral structure for the three-dimensional disk-core/halo system is tending to dissipate by the time bar formation is well in progress, as determined from the azimuthal density variation. Thus, even for systems with large core/halo components, two-dimensional disk models appear sufficient to simulate evolution of spiral and other global structures of disklike galaxies. The primary effect of performing the simulation in three dimensions is a reduction in the growth rate of global instabilities.

The range of initial conditions for this study of the fully three-dimensional, collisionless collapse of uniform spheres of stars covered some models which remained axisymmetric and others which developed bar-shaped structures. The first four models had been treated previously by Gott in a manner which precluded the development of nonaxisymmetric features. Our results for models I to III showed that where large-scale axial symmetry was retained, even the detailed features were well represented by the strictly axisymmetric calculations. The energy distributions, density profiles, systematic velocities, and random velocities were all similar to those obtained by Gott. Moreover, no significant redistribution of angular momentum occurred, even though permitted in principle by the numerical treatment. Nevertheless, the present results for models IV and V illustrate the limitations of the axisymmetric calculation. These limits had been predicted reliably by Gott himself using the Ostriker-Peebles criterion. For model III, the ratio of kinetic energy in rotation to total potential energy was too close to the Ostriker-Peebles stability limit of 0.14 to make a definitive judgment. The present results suggest once again that the natural outcome of strong nonaxisymmetric instabilities is bar formation.

The flattest oblate system obtained here was model III, which resembles the appearance of an E2 galaxy. The bar instability of model IV prevented the development of an oblate system as flat as an E5, such as Gott had done with his constrained model. On the other hand, bar formation led to even flatter, albeit triaxial, systems. Model V, which can appear as flat as an E8, is the more extreme example.

The bar-forming models display a distinct separation between the collapse and the bar phases. The bars appear to form during or after the second collapse along the rotation axis. Prior to this time the evolution is dominated by axially symmetric collapse dynamics. Model IV provides an excellent example of this since a good deal of similarity prevails between the properties of the present model IV at $t = 2$ and the final form of the axially constrained version. This same comparison made at $t = 5$ suggests the following effects of the bar upon the detailed properties: (1) the distinct core and halo components

produced by the collapse are obliterated by the bar; (2) the density is more clearly represented as a combination of two exponentials; (3) the central region of solid body rotation is substantially reduced; (4) the dispersions of the horizontal velocity components are increased by 30 to 40 percent while the dispersions of the vertical component are nearly unaffected.

Given the recent observational data on the apparent low systematic velocities in ellipticals, the bar models seem much more viable for galaxy formation than the oblate ones. We have explored extensively the equilibrium properties of only one bar model. Although there are many viewing directions which are reconcilable with the observations (at least observations made solely along the apparent major axis), there are uncomfortably many others which would suggest high rotation. No doubt, a more satisfactory model could be constructed by using different initial conditions than those employed in model IV. Certainly less rotation should be applied and perhaps even slightly greater initial velocity dispersion.

It is clear that there is one observational test which even a finely tuned triaxial model must pass. The data in table II indicate how sensitive the measured rotation of the bar models can be to the slit orientation. Thus, for many real triaxial systems of the type modeled by the final two examples, there ought to be some slit orientations which produce substantially greater measured rotation than a slit orientation corresponding to the apparent major axis.

Langley Research Center
National Aeronautics and Space Administration
Hampton, VA 23665
March 6, 1979

APPENDIX

COMPUTER PROGRAM FOR GENERATING THE THREE-DIMENSIONAL GRAVITATIONAL POTENTIAL DISTRIBUTION OF ISOLATED GALAXIES

Mathematical Summary

The scaled gravitational potential at the center of cell (x,y,z) is defined by the triple summation over the three-dimensional array of cells

$$\phi_{x,y,z} = \sum_{i=0}^{2n-1} \sum_{j=0}^{2n-1} \sum_{k=0}^{2h-1} \rho_{i,j,k} H_{i-x,j-y,k-z} \tag{A1}$$

where

$$H_{i,j,k} = (i^2 + j^2 + k^2)^{-1/2} \quad \text{for} \quad i + j + k \neq 0$$

$$H_{0,0,0} = 1$$

and $\rho_{i,j,k}$ is the mass density in cell (i,j,k). Because direct summation is much too time consuming to be practical, the triple summation is evaluated by the convolution method using fast Fourier transforms (ref. 2). That is, the Fourier transform of the potential equals the product of the Fourier transforms of ρ and H:

$$\tilde{\phi}_{\xi,\eta,\zeta} = \tilde{\rho}_{\xi,\eta,\zeta} \tilde{H}_{\xi,\eta,\zeta} \tag{A2}$$

The gravitational potential $\phi_{x,y,z}$ is obtained by taking the inverse Fourier transform of equation (A2). Rather than the usual complex Fourier series, a real expansion is used here. For example, the Fourier transform of the density $\rho_{x,y,z}$ is given by

$$\tilde{\rho}_{\xi,\eta,\zeta} = \sum_{z=0}^{2h-1} \sum_{y=0}^{2n-1} \sum_{x=0}^{2n-1} c(x,n)\ c(y,n)\ c(z,h)\ \rho_{x,y,z}\ f(\xi,x,n)$$

$$\times\ f(\eta,y,n)\ f(\zeta,z,h) \tag{A3}$$

where

$$f(\xi,x,n) = \begin{cases} \cos\ (\pi\xi x/n) & 0 \leqq \xi \leqq n \\ \sin\ \pi(\xi - n)x/n & n < \xi \leqq 2n - 1 \end{cases}$$

$$c(x,n) = \begin{cases} 1/\sqrt{2} & \text{if } x = 0 \text{ or } x = n \\ 1 & \text{Otherwise} \end{cases}$$

The symbols n and h define the $n \times n \times h$ active array and also the $(2n) \times (2n) \times (2h)$ larger array over which the Fourier transform must be taken so that the potential for an isolated galaxy is obtained (see fig. 69). Note that the density may be nonzero only in the smaller $n \times n \times h$ array. Because of the symmetry of $H_{x,y,z}$, the Fourier transform $\tilde{H}_{\xi,\eta,\zeta}$ can be obtained by a finite cosine transform

$$\tilde{H}_{\xi,\eta,\zeta} = \sum_{z=0}^{h} \sum_{y=0}^{n} \sum_{x=0}^{n} c^2(x,n)\ c^2(y,n)\ c^2(z,h)\ H_{x,y,z}$$

$$\times \cos\ (\pi\xi x/n) \cos\ (\pi\eta y/n) \cos\ (\pi\zeta z/h) \qquad \text{(A4)}$$

for $0 \leqq \xi,\eta \leqq n$ and $0 \leqq \zeta \leqq h$, and

$$\tilde{H}_{\xi+n,\eta,\zeta} = \tilde{H}_{\xi+n,\eta+n,\zeta} = \tilde{H}_{\xi+n,\eta,\zeta+h} = \tilde{H}_{\xi+n,\eta+n,\zeta+h}$$
$$= \tilde{H}_{\xi,\eta+n,\zeta} = \tilde{H}_{\xi,\eta+n,\zeta+h} = \tilde{H}_{\xi,\eta,\zeta+h} = \tilde{H}_{\xi,\eta,\zeta}$$

The next step in obtaining the potential is to multiply $\tilde{\rho}_{\xi,\eta,\zeta}$ by $\tilde{H}_{\xi,\eta,\zeta}$ to obtain $\tilde{\phi}_{\xi,\eta,\zeta}$ (eq. (A2)).

The gravitational potential for an isolated galaxy correctly defined over the $n \times n \times h$ array is obtained by the Fourier synthesis

$$\phi_{x,y,z} = \frac{1}{N^3} \sum_{\zeta=0}^{2h-1} \sum_{\eta=0}^{2n-1} \sum_{\xi=0}^{2n-1} \tilde{\phi}_{\xi,\eta,\zeta}\ f(\xi,x,n)\ f(\eta,y,n)\ f(\zeta,z,h) \qquad \text{(A5)}$$

Note also, that since

$$\tilde{H}_{\xi,\eta,\zeta} = \tilde{H}_{\xi,\zeta,\eta} = \tilde{H}_{\eta,\xi,\zeta} = \cdots$$

different permutations of the same set of indices need not be stored. Thus, the transformed Green's function can be converted to a one-dimensional array

$$\tilde{H}_{\xi,\eta,\zeta} = \tilde{F}_n$$

where different permutations of ξ,η,ζ are stored in the same location n given by

$$n = \sum_{i=2}^{\xi} \frac{i}{2}(i - 1) + \frac{\eta}{2}(\eta - 1) + \zeta$$

$$= \xi(\xi - 1)(2\xi - 1)/12 + \xi(\xi - 1)/4 + \eta(\eta - 1)/2 + \zeta$$

Computer Program Subroutine Which Uses Only Core Storage

At the end of this appendix, FORTRAN listing I is given of computer program GETPHI which may be used to obtain the potential ϕ by use of a $(2n) \times (2n) \times h$ array of cells. The variable I2A defines the x and y dimensions, and I3A the z dimension of the array used for the potential calculations. When the subroutine GETPHI is called, RHO(I,J,K) contains the mass density and GETPHI places the values of the corresponding gravitational potential in RHO(I,J,K). The subroutine FTRANS(I,I2B), written by R. Hockney (ref. 37), performs a finite Fourier analysis or synthesis on the common input array Z and places the result in the common output array Y. The subroutine performs a cosine analysis for I = 2, a periodic analysis for I = 3, and a periodic synthesis for I = 4. The subroutine GETSET(I,I2B) initializes FTRANS and is called every time the arguments of FTRANS(I,I2B) are changed. The Fourier transform $\tilde{H}_{\xi,\eta,\zeta}$ is calculated on an $(n + 1) \times (n + 1) \times (h + 1)$ array only the first time that the subroutine is called and is kept in storage for subsequent use.

The Fourier transform of $\rho_{x,y,z}$ in the x-direction is generated by obtaining the partial transform $\tilde{\rho}_{\xi,y,z}$ for $0 \leq \xi \leq 2n - 1$, $0 \leq y \leq n - 1$, and $0 \leq z \leq h - 1$. The transform $\tilde{\rho}_{\xi,y,z}$ is zero outside of this region because $\rho_{x,y,z}$ is nonzero only over the $n \times n \times h$ active array. Next, the Fourier transform of $\tilde{\rho}_{\xi,y,z}$ is performed in the y-direction obtaining the x-y partial transform $\tilde{\rho}_{\xi,\eta,z}$ for $0 \leq \xi \leq 2n - 1$, $0 \leq \eta \leq 2n - 1$, and $0 \leq z \leq h - 1$. Since $\tilde{\rho}_{\xi,\eta,z}$ is zero for $h \leq z \leq 2h - 1$, by use of one-dimensional arrays Y

and Z the Fourier transform of $\tilde{\rho}_{\xi,\eta,z}$ can be taken in the z-direction to obtain the total transform $\tilde{\rho}_{\xi,\eta,\zeta}$ for $0 \leqq \zeta \leqq 2h - 1$. Next, $\tilde{\rho}_{\xi,\eta,\zeta}$ is multiplied by $\tilde{H}_{\xi,\eta,\zeta}$ to obtain $\tilde{\phi}_{\xi,\eta,\zeta}$ and the inverse Fourier transform is performed in the z-direction. The resulting partial x-y transform $\tilde{\phi}_{\xi,\eta,z}$ is placed in the $2n \times 2n \times h$ RHO(I,J,K) array for $0 \leqq \xi \leqq 2n - 1$, $0 \leqq \eta \leqq 2n - 1$, and $0 \leqq z \leqq h - 1$ with values for $h \leqq z \leqq 2h - 1$ discarded. (The use of these one-dimensional arrays was first presented in ref. 23 for a two-dimensional potential solver.) Next, the inverse Fourier transform of $\tilde{\phi}_{\xi,\eta,z}$ is generated in the y-direction to obtain the x partial transform

$\tilde{\phi}_{\xi,y,z}$ for $0 \leqq \xi \leqq 2n - 1$, $0 \leqq y \leqq n - 1$, and $0 \leqq z \leqq h - 1$. The final step is to perform the inverse Fourier transform in the x-direction for $0 \leqq y \leqq n - 1$ and $0 \leqq z \leqq h - 1$ to yield the correct gravitational potential $\phi_{x,y,z}$ for an isolated galaxy over the $n \times n \times h$ array.

Overlayed Computer Program Which Uses Core and Disk Storage

Use of program GETPHI, with the $64 \times 64 \times 16$ active density/potential array used in this report would have necessitated the dimensioning of the RHO array at $128 \times 128 \times 16$ and the H array at $65 \times 65 \times 17$. Since such large dimensions would have precluded use of the CDC 6600 computer, program GETPHI was modified to include use of overlayed programs and disk storage resulting in a maximum core storage requirement at any one time equal to about five-fourths of the active array. The listing of this program (listing II) includes (1) a section of an initializing overlay in which relevant constants are computed, (2) a section of the star advancing overlay in which "chunks" of the density array are written on appropriate disk files, (3) another section of the star advancing overlay in which chunks of the computed potential array are read from disk files, (4) the GETH overlay which computes $\tilde{H}$, and (5) the GETPHI overlay which computes the potential array from the density array. Figures 70 through 74 are presented to facilitate description of the overlayed program. For clarity, figures 69 through 74 are drawn for an active array dimensioned $n \times n \times h = 8 \times 8 \times 4$; table III compares the array dimensions of these figures with those of the overlayed program.

The method used is the alignment in the direction of transformation of four identical arrays named RHO1, RHO2, RHO3, and RHO4, each of which is dimensioned $(n/2) \times (n/2) \times h$ within the GETPHI overlay. (See figs. 70 and 73.) The active array is dimensioned as the PHI array within the initializing and star advancing overlays (see figs. 69 and 71) but is not dimensioned within the GETPHI overlay. As figure 70 suggests, the chunks RHO1, RHO2, RHO3, and RHO4 may be visualized as forming either a row or a column of the lower half ($0 \leqq z \leqq h - 1$) of the extended array. Switching the lineup to a different row or column is accomplished by storing the array associated with each chunk location on a separate file; these eight files are also indicated in figure 70.

As shown in figure 71, one chunk size array named OI is dimensioned in the initializing and star advancing overlays. Chunks of the active array are transferred between the PHI array of these overlays and the arrays RHO1, RHO2, RHO3, and RHO4 of the GETPHI overlay via "do loop" transfer to/from the OI array and storage on files 1, 2, 5, and 6.

TABLE III.- ARRAY DIMENSIONS FOR PROGRAM OF LISTING II

Array name	General dimensions (a)	Dimensions used in actual runs	Dimensions shown in figs. 69-74	Overlays in which dimensioned		
				Star advancing and initializing	GETH	GETPHI
PHI (active)	n × n × h	64 × 64 × 16	8 × 8 × 4	X		
OI	(n/2) × (n/2) × h	32 × 32 × 16	4 × 4 × 4	X		
H	(n + 1) × (n + 1) × (h + 1)	65 × 65 × 17	9 × 9 × 5		X	
HH	(n/2) × (n/2) × (h + 1)	32 × 32 × 17	4 × 4 × 5		X	X
[b]HN21	(n + 1) × (h + 1)	65 × 17	9 × 5		X	X
RHO1, RHO2, RHO3, RHO4	(n/2) × (n/2) × h	32 × 32 × 16	4 × 4 × 4			X
Extended PHI	(2n) × (2n) × (2h)	128 × 128 × 32	16 × 16 × 8	(c)		

[a]The notation a × b × c represents the array dimensions of the subscripts x, y, and z, respectively (or the subscripts ξ, η, and ζ, respectively, of the transformed array) such that a × b × c equals the total number of array elements. The FORTRAN variables N and NH are equal to 2n and 2h, respectively.

[b]HN21 is a two-dimensional array containing a boundary plane of $\tilde{H}_{\xi,\eta,\zeta}$ elements. Its first subscript corresponds to ξ or η equivalently, while its second subscript corresponds to ζ.

[c]Not actually dimensioned. While the program uses smaller arrays in order to avoid dimensioning the (2n) × (2n) × (2h) extended PHI array of figure 69, its mathematical existence is necessary for the Fourier solution of the potential of an isolated galaxy.

APPENDIX

At the beginning of a program run, the GETH overlay computes $\tilde{H}$ in the $(n + 1) \times (n + 1) \times (h + 1)$ H array in the same manner as listing I. All of $\tilde{H}_{\xi,\eta,\zeta}$, except for two boundary planes of elements ($\xi = n$, $0 \leqq \eta \leqq n$, $0 \leqq \zeta \leqq h$, and $0 \leqq \xi \leqq n$, $\eta = n$, $0 \leqq \zeta \leqq h$) is then transferred in portions via "do loop" to the $(n/2) \times (n/2) \times (h + 1)$ HH array from which it is written on disk file 9 (see fig. 72). Elements of one boundary plane of $\tilde{H}_{\xi,\eta,\zeta}$ ($\xi = n$, $0 \leqq \eta \leqq n$, $0 \leqq \zeta \leqq h$) are transferred to the $(n + 1) \times (h + 1)$ HN21 array which is in common with the GETPHI overlay; the ζ-η transpose of that boundary plane is equal to the other boundary plane ($0 \leqq \xi \leqq n$, $\eta = n$, $0 \leqq \zeta \leqq h$) because of the symmetry of $\tilde{H}$ across the $\xi=\eta$ diagonal plane. During each potential solution the portions of $\tilde{H}$ on file 9 are read sequentially into an $(n/2) \times (n/2) \times (h + 1)$ HH array of the GETPHI overlay from which $\tilde{H}$ elements, along with those in the HN21 array, are multiplied with $\tilde{\rho}$. This sequence (listed in table IV) utilizes the symmetry and periodicity of $\tilde{H}$ (eq. (A4)) to provide a full set of $(2n) \times (2n) \times (2h)$ $\tilde{H}$ elements to the GETPHI overlay in a manner which minimizes the reading of file 9.

TABLE IV.- STORAGE OF THE FOURIER TRANSFORMED GREEN'S FUNCTION $\tilde{H}$ ON DISK FILE 9

[Program of listing II]

Record no. of file 9	Storage sequence within GETH overlay (a)	Use sequence within GETPHI overlay (b)
1	A	(1,1), (1,3)
2	B	(1,2), (1,4), (3,2), (3,4)
3	A	(3,1), (3,3)
4	C	(2,1), (2,3)
5	D	(2,2), (2,4), (4,2), (4,4)
6	C	(4,1), (4,3)

[a]Within the GETH overlay, this is the location in the H array (as designated by letters A-D of fig. 72) from which "do loop" transfer is made to the HH array followed by writing on the indicated record of disk file 9.

[b]Following reading of the indicated record of disk file 9 into the HH array within the GETPHI overlay, this is the sequence of locations in the extended PHI array (as designated by "chunks" (IROW,JCOLUMN) of fig. 70) upon which z-direction one-dimensional array operations are performed. These operations include multiplications by $\tilde{H}$, the appropriate portion of which is now contained in the HH array. This method minimizes reading of file 9 by using the periodicity and symmetry of $\tilde{H}$.

APPENDIX

The GETPHI overlay consists of subroutines ANLX(JCOLUMN), ANLSYN(IROW), and SYNX(JCOLUMN) which dimension in common the arrays HH, HN21, RHO1, RHO2, RHO3, and RHO4, as pictured in figure 73. Figure 74 indicates the lineup of chunks associated with each call to a subroutine. The potential solution is mathematically identical with that described for listing I. Calling ANLX(1) and ANLX(2) performs the Fourier transform of $\rho_{x,y,z}$ in the x-direction to form $\tilde{\rho}_{\xi,y,z}$. Calling ANLSYN(1), ANLSYN(3), ANLSYN(2), and ANLSYN(4) in sequence performs the following: (1) a Fourier transform of $\tilde{\rho}_{\xi,y,z}$ in the y- and z-directions to form $\tilde{\rho}_{\xi,\eta,\zeta}$; (2) multiplication with $\tilde{H}_{\xi,\eta,\zeta}$ to form $\tilde{\phi}_{\xi,\eta,\zeta}$; and (3) the inverse Fourier transform of $\tilde{\phi}_{\xi,\eta,\zeta}$ in the z- and y-directions to form $\tilde{\phi}_{\xi,y,z}$. Calling SYNX(1) and SYNX(2) performs the inverse Fourier transform of $\tilde{\phi}_{\xi,y,z}$ in the x-direction to form $\phi_{x,y,z}$. The GETPHI overlay is outlined in more detail in table V.

Comparison of the Two Computer Programs

The overlayed program (listing II) is preferable to the original program (listing I) because the addition of some peripheral processing time and a small increase in central processing time are much more than compensated by a 75-percent decrease in the required core storage. The maximum number of active array elements dimensionable on the CDC 6600 with the original program is 16384 (e.g., 32 × 32 × 16) and with the overlayed program, 65536 (e.g., 64 × 64 × 16); the latter program can have other potentially useful active array dimensions of 32 × 32 × 8, 32 × 32 × 16, and 32 × 32 × 32. Solution of the 64 × 64 × 16 active array by the CDC 6600 requires about 300 000 (octal) words of core storage and with $\tilde{H}$ already computed takes about 75 seconds of central processing time.

TABLE V.- OUTLINE OF THE GETPHI OVERLAY OF THE PROGRAM OF LISTING II

[Refer to figure 74 for orientation of arrays RHO1, RHO2, RHO3, and RHO4 and to figure 70 for file numbers corresponding to the locations of these arrays]

	Listing II line nos.
A. CALL ANLX(1) (fig. 74(a))	
1. Read files 1 and 2 into RHO1 and RHO2, respectively	299-302
2. Set RHO3 = RHO4 = 0	316-317
3. Perform Fourier transform in x-direction over RHO1, RHO2, RHO3, and RHO4: $\rho_{x,y,z} \rightarrow \tilde{\rho}_{\xi,y,z}$	310-323
4. Write RHO1, RHO2, RHO3, and RHO4 onto files 1, 2, 3, and 4, respectively	325-332
B. CALL ANLX(2) (fig. 74(b))	
1. Read files 5 and 6 into RHO1 and RHO2, respectively	305-308
2. Same as steps A.2 and A.3	
3. Write RHO1, RHO2, RHO3, and RHO4 onto files 5, 6, 7, and 8, respectively	335-342
C. CALL ANLSYN(1) (fig. 74(c))	
1. Read files 1 and 5 into RHO1 and RHO2, respectively	353-356
2. Set RHO3 = RHO4 = 0	382-383
3. Perform Fourier transform in y-direction over RHO1, RHO2, RHO3, and RHO4: $\tilde{\rho}_{\xi,y,z} \rightarrow \tilde{\rho}_{\xi,\eta,z}$	376-389
4. Read record 1 of file 9 into HH	393
5. For each one-dimensional array in z-direction of which RHO1 is composed	394-407, 477-483
a. Transfer to one-dimensional array Z, dimensioned at least 2h + 1	
b. Set Z = 0 for $z \geq h$	
c. Perform Fourier transform in z-direction over Z for $0 \leq z \leq 2h - 1$ with the result appearing in one-dimensional array Y: $\tilde{\rho}_{\xi,\eta,z} \rightarrow \tilde{\rho}_{\xi,\eta,\zeta}$	
d. Multiply Y by $\tilde{H}_{\xi,\eta,\zeta}$ to form $\tilde{\phi}_{\xi,\eta,\zeta} = \tilde{\rho}_{\xi,\eta,\zeta} \tilde{H}_{\xi,\eta,\zeta}$	
e. Perform inverse Fourier transform in z-direction over Y and store result for $0 \leq z \leq h - 1$ in RHO1: $\tilde{\phi}_{\xi,\eta,\zeta} \rightarrow \tilde{\phi}_{\xi,\eta,z}$	
6. Repeat step C.5 for RHO3	426-454, 471-483
7. Read record 2 of file 9 into HH	410
8. Repeat step C.5 for RHO2 and RHO4	411-424, 456-469, 477-483
9. Perform inverse Fourier transform in y-direction over RHO1, RHO2, RHO3, and RHO4: $\tilde{\phi}_{\xi,\eta,z} \rightarrow \tilde{\phi}_{\xi,y,z}$	486-497
10. Write RHO1 and RHO2 onto files 1 and 5, respectively	500-503

TABLE V.- Concluded

	Listing II line nos.
D. CALL ANLSYN(3) (fig. 74(e))	
1. Read files 3 and 7 into RHO1 and RHO2, respectively	365-368
2. Same as steps C.2 to C.9 except for sequencing of reading tape 9 into HH and the z-directional operations. Table IV details this sequencing.	
3. Write RHO1 and RHO2 onto files 3 and 7, respectively	512-515
E. CALL ANLSYN(2) (fig. 74(d))	
1. Same as step D except that files 2 and 6 correspond to RHO1 and RHO2, respectively, for read and write operations	
F. CALL ANLSYN(4) (fig. 74(f))	
1. Same as step D except that files 4 and 8 correspond to RHO1 and RHO2, respectively, for read and write operations	
G. CALL SYNX(1) (fig. 74(a))	
1. Read files 1, 2, 3, and 4 into RHO1, RHO2, RHO3, and RHO4, respectively	530-537
2. Perform inverse Fourier transform in x-direction over RHO1, RHO2, RHO3, and RHO4: $\tilde{\phi}_{\xi,y,z} \rightarrow \phi_{x,y,z}$	550-560
3. Write RHO1 and RHO2 onto files 1 and 2, respectively	562-565
H. CALL SYNX(2) (fig. 74(b))	
1. Read files 5, 6, 7, and 8 into RHO1, RHO2, RHO3, and RHO4, respectively	540-547
2. Same as step G.2	
3. Write RHO1 and RHO2 onto files 5 and 6, respectively	568-571

APPENDIX

LISTING I.- SUBROUTINE GETPHI FOR CALCULATING THE THREE-DIMENSIONAL GRAVITATIONAL POTENTIAL USING ONLY CORE STORAGE

```
      SUBROUTINE GETPHI
      COMMON Z(1025),Y(1025),RHO(64,64,16),I2A,I3A,ITEST
      DIMENSION H(33,33,17)
      IF(ITEST.EQ.0) GO TO 11
      ITEST=0
      I2B=I2A-1
      N=2**I2A
      NO2=N/2
      N21=NO2+1
      I3B=I3A-1
      NH=2**I3A
      NHO2=NH/2
      NH21=NHO2+1
      RNI=1./(N*N*NH)
      DO 1 K=1,NH21
      DO 1 J=1,N21
      DO 1 I=1,N21
      RI=(K-1)*(K-1)+(J-1)*(J-1)+(I-1)*(I-1)
      IF(RI.LT.1.) RI=1.
      H(I,J,K)=RNI/SQRT(RI)
    1 CONTINUE
      CALL GETSET(2,I2B)
      DO 2 K=1,NH21
      DO 2 J=1,N21
      DO 3 I=1,N21
    3 Z(I)=H(I,J,K)
      CALL FTRANS(2,I2B)
      DO 4 I=1,N21
    4 H(I,J,K)=Y(I)
    2 CONTINUE
      DO 5 K=1,NH21
      DO 5 I=1,N21
      DO 6 J=1,N21
    6 Z(J)=H(I,J,K)
      CALL FTRANS(2,I2B)
      DO 7 J=1,N21
    7 H(I,J,K)=Y(J)
    5 CONTINUE
      CALL GETSET(2,I3B)
      DO 10 J=1,N21
      DO 10 I=1,N21
      DO 8 K=1,NH21
    8 Z(K)=H(I,J,K)
      CALL FTRANS(2,I3B)
      DO 9 K=1,NH21
    9 H(I,J,K)=Y(K)
   10 CONTINUE
   11 CONTINUE
      WRITE(6,43)
   43 FORMAT(10H  H(I,J,K))
      DO  42 K=1,NH21
      DO 42 J=1,N21
      WRITE(6,41) J,K
      WRITE(6,40) (H(I,J,K),I=1,N21)
   41 FORMAT(14H  I=1,N21   J=13,5H   K=13)
   40 FORMAT(2H  8E16.8)
   42 CONTINUE
      CALL GETSET(3,I2A)
      DO 14 K=1,NHO2
      DO 14 J=1,NO2
      DO 12 I=1,N
   12 Z(I)=RHO(I,J,K)
      CALL FTRANS(3,I2A)
      DO 13 I=1,N
   13 RHO(I,J,K)=Y(I)
   14 CONTINUE
```

```
      DO 17 K=1,NHO2
      DO 17 I=1,N
      DO 15 J=1,N
   15 Z(J)=RHO(I,J,K)
      CALL FTRANS(3,12A)
      DO 16 J=1,N
   16 RHO(I,J,K)=Y(J)
   17 CONTINUE
      DO 20 I=1,N
      DO 20 J=1,N
      DO 18 K=1,NHO2
      Z(K)=RHO(I,J,K)
   18 Z(K+NHO2)=0.
      CALL GETSET(3,13A)
      CALL FTRANS(3,13A)
      IF(I.GT.N21.AND.J.LE.N21) GO TO 22
      IF(I.LE.N21.AND.J.GT.N21) GO TO 24
      IF(I.GT.N21.AND.J.GT.N21) GO TO 26
      DO 19 K=1,NHO2
      Z(K)=Y(K)*H(I,J,K)
   19 Z(K+NHO2)=Y(K+NHO2)*H(I,J,K)
      Z(1)=Y(1)*H(I,J,1)
      Z(NH21)=Y(NH21)*H(I,J,NH21)
      GO TO 21
   22 DO 23 K=2,NHO2
      Z(K)=Y(K)*H(I-NO2,J,K)
   23 Z(K+NHO2)=Y(K+NHO2)*H(I-NO2,J,K)
      Z(1)=Y(1)*H(I-NO2,J,1)
      Z(NH21)=Y(NH21)*H(I-NO2,J,NH21)
      GO TO 21
   24 DO 25 K=2,NHO2
      Z(K)=Y(K)*H(I,J-NO2,K)
   25 Z(K+NHO2)=Y(K+NHO2)*H(I,J-NO2,K)
      Z(1)=Y(1)*H(I,J-NO2,1)
      Z(NH21)=Y(NH21)*H(I,J-NO2,NH21)
      GO TO 21
   26 DO 27 K=2,NHO2
      Z(K)=Y(K)*H(I-NO2,J-NO2,K)
   27 Z(K+NHO2)=Y(K+NHO2)*H(I-NO2,J-NO2,K)
      Z(1)=Y(1)*H(I-NO2,J-NO2,1)
      Z(NH21)=Y(NH21)*H(I-NO2,J-NO2,NH21)
   21 CONTINUE
      CALL GETSET(4,13A)
      CALL FTRANS(4,13A)
      DO  28 K=1,NHO2
   28 RHO(I,J,K)=Y(K)
   20 CONTINUE
      CALL GETSET(4,12A)
      DO 29 K=1,NHO2
      DO 29 J=1,N
      DO 30 I=1,N
   30 Z(I)=RHO(I,J,K)
      CALL FTRANS(4,12A)
      DO 31 I=1,N
   31 RHO(I,J,K)=Y(I)
   29 CONTINUE
      DO 32 K=1,NHO2
      DO 32 I=1,NO2
      DO 33 J=1,N
   33 Z(J)=RHO(I,J,K)
      CALL FTRANS(4,12A)
      DO 34 J=1,NO2
   34 RHO(I,J,K)=Y(J)
   32 CONTINUE
      RETURN
      END
```

APPENDIX

LISTING II.- OVERLAYS FOR CALCULATING THE THREE-DIMENSIONAL GRAVITATIONAL POTENTIAL USING CORE AND DISK STORAGE

```
C THE FOLLOWING IS THE SECTION OF AN INITIALIZING OVERLAY IN WHICH CONSTANTS 001
C RELATED TO THE DIMENSIONS OF THE PHI (DENSITY/POTENTIAL) ARRAY ARE COM-    002
C PUTED.  IT IS CALLED ONCE AT THE BEGINNING OF A PROGRAM RUN.  IN THIS      003
C LISTING THE VALUES OF I2A, I3A AND THE DIMENSION AND LABELED COMMON        004
C STATEMENTS ARE SET FOR AN ACTIVE PHI ARRAY DIMENSIONED 64 BY 64 BY 16.     005
      I2A=7                                                                  006
      I3A=5                                                                  007
      I2B=I2A-1                                                              008
      I3B=I3A-1                                                              009
      N=2**I2A                                                               010
      NO2=N/2                                                                011
      N21=NO2+1                                                              012
      NO4=N/4                                                                013
      N34=NO2+NO4                                                            014
      NH=2**I3A                                                              015
      NH02=NH/2                                                              016
      NH21=NH02+1                                                            017
C                                                                            018
C                                                                            019
C                                                                            020
C ***************************************************************************021
C ***************************************************************************022
C THE FOLLOWING IS THE SECTION OF THE STAR ADVANCING OVERLAY IN WHICH CHUNKS 023
C OF THE PHI ARRAY (CONTAINING THE DENSITY MESH) ARE WRITTEN ONTO DISK FILES 024
C 1,2,5 AND 6.  THE STAR ADVANCING OVERLAY IS CALLED ONCE PER TIME STEP.     025
      DIMENSION PHI(64,64,16),OI(32,32,16)                                   026
      DO 520 K=1,NH02                                                        027
      DO 520 J=1,NO4                                                         028
      DO 520 I=1,NO4                                                         029
  520 OI(I,J,K)=PHI(I,J,K)                                                   030
      WRITE(1) OI                                                            031
      REWIND 1                                                               032
      DO 525 K=1,NH02                                                        033
      DO 525 J=1,NO4                                                         034
      DO 525 I=1,NO4                                                         035
  525 OI(I,J,K)=PHI(I,NO4+J,K)                                               036
      WRITE(5) OI                                                            037
      REWIND 5                                                               038
      DO 530 K=1,NH02                                                        039
      DO 530 J=1,NO4                                                         040
      DO 530 I=1,NO4                                                         041
  530 OI(I,J,K)=PHI(NO4+I,J,K)                                               042
      WRITE(2) OI                                                            043
      REWIND 2                                                               044
      DO 535 K=1,NH02                                                        045
      DO 535 J=1,NO4                                                         046
      DO 535 I=1,NO4                                                         047
  535 OI(I,J,K)=PHI(NO4+I,NO4+J,K)                                           048
      WRITE(6) OI                                                            049
      REWIND 6                                                               050
C                                                                            051
C                                                                            052
C                                                                            053
C*************************************************************************** 054
C*************************************************************************** 055
C THE FOLLOWING IS THE SECTION OF THE STAR ADVANCING OVERLAY IN WHICH CHUNKS 056
C OF THE PHI ARRAY (CONTAINING THE POTENTIAL MESH) ARE READ FROM DISK FILES  057
C 1,2,5 AND 6.                                                               058
```

```
      DIMENSION PHI(64,64,16),OI(32,32,16)                                059
      READ(1) OI                                                          060
      REWIND 1                                                            061
      DO 30 K=1,NH02                                                      062
      DO 30 J=1,NO4                                                       063
      DO 30 I=1,NO4                                                       064
   30 PHI(I,J,K)=OI(I,J,K)                                                065
      READ(5) OI                                                          066
      REWIND 5                                                            067
      DO 40 K=1,NH02                                                      068
      DO 40 J=1,NO4                                                       069
      DO 40 I=1,NO4                                                       070
   40 PHI(I,NO4+J,K)=OI(I,J,K)                                            071
      READ(2) OI                                                          072
      REWIND 2                                                            073
      DO 50 K=1,NH02                                                      074
      DO 50 J=1,NO4                                                       075
      DO 50 I=1,NO4                                                       076
   50 PHI(NO4+I,J,K)=OI(I,J,K)                                            077
      READ(6) OI                                                          078
      REWIND 6                                                            079
      DO 60 K=1,NH02                                                      080
      DO 60 J=1,NO4                                                       081
      DO 60 I=1,NO4                                                       082
   60 PHI(NO4+I,NO4+J,K)=OI(I,J,K)                                        083
C                                                                         084
C                                                                         085
C                                                                         086
C*************************************************************************087
C*************************************************************************088
C THE FOLLOWING IS THE GETH OVERLAY.  WHICH COMPUTES AND STORES THE TRANS-089
C FORMED GREENS FUNCTION.  IT IS CALLED ONCE AT THE BEGINNING OF A PROGRAM 090
C RUN.                                                                    091
      OVERLAY(IFILE,4,0)                                                  092
      PROGRAM GETH                                                        093
C THIS OVERLAY PERFORMS A COSINE ANALYSIS OF THE THREE-DIMENSIONAL GREENS 094
C FUNCTION ARRAY.  IT THEN WRITES CHUNKS OF THIS ARRAY ON DISK FILE 9 IN THE 095
C ORDER IN WHICH THEY WILL BE READ INTO THE HH ARRAY DURING THE GETPHI    096
C OVERLAY.  VALUES FOR I=N/2+1 AND J=N/2+1 ARE TRANSFERRED TO THE HN21 ARRAY 097
C WHICH IS IN COMMON WITH THE GETPHI OVERLAY.                             098
      COMMON/ALLCOM/N,NO2,N21,NO4,N34,NH,NH02,NH21,I2A,I2B,I3A,I3B        099
      COMMON/HN21COM/HN21(65,17)                                          100
      COMMON Z(1025), Y(1025)                                             101
      DIMENSION H(65,65,17),HH(32,32,17)                                  102
      RNI=1./(N*N*NH)                                                     103
      DO 1 K=1,NH21                                                       104
      DO 1 J=1,N21                                                        105
      DO 1 I=1,N21                                                        106
      RI=(K-1)*(K-1)+(J-1)*(J-1)+(I-1)*(I-1)                              107
      IF(RI.LT.1.) RI=1.                                                  108
      H(I,J,K)=RNI/SQRT(RI)                                               109
    1 CONTINUE                                                            110
      CALL GETSET(2,I2B)                                                  111
      DO 2 K=1,NH21                                                       112
      DO 2 J=1,N21                                                        113
      DO 3 I=1,N21                                                        114
    3 Z(I)=H(I,J,K)                                                       115
```

```
      CALL FTRANS(2,12B)                                          116
      DO 4 I=1,N21                                                117
    4 H(I,J,K)=Y(I)                                               118
    2 CONTINUE                                                    119
      DO 5 K=1,NH21                                               120
      DO 5 I=1,N21                                                121
      DO 6 J=1,N21                                                122
    6 Z(J)=H(I,J,K)                                               123
      CALL FTRANS(2,12B)                                          124
      DO 7 J=1,N21                                                125
    7 H(I,J,K)=Y(J)                                               126
    5 CONTINUE                                                    127
      CALL GETSET(2,13B)                                          128
      DO 10 J=1,N21                                               129
      DO 10 I=1,N21                                               130
      DO 8 K=1,NH21                                               131
    8 Z(K)=H(I,J,K)                                               132
      CALL FTRANS(2,13B)                                          133
      DO 9 K=1,NH21                                               134
    9 H(I,J,K)=Y(K)                                               135
   10 CONTINUE                                                    136
      DO 30 I=1,N04                                               137
      DO 30 J=1,N04                                               138
      DO 30 K=1,NH21                                              139
   30 HH(I,J,K)=H(I,J,K)                                          140
      WRITE(9) HH                                                 141
      DO 35 I=1,N04                                               142
      DO 35 J=1,N04                                               143
      DO 35 K=1,NH21                                              144
   35 HH(I,J,K)=H(I,N04+J,K)                                      145
      WRITE(9) HH                                                 146
      DO 40 I=1,N04                                               147
      DO 40 J=1,N04                                               148
      DO 40 K=1,NH21                                              149
   40 HH(I,J,K)=H(I,J,K)                                          150
      WRITE(9) HH                                                 151
      DO 45 I=1,N04                                               152
      DO 45 J=1,N04                                               153
      DO 45 K=1,NH21                                              154
   45 HH(I,J,K)=H(N04+I,J,K)                                      155
      WRITE(9) HH                                                 156
      DO 50 I=1,N04                                               157
      DO 50 J=1,N04                                               158
      DO 50 K=1,NH21                                              159
   50 HH(I,J,K)=H(N04+I,N04+J,K)                                  160
      WRITE(9) HH                                                 161
      DO 55 I=1,N04                                               162
      DO 55 J=1,N04                                               163
      DO 55 K=1,NH21                                              164
   55 HH(I,J,K)=H(N04+I,J,K)                                      165
      WRITE(9) HH                                                 166
      REWIND 9                                                    167
      DO 15 K=1,NH21                                              168
      DO 15 I=1,N21                                               169
   15 HN21(I,K)=H(I,N21,K)                                        170
      RETURN                                                      171
      END                                                         172
```

```
C                                                                               173
C                                                                               174
C                                                                               175
C*******************************************************************************176
C*******************************************************************************177
C THE FOLLOWING IS THE GETPHI OVERLAY. WHICH COMPUTES THE POTENTIAL MESH.       178
C IT REPLACES CHUNKS OF DENSITY STORED ON DISK FILES 1.2.5 AND 6 WITH           179
C CORRESPONDING CHUNKS OF THE POTENTIAL MESH.  IT IS CALLED ONCE PER TIME       180
C STEP.                                                                         181
      OVERLAY(GFILE.5.0)                                                        182
      PROGRAM GETPHI                                                            183
C THIS OVERLAY SOLVES FOR THE POTENTIAL MESH (DIMENSIONED N/2 BY N/2 BY         184
C NH/2) DUE TO A DENSITY MESH (DIMENSIONED N/2 BY N/2 BY NH/2) BY DOING A       185
C PERIODIC ANALYSIS OF THE DENSITY AND THEN A PERIODIC SYNTHESIS OF THE         186
C PRODUCT OF THE TRANSFORMED GREENS FUNCTION (DIMENSIONED (N/2+1) BY (N/2+1)    187
C BY (NH/2+1)) AND THE TRANSFORMED DENSITY.  FORMALLY SPEAKING. EACH OF THE     188
C TRANSFORMS (EXCEPT THE COSINE ANALYSIS OF THE GREENS FUNCTION. WHICH IS       189
C PERFORMED IN THE GETH OVERLAY) REQUIRES AN ARRAY DIMENSIONED N BY N BY        190
C NH.  TO REDUCE CORE STORAGE THIS OVERLAY PERFORMS THESE TRANSFORMS IN         191
C CHUNKS BY THE ALIGNMENT OF FOUR SMALLER ARRAYS NAMED RHO1. RHO2. RHO3. AND   192
C RHO4. EACH OF WHICH IS DIMENSIONED N/4 BY N/4 BY NH/2.  THE CHUNKS OF THE    193
C LOWER HALF (1 .LE. Z .LE. NH/2) OF THE EXTENDED ARRAY NOT IN CORE AT ANY      194
C ONE TIME ARE STORED ON DISK FILES 1 THROUGH 8.  THE FOLLOWING ARE TWO TOP     195
C VIEWS OF THE LOWER HALF OF THE EXTENDED ARRAY.  BOTH OF THESE VIEWS           196
C DESIGNATE THE CHUNKS AS IROW AND JCOLUMN.   IROW 1 AND 2 OF JCOLUMN           197
C 1 AND 2 CONSTITUTE THE ACTIVE MESH.  IN THE DIAGRAM ON THE LEFT THE           198
C NUMBERS WITHIN THE CHUNKS OF JCOLUMN 1 AND 2 INDICATE THE DISK FILES ON       199
C WHICH THOSE CHUNKS ARE STORED. (NO DISK STORAGE IS REQUIRED FOR JCOLUMN 3     200
C OR 4.)  REFERRING TO THE DIAGRAM ON THE RIGHT. THE NUMBERS WITHIN THE         201
C CHUNKS ARE THE ORDER IN WHICH CHUNKS OF THE TRANSFORMED DENSITY ARE           202
C MUTIPLIED (ELEMENT BY ELEMENT) BY THE APPROPRIATE PORTION OF THE              203
C TRANSFORMED GREENS FUNCTION WHICH HAS BEEN READ FROM DISK FILE 9 INTO         204
C ARRAY HH(N/4.N/4.NH/2+1).  (AN EXCEPTION IS THE SET OF TRANSFORMED GREENS     205
C FUNCTION BOUNDARY VALUES FOR I=N/2+1 AND J=N/2+1 WHICH REMAIN AT ALL TIMES    206
C IN COMMON IN THE ARRAY HN21(N/2+1.NH/2+1).)  A PLUS IN A CHUNK INDICATES      207
C THAT NEW VALUES MUST BE READ INTO ARRAY HH BEFORE THAT CHUNK IS MULTIPLIED    208
C BY HH.  THIS SYSTEM MINIMIZES PERIPHERAL PROCESS TIME BY UTILIZING THE        209
C PERIODICITY OF THE TRANSFORMED GREENS FUNCTION.                               210
C                                                                               211
C                                                                               212
C                                                                               213
C     TWO TOP VIEWS OF LOWER HALF OF EXTENDED MESH(N BY N BY NH/2) - IROW 1     214
C         AND 2 OF JCOLUMN 1 AND 2 CONSTITUTE THE ACTIVE MESH(N/2 BY N/2 BY     215
C         NH/2).  THE DIRECTIONS ARE X(I) AND OMEGAX(I) - DOWN ON PAGE.         216
C         Y(J) AND OMEGAY(J) - TO RIGHT ON PAGE. Z(K) AND OMEGAZ(K) - OUT OF    217
C         PAGE.                                                                 218
C                                                                               219
C                                                                               220
C                        JCOLUMN                                  JCOLUMN      221
C                      1   2   3   4                          1   2   3   4     222
C                                                                               223
C                    **********                               **********         224
C                    *   *   *   *   *                        * + * + *   *   *  225
C           IROW=1   * 1 * 5 *   *   *              IROW=1   * 1 * 3 * 2 * 4 *  226
C                    **********                               **********         227
C                    *   *   *   *   *                        * + * + *   *   *  228
C           IROW=2   * 2 * 6 *   *   *              IROW=2   * 9 *11 *10 *12 *  229
C                    **********                               **********         230
C                    *   *   *   *   *                        * + *   *   *   *  231
C           IROW=3   * 3 * 7 *   *   *              IROW=3   * 7 * 5 * 8 * 6 *  232
C                    **********                               **********         233
C                    *   *   *   *   *                        * + *   *   *   *  234
C           IROW=4   * 4 * 8 *   *   *              IROW=4   *15 *13 *16 *14 *  235
C                    **********                               **********         236
C                                                                               237
C           DISK FILES ON WHICH CHUNKS               ORDER IN WHICH CHUNKS ARE  238
C           ARE STORED                               MULTIPLIED BY APPROPRIATE  239
C                                                    PORTION OF TRANSFORMED     240
C                                                    GREENS FUNCTION            241
C                                                                               242
C                                                                               243
```

```
C                                                                       244
      COMMON/ALLCOM/N,NO2,N21,NO4,N34,NH,NHO2,NH21,I2A,I2B,I3A,I3B      245
      COMMON/TRANCOM/RHO1(32,32,16),RHO2(32,32,16),RHO3(32,32,16),      246
     1     RHO4(32,32,16),HH(32,32,17)                                  247
      COMMON/HN21COM/HN21(65,17)                                        248
C THE INITIALIZING OVERLAY OR STAR ADVANCING OVERLAY STORES THE DENSITY  249
C CHUNKS OF IROW 1 AND 2 FOR JCOLUMN=1 ON DISK FILES 1 AND 2 RESPECTIVELY 250
C AND FOR JCOLUMN=2 ON DISK FILES 5 AND 6 RESPECTIVELY.  THE GETPHI OVERLAY 251
C REPLACES THE DENSITY ON THESE DISK FILES WITH THE CORRESPONDING VALUES OF 252
C POTENTIAL WHICH ARE THEN USED IN THE STAR ADVANCING OVERLAY.  THIS IS   253
C ACCOMPLISHED THROUGH CALLING SUBROUTINES ANLX(JCOLUMN), ANLSYN(IROW) AND 254
C SYNX(JCOLUMN) AS DETAILED BELOW.                                      255
C                                                                       256
C                                                                       257
C SUBROUTINE ANLX(JCOLUMN) READS RESPECTIVELY IROW 1 AND 2 FROM THE     258
C FOLLOWING DISK FILES - 1 AND 2 FOR JCOLUMN=1.  - 5 AND 6 FOR JCOLUMN=2. 259
C IT THEN PERFORMS A PERIODIC ANALYSIS IN THE X DIRECTION OVER JCOLUMN FOR 260
C I=1,N AND WRITES THE RESULTS RESPECTIVELY FOR IROW 1,2,3, AND 4 ON THE 261
C FOLLOWING DISK FILES - 1,2,3, AND 4 FOR JCOLUMN=1.  - 5,6,7, AND 8 FOR 262
C JCOLUMN=2.                                                            263
      CALL ANLX(1)                                                      264
      CALL ANLX(2)                                                      265
C SUBROUTINE ANLSYN(IROW) READS RESPECTIVELY JCOLUMN 1 AND 2 FROM THE   266
C FOLLOWING DISK FILES - 1 AND 5 FOR IROW=1.  - 2 AND 6 FOR IROW=2.  - 3 AND 267
C 7 FOR IROW=3.  - 4 AND 8 FOR IROW=4.  IT THEN PERFORMS A PERIODIC ANALYSIS 268
C IN THE Y DIRECTION OVER IROW FOR J=1,N.  FOR EACH CHUNK IT THEN PERFORMS A 269
C PERIODIC ANALYSIS IN THE Z DIRECTION FOR K=1,NH, ELEMENT BY ELEMENT   270
C MULTIPLICATION WITH A SIMILARLY SHAPED CHUNK OF THE TRANSFORMED GREENS 271
C FUNCTION AND THEN A PERIODIC SYNTHESIS IN THE Z DIRECTION FOR K=1,NH.  THE 272
C RESULT FOR K=1,NH/2 IS THEN PERIODICALLY SYNTHESIZED IN THE Y DIRECTION 273
C OVER IROW FOR J=1,N.  THIS LAST RESULT FOR JCOLUMN 1 AND 2 IS WRITTEN 274
C RESPECTIVELY ON THE FOLLOWING DISK FILES - 1 AND 5 FOR IROW=1.  - 2 AND 6 275
C FOR IROW=2.  - 3 AND 7 FOR IROW=3.  - 4 AND 8 FOR IROW=4.  THE ORDER IN 276
C WHICH ANLSYN IS CALLED FOR IROW 1 THROUGH 4 MINIMIZES READING FROM DISK 277
C FILE 9 OF CHUNKS OF THE TRANSFORMED GREENS FUNCTION AS MENTIONED ABOVE. 278
      CALL ANLSYN(1)                                                    279
      CALL ANLSYN(3)                                                    280
      CALL ANLSYN(2)                                                    281
      CALL ANLSYN(4)                                                    282
C SUBROUTINE SYNX(JCOLUMN) READS RESPECTIVELY IROW 1,2,3, AND 4 FROM THE 283
C FOLLOWING DISK FILES - 1,2,3, AND 4 FOR JCOLUMN=1.  - 5,6,7, AND 8 FOR 284
C JCOLUMN=2.  IT THEN PERFORMS A PERIODIC SYNTHESIS IN THE X DIRECTION OVER 285
C JCOLUMN FOR J=1,N.  IT THEN WRITES THE RESULT RESPECTIVELY FOR IROW 1 AND 286
C 2 ON THE FOLLOWING DISK FILES - 1 AND 2 FOR JCOLUMN=1.  - 5 AND 6 FOR 287
C JCOLUMN=2.                                                            288
      CALL SYNX(1)                                                      289
      CALL SYNX(2)                                                      290
      RETURN                                                            291
      END                                                               292
      SUBROUTINE ANLX(JCOLUMN)                                          293
      COMMON/ALLCOM/N,NO2,N21,NO4,N34,NH,NHO2,NH21,I2A,I2B,I3A,I3B      294
      COMMON/TRANCOM/RHO1(32,32,16),RHO2(32,32,16),RHO3(32,32,16),      295
     1     RHO4(32,32,16),HH(32,32,17)                                  296
      COMMON Z(1025), Y(1025)                                           297
      IF(JCOLUMN.EQ.2) GO TO 2                                          298
      READ(1) RHO1                                                      299
      REWIND 1                                                          300
      READ(2) RHO2                                                      301
      REWIND 2                                                          302
      GO TO 3                                                           303
    2 CONTINUE                                                          304
      READ(5) RHO1                                                      305
      REWIND 5                                                          306
      READ(6) RHO2                                                      307
      REWIND 6                                                          308
    3 CONTINUE                                                          309
      CALL GETSET(3,I2A)                                                310
      DO 10 K=1,NHO2                                                    311
      DO 10 J=1,NO4                                                     312
      DO  5 I=1,NO4                                                     313
      Z(I)=RHO1(I,J,K)                                                  314
      Z(NO4+I)=RHO2(I,J,K)                                              315
```

```
      Z(NO2+I)=0.                                                        316
    5 Z(N34+I)=0.                                                        317
      CALL FTRANS(3,I2A)                                                 318
      DO 10 I=1,NO4                                                      319
      RHO1(I,J,K)=Y(I)                                                   320
      RHO2(I,J,K)=Y(NO4+I)                                               321
      RHO3(I,J,K)=Y(NO2+I)                                               322
   10 RHO4(I,J,K)=Y(N34+I)                                               323
      IF(JCOLUMN.EQ.2) GO TO 12                                          324
      WRITE(1) RHO1                                                      325
      REWIND 1                                                           326
      WRITE(2) RHO2                                                      327
      REWIND 2                                                           328
      WRITE(3) RHO3                                                      329
      REWIND 3                                                           330
      WRITE(4) RHO4                                                      331
      REWIND 4                                                           332
      GO TO 15                                                           333
   12 CONTINUE                                                           334
      WRITE(5) RHO1                                                      335
      REWIND 5                                                           336
      WRITE(6) RHO2                                                      337
      REWIND 6                                                           338
      WRITE(7) RHO3                                                      339
      REWIND 7                                                           340
      WRITE(8) RHO4                                                      341
      REWIND 8                                                           342
   15 RETURN                                                             343
      END                                                                344
      SUBROUTINE ANLSYN(IROW)                                            345
      COMMON/ALLCOM/N,NO2,N21,NO4,N34,NH,NH02,NH21,I2A,I2B,I3A,I3B       346
      COMMON/TRANCOM/RHO1(32,32,16),RHO2(32,32,16),RHO3(32,32,16),       347
     1     RHO4(32,32,16),HH(32,32,17)                                   348
      COMMON/HN21COM/HN21(65,17)                                         349
      COMMON Z(1025), Y(1025)                                            350
      GO TO(1,2,3,4) IROW                                                351
    1 CONTINUE                                                           352
      READ(1) RHO1                                                       353
      REWIND 1                                                           354
      READ(5) RHO2                                                       355
      REWIND 5                                                           356
      GO TO 5                                                            357
    2 CONTINUE                                                           358
      READ(2) RHO1                                                       359
      REWIND 2                                                           360
      READ(6) RHO2                                                       361
      REWIND 6                                                           362
      GO TO 5                                                            363
    3 CONTINUE                                                           364
      READ(3) RHO1                                                       365
      REWIND 3                                                           366
      READ(7) RHO2                                                       367
      REWIND 7                                                           368
      GO TO 5                                                            369
    4 CONTINUE                                                           370
      READ(4) RHO1                                                       371
      REWIND 4                                                           372
      READ(8) RHO2                                                       373
      REWIND 8                                                           374
    5 CONTINUE                                                           375
      CALL GETSET(3,I2A)                                                 376
      DO 10 K=1,NH02                                                     377
      DO 10 I=1,NO4                                                      378
      DO  7 J=1,NO4                                                      379
      Z(J)=RHO1(I,J,K)                                                   380
      Z(NO4+J)=RHO2(I,J,K)                                               381
      Z(NO2+J)=0.                                                        382
    7 Z(N34+J)=0.                                                        383
      CALL FTRANS(3,I2A)                                                 384
```

```
      DO 10 J=1,NO4                                                    385
      RHO1(I,J,K)=Y(J)                                                 386
      RHO2(I,J,K)=Y(NO4+J)                                             387
      RHO3(I,J,K)=Y(NO2+J)                                             388
   10 RHO4(I,J,K)=Y(N34+J)                                             389
      GO TO(30,49,75,75) IROW                                          390
   49 CONTINUE                                                         391
   30 CONTINUE                                                         392
      READ(9) HH                                                       393
   50 JCOLUMN=1                                                        394
      DO 70 I=1,NO4                                                    395
      DO 70 J=1,NO4                                                    396
      DO 52 K=1,NHO2                                                   397
      Z(K)=RHO1(I,J,K)                                                 398
   52 Z(NHO2+K)=0.                                                     399
      CALL GETSET(3,13A)                                               400
      CALL FTRANS(3,13A)                                               401
      IF(IROW.NE.3) GO TO 300                                          402
      IF(I.NE.1)GO TO 300                                              403
      LL=J                                                             404
      GO TO 200                                                        405
   54 DO 70 K=1,NHO2                                                   406
   70 RHO1(I,J,K)=Y(K)                                                 407
      GO TO 100                                                        408
   74 CONTINUE                                                         409
      READ(9) HH                                                       410
   75 JCOLUMN=2                                                        411
      DO 95 I=1,NO4                                                    412
      DO 95 J=1,NO4                                                    413
      DO 77 K=1,NHO2                                                   414
      Z(K)=RHO2(I,J,K)                                                 415
   77 Z(NHO2+K)=0.                                                     416
      CALL GETSET(3,13A)                                               417
      CALL FTRANS(3,13A)                                               418
      IF(IROW.NE.3) GO TO 300                                          419
      IF(I.NE.1)GO TO 300                                              420
      LL=NO4+J                                                         421
      GO TO 200                                                        422
   79 DO 95 K=1,NHO2                                                   423
   95 RHO2(I,J,K)=Y(K)                                                 424
      GO TO 125                                                        425
  100 JCOLUMN=3                                                        426
      DO 120 I=1,NO4                                                   427
      DO 120 J=1,NO4                                                   428
      DO 101 K=1,NHO2                                                  429
      Z(K)=RHO3(I,J,K)                                                 430
  101 Z(NHO2+K)=0.                                                     431
      CALL GETSET(3,13A)                                               432
      CALL FTRANS(3,13A)                                               433
      GO TO(103,105,107,115) IROW                                      434
  103 IF(J.NE.1)GO TO 300                                              435
      LL=I                                                             436
      GO TO 200                                                        437
  105 IF(J.NE.1)GO TO 300                                              438
      LL=NO4+I                                                         439
      GO TO 200                                                        440
  107 IF(I.NE.1.AND.J.NE.1)GO TO 300                                   441
      IF(I.EQ.1.AND.J.EQ.1)GO TO 111                                   442
      IF(I.EQ.1)GO TO 109                                              443
      LL=I                                                             444
      GO TO 200                                                        445
  109 LL=J                                                             446
      GO TO 200                                                        447
  111 LL=N21                                                           448
      GO TO 200                                                        449
  115 IF(J.NE.1) GO TO 300                                             450
      LL=NO4+I                                                         451
      GO TO 200                                                        452
  117 DO 120 K=1,NHO2                                                  453
  120 RHO3(I,J,K)=Y(K)                                                 454
      GO TO(74,74,400,390) IROW                                        455
  125 JCOLUMN=4                                                        456
```

```
      DO 145 I=1,NO4                                                    457
      DO 145 J=1,NO4                                                    458
      DO 127 K=1,NHO2                                                   459
      Z(K)=RHO4(I,J,K)                                                  460
  127 Z(NHO2+K)=0.                                                      461
      CALL GETSET(3,13A)                                                462
      CALL FTRANS(3,13A)                                                463
      IF(IROW.NE.3) GO TO 300                                           464
      IF(I.NE.1)GO TO 300                                               465
      LL=NO4+J                                                          466
      GO TO 200                                                         467
  129 DO 145 K=1,NHO2                                                   468
  145 RHO4(I,J,K)=Y(K)                                                  469
      GO TO (400,400,49,49) IROW                                        470
  200 DO 205 K=2,NHO2                                                   471
      Z(K)=Y(K)*HN21(LL,K)                                              472
  205 Z(NHO2+K)=Y(NHO2+K)*HN21(LL,K)                                    473
      Z(1)=Y(1)*HN21(LL,1)                                              474
      Z(NH21)=Y(NH21)*HN21(LL,NH21)                                     475
      GO TO 310                                                         476
  300 DO 305 K=2,NHO2                                                   477
      Z(K)=Y(K)*HH(I,J,K)                                               478
  305 Z(NHO2+K)=Y(NHO2+K)*HH(I,J,K)                                     479
      Z(1)=Y(1)*HH(I,J,1)                                               480
      Z(NH21)=Y(NH21)*HH(I,J,NH21)                                      481
  310 CALL GETSET(4,13A)                                                482
      CALL FTRANS(4,13A)                                                483
      GO TO(54,79,117,129) JCOLUMN                                      484
  390 REWIND 9                                                          485
  400 CALL GETSET(4,12A)                                                486
      DO 410 K=1,NHO2                                                   487
      DO 410 I=1,NO4                                                    488
      DO 405 J=1,NO4                                                    489
      Z(J)=RHO1(I,J,K)                                                  490
      Z(NO4+J)=RHO2(I,J,K)                                              491
      Z(NO2+J)=RHO3(I,J,K)                                              492
  405 Z(N34+J)=RHO4(I,J,K)                                              493
      CALL FTRANS(4,12A)                                                494
      DO 410 J=1,NO4                                                    495
      RHO1(I,J,K)=Y(J)                                                  496
  410 RHO2(I,J,K)=Y(NO4+J)                                              497
      GO TO(415,420,425,430) IROW                                       498
  415 CONTINUE                                                          499
      WRITE(1) RHO1                                                     500
      REWIND 1                                                          501
      WRITE(5) RHO2                                                     502
      REWIND 5                                                          503
      GO TO 435                                                         504
  420 CONTINUE                                                          505
      WRITE(2) RHO1                                                     506
      REWIND 2                                                          507
      WRITE(6) RHO2                                                     508
      REWIND 6                                                          509
      GO TO 435                                                         510
  425 CONTINUE                                                          511
      WRITE(3) RHO1                                                     512
      REWIND 3                                                          513
      WRITE(7) RHO2                                                     514
      REWIND 7                                                          515
      GO TO 435                                                         516
  430 CONTINUE                                                          517
      WRITE(4) RHO1                                                     518
      REWIND 4                                                          519
      WRITE(8) RHO2                                                     520
      REWIND 8                                                          521
  435 RETURN                                                            522
      END                                                               523
      SUBROUTINE SYNX(JCOLUMN)                                          524
      COMMON/ALLCOM/N,NO2,N21,NO4,N34,NH,NHO2,NH21,12A,12B,13A,13B      525
      COMMON/TRANCOM/RHO1(32,32,16),RHO2(32,32,16),RHO3(32,32,16),      526
     1     RHO4(32,32,16),HH(32,32,17)                                  527
      COMMON Z(1025),Y(1025)                                            528
      IF(JCOLUMN.EQ.2) GO TO 1                                          529
```

```
      READ(1) RHO1                                                    530
      REWIND 1                                                        531
      READ(2) RHO2                                                    532
      REWIND 2                                                        533
      READ(3) RHO3                                                    534
      REWIND 3                                                        535
      READ(4) RHO4                                                    536
      REWIND 4                                                        537
      GO TO 2                                                         538
    1 CONTINUE                                                        539
      READ(5) RHO1                                                    540
      REWIND 5                                                        541
      READ(6) RHO2                                                    542
      REWIND 6                                                        543
      READ(7) RHO3                                                    544
      REWIND 7                                                        545
      READ(8) RHO4                                                    546
      REWIND 8                                                        547
    2 CONTINUE                                                        548
    4 CALL GETSET(4,I2A)                                              549
      DO 10 K=1,NHO2                                                  550
      DO 10 J=1,NO4                                                   551
      DO  5 I=1,NO4                                                   552
      Z(I)=RHO1(I,J,K)                                                553
      Z(NO4+I)=RHO2(I,J,K)                                            554
      Z(NO2+I)=RHO3(I,J,K)                                            555
    5 Z(N34+I)=RHO4(I,J,K)                                            556
      CALL FTRANS(4,I2A)                                              557
      DO 10 I=1,NO4                                                   558
      RHO1(I,J,K)=Y(I)                                                559
   10 RHO2(I,J,K)=Y(NO4+I)                                            560
      IF(JCOLUMN.EQ.2) GO TO 12                                       561
      WRITE(1) RHO1                                                   562
      REWIND 1                                                        563
      WRITE(2) RHO2                                                   564
      REWIND 2                                                        565
      GO TO 15                                                        566
   12 CONTINUE                                                        567
      WRITE(5) RHO1                                                   568
      REWIND 5                                                        569
      WRITE(6) RHO2                                                   570
      REWIND 6                                                        571
   15 RETURN                                                          572
      END                                                             573
```

REFERENCES

1. Miller, R. H.; and Prendergast, K. H.: Stellar Dynamics in a Discrete Phase Space. Astrophys. J., vol. 151, no. 2, Feb. 1968, pp. 699-709.

2. Hohl, Frank; and Hockney, R. W.: A Computer Model of Disks of Stars. J. Comput. Phys., vol. 4, no. 3, Oct. 1969, pp. 306-324.

3. Miller, R. H.; Prendergast, K. H.; and Quirk, William J.: Numerical Experiments on Spiral Structure. Astrophys. J., vol. 161, no. 3, pt. 1, Sept. 1970, pp. 903-916.

4. Hohl, Frank: Numerical Experiments With a Disk of Stars. Astrophys. J., vol. 168, pt. 1, Sept. 15, 1971, pp. 343-359.

5. Toomre, Alar: On the Gravitational Stability of a Disk of Stars. Astrophys. J., vol. 139, no. 4, May 15, 1964, pp. 1217-1238.

6. Hunter, C.: The Structure and Stability of Self-Gravitating Disks. Mon. Notic. R. Astron. Soc., vol. 126, no. 4, 1963, pp. 299-315.

7. Kalnajs, Agris J.: The Equilibria and Oscillations of a Family of Uniformly Rotating Stellar Disks. Astrophys. J., vol. 175, no. 1, pt. 1, July 1, 1972, pp. 63-76.

8. Ostriker, J. P.; and Peebles, P. J. E.: A Numerical Study of the Stability of Flattened Galaxies: Or, Can Cold Galaxies Survive? Astrophys. J., vol. 186, no. 2, pt. 1, Dec. 1, 1973, pp. 467-480.

9. Hohl, Frank: Dynamical Evolution of Disk Galaxies. NASA TR R-343, 1970.

10. Hockney, R. W.; and Brownrigg, D. R. K.: Effect of Population II Stars and Three-Dimensional Motion on Spiral Structure. Mon. Notic. R. Astron. Soc., vol. 167, no. 2, May 1974, pp. 351-357.

11. Hohl, F.: Suppression of Bar Instability by a Massive Halo. Astron. J., vol. 81, no. 1, Jan. 1976, pp. 30-36.

12. Larson, R. B.: The Collapse and Formation of Galaxies. Dynamics of Stellar Systems, Avram Hayli, ed., D. Reidel Pub. Co., 1975, pp. 247-269.

13. Jones, Bernard J. T.: The Origin of Galaxies: A Review of Recent Theoretical Developments and Their Confrontation With Observation. Rev. Mod. Phys., vol. 48, no. 1, Jan. 1976, pp. 107-149.

14. Gott, J. Richard, III: Recent Theories of Galaxy Formation. Annual Review of Astronomy and Astrophysics, Volume 15, Geoffrey Burbidge, David Layzer, and John G. Phillips, eds. of vol., Annu. Rev., Inc., 1977, pp. 235-266.

15. Bouvier, P.; and Janin, G.: Dynamical Mixing of Orbits in the Spherical Water-Bag Model. Astron. & Astrophys., vol. 5, no. 1, Mar. 1970, pp. 127-134.

16. Hénon, M.: Numerical Experiments on the Stability of Spherical Stellar Systems. Astron. & Astrophys., vol. 24, no. 2, Apr. 1973, pp. 229-238.

17. Gott, J. Richard, III: Dynamics of Rotating Stellar Systems: Collapse and Violent Relaxation. Astrophys. J., vol. 186, no. 2, pt. 1, Dec. 1, 1973, pp. 481-500.

18. Gott, J. Richard, III: On the Formation of Elliptical Galaxies. Astrophys. J., vol. 201, no. 2, pt. 1, Oct. 15, 1975, pp. 296-310.

19. Miller, R. H.: Free Collapse of a Rotating Sphere of Stars. Astrophys. J., vol. 223, no. 1, pt. 1, July 1, 1978, pp. 122-128.

20. Miller, R. H.; and Smith, B. F.: Six Collapses. Astrophys. J., vol. 227, no. 2, pt. 1, Jan. 15, 1979, pp. 407-414.

21. Illingworth, Garth: Rotation (?) in 13 Elliptical Galaxies. Astrophys. J., vol. 218, no. 2, pt. 2, Dec. 1, 1977, pp. L43-L47.

22. Peterson, Charles J.: Rotation of 10 Early-Type Galaxies. Astrophys. J., vol. 222, no. 1, pt. 1, May 15, 1978, pp. 84-94.

23. Hohl, Frank: Evolution of a Stationary Disk of Stars. J. Computational Phys., vol. 9, no. 1, Feb. 1972, pp. 20-25.

24. Hohl, Frank: Relaxation Time in Disk Galaxy Simulations. Astrophys. J., vol. 184, no. 2, pt. 1, Sept. 1, 1973, pp. 353-359.

25. DeVaucouleurs, G.: General Physical Properties of External Galaxies. Encycl. Phys., Vol. LIII, Astrophysics IV: Stellar Systems, S. Flügge, ed., Springer-Verlag, 1959, pp. 311-372.

26. Freeman, K. C.: On the Disks of Spiral and S0 Galaxies. Astrophys. J., vol. 160, no. 3, pt. 1, June 1970, pp. 811-830.

27. Kormendy, John: Brightness Distribution in Compact and Normal Galaxies. III. Decomposition of Observed Profiles Into Spheroid and Disk Components. Astrophys. J., vol. 217, no. 2, pt. 1, Oct. 15, 1977, pp. 406-419.

28. Hohl, Frank; and Feix, Marc R.: Numerical Experiments With a One-Dimensional Model for a Self-Gravitating Star System. Astrophys. J., vol. 147, no. 3, Mar. 1967, pp. 1164-1180.

29. Toomre, Alar: How Can It All Be Stable? Highlights of Astronomy, Volume 3, G. Contopoulos, ed., D. Reidel Pub. Co., 1974, pp. 457-465.

30. Toomre, Alar: Theories of Spiral Structure. Annual Review of Astronomy and Astrophysics, Volume 15, Geoffrey Burbidge, David Layzer, and John G. Phillips, eds. of vol., Annu. Rev., Inc., 1977, pp. 437-478.

31. Lynden-Bell, D.: Statistical Mechanics of Violent Relaxation in Stellar Systems. Mon. Notic. R. Astron. Soc., vol. 136, no. 1, 1967, pp. 101-121.

32. Lynden-Bell, D.: On Large-Scale Instabilities During Gravitational Collapse and the Evolution of Shrinking Maclaurin Spheroids. Astrophys. J., vol. 139, no. 4, May 15, 1964, pp. 1195-1216.

33. Gott, J. Richard, III; and Thuan, Trinh X.: On the Formation of Spiral and Elliptical Galaxies. Astrophys. J., vol. 204, no. 3, pt. 1, Mar. 15, 1976, pp. 649-667.

34. Di Fazio, A.; and Occhionero, F.: Dynamical Evolution of Elliptical Protogalaxies. Astron. & Astrophys., vol. 62, no. 3, Jan. 1978, pp. 349-354.

35. Wilson, Christopher P.: Dynamical Models of Elliptical Galaxies. Astron. J., vol. 80, no. 3, Mar. 1975, pp. 175-187.

36. Vandervoort, Peter O.: Density Waves in a Highly Flattened, Rapidly Rotating Galaxy. Astrophys. J., vol. 161, no. 1, pt. 1, July 1970, pp. 87-102.

37. Hockney, R. W.: The Potential Calculation and Some Applications. Methods in Computational Physics, Volume 9 - Plasma Physics, Berni Alder, Sidney Ferbach, and Manuel Rotenberg, eds., Academic Press, 1970, pp. 135-211.

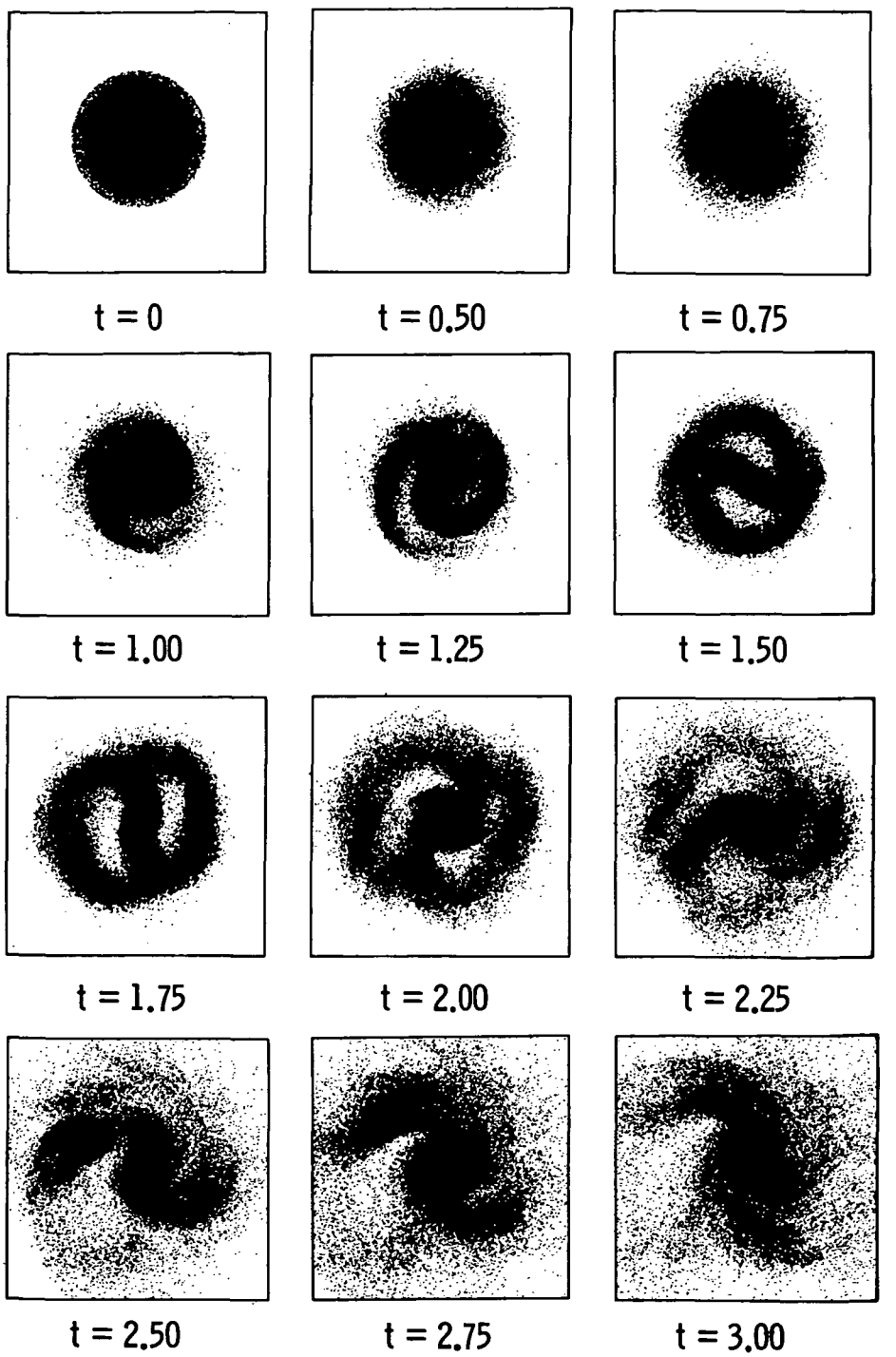

Figure 1.- Evolution of an initially balanced, infinitesimally thin disk of 100 000 stars with an exponential radial density variation. The stars have an initial velocity dispersion given by Toomre's criterion (ref. 5). Time is given in units of $2\pi/\omega_o$.

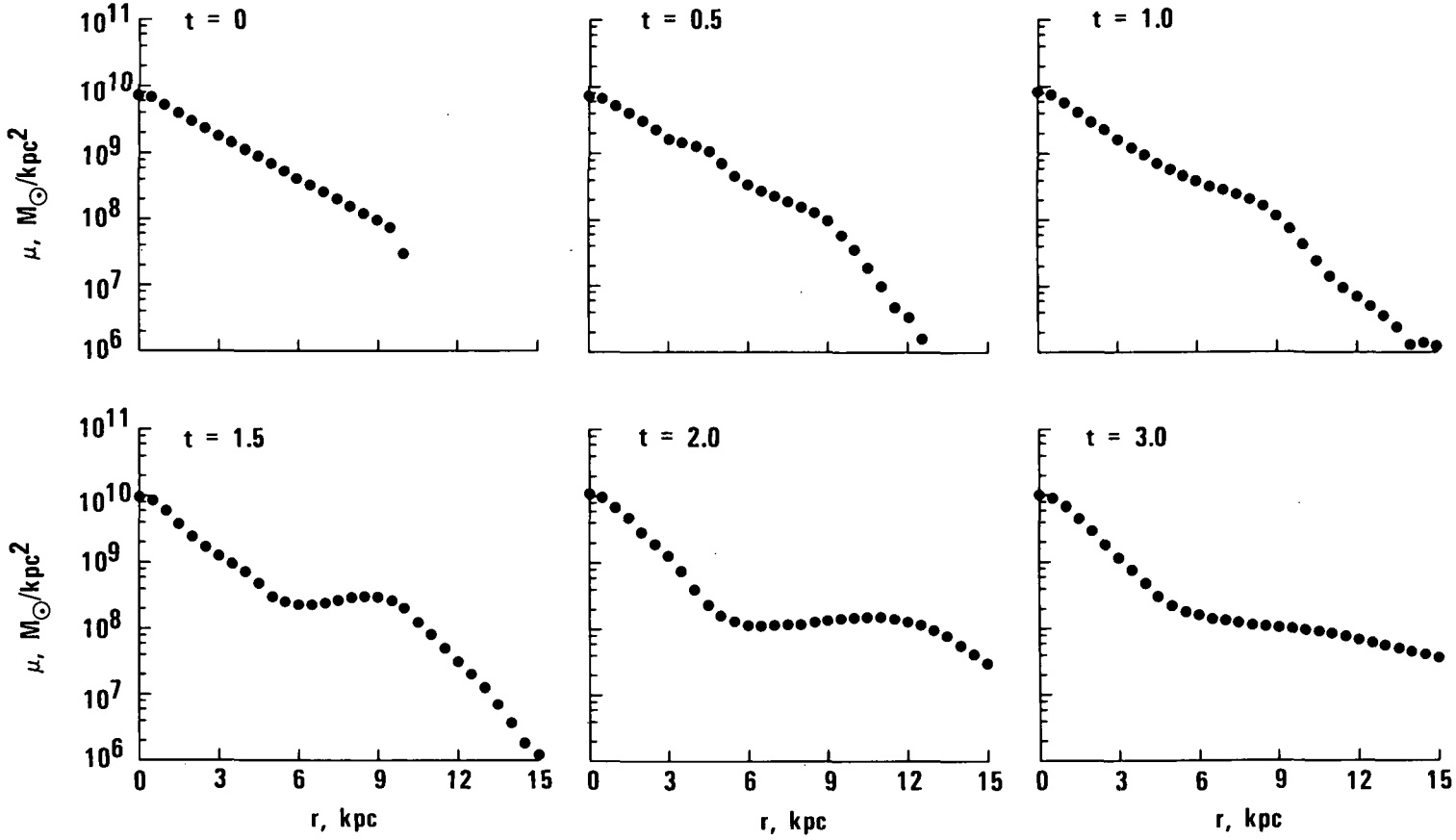

Figure 2.- Evolution of the azimuthally averaged surface mass density as a function of radius for the two-dimensional disk system. Note that the final density at t = 3.0 approaches the sum of two exponentials.

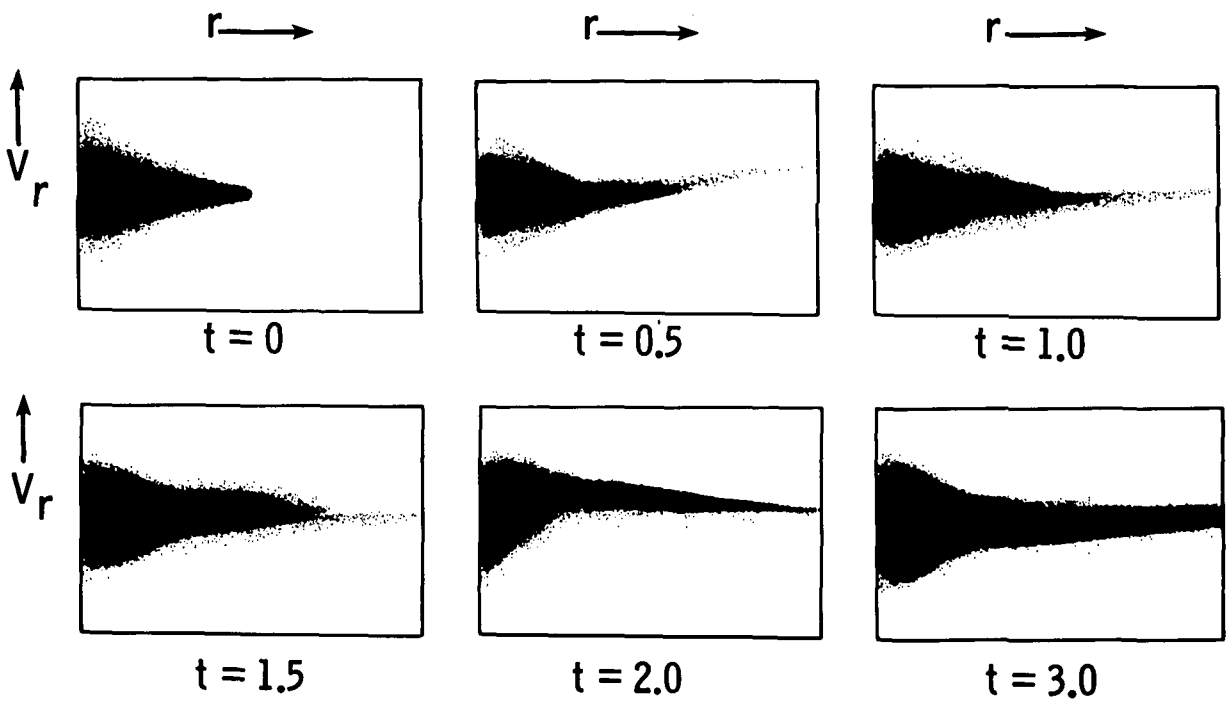

(a) Radial velocities.

Figure 3.- Evolution of the velocity distributions as a function of radius for the two-dimensional disk system.

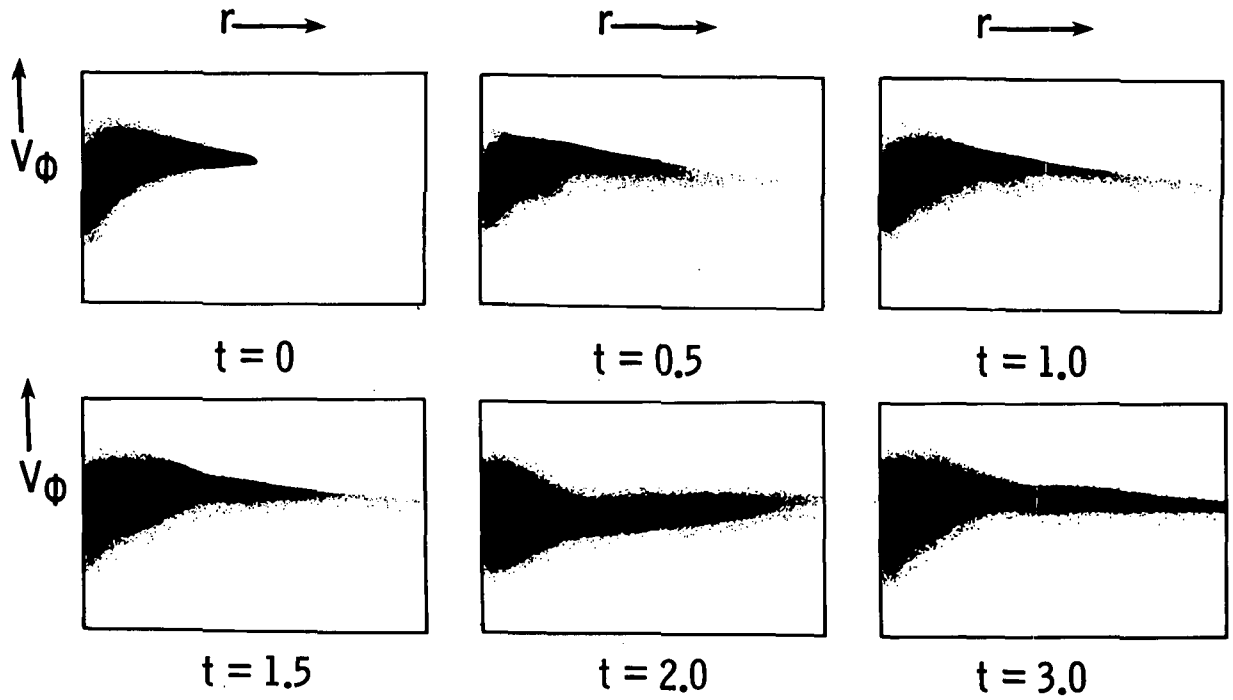

(b) Azimuthal velocities.

Figure 3.- Concluded.

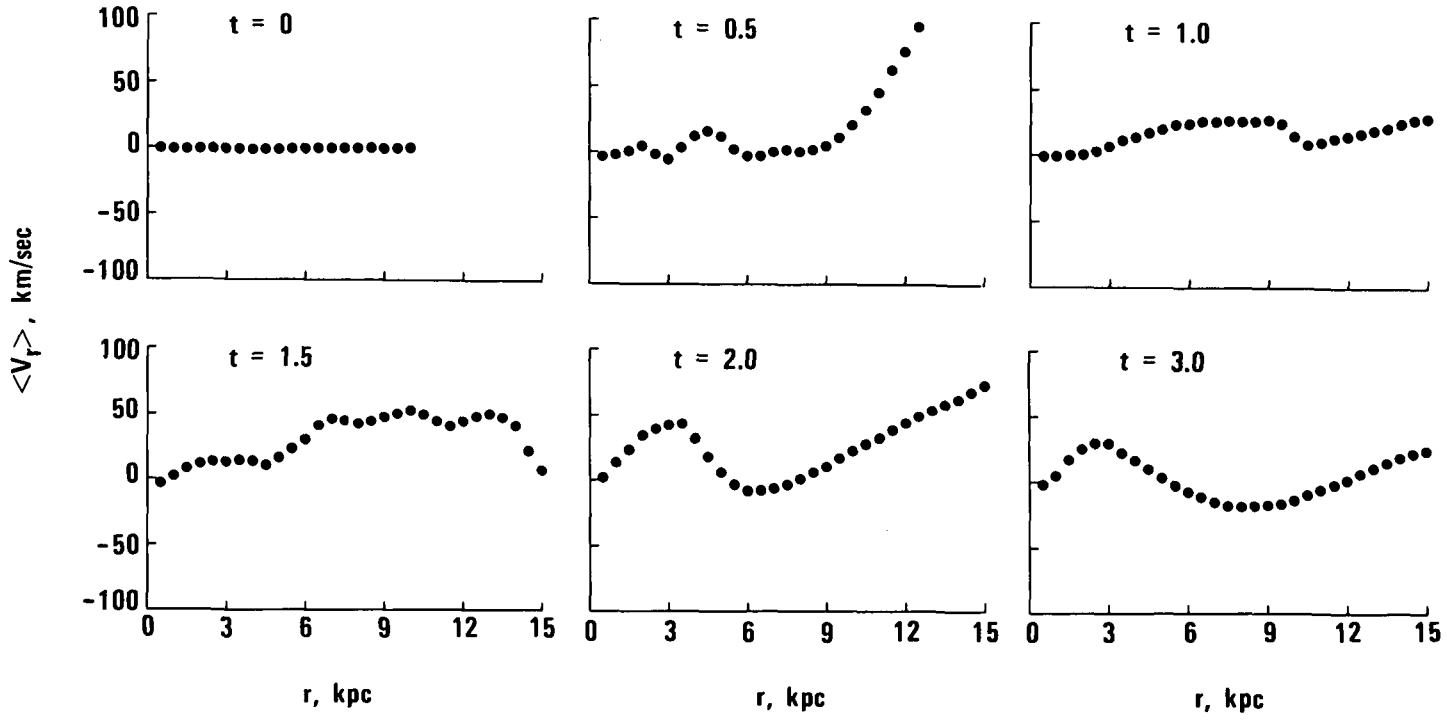

Figure 4.- Evolution of the azimuthally averaged, mean radial velocity as a function of radius for the two-dimensional disk system. Note that considerable radial mass motion is in progress even at t = 3.0.

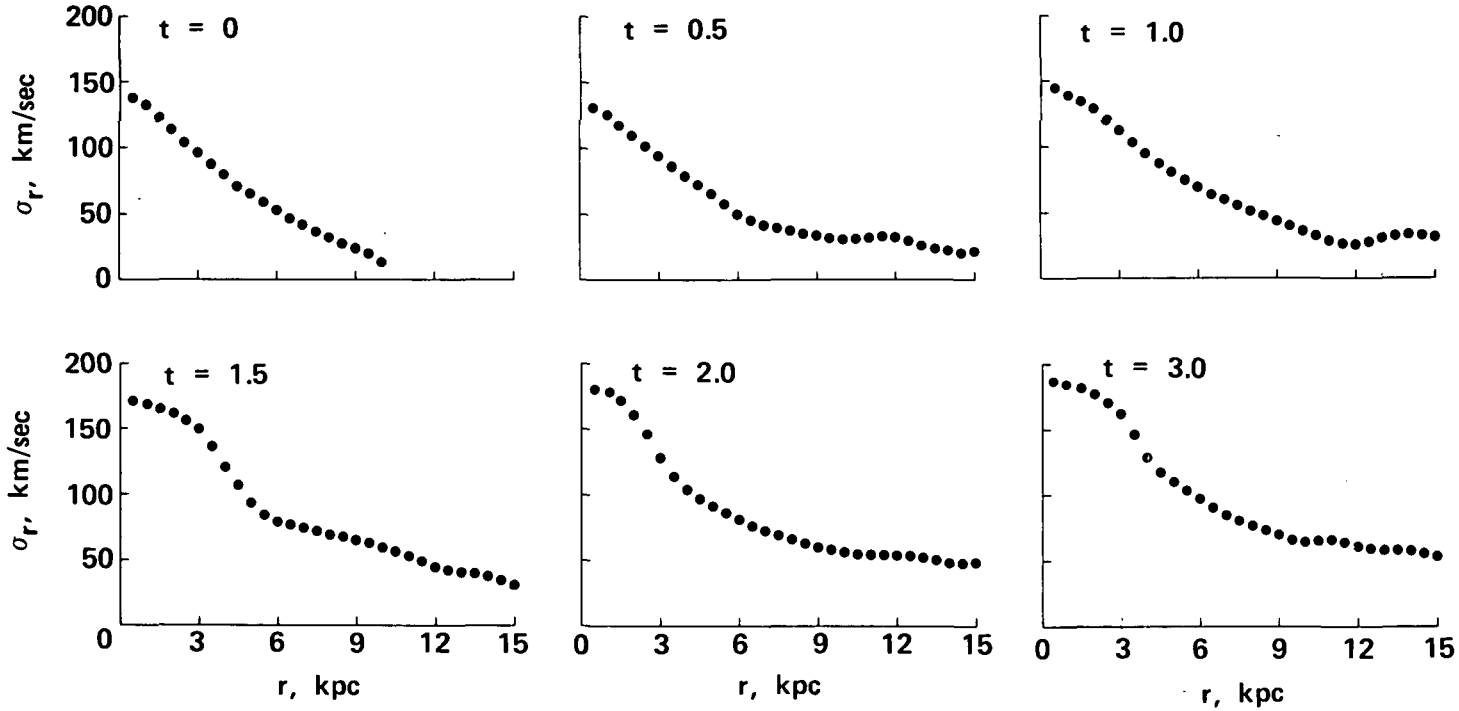

(a) Radial velocity dispersion.

Figure 5.- Evolution of the azimuthally averaged velocity dispersions as a function of radius for the two-dimensional disk system.

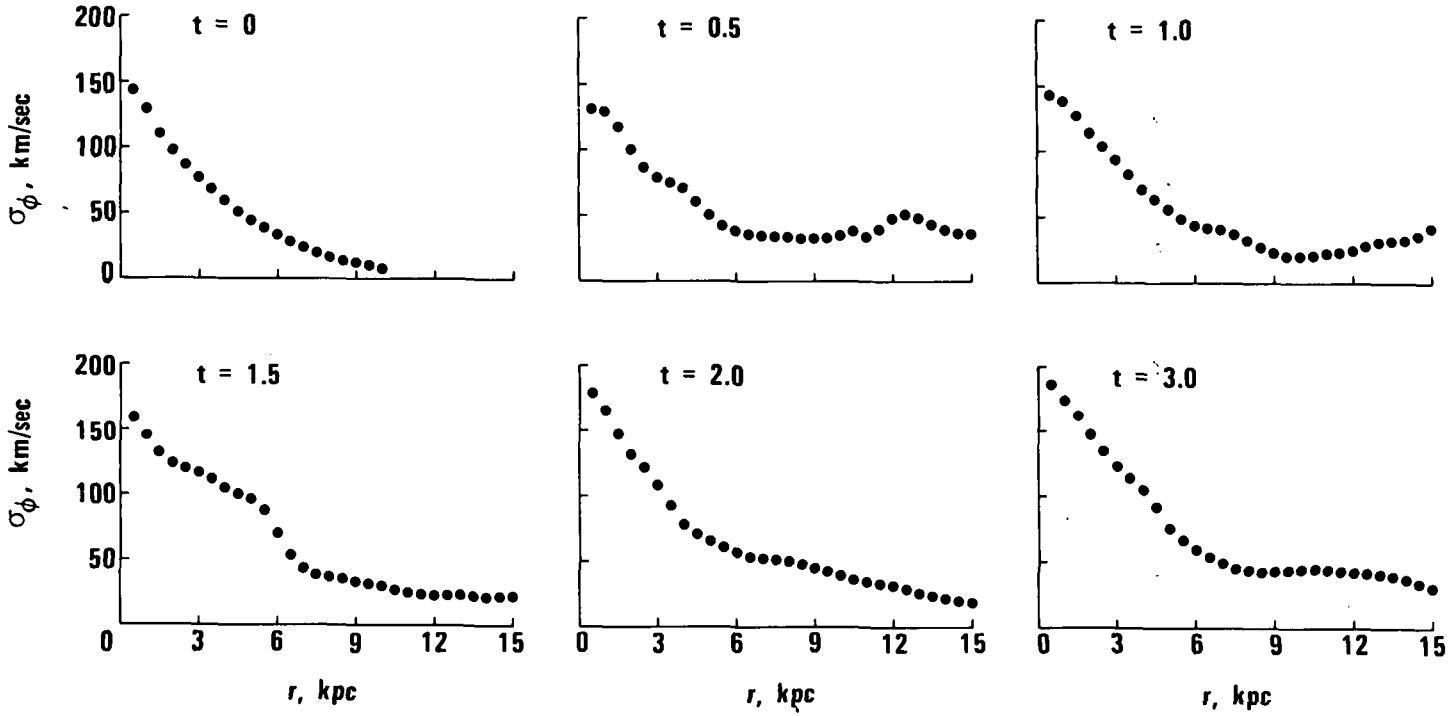

(b) Azimuthal velocity dispersion.

Figure 5.- Concluded.

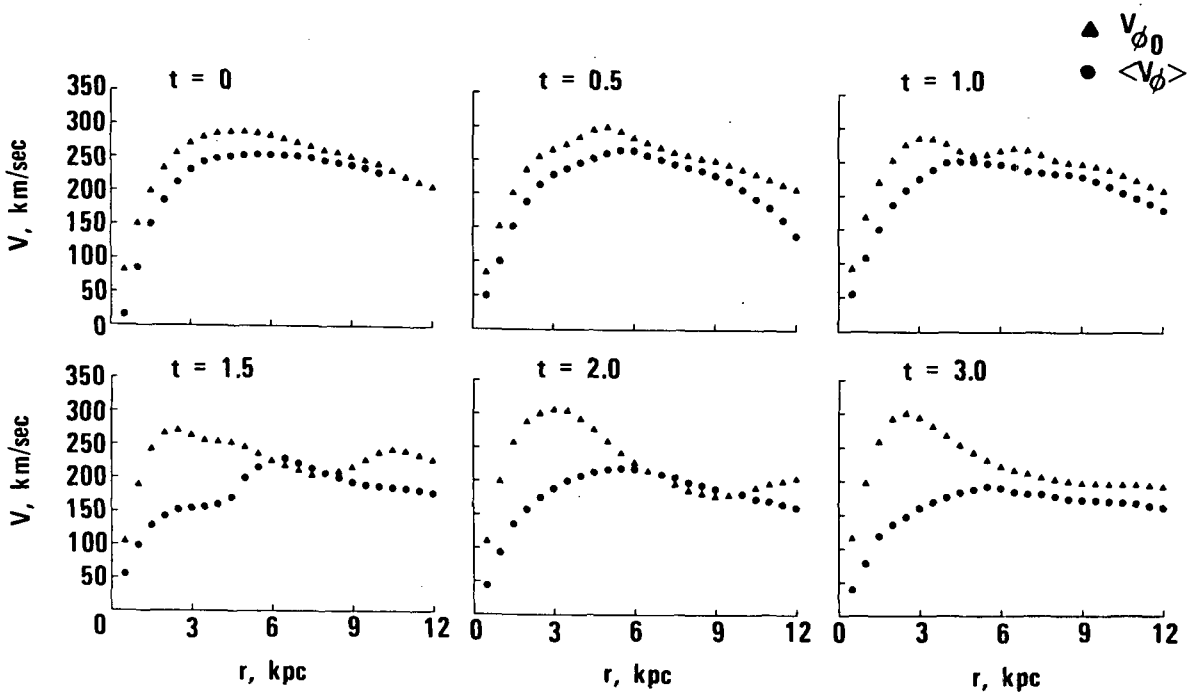

Figure 6.- Comparison of the circular velocity $V_{\phi_o} = \sqrt{rK_r}$ with the mean azimuthal velocity $\langle V_\phi \rangle$ for the two-dimensional disk system.

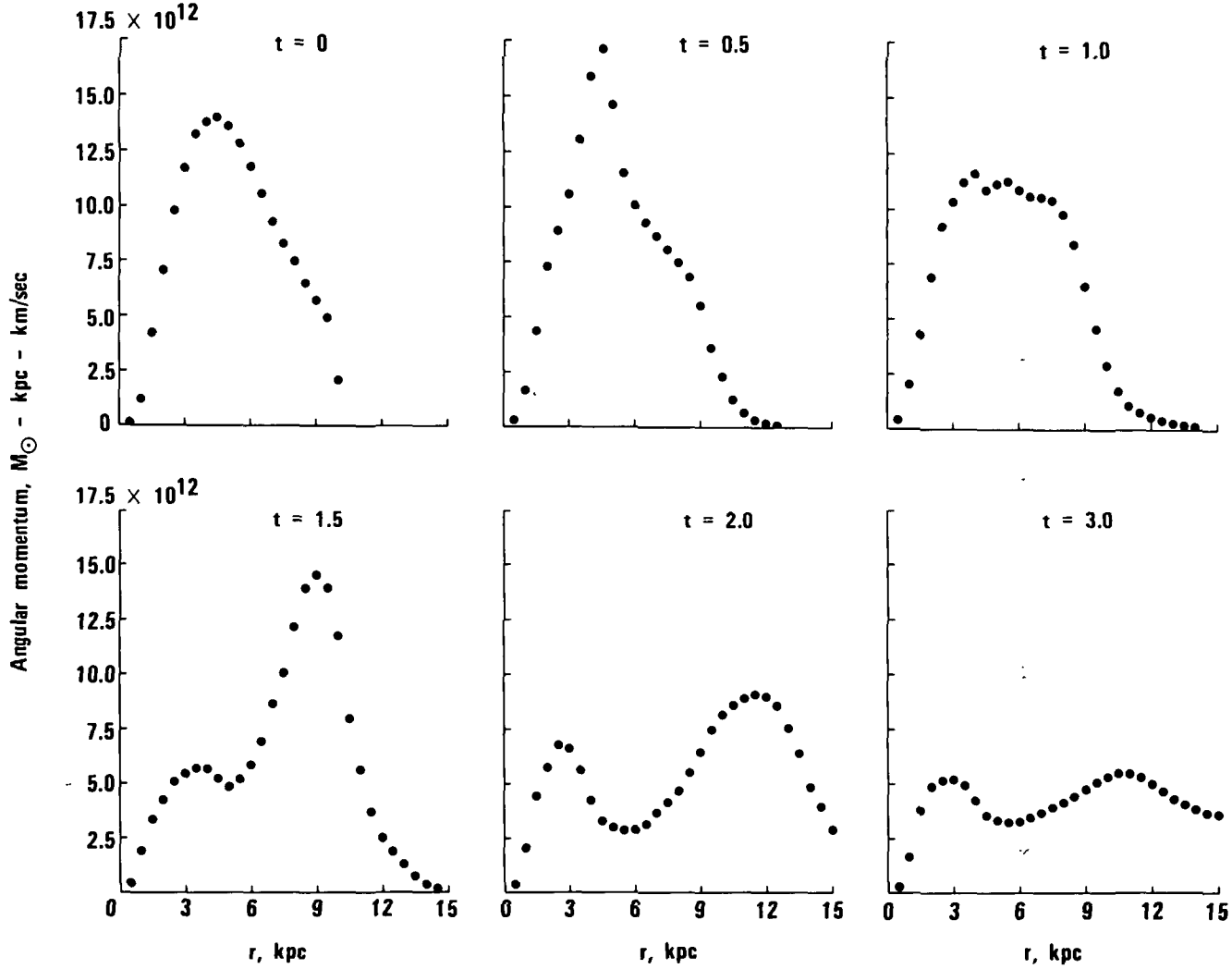

Figure 7.- Evolution of the angular momentum distribution for the two-dimensional disk system. Note the violent redistribution of angular momentum that follows bar formation.

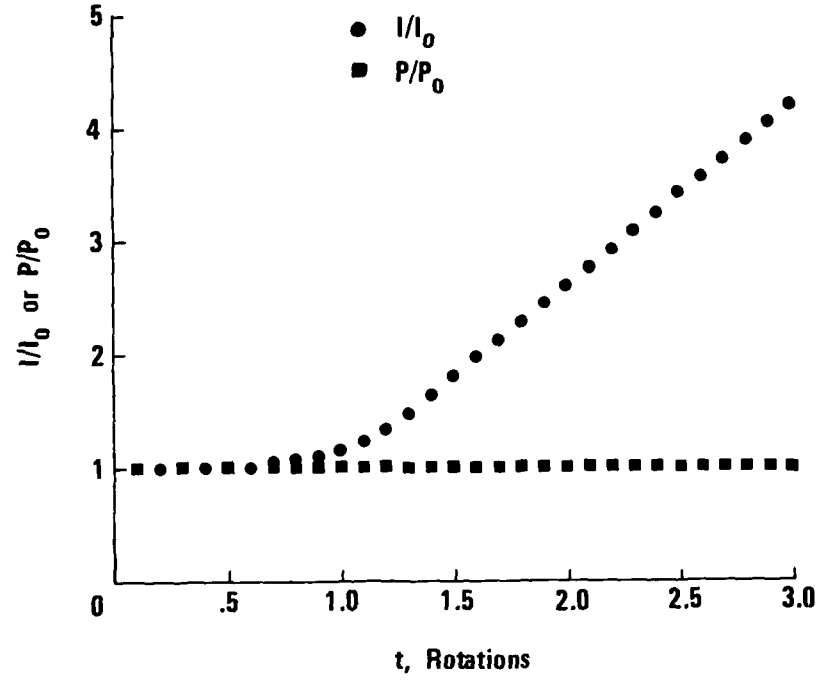

Figure 8.- Evolution of the angular momentum P and the moment of inertia I (divided by their initial values) for the two-dimensional disk system. Note the rapid increase in I as the bar begins to form at t = 1.0.

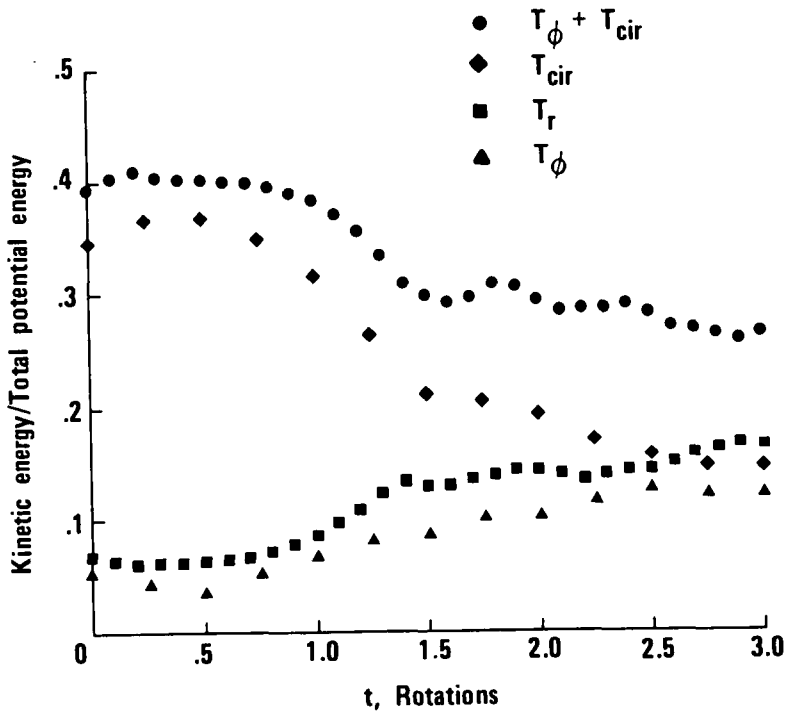

Figure 9.- Evolution of various ratios of kinetic energy to total potential energy for the two-dimensional disk system. Note that the ratio of rotational to potential energy is approaching the value of 0.14 predicted by Ostriker and Peebles (ref. 8) as being required for stability.

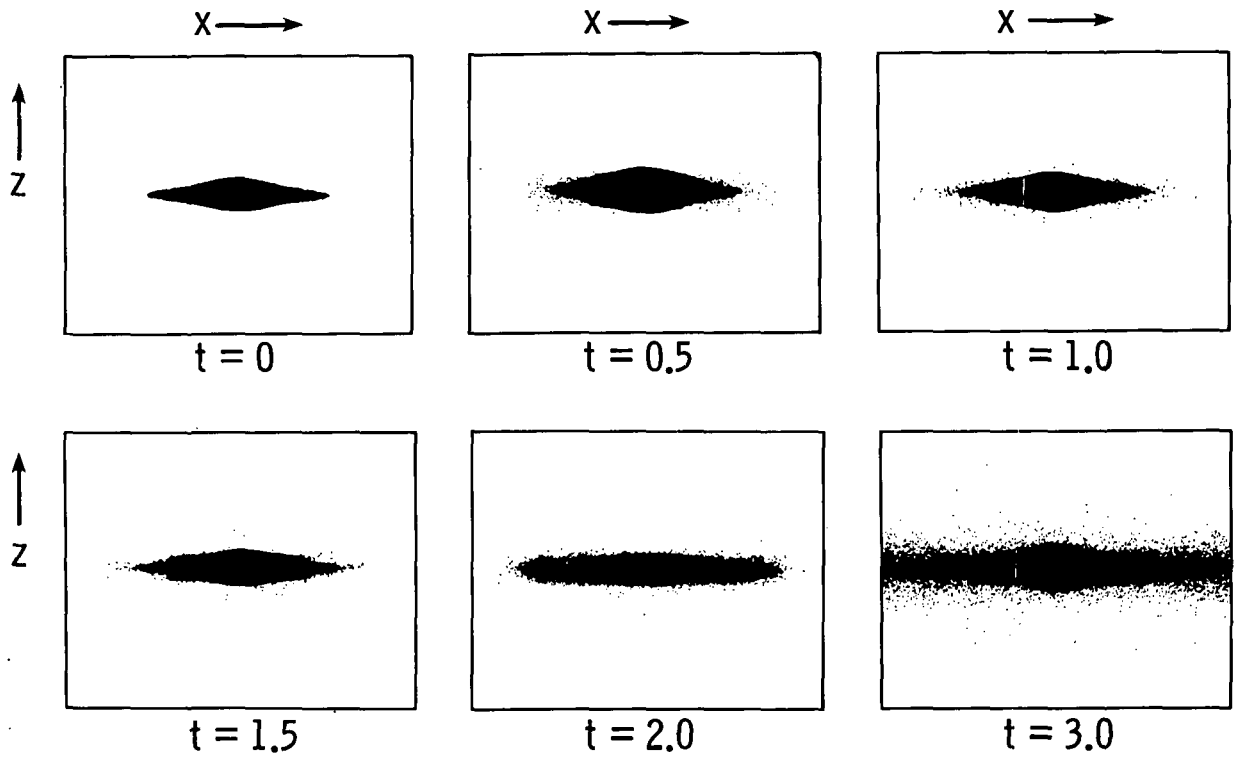

(a) x-z projection.

Figure 10.- Side views of the evolution of the three-dimensional disk system. The bar instability results in a rapid expansion in the plane of the disk.

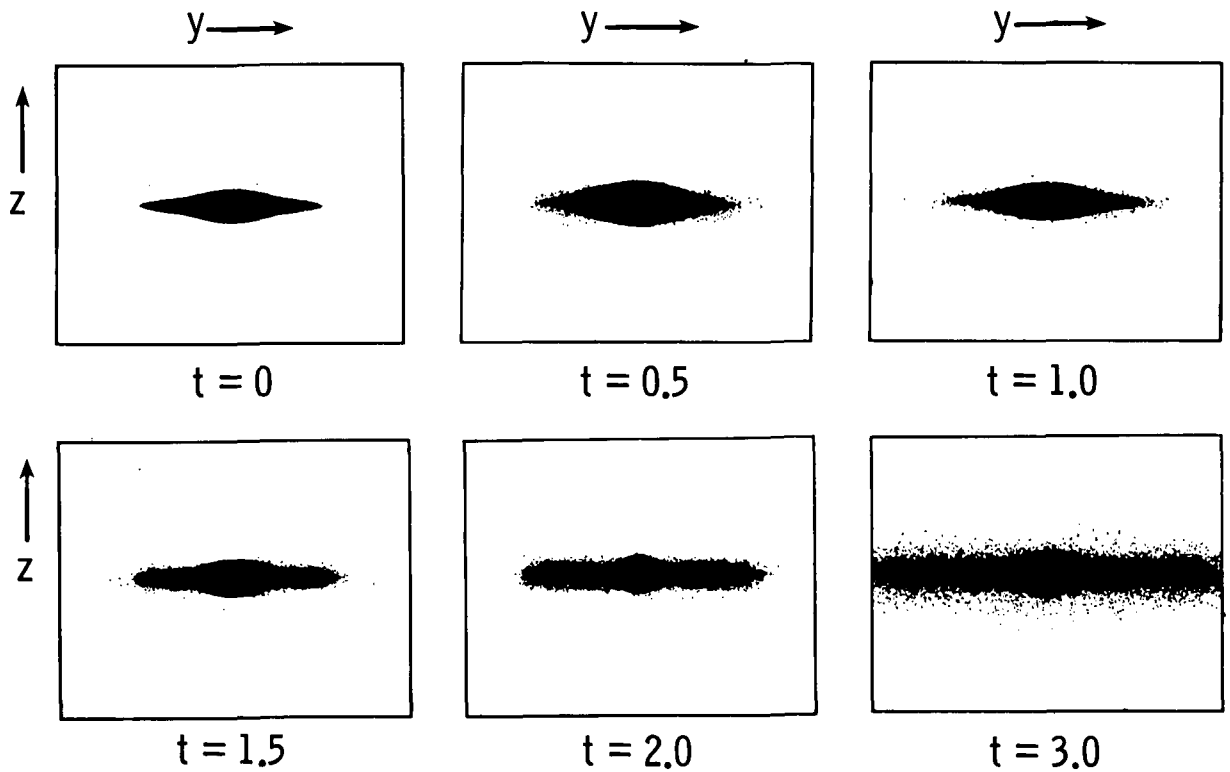

(b) y-z projection.

Figure 10.- Concluded.

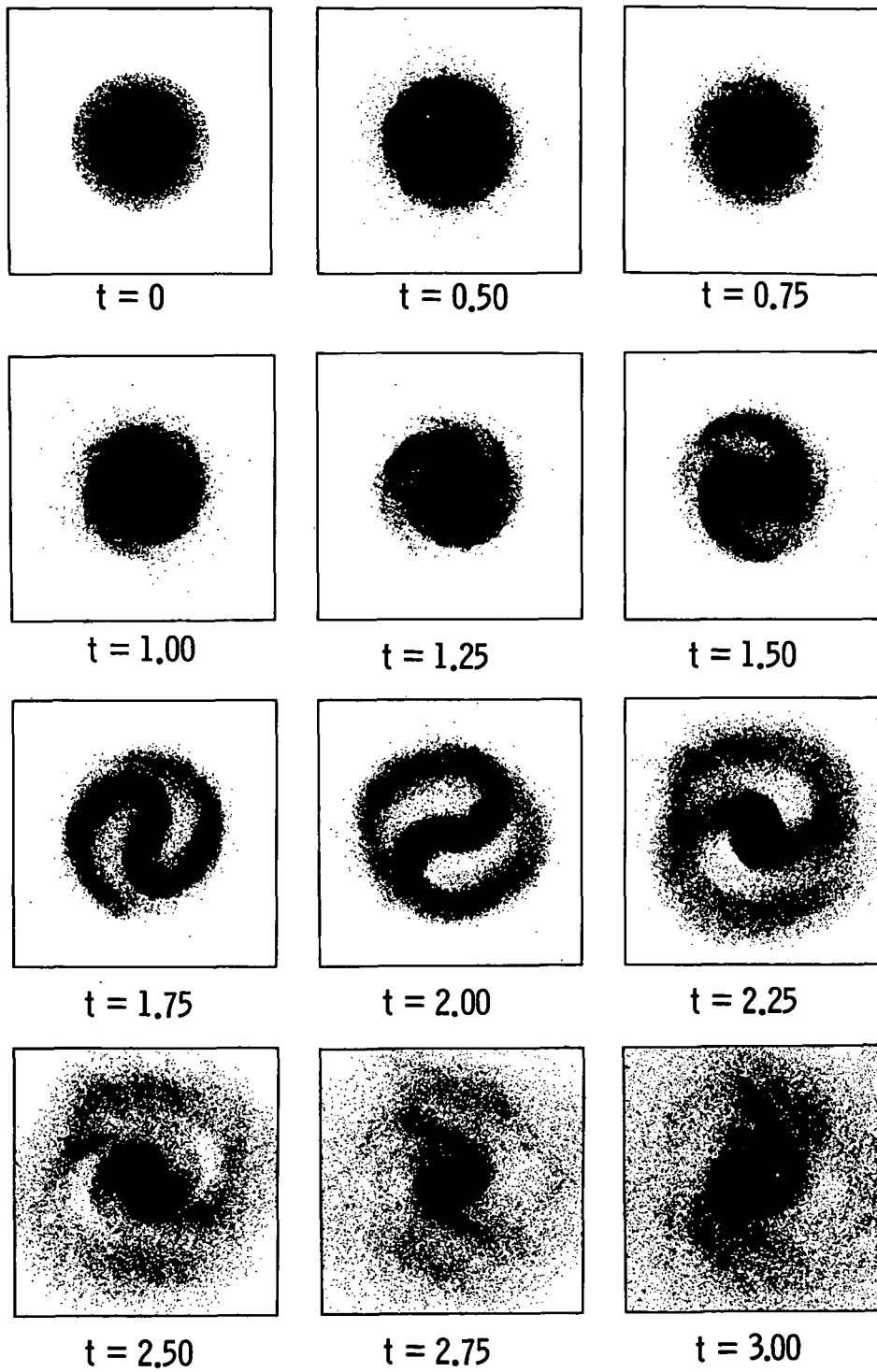

Figure 11.- Evolution of an initially balanced, three-dimensional disk system of 100 000 stars with an exponential radial density variation.

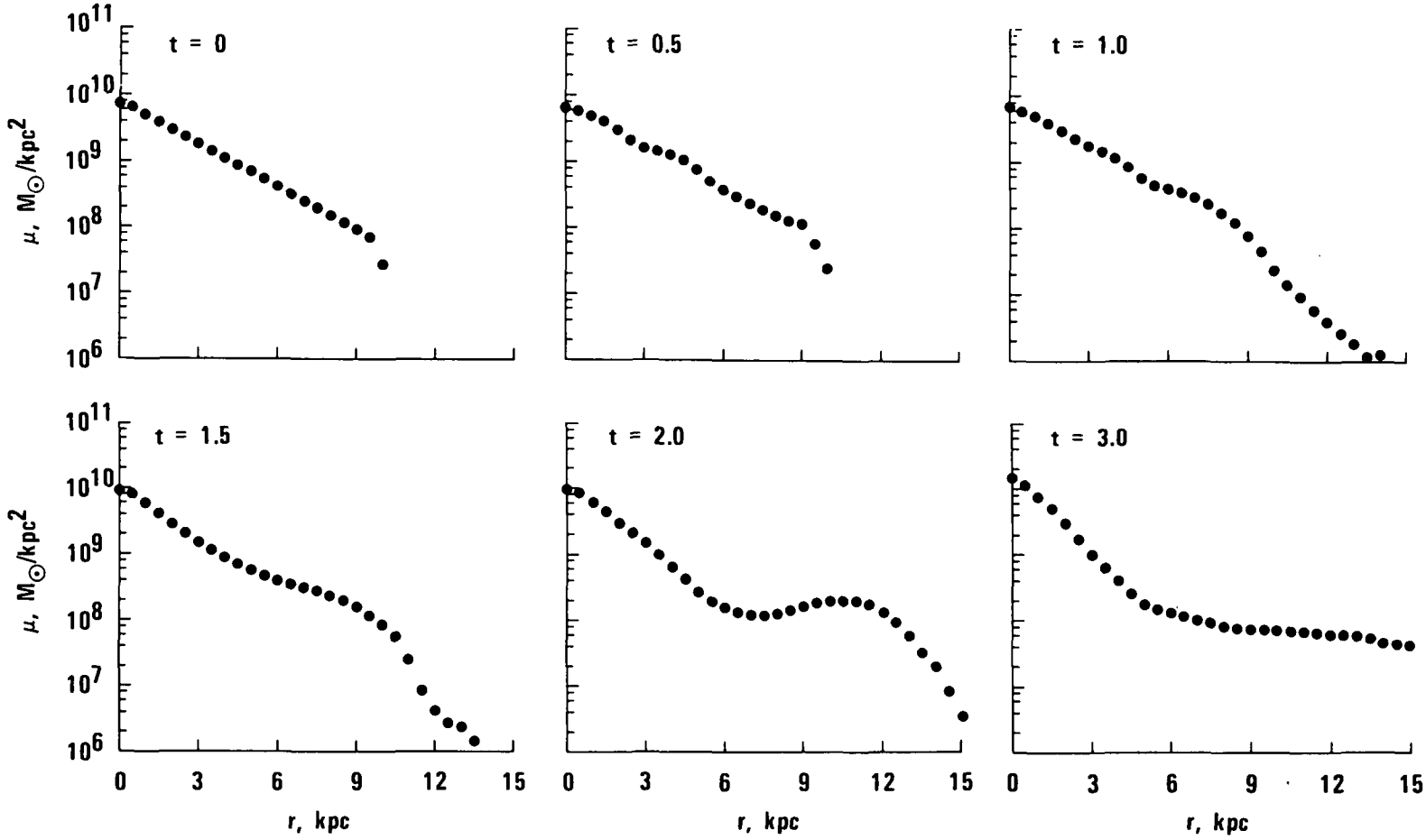

Figure 12.- Evolution of the azimuthally averaged projected surface mass density as a function of radius for the three-dimensional disk system.

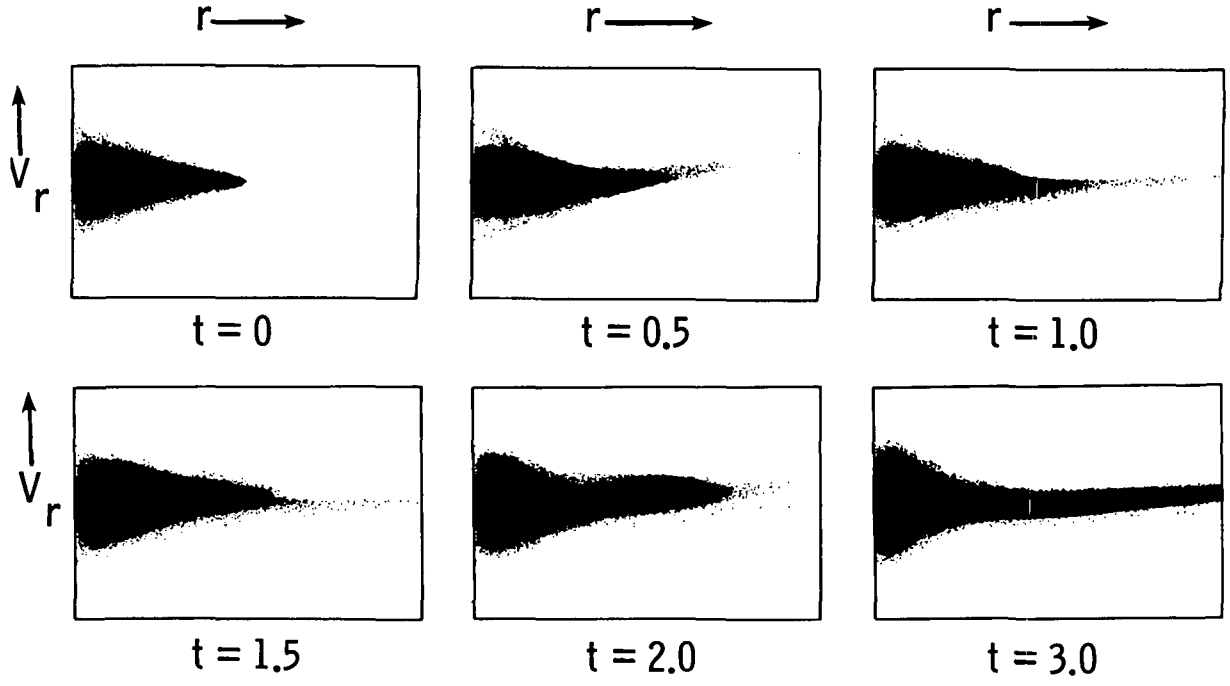

(a) Radial velocities.

Figure 13.- Evolution of the velocity distributions as a function of radius for the three-dimensional disk system.

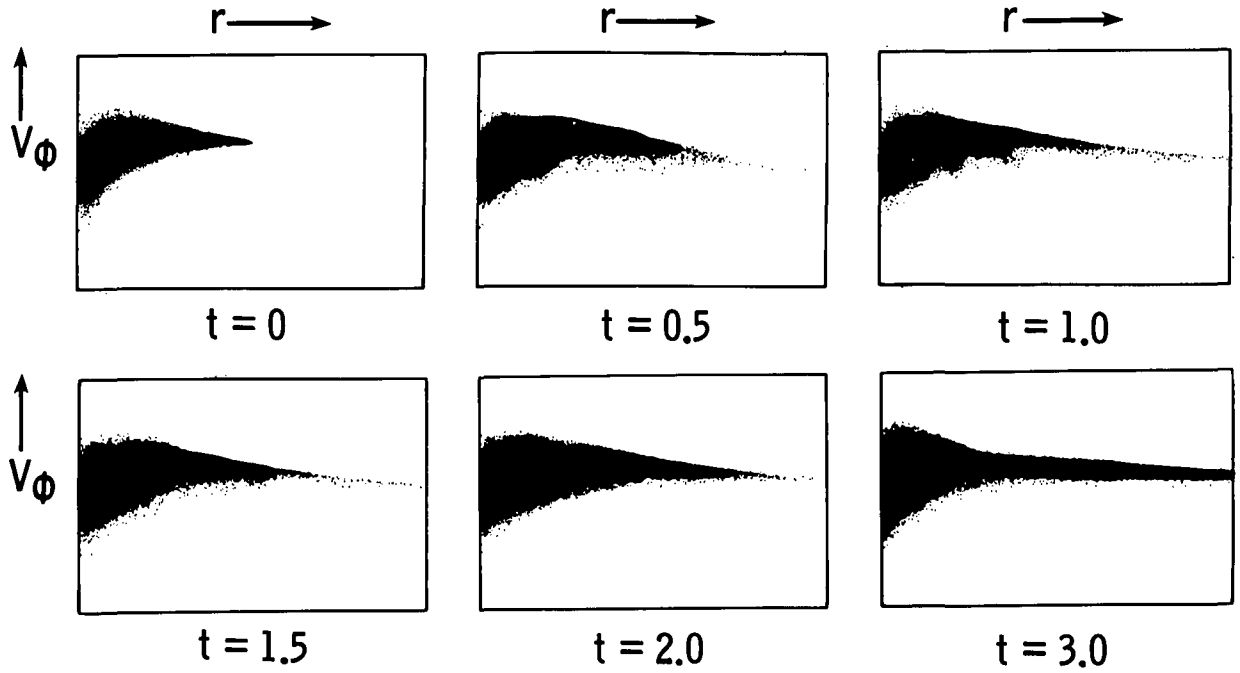

(b) Azimuthal velocities.

Figure 13.- Continued.

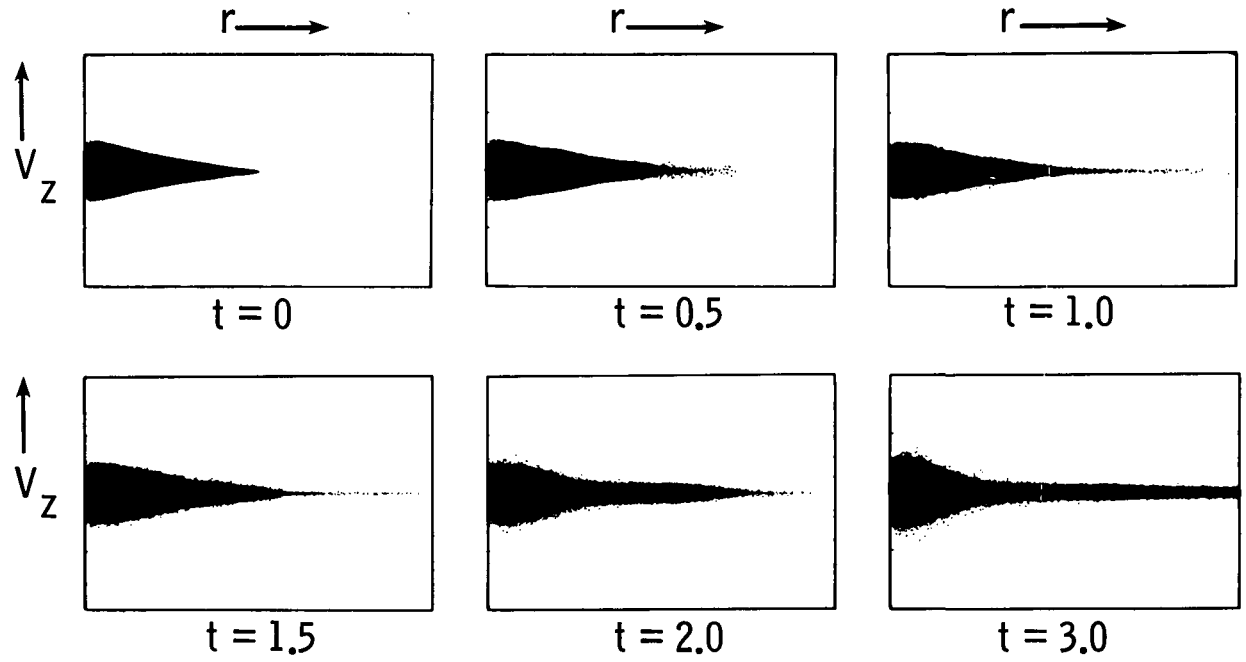

(c) Axial velocities.

Figure 13.- Concluded.

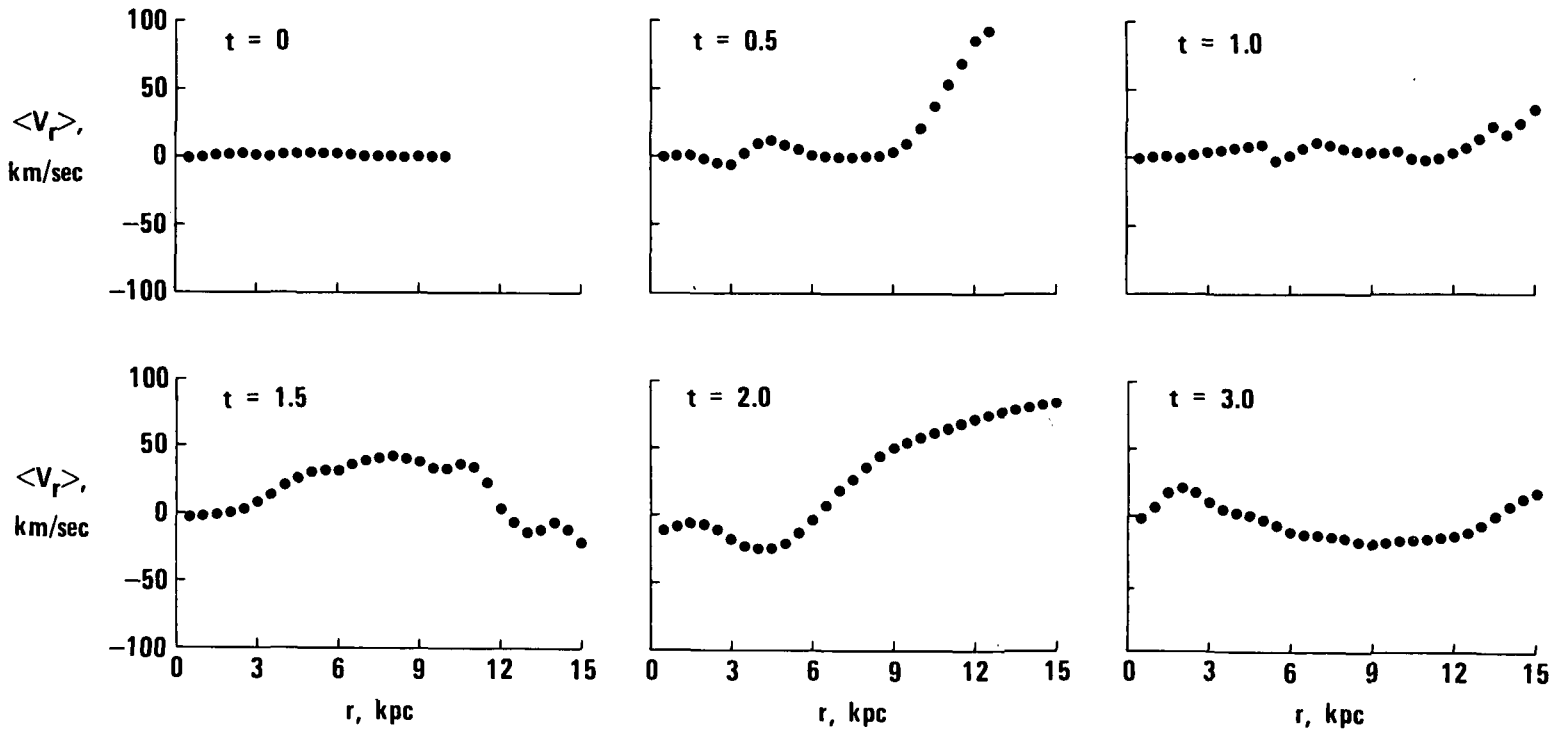

Figure 14.- Evolution of the azimuthally averaged, mean radial velocity as a function of radius for the three-dimensional disk system.

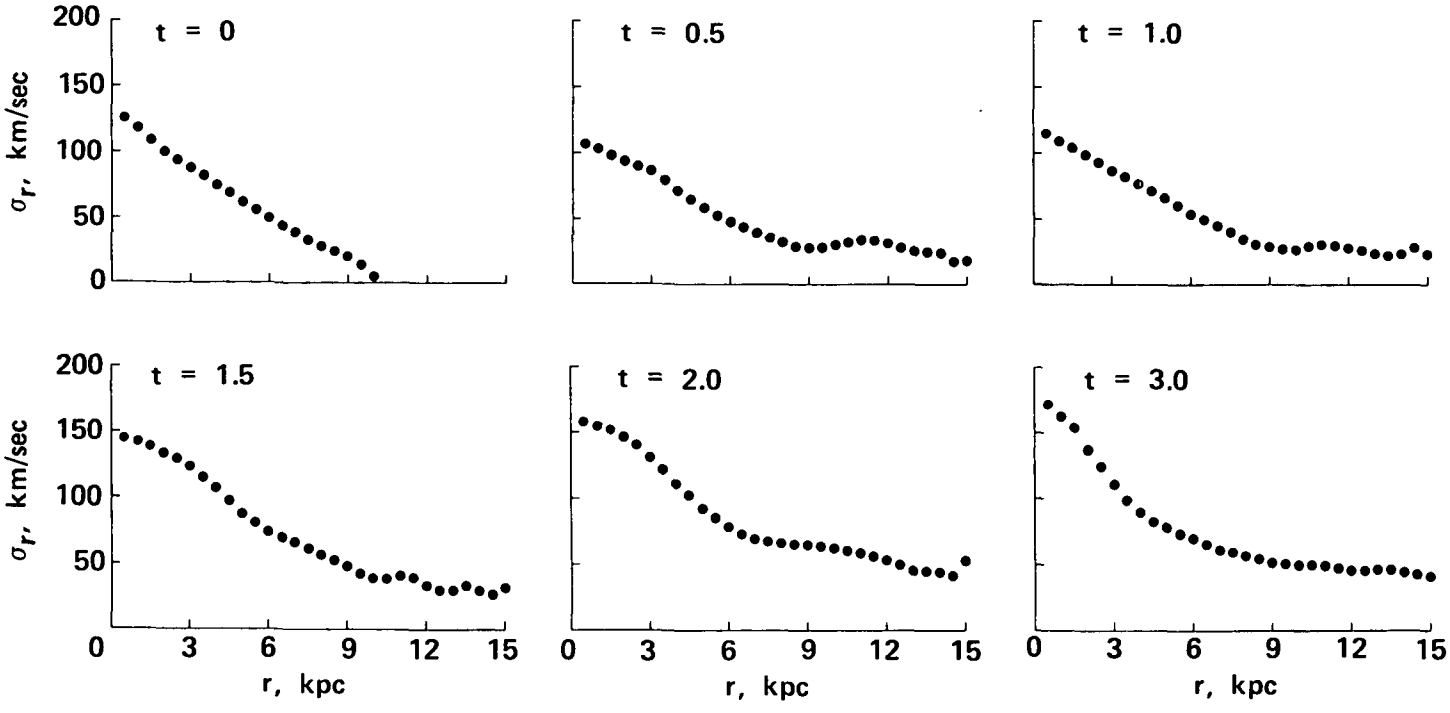

(a) Radial velocity dispersion.

Figure 15.- Evolution of the azimuthally averaged velocity dispersions as a function of radius for the three-dimensional disk system.

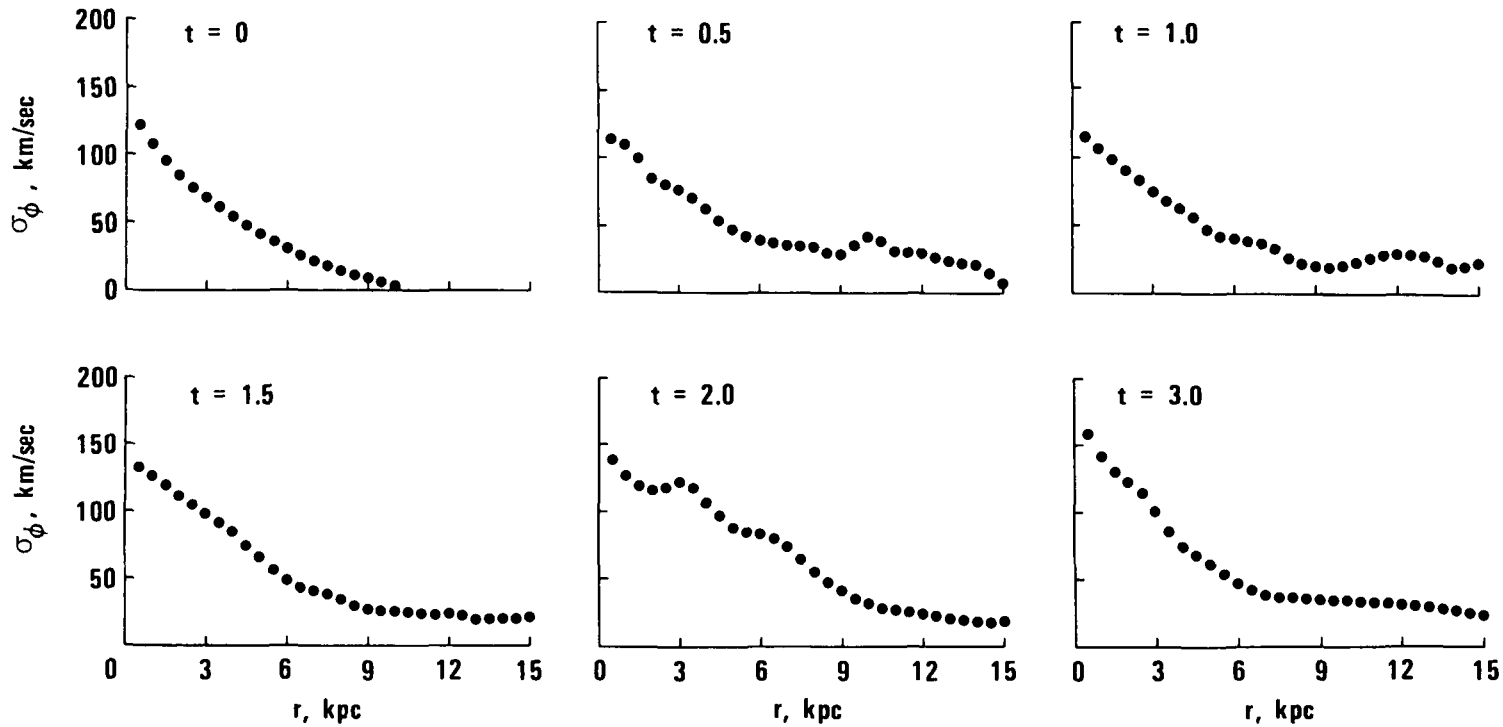

(b) Azimuthal velocity dispersion.

Figure 15.- Continued.

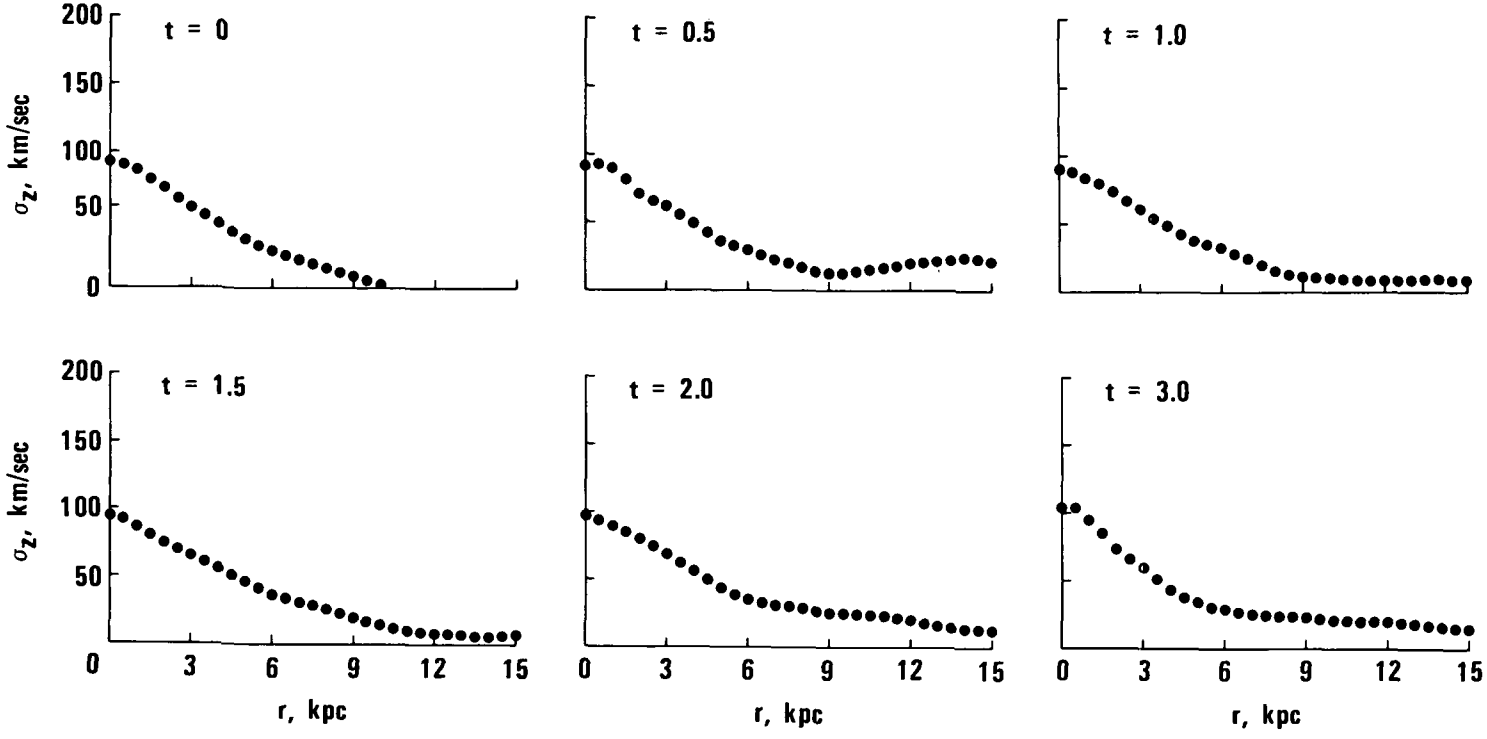

(c) Axial velocity dispersion.

Figure 15.- Concluded.

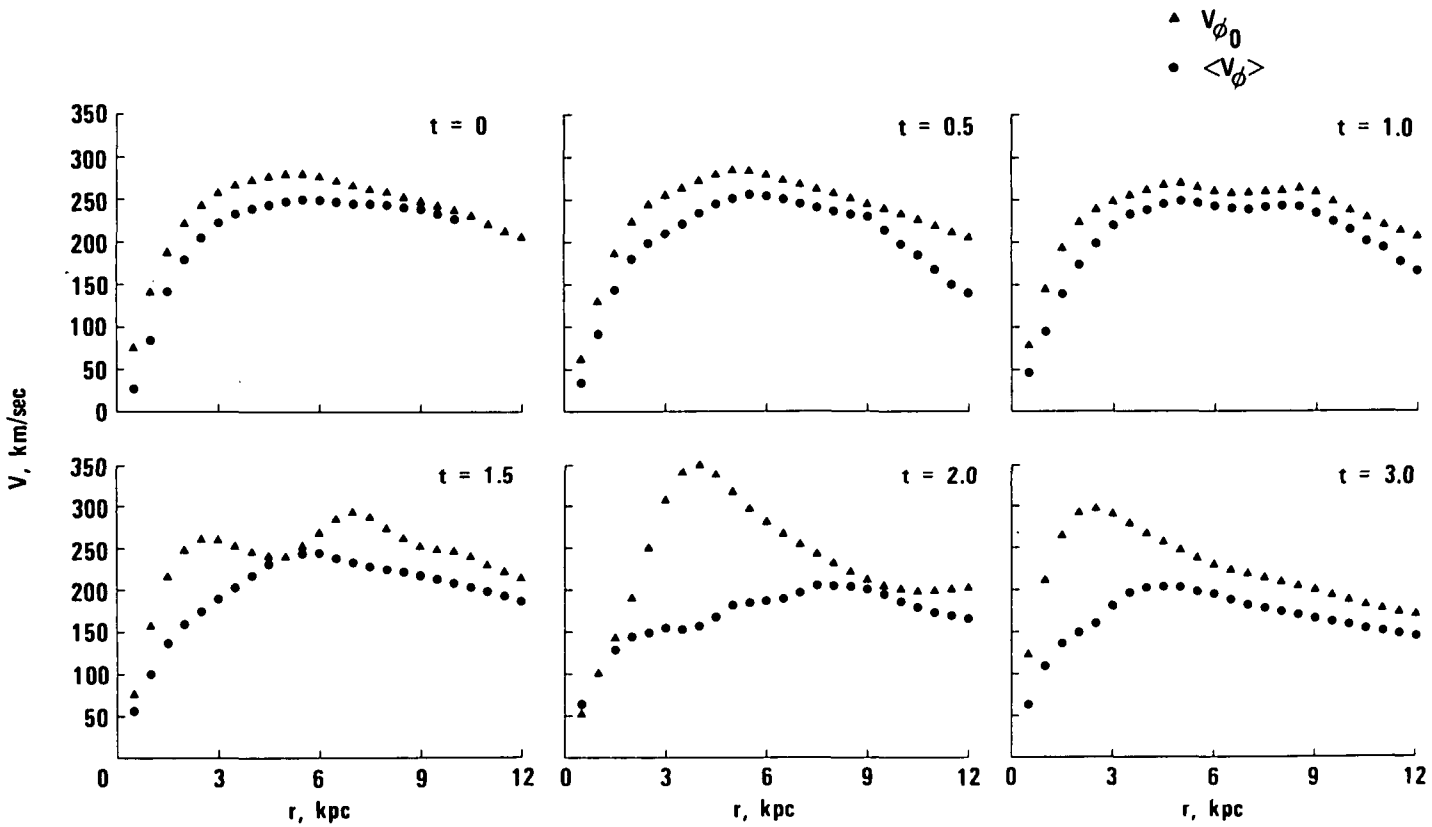

Figure 16.- Comparison of the circular velocity $V_{\phi_o} = \sqrt{K_r(z=0)\,r}$ and the mean azimuthal velocity $\langle V_\phi \rangle$ for the three-dimensional disk system.

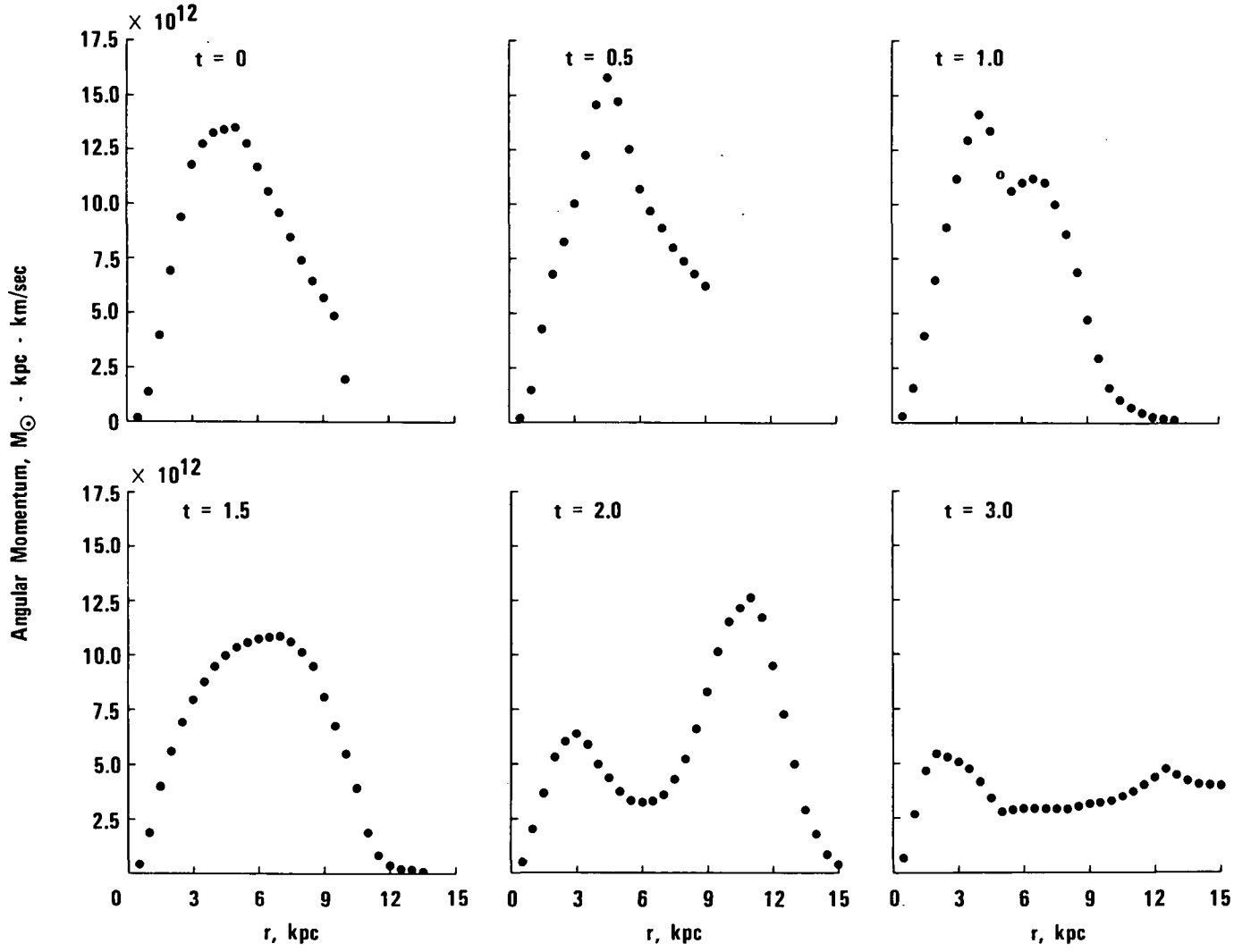

Figure 17.- Evolution of the angular momentum distribution for the three-dimensional disk system.

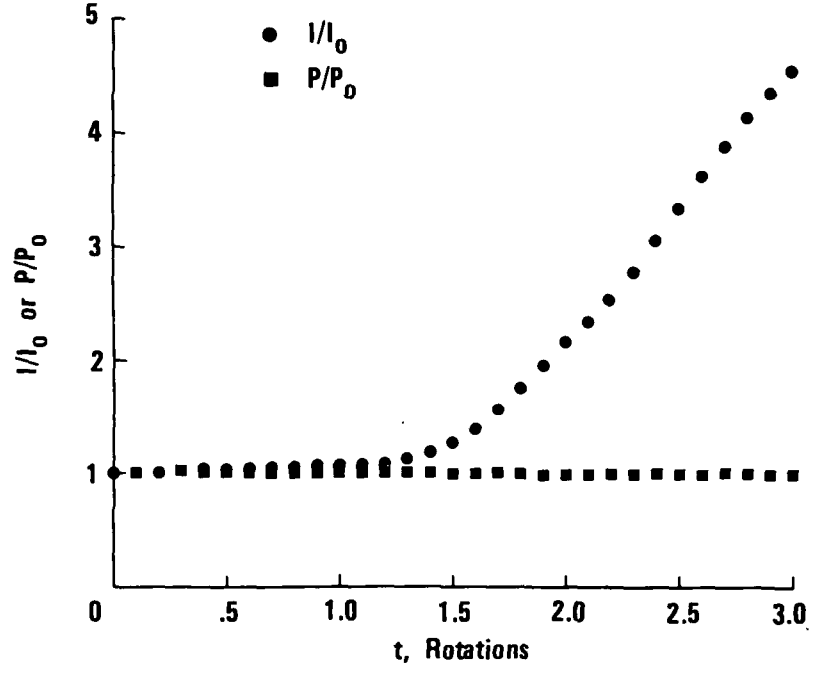

Figure 18.- Evolution of the angular momentum P and the moment of inertia I (divided by their initial values) for the three-dimensional disk system.

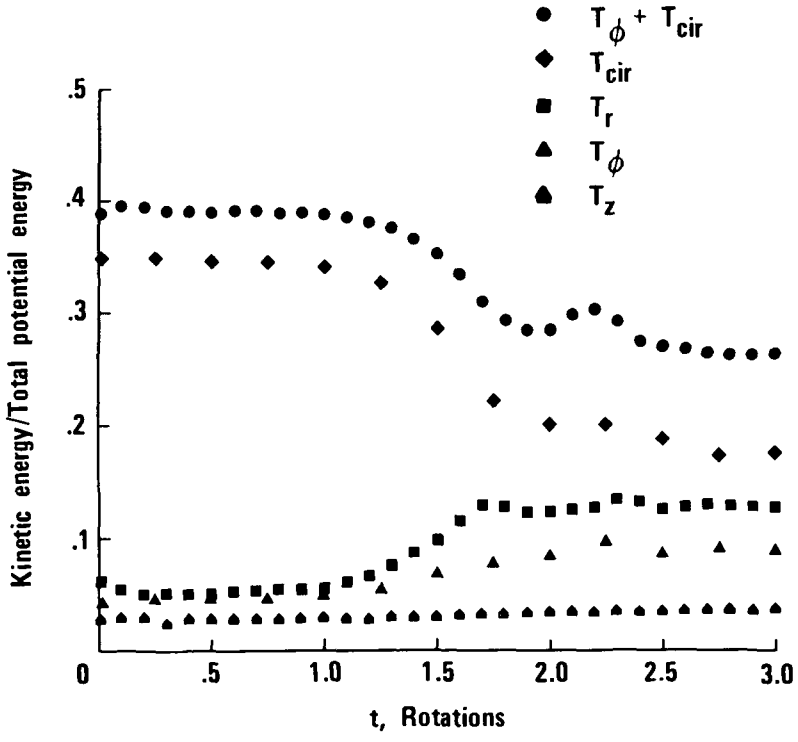

Figure 19.- Evolution of various ratios of kinetic energy to total potential energy for the three-dimensional disk system. Note that the evolutions of the energy ratios are similar to those shown in figure 9.

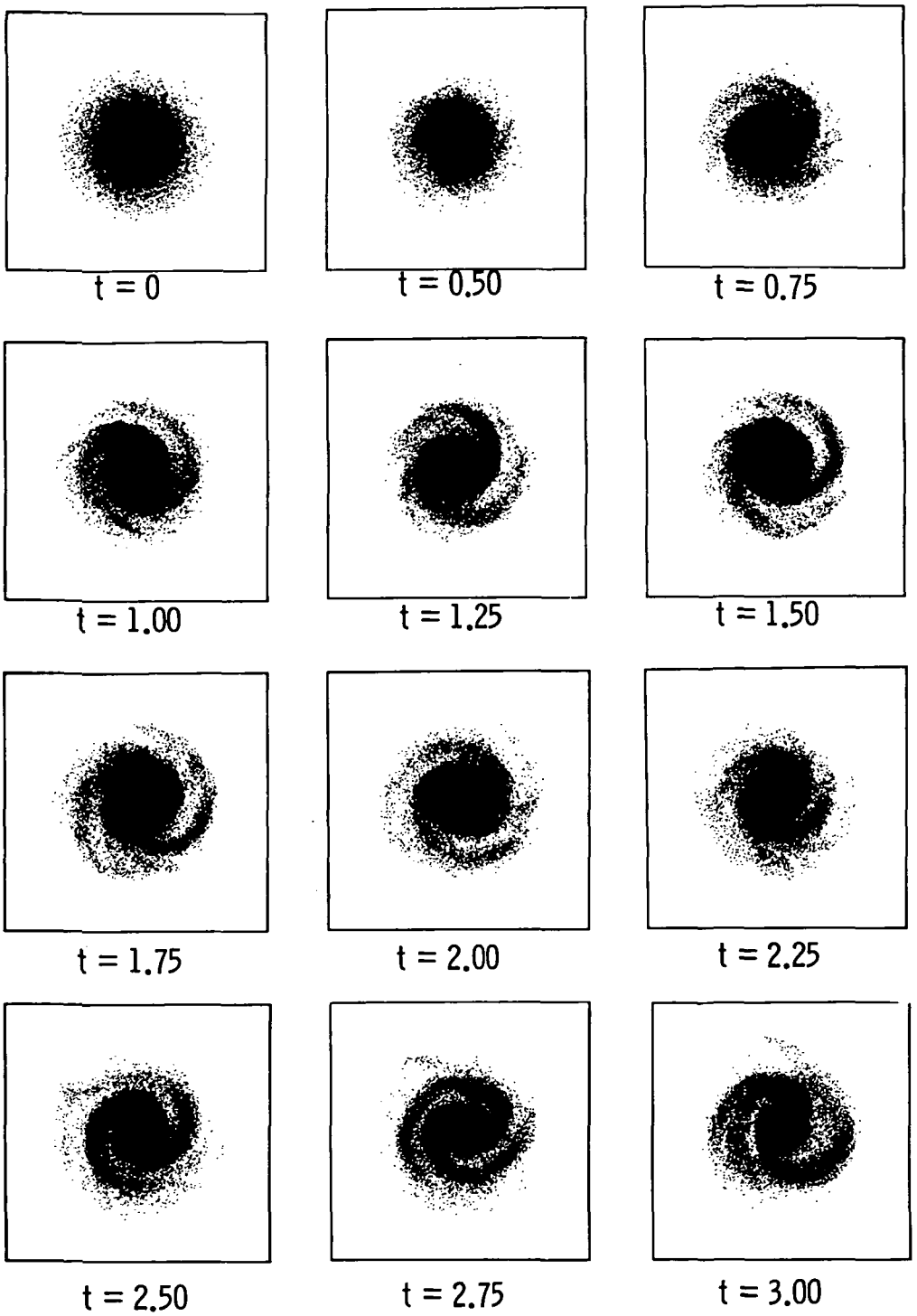

Figure 20.- Evolution of an infinitesimally thin exponential disk with a self-consistent exponential core component. Note that the evolution is considerably less violent than that displayed in figure 1.

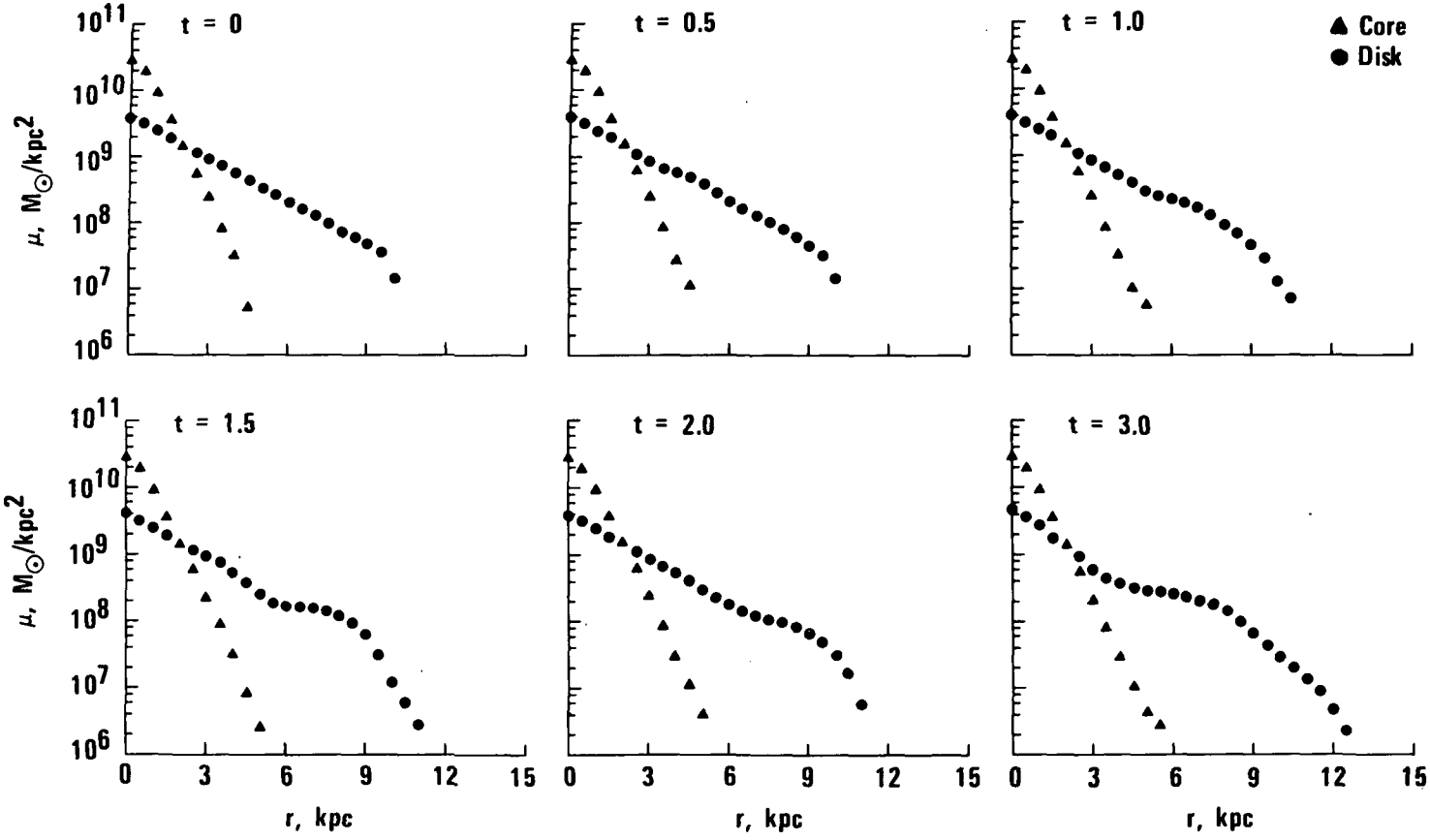

Figure 21.- Evolution of the azimuthally averaged surface mass density for the two-dimensional disk-core system. Note that there is practically no change in the core structure, whereas the bar instability in the disk causes an increase in the density at larger radii.

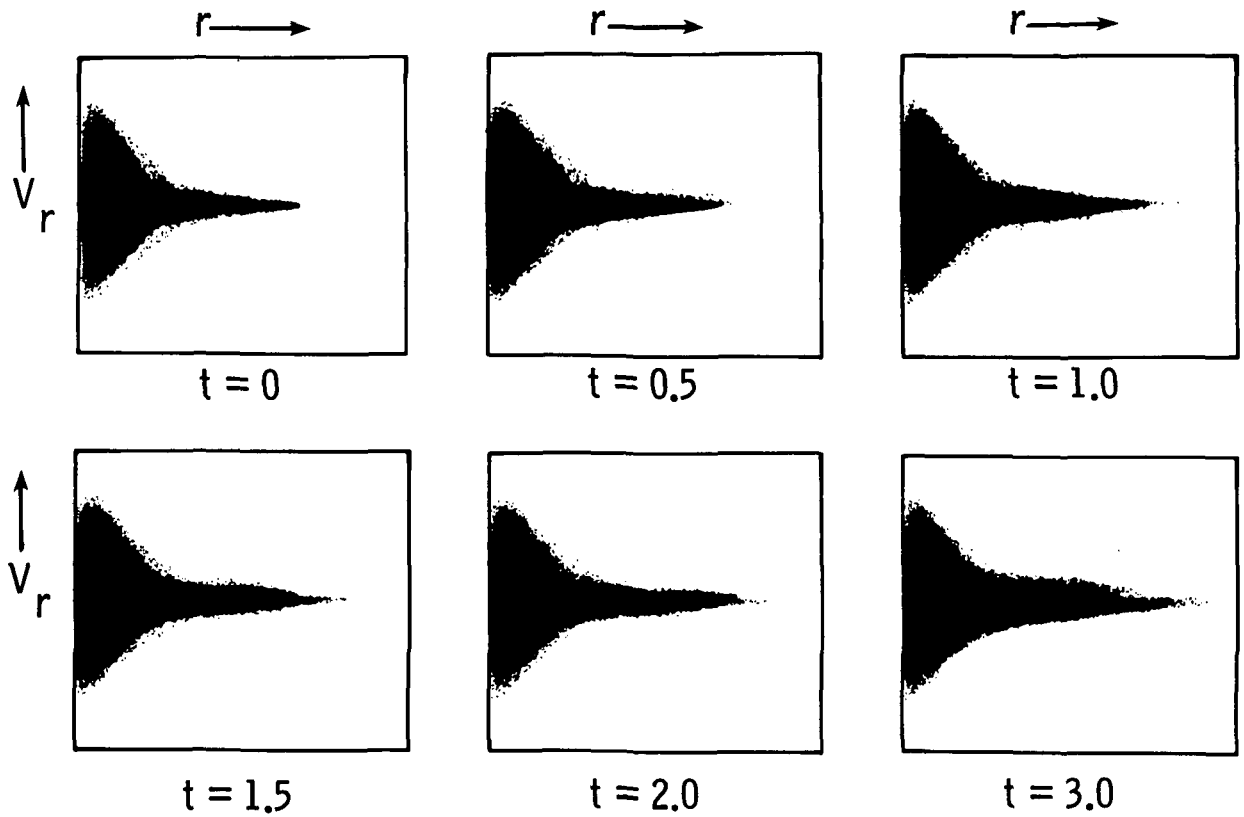

(a) Radial velocities.

Figure 22.- Evolution of the velocity distribution as a function of radius for the two-dimensional disk-core system.

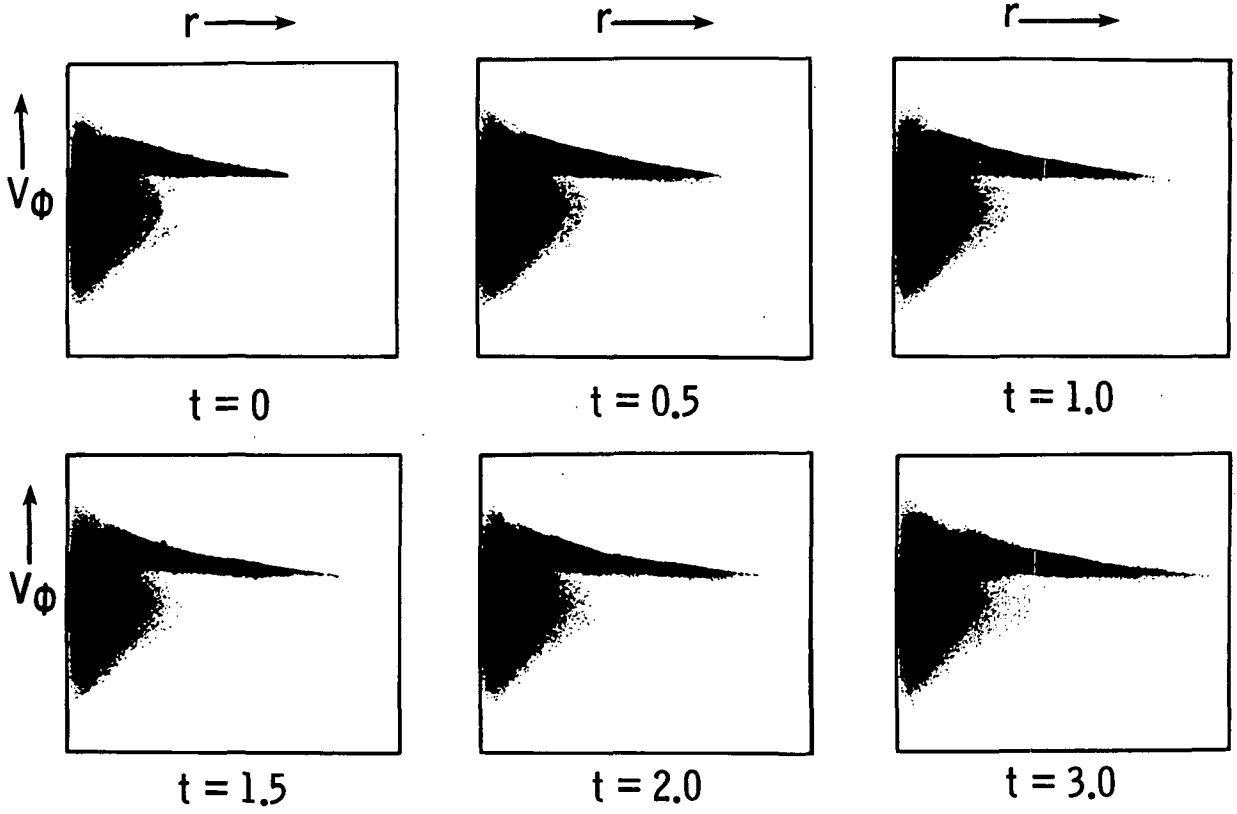

(b) Azimuthal velocities.

Figure 22.- Concluded.

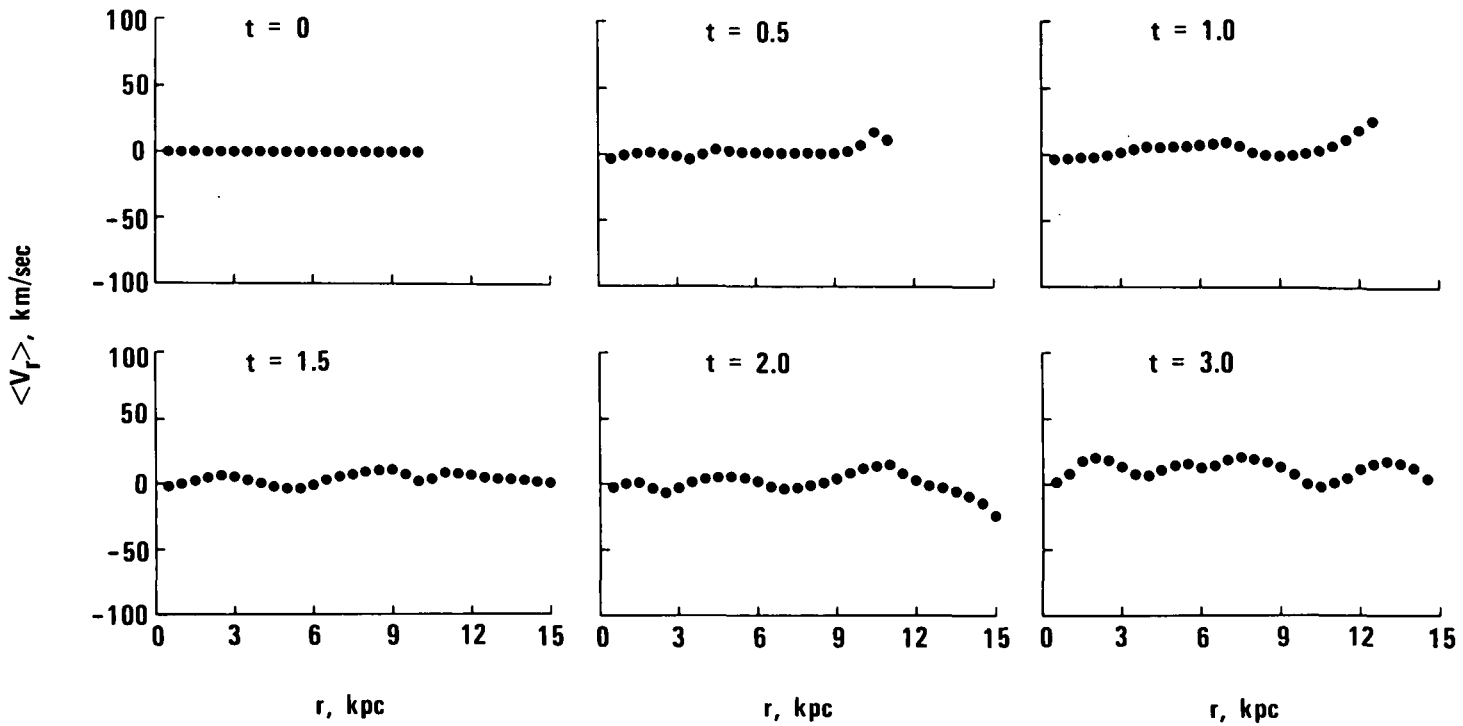

Figure 23.- Evolution of the azimuthally averaged, mean radial velocity as a function of radius for two-dimensional disk-core system. Note the large reduction in $\langle V_r \rangle$ when compared with figure 4.

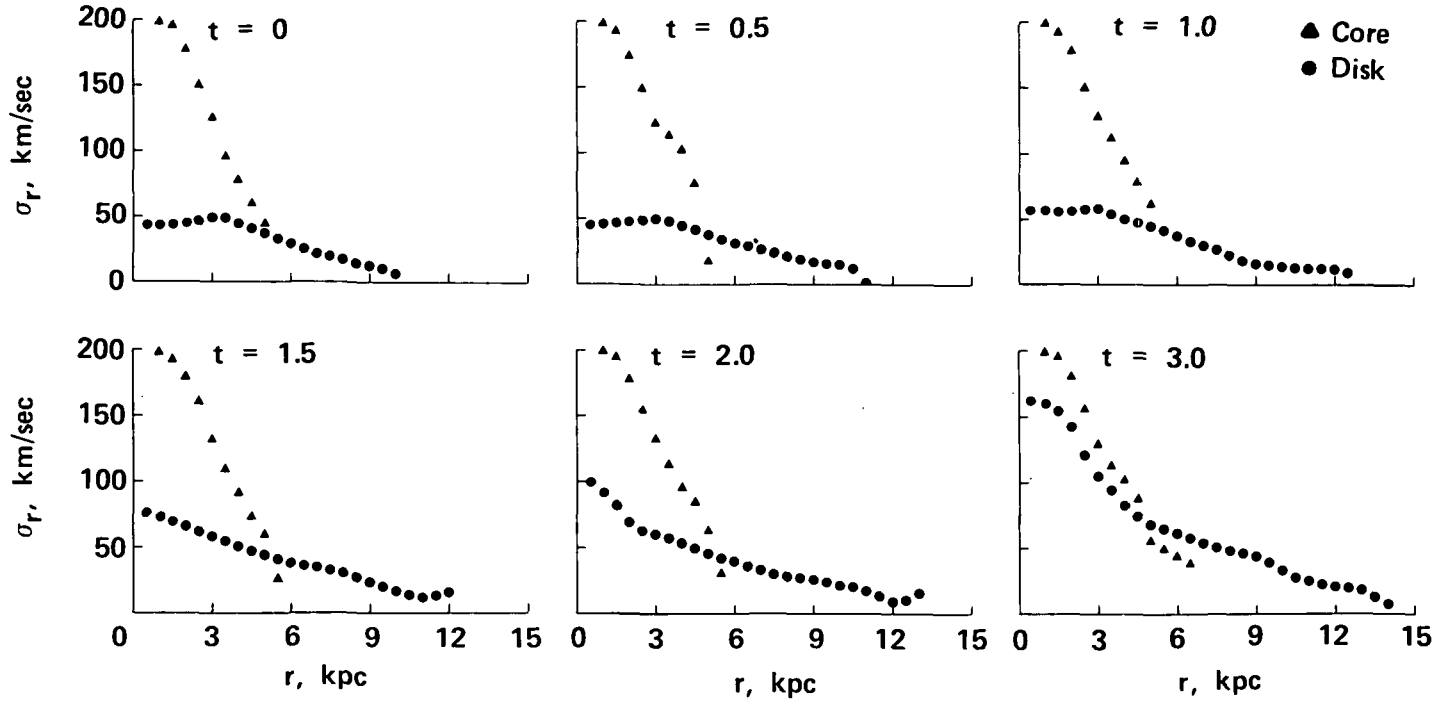

(a) Radial velocity dispersion.

Figure 24.- Evolution of the azimuthally averaged velocity dispersions as a function of radius for the two-dimensional disk-core system.

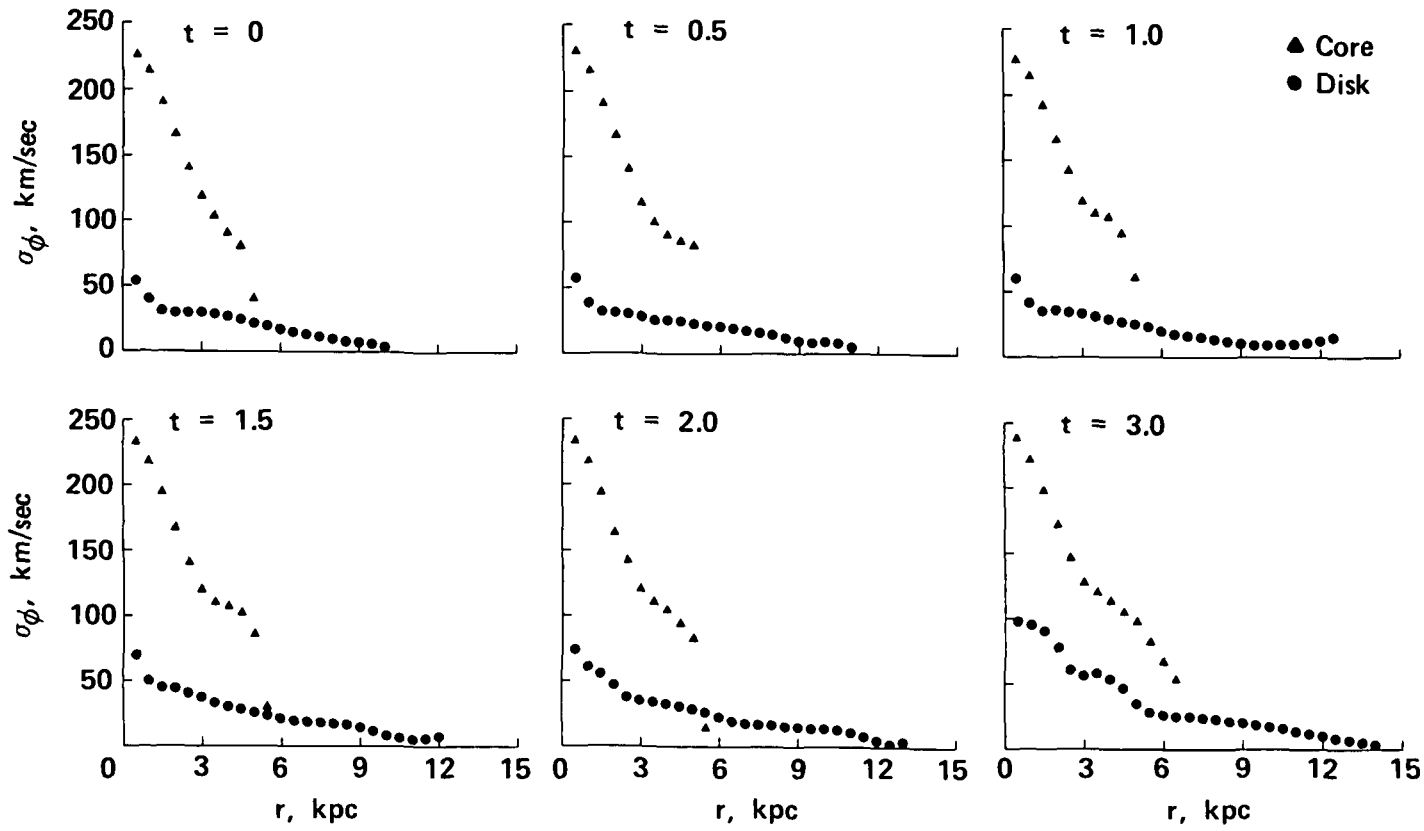

(b) Azimuthal velocity dispersion.

Figure 24.- Concluded.

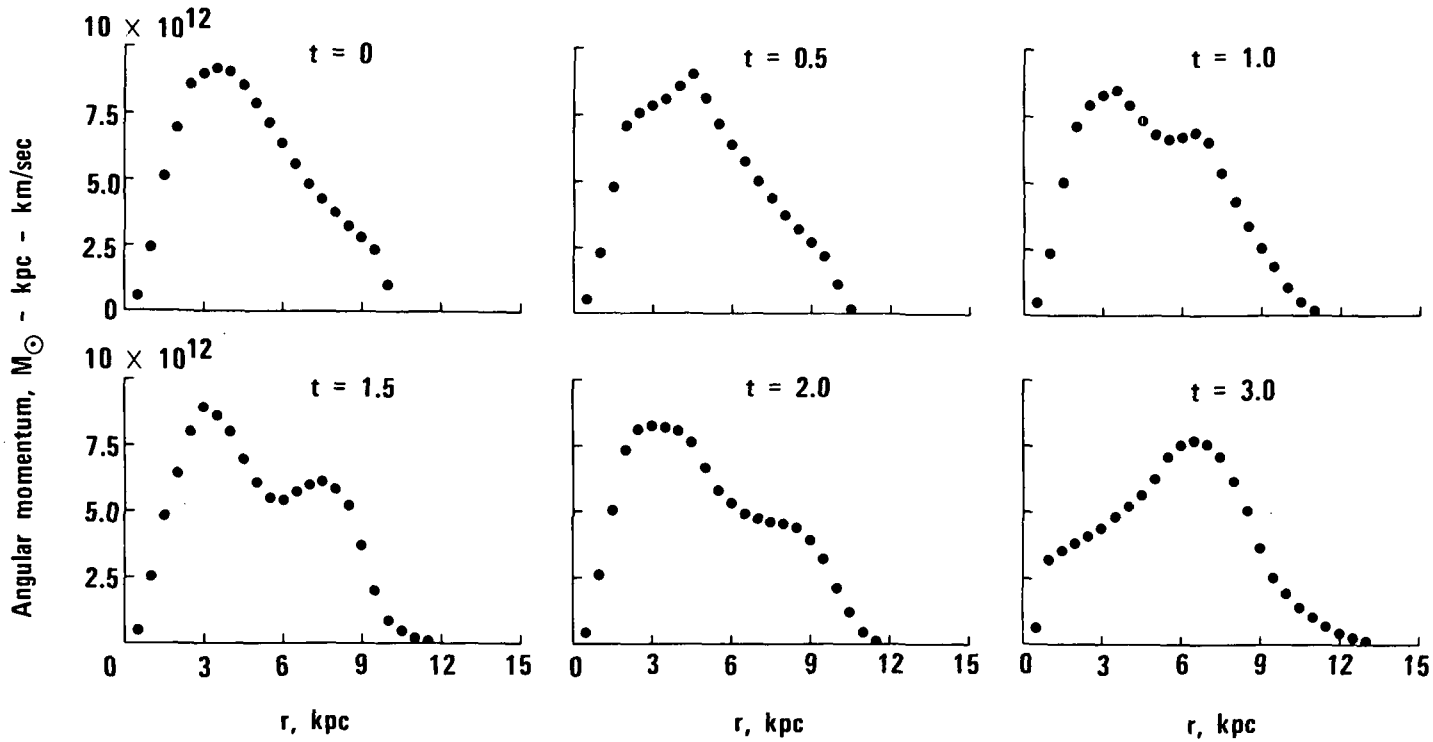

Figure 25.- Evolution of the angular momentum distribution for the two-dimensional disk-core system.

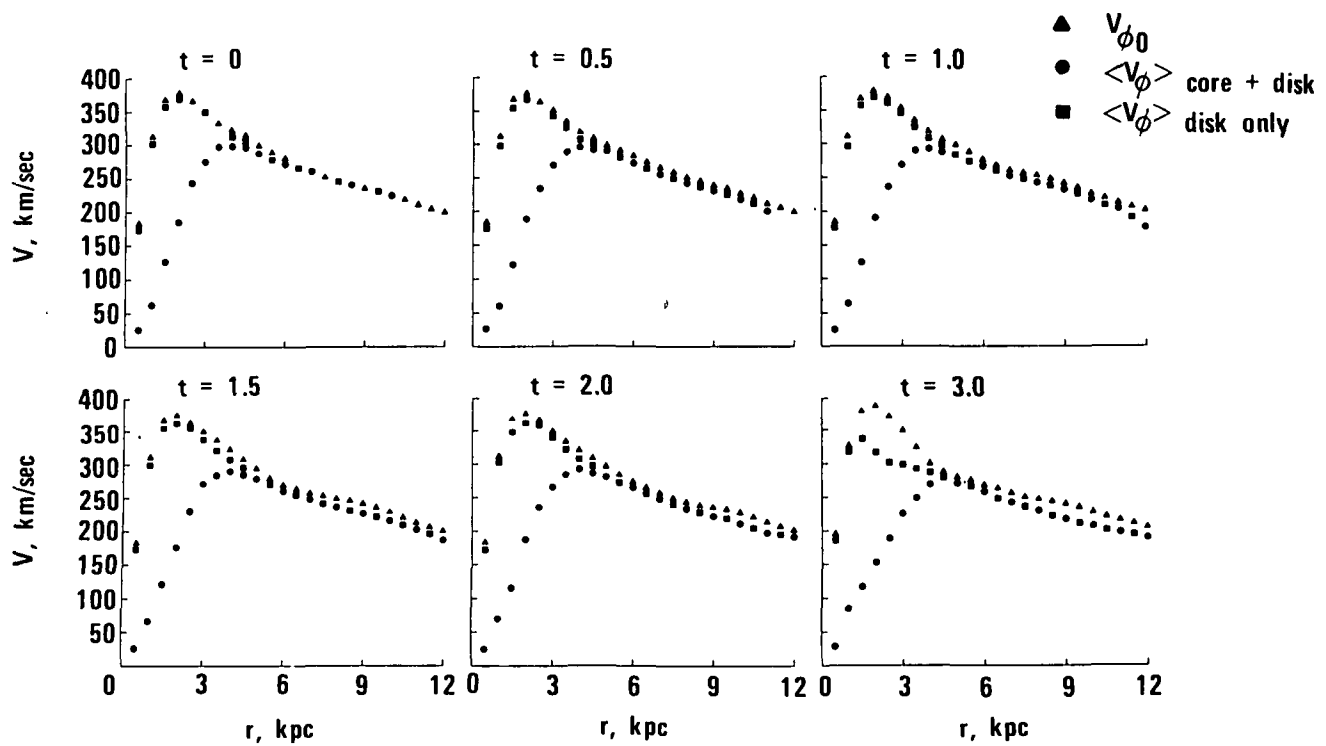

Figure 26.- Comparison of the circular velocity V_{ϕ_o} and the mean azimuthal velocity $\langle V_\phi \rangle$ for the two-dimensional disk-core system.

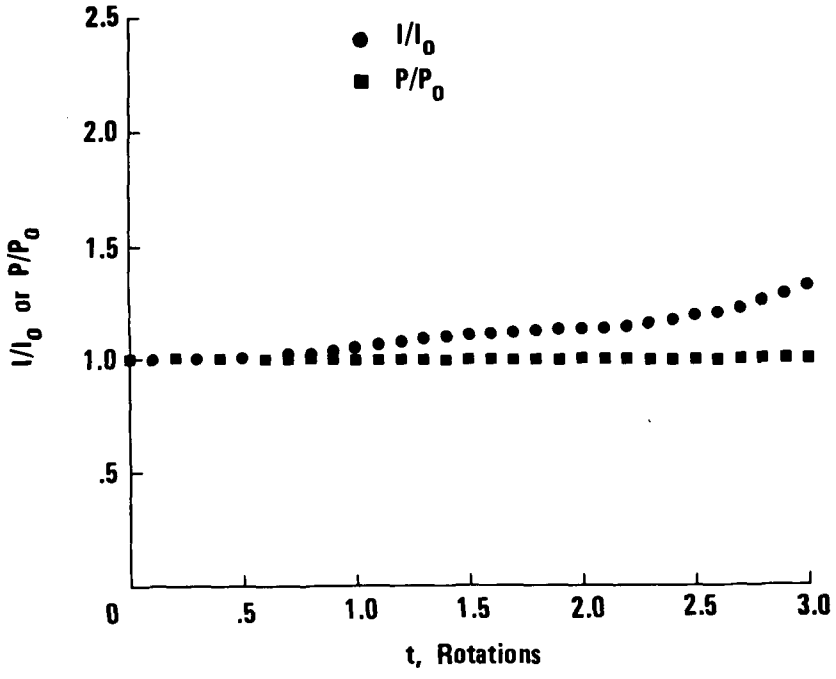

Figure 27.- Evolution of the moment of inertia I and the angular momentum P (divided by their initial values) for the two-dimensional disk-core system.

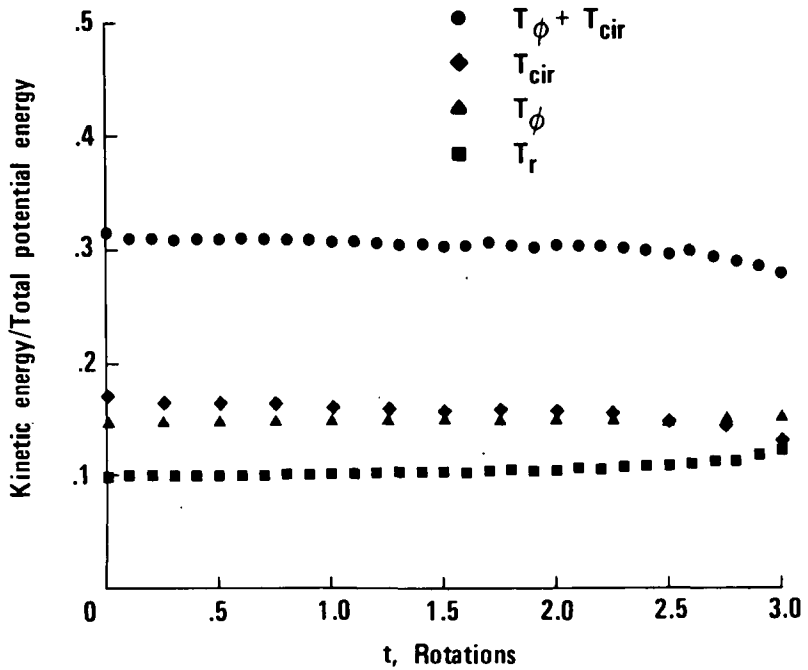

Figure 28.- Evolution of various ratios of kinetic energy to potential energy for the two-dimensional disk-core system.

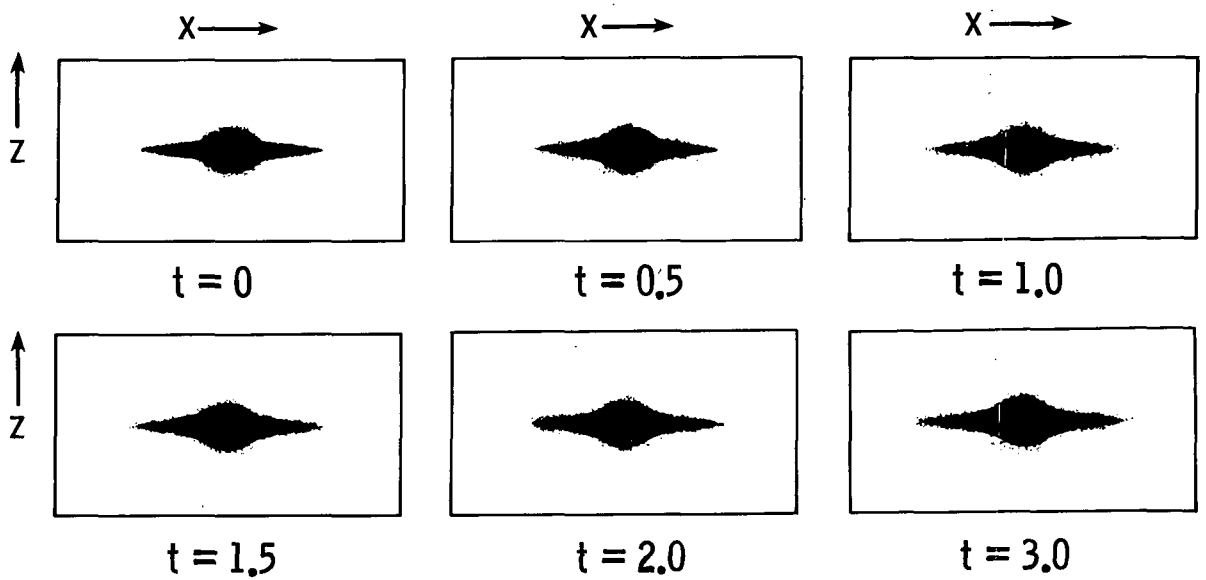

(a) x-z projection.

Figure 29.- Side views of the evolution of the three-dimensional disk-core system. Note the remarkable stability when compared with the three-dimensional disk system shown in figure 10.

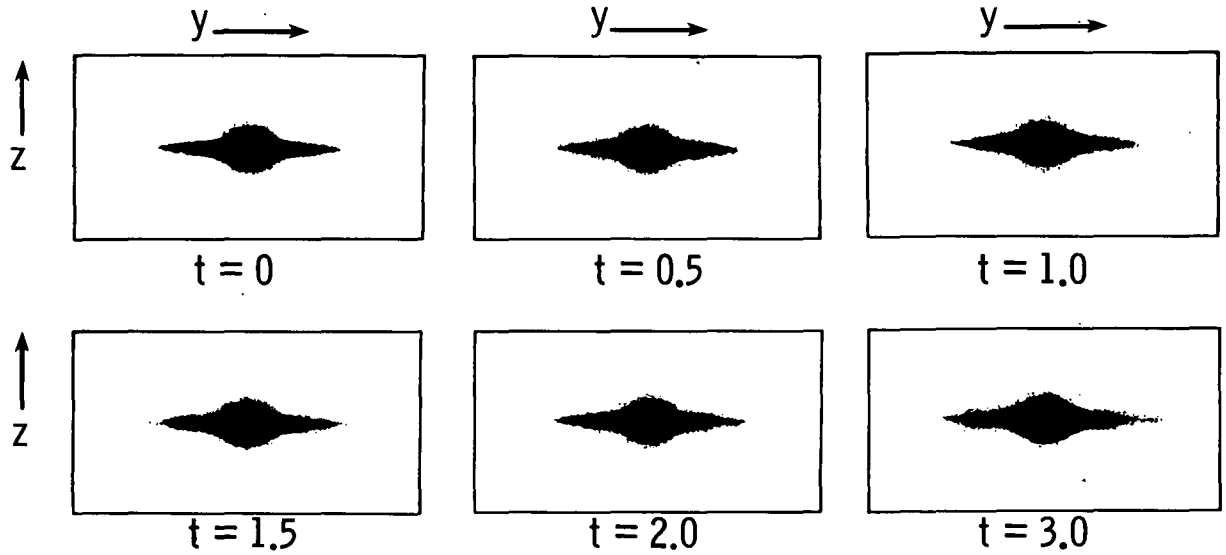

(b) y-z projection.

Figure 29.- Concluded.

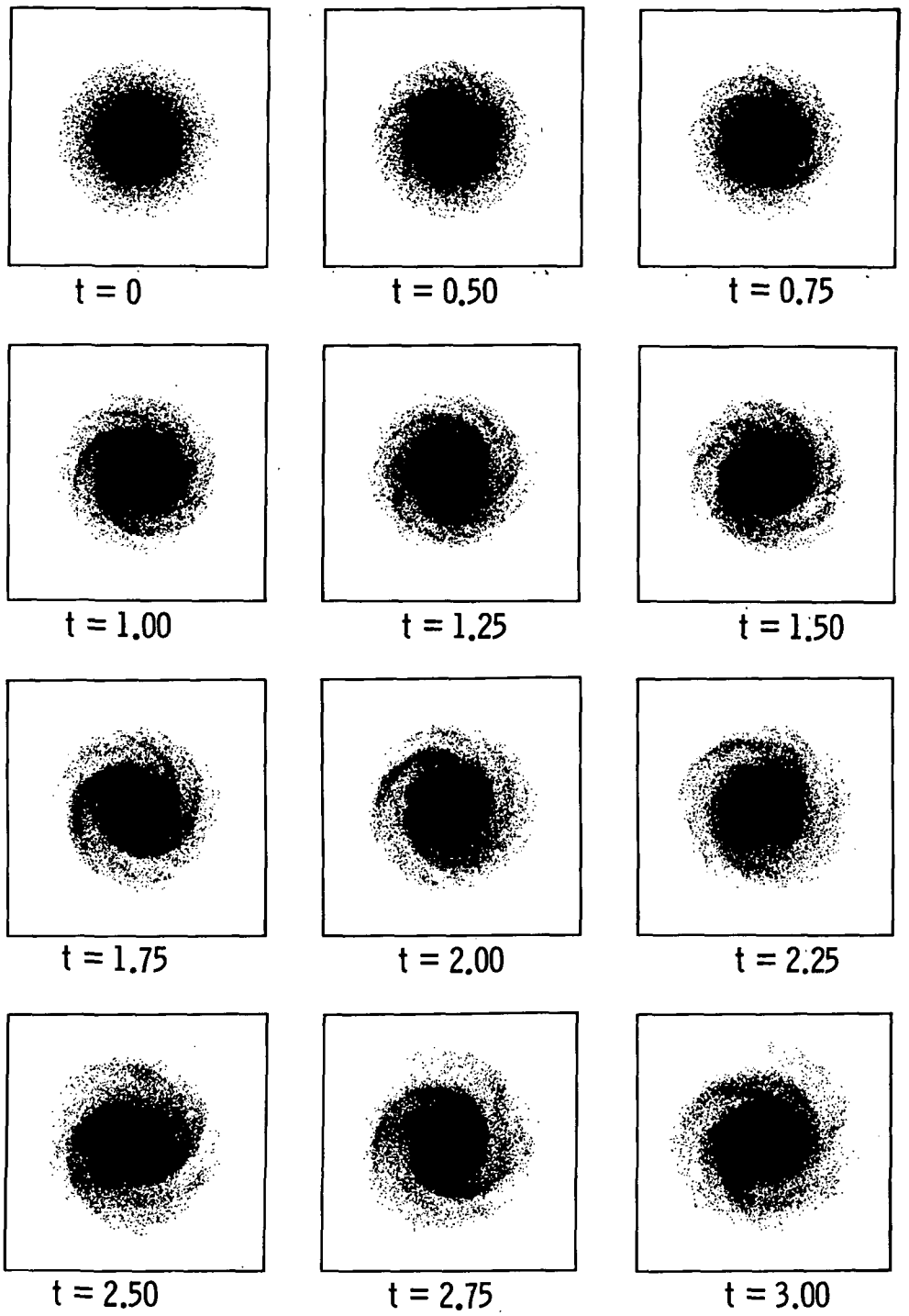

Figure 30.- Evolution of the three-dimensional exponential disk-core system viewed in the equatorial (x-y) plane. Note the development of the comparatively weak spiral structure.

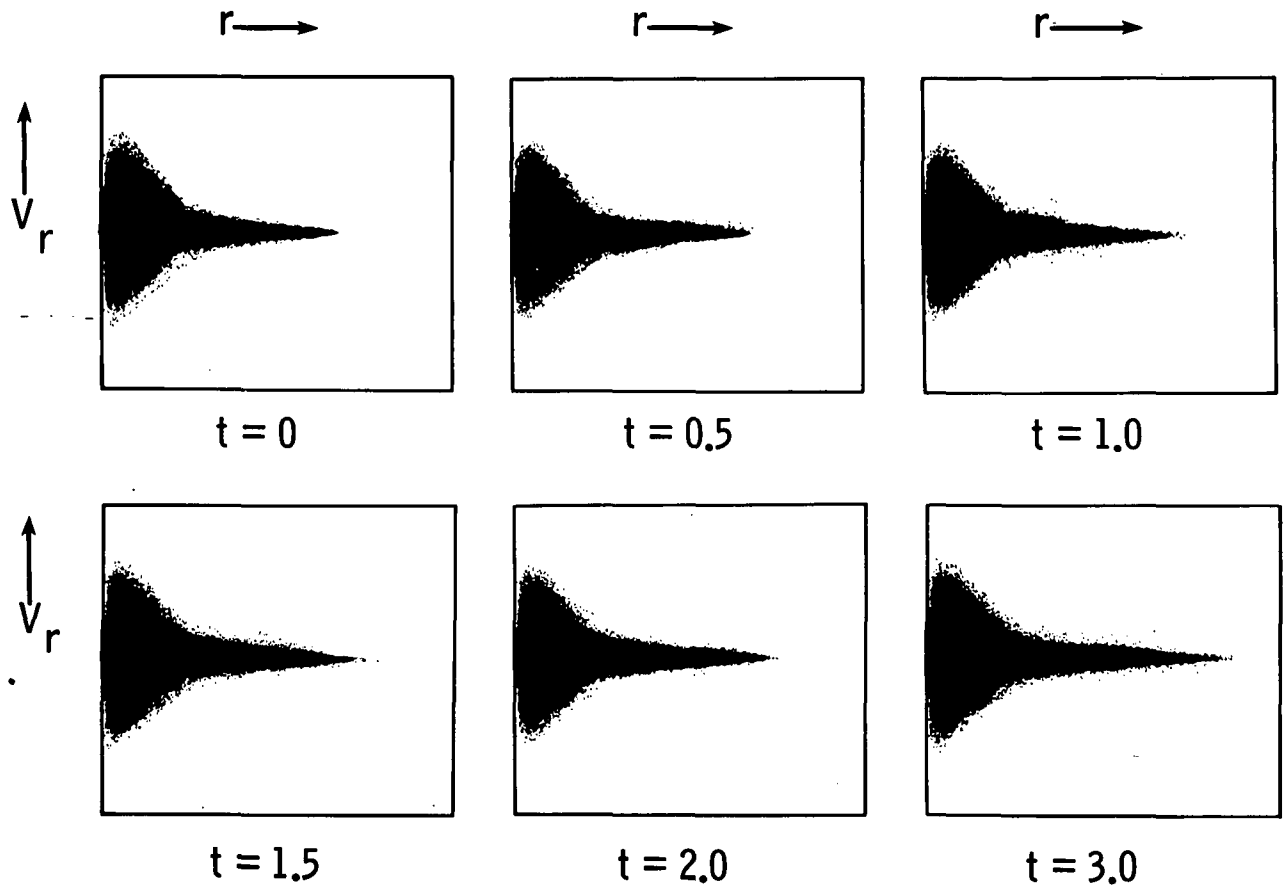

(a) Radial velocities.

Figure 31.- Evolution of the velocity distribution as a function of radius for the three-dimensional disk-core system.

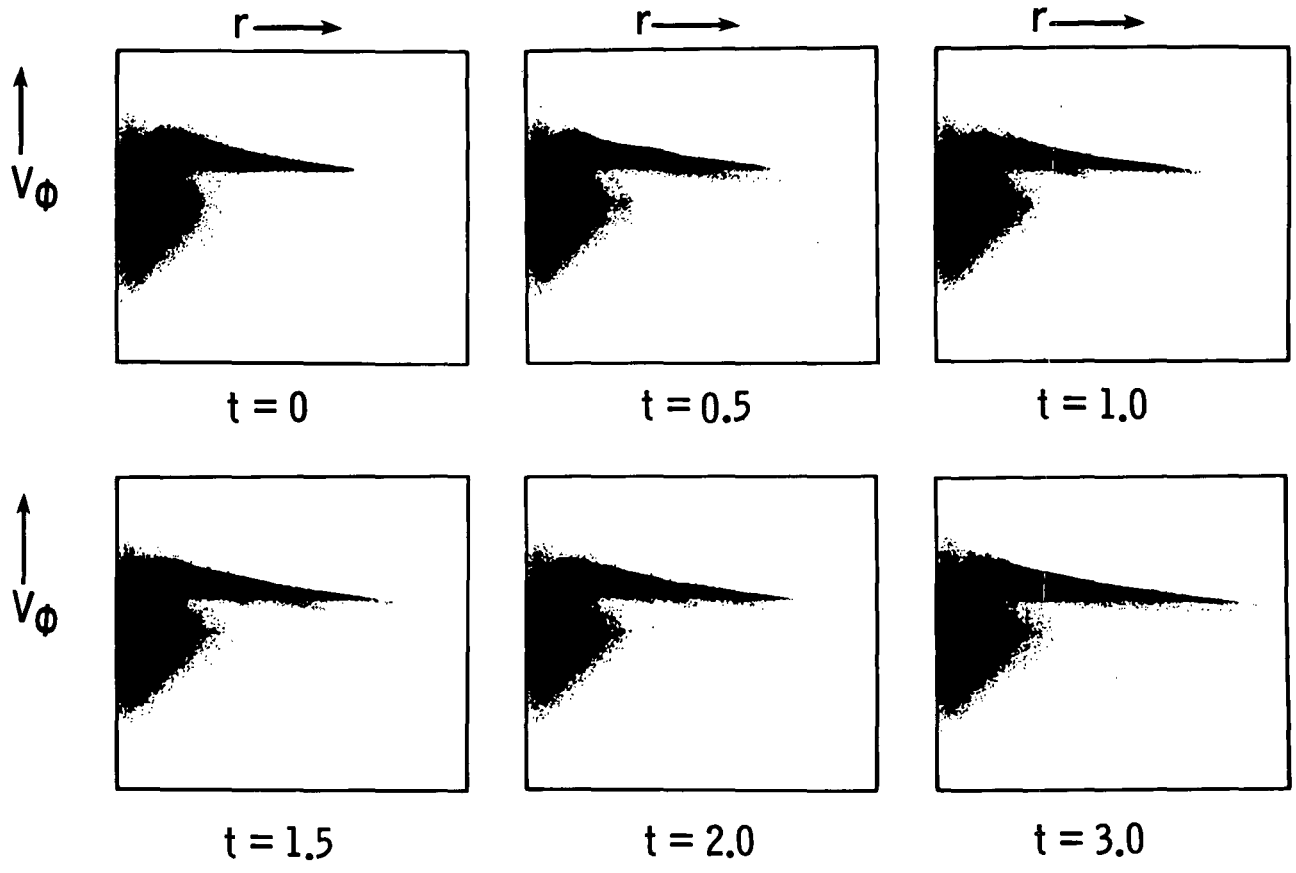

(b) Azimuthal velocities.

Figure 31.- Continued.

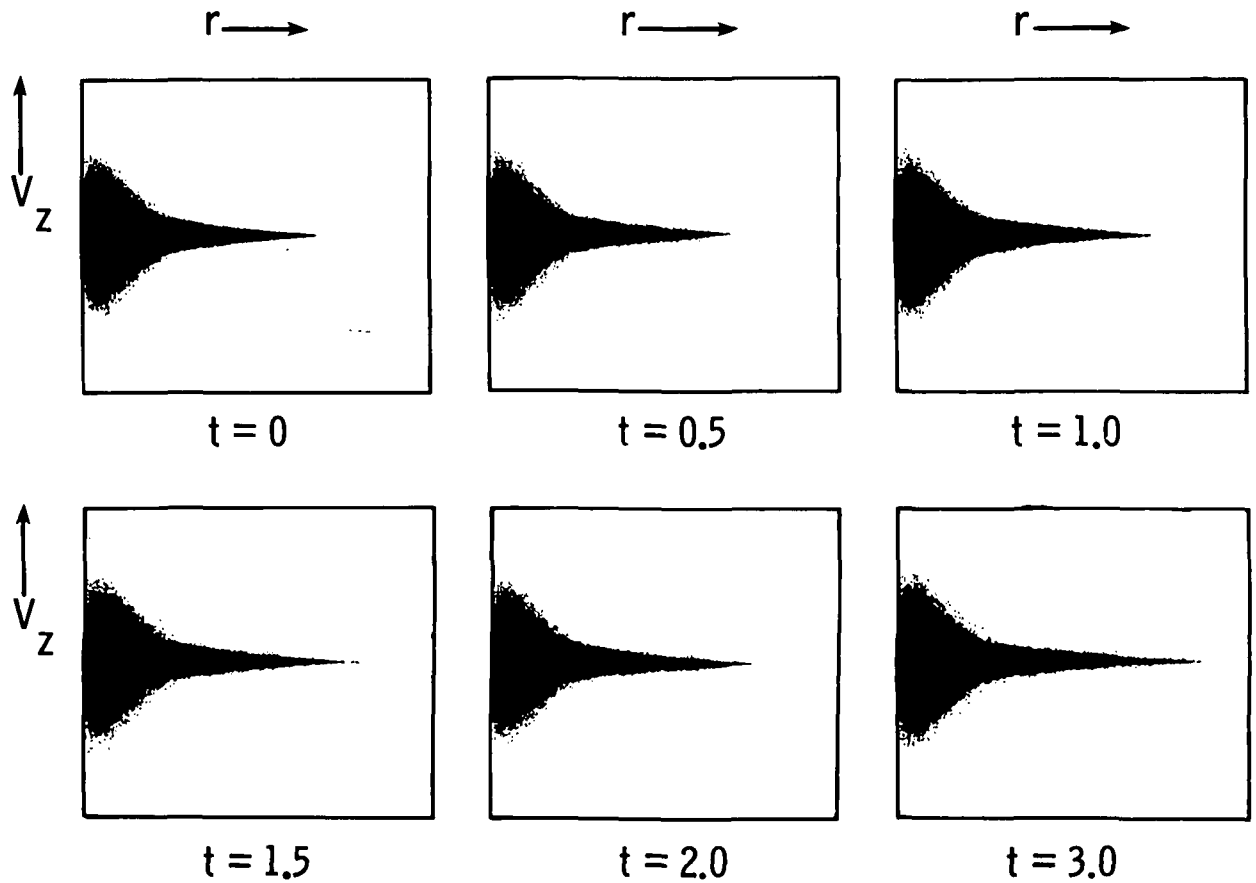

(c) Axial velocities.

Figure 31.- Concluded.

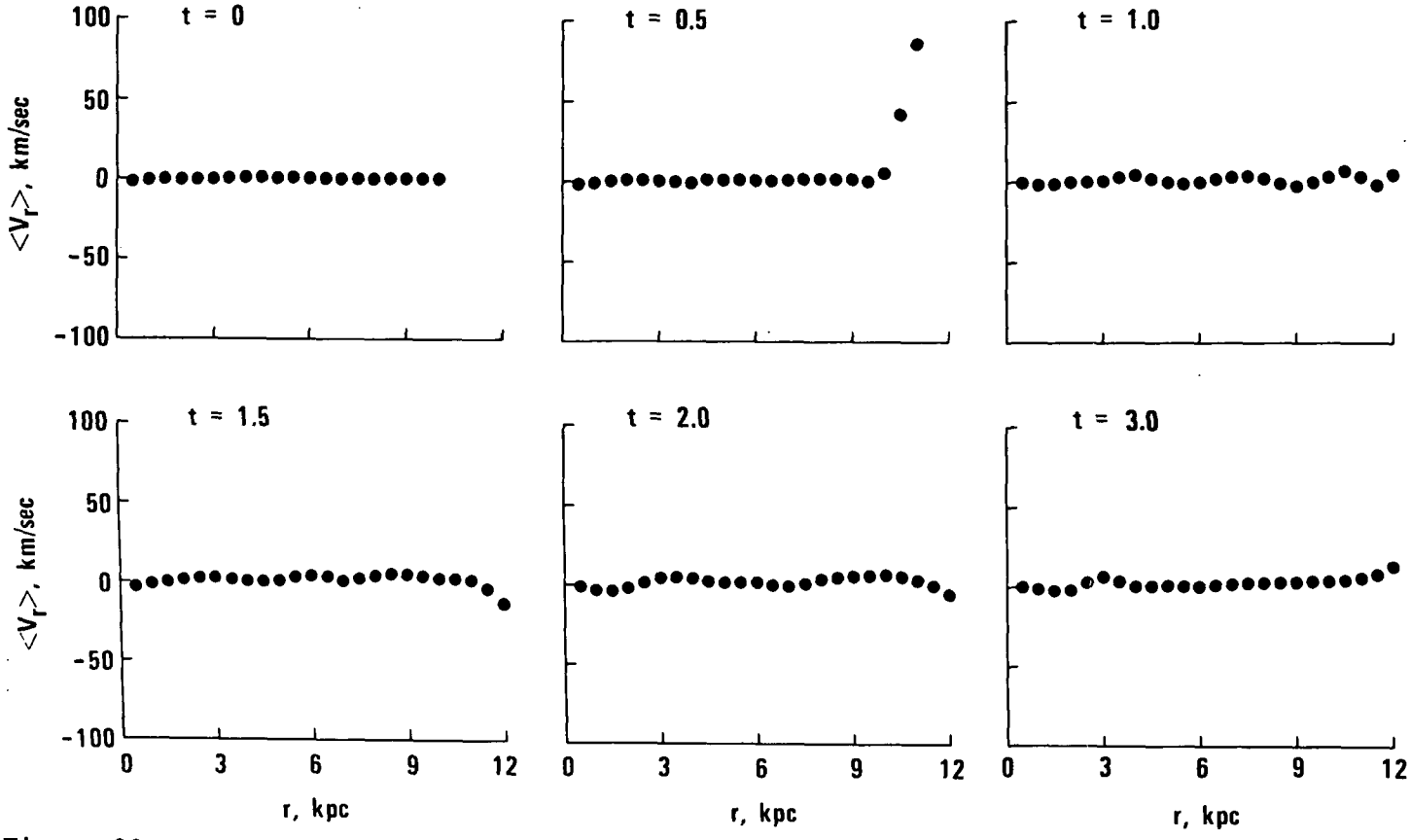

Figure 32.- Evolution of the azimuthally averaged, mean radial velocity as a function of radius for the three-dimensional disk-core system. Note that there is practically no net radial mass motion.

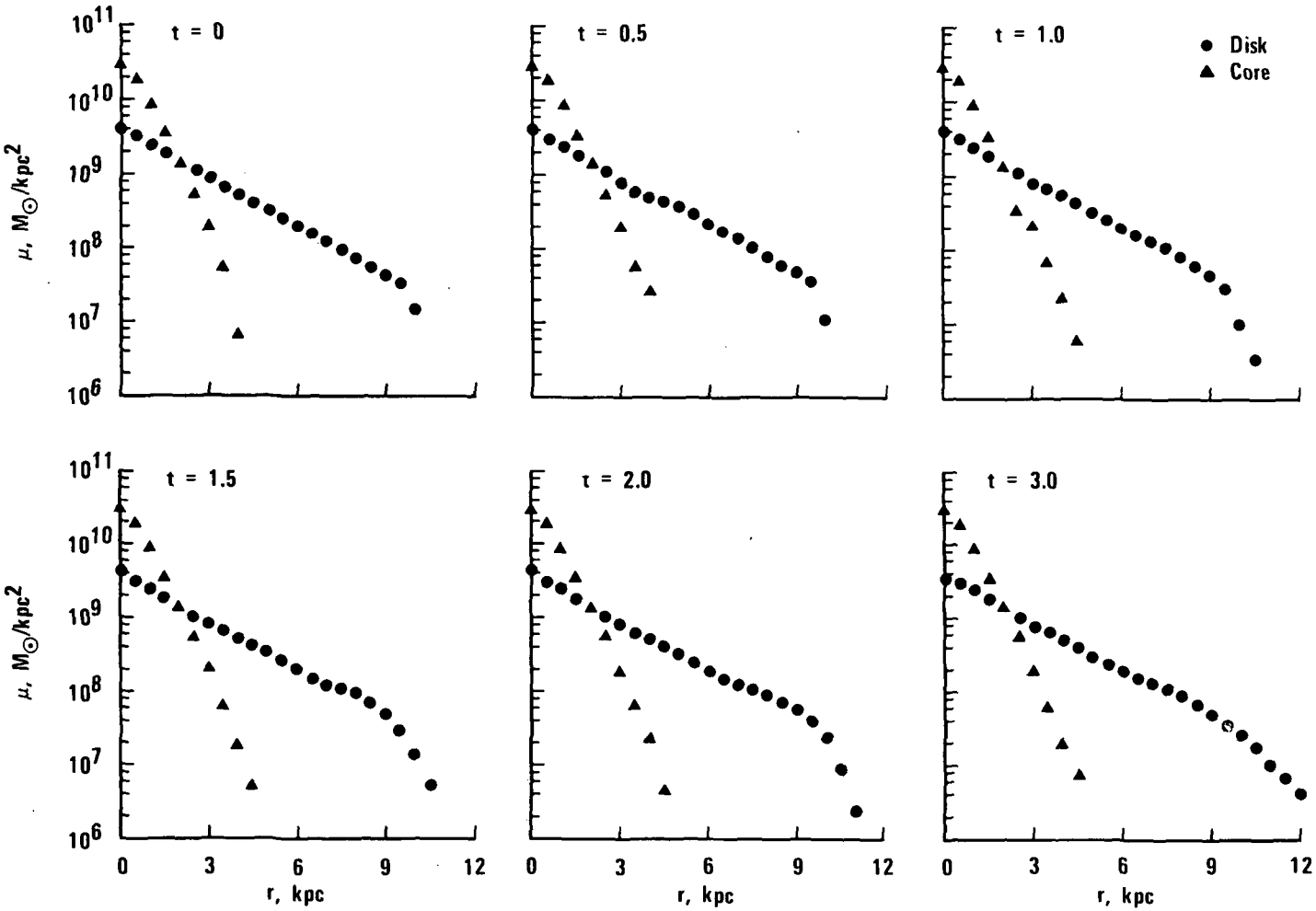

Figure 33.- Evolution of the azimuthally averaged projected surface mass density for the three-dimensional disk-core system shown in figure 30.

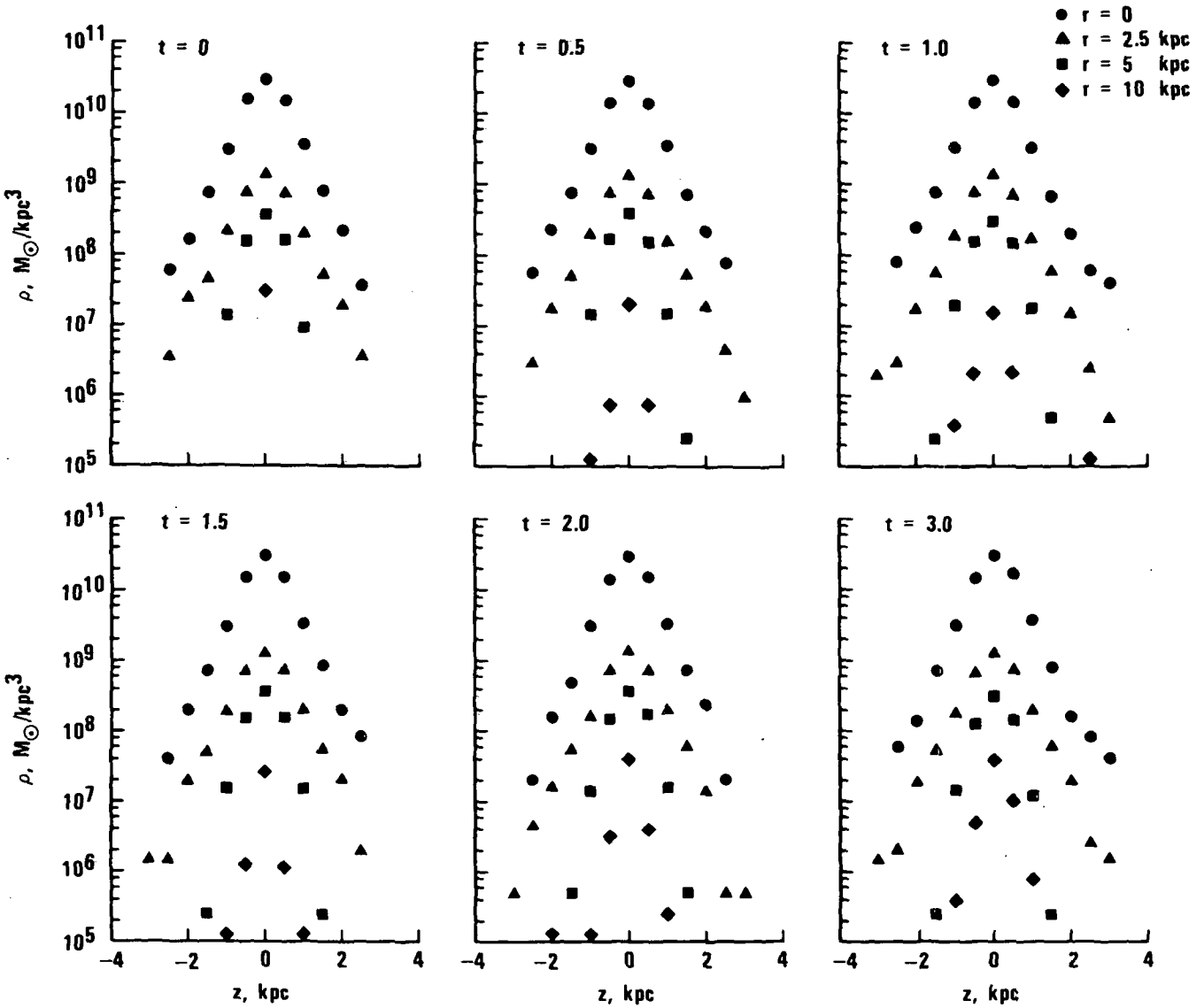

Figure 34.- Evolution of azimuthally averaged volume-mass density as a function of z for various radii for the three-dimensional disk-core system.

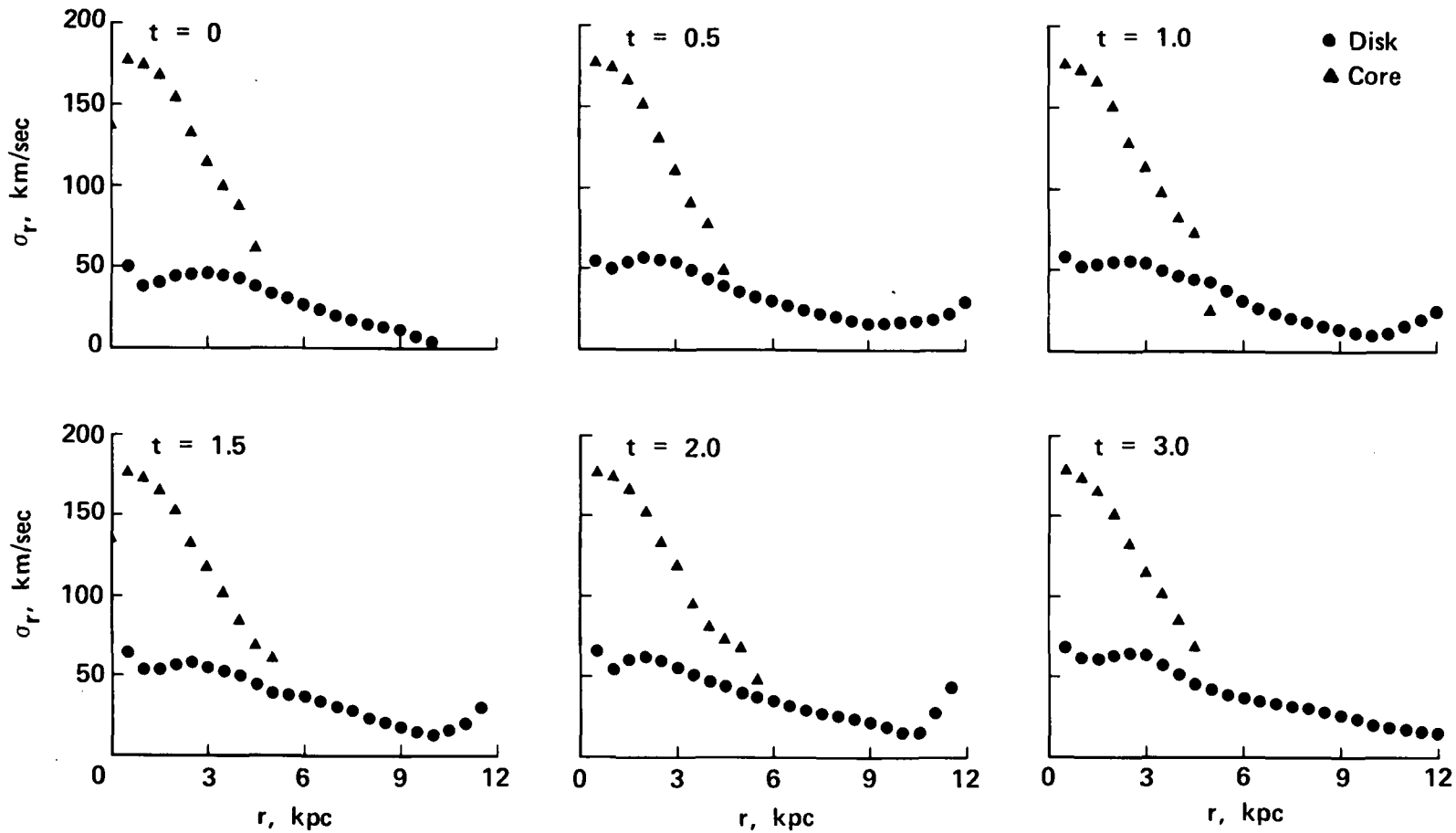

(a) Radial velocity dispersion.

Figure 35.- Evolution of the azimuthally averaged velocity dispersions as a function of radius for the three-dimensional disk-core system.

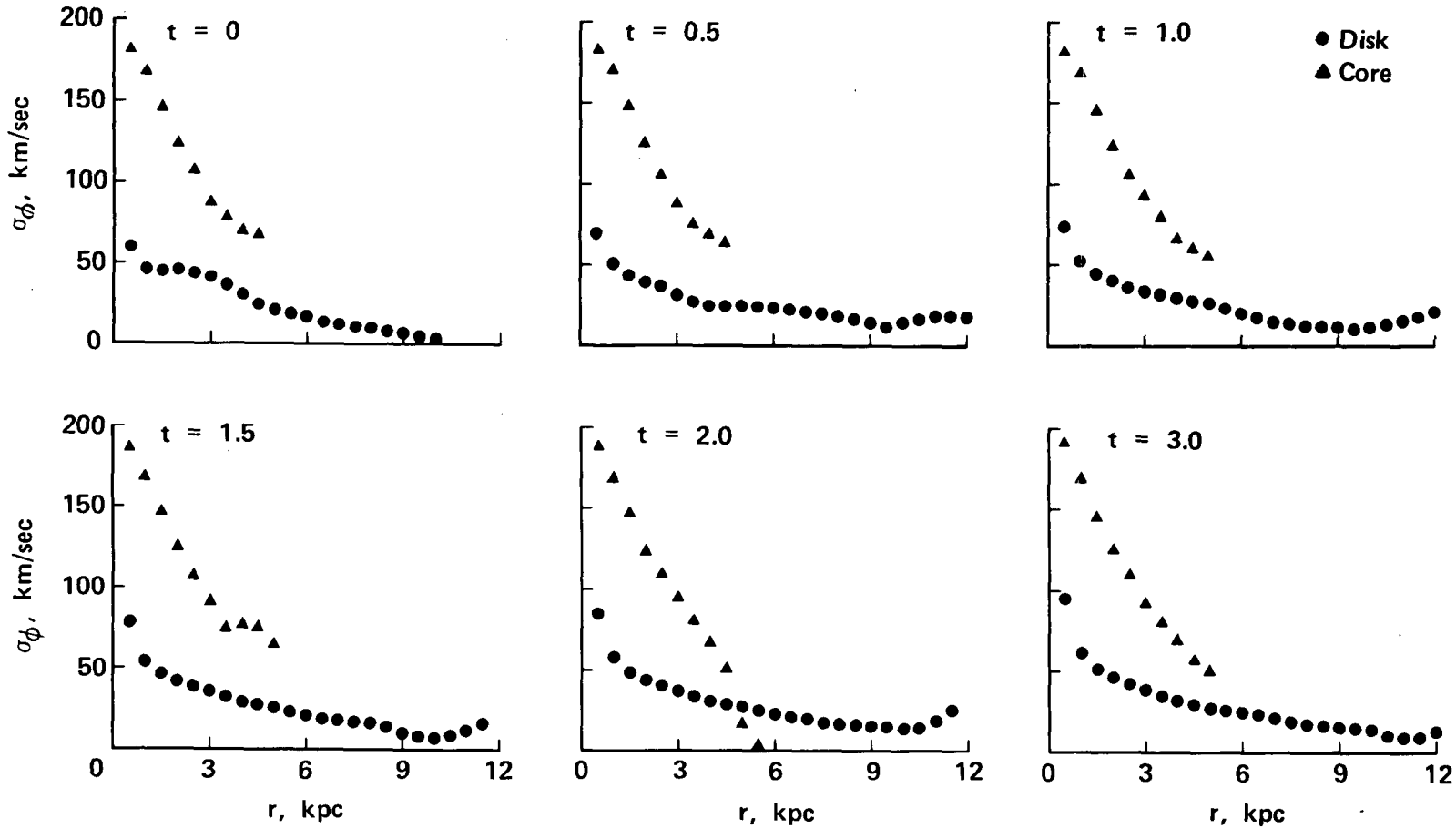

(b) Azimuthal velocity dispersion.

Figure 35.- Continued.

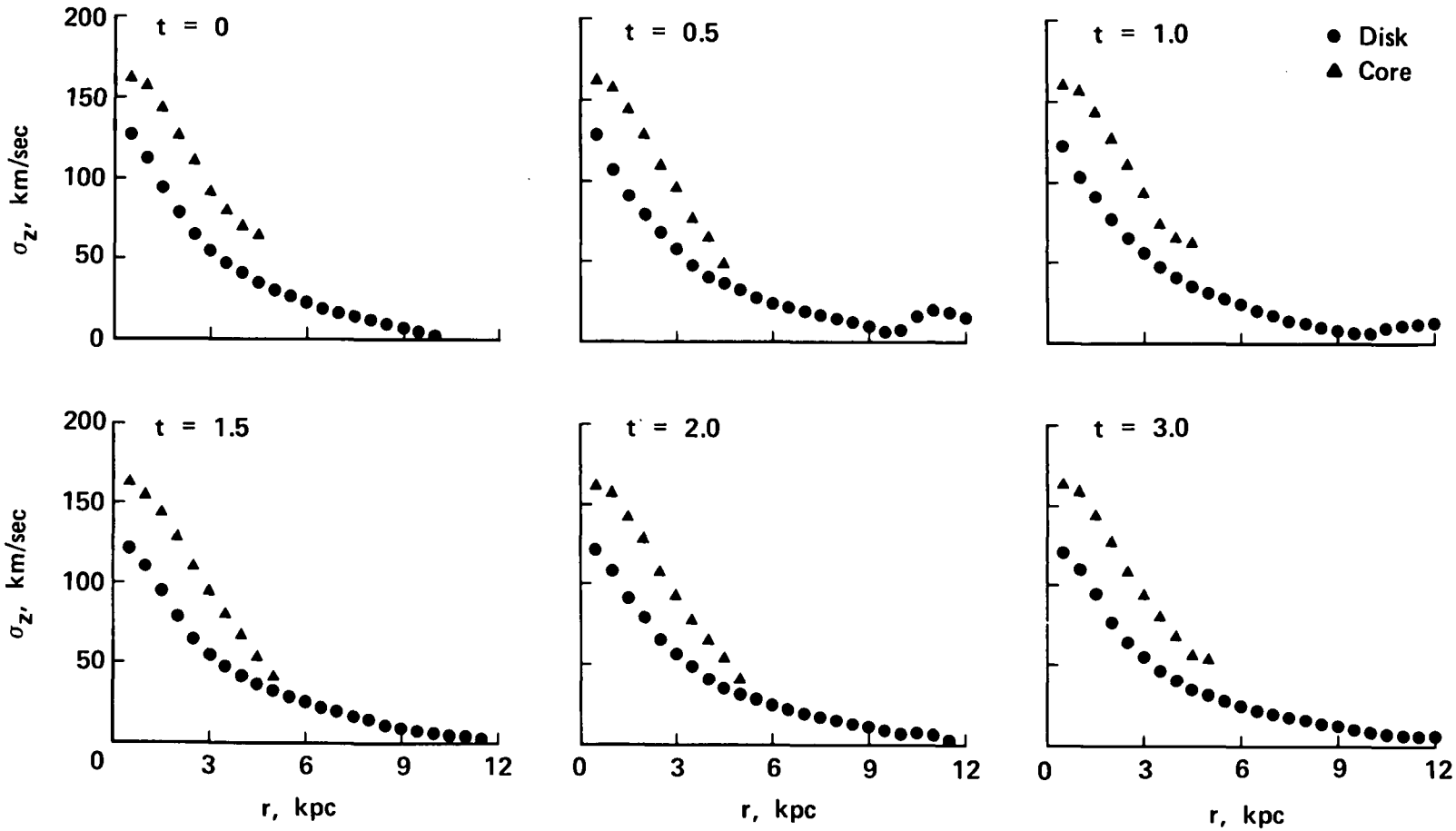

(c) Axial velocity dispersion.

Figure 35.- Concluded.

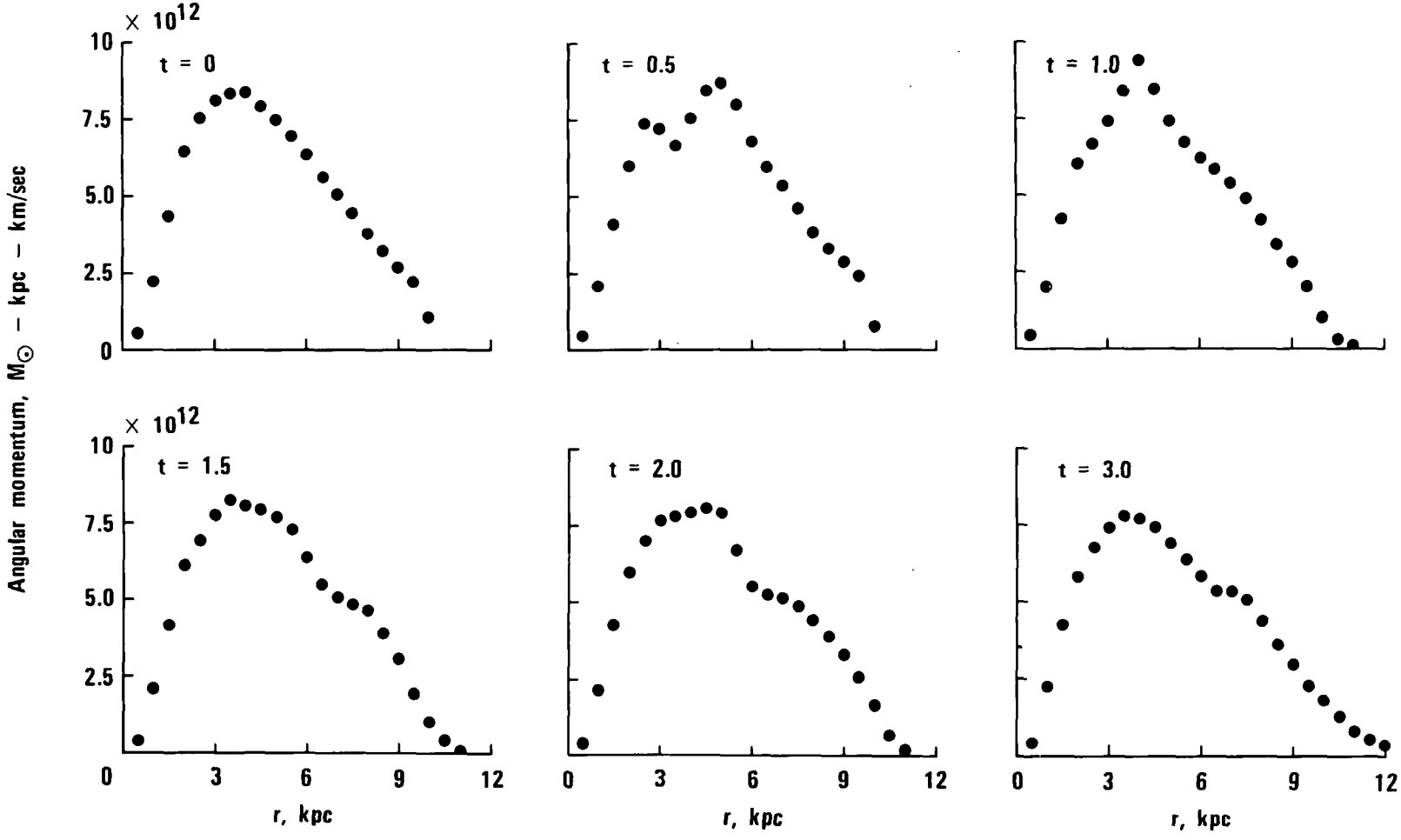

Figure 36.- Evolution of the angular momentum distribution for the three-dimensional disk-core system.

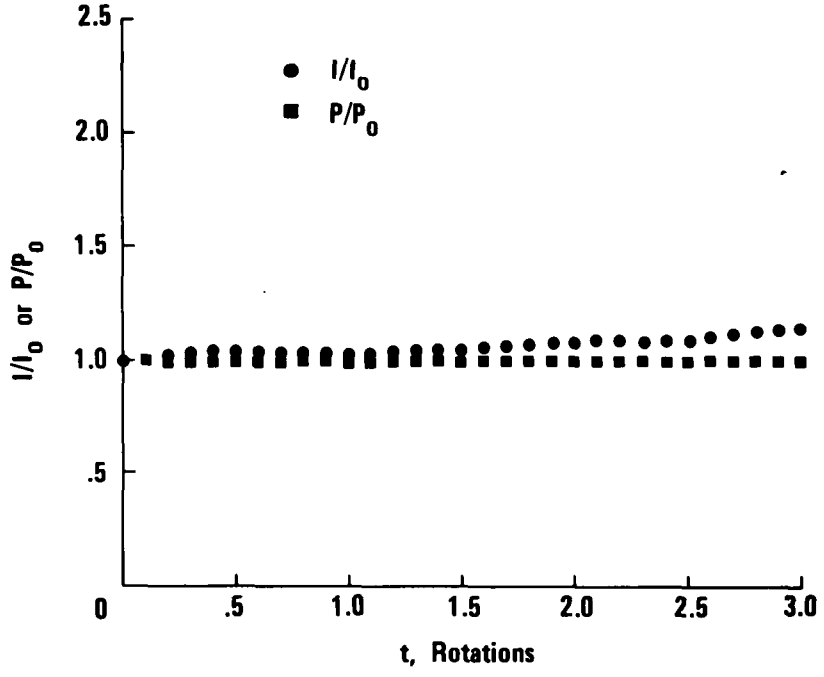

Figure 37.- Evolution of the angular momentum P and the moment of inertia I (divided by their initial values) for the three-dimensional disk-core system.

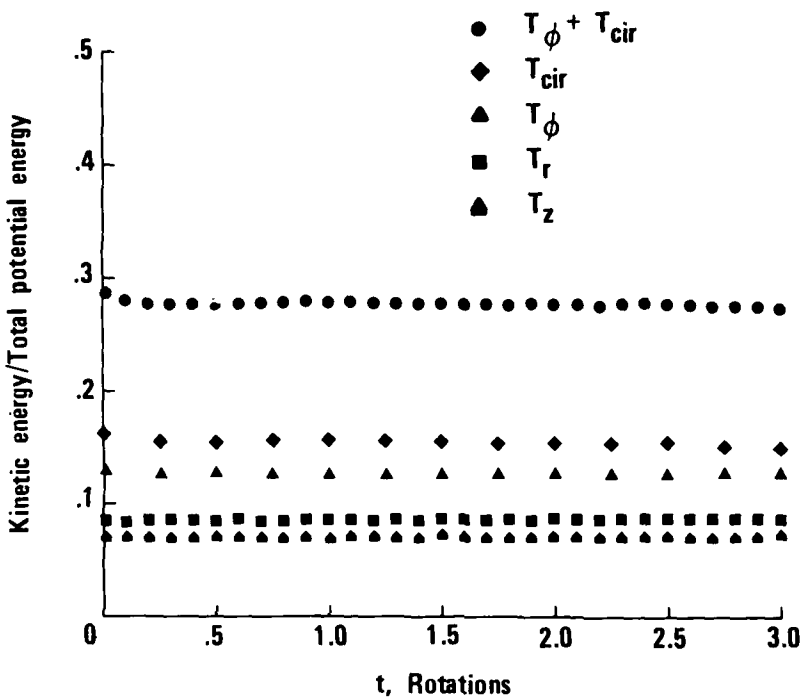

Figure 38.- Evolution of various ratios of kinetic energy to total potential energy for the three-dimensional disk-core system.

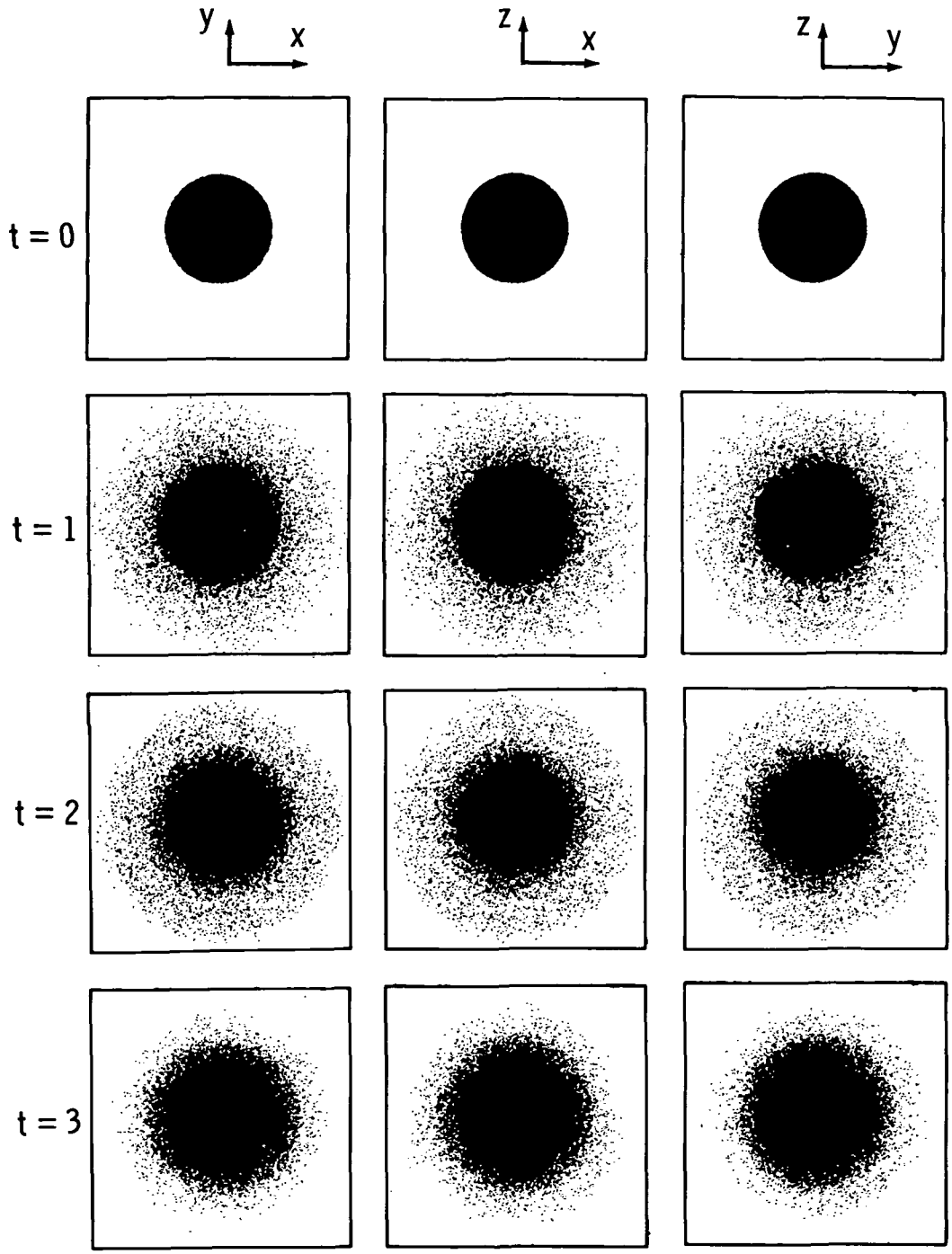

Figure 39.- Orthogonal views of the evolution of an initially non-rotating spherical system of 100 000 stars (model I). Time is given in units of $2\pi/\Omega_o$. Note that the system remains spherically symmetric.

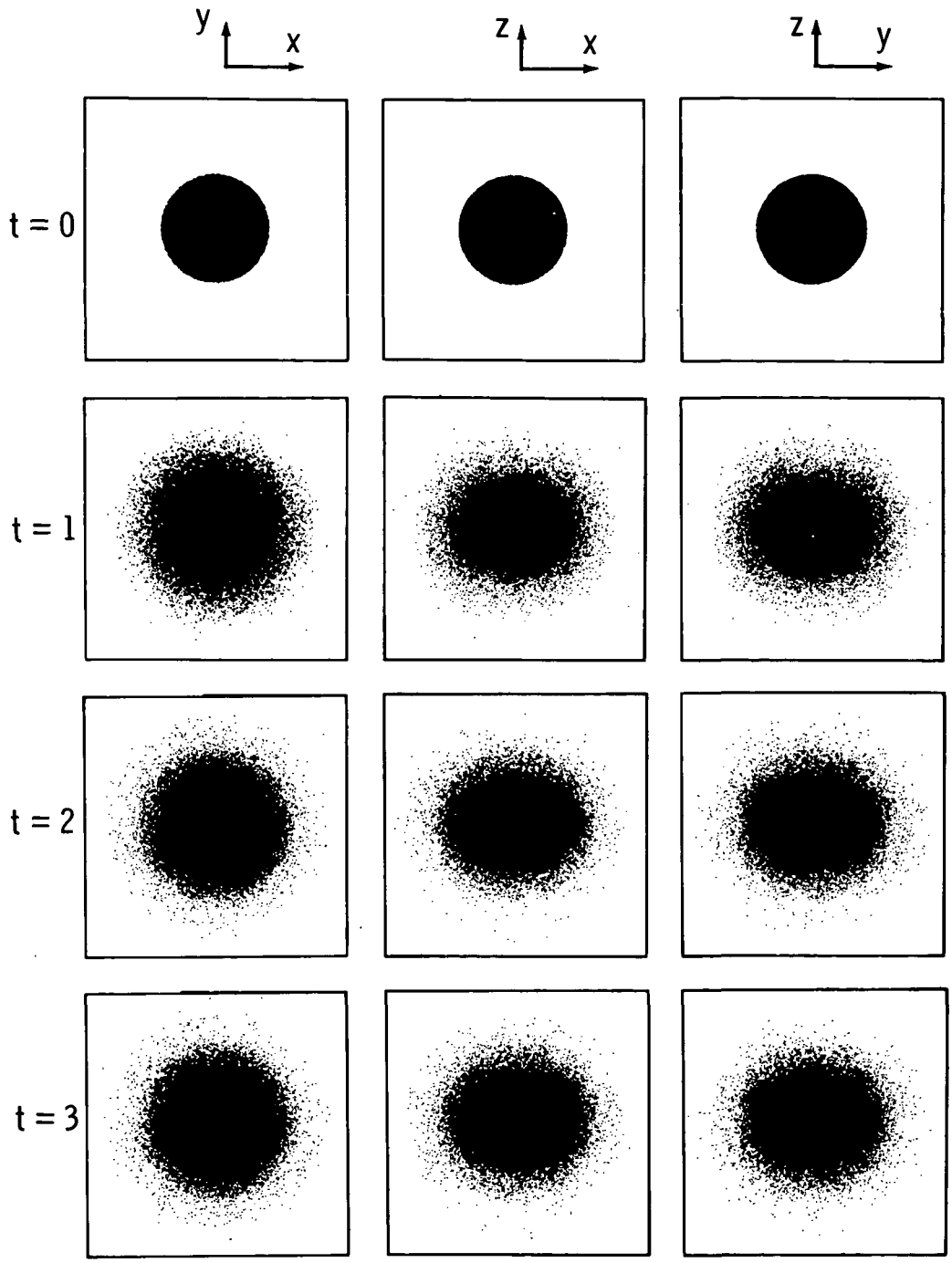

Figure 40.- Evolution of an initially spherical system of 100 000 stars with an initial solid body rotation given by $\Omega = 0.5\Omega_o$ (model II). Note that the final state is an oblate system.

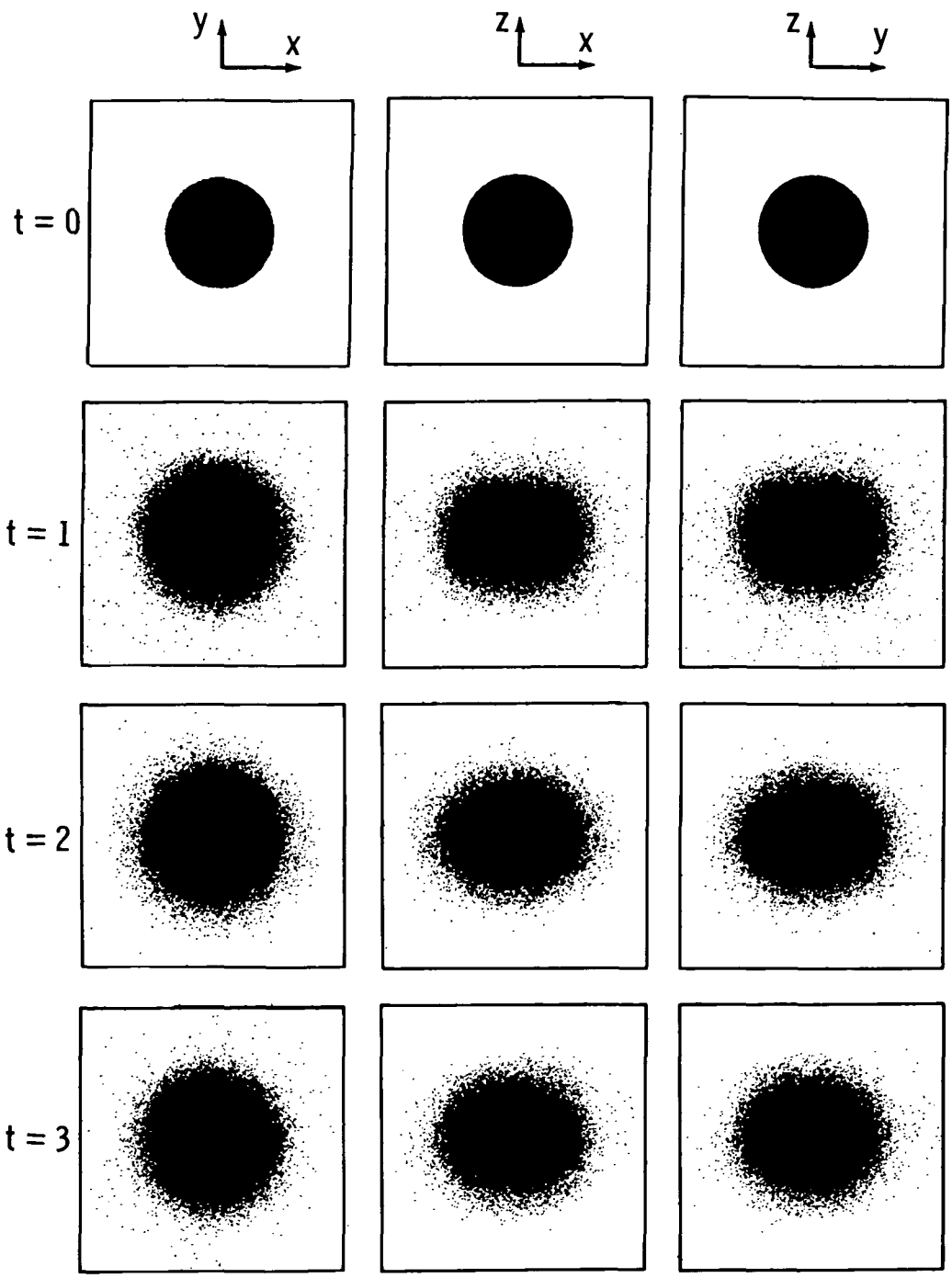

Figure 41.- Evolution of an initially spherical system of 100 000 stars with an initial solid body rotation given by $\Omega = 0.707\Omega_o$ (model III). The system remains axisymmetric and acquires an oblate shape.

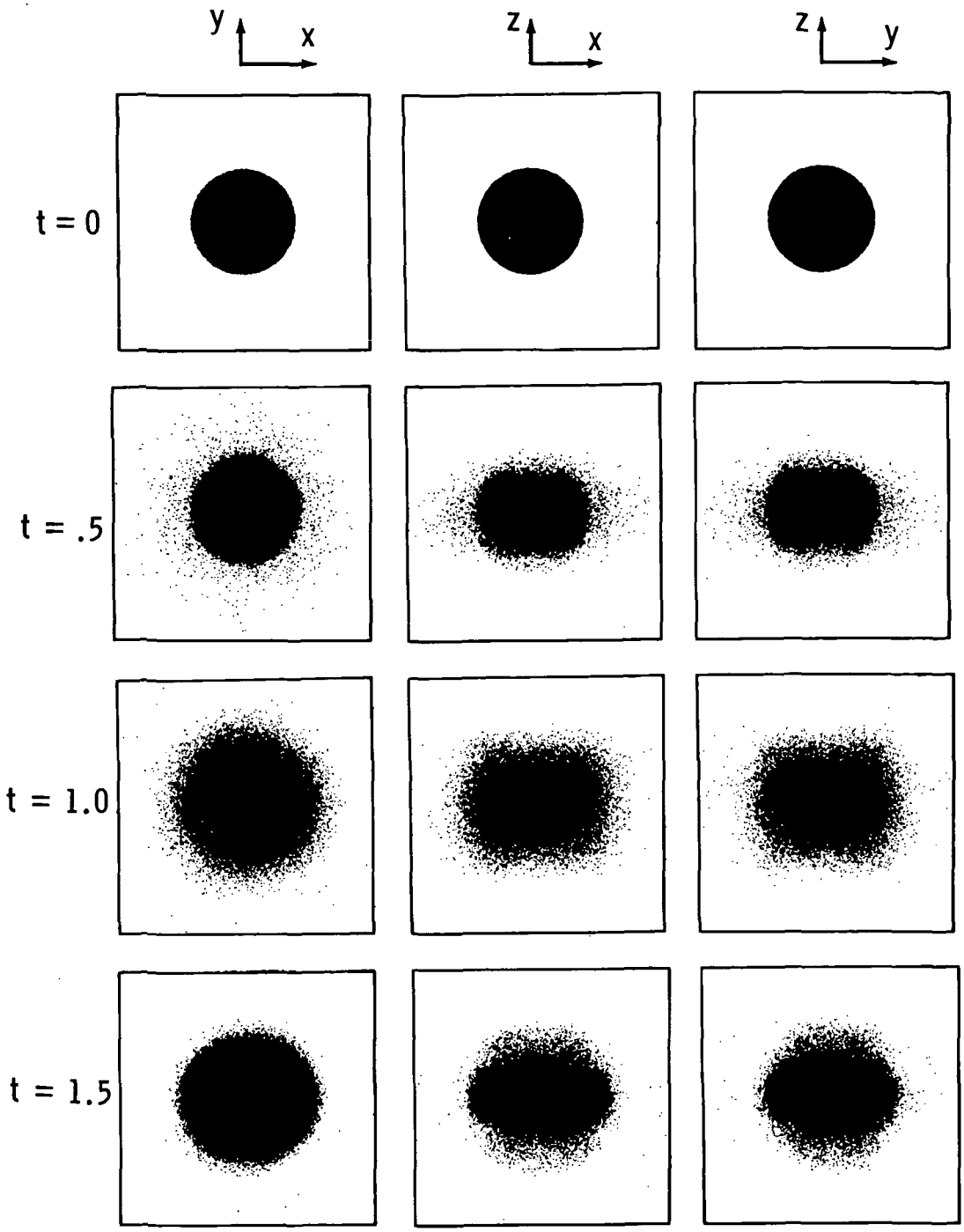

(a) Evolution with each projection containing 100 000 stars.

Figure 42.- Evolution of initially spherical system with an initial solid body rotation given by $\Omega = 0.866\Omega_o$ (model IV). The initial energy in random motion is 1/2 that of the systems shown in figures 39 through 41. Note that the system quickly forms a bar and has reached an essentially steady state at $t = 5$.

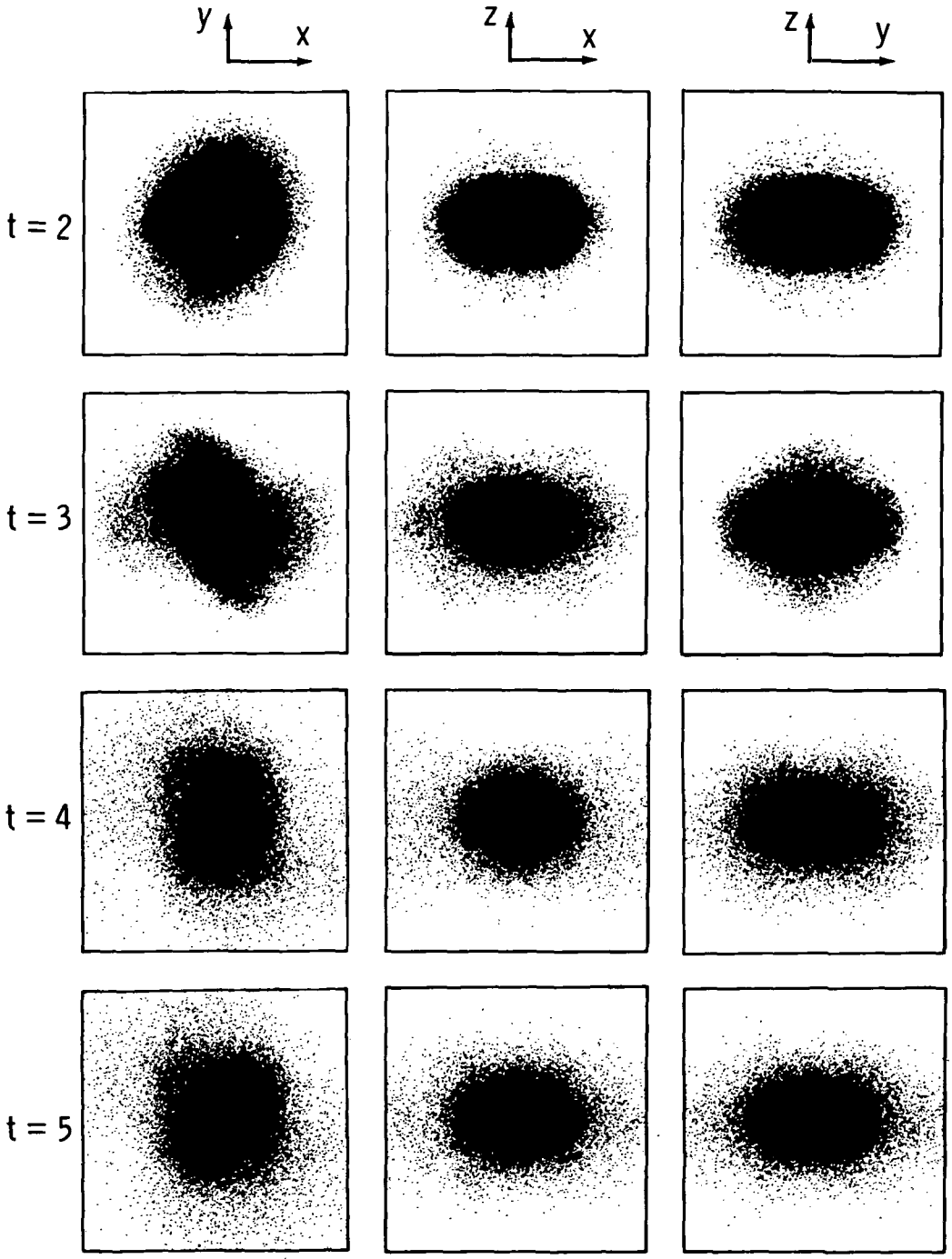

(a) Concluded.

Figure 42.- Continued.

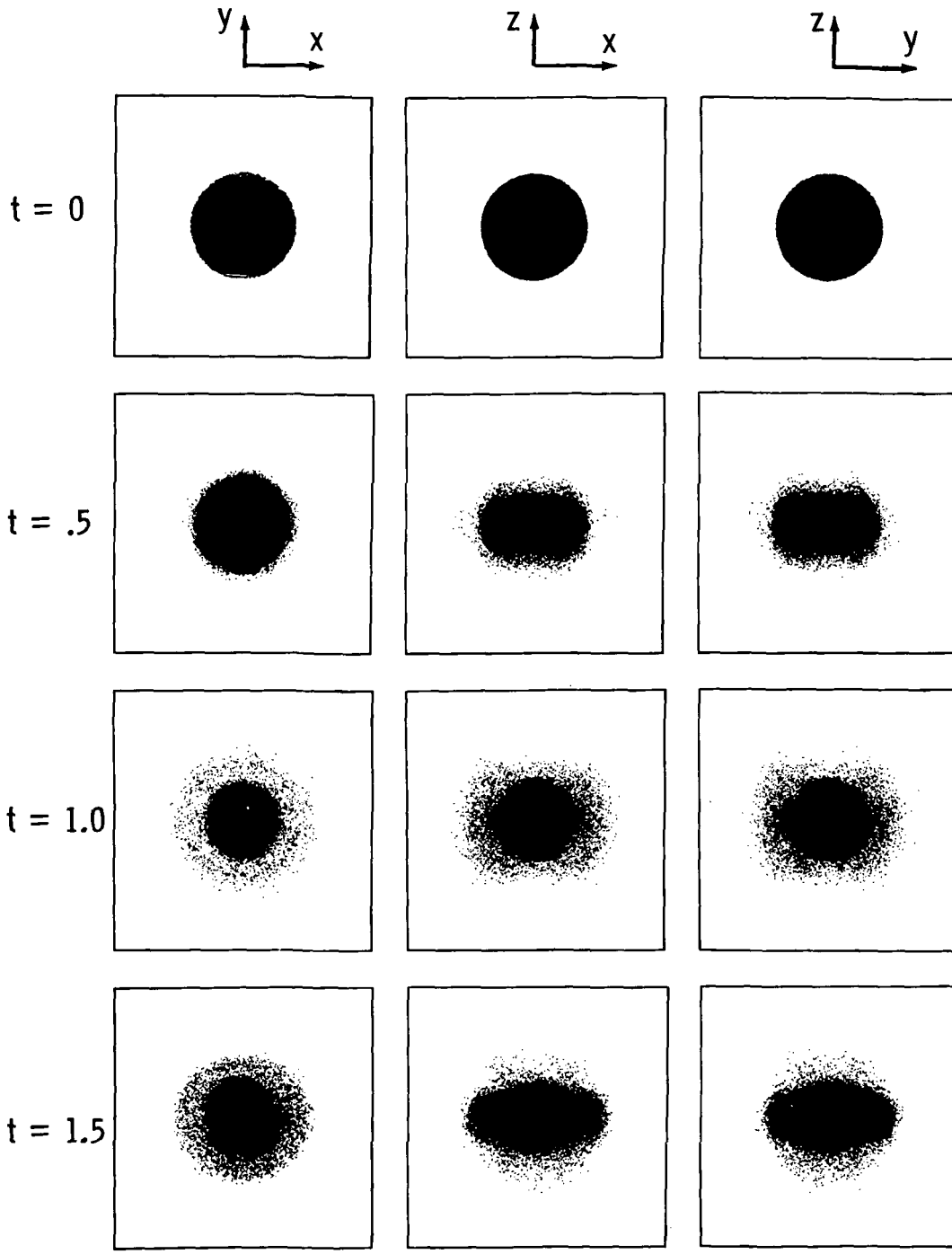

(b) Evolution with x-y projection containing 50 000 stars.

Figure 42.- Continued.

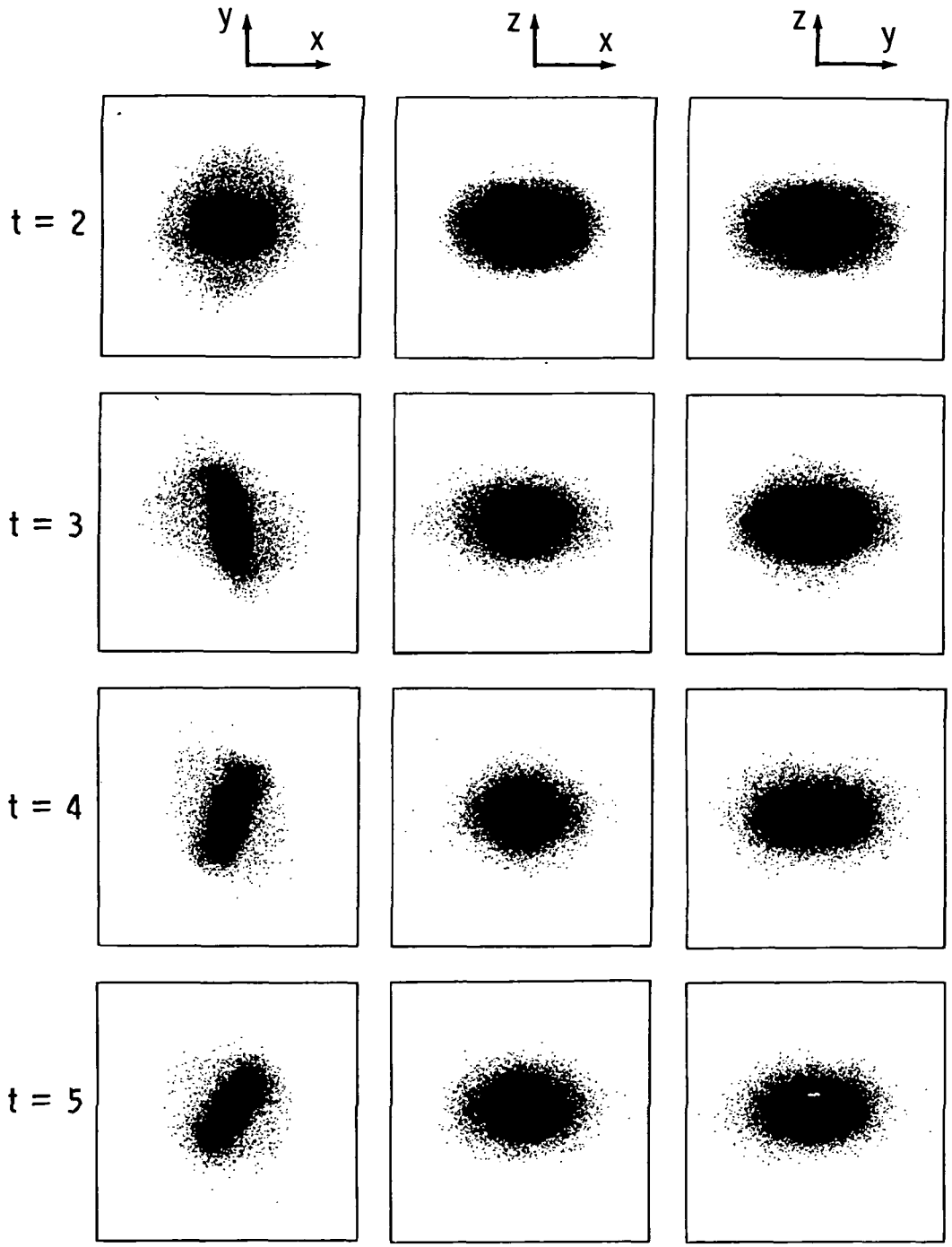

(b) Concluded.

Figure 42.- Concluded.

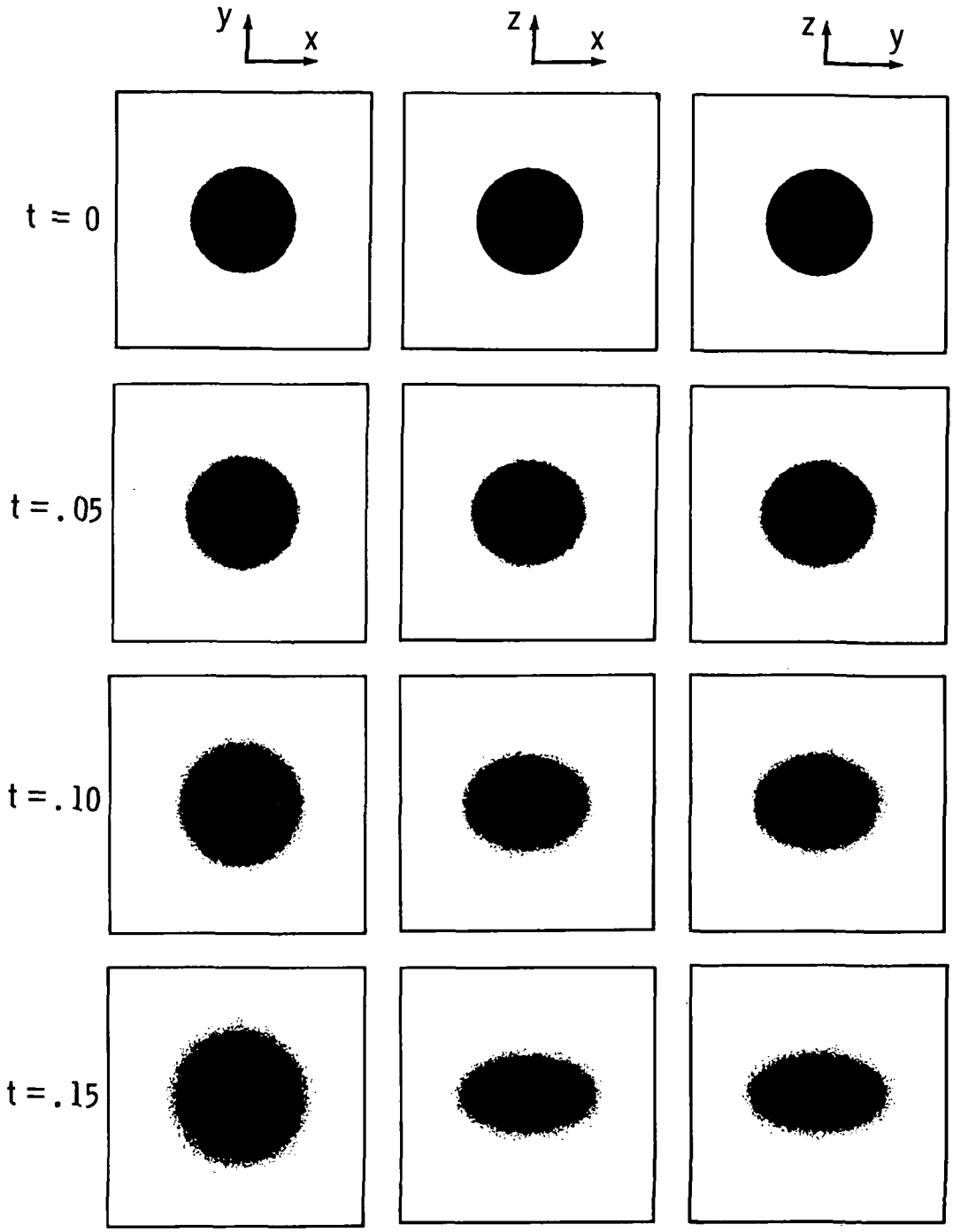

(a) Evolution with each projection containing 100 000 stars.

Figure 43.- Evolution of an initially spherical system with an initial solid body rotation given by $\Omega = 1.159\Omega_o$ (model V). The initial energy in random motion is 1/5 that of the systems shown in figures 39 through 41. Again the system forms a bar.

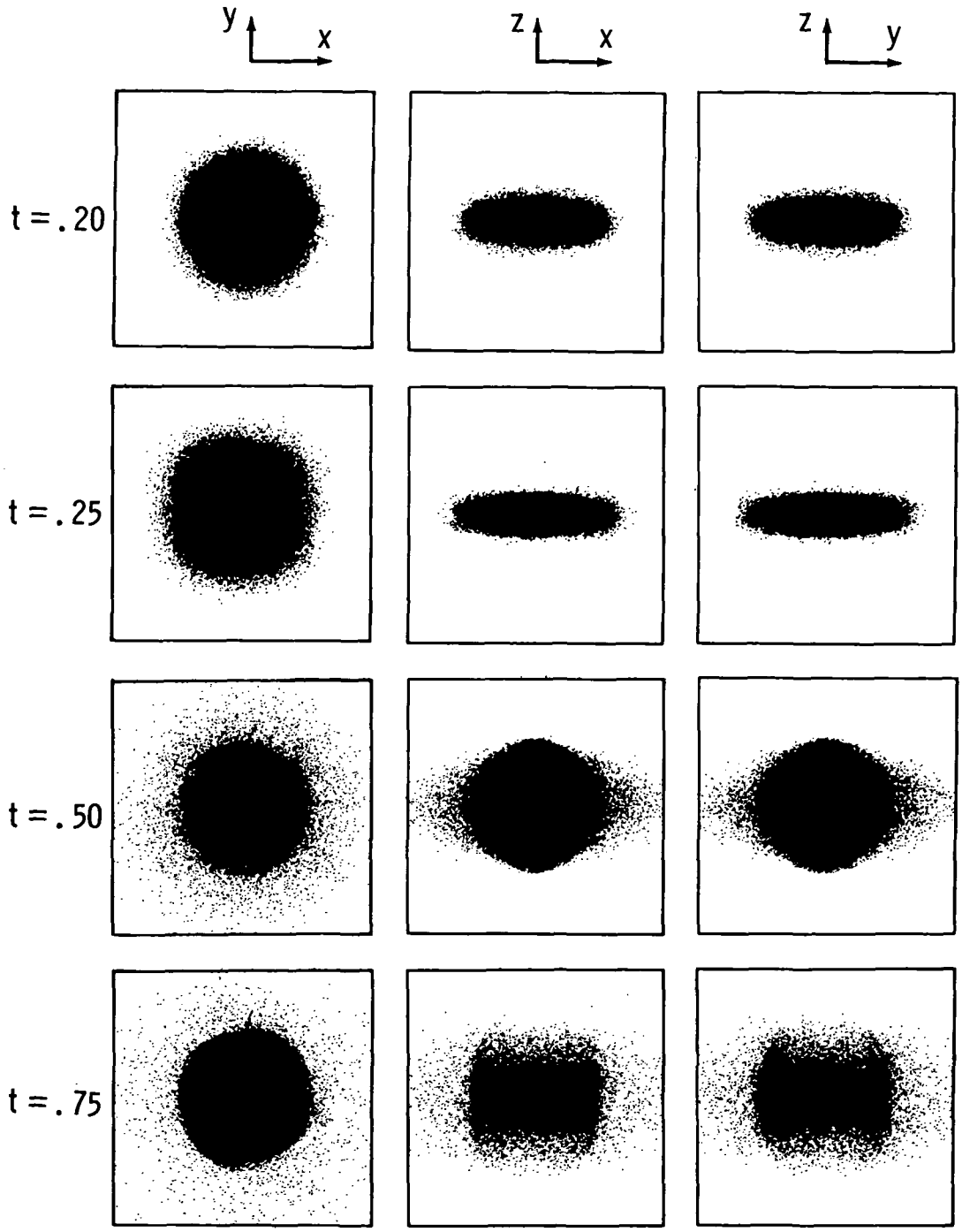

(a) Continued.

Figure 43.- Continued.

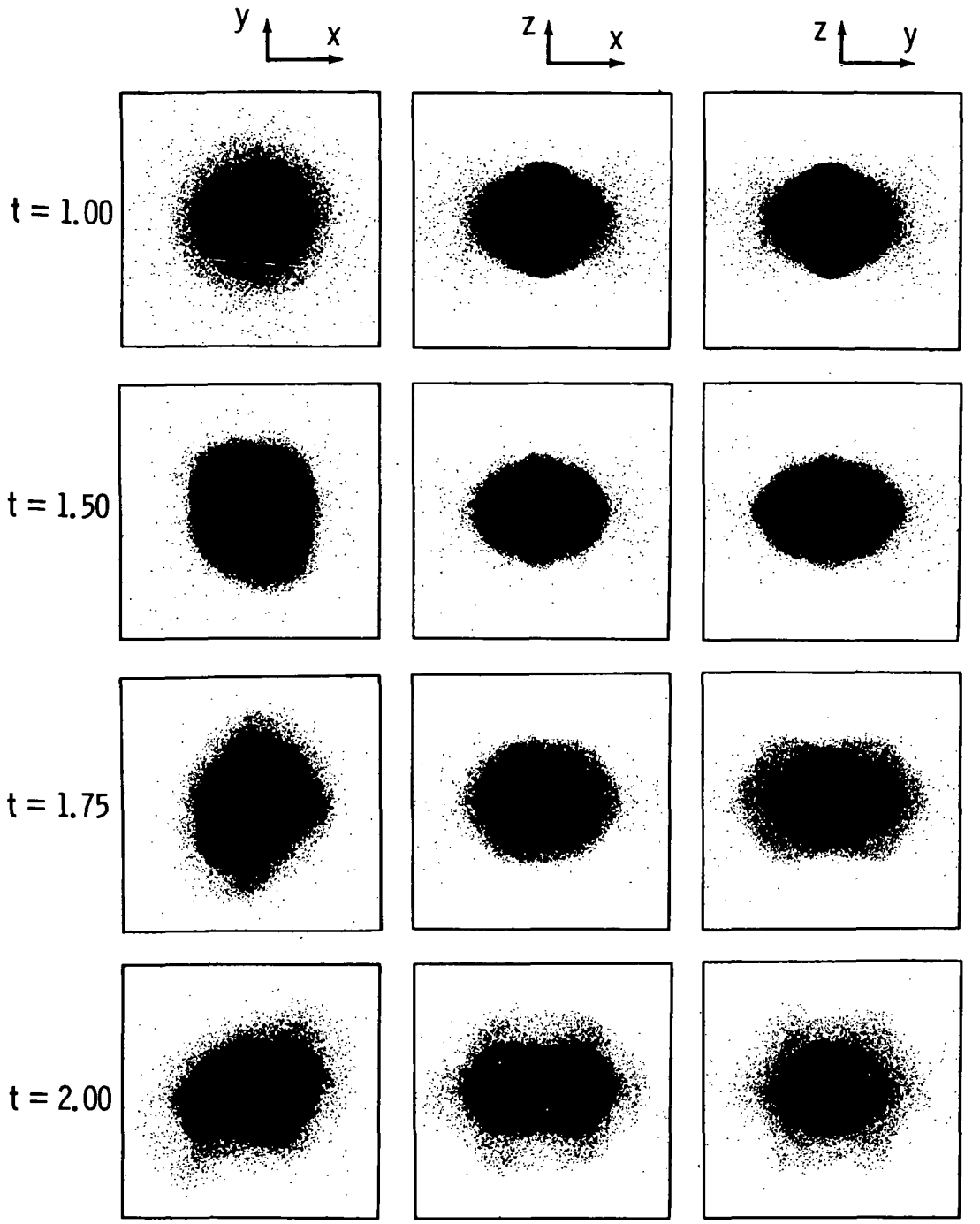

(a) Continued.

Figure 43.- Continued.

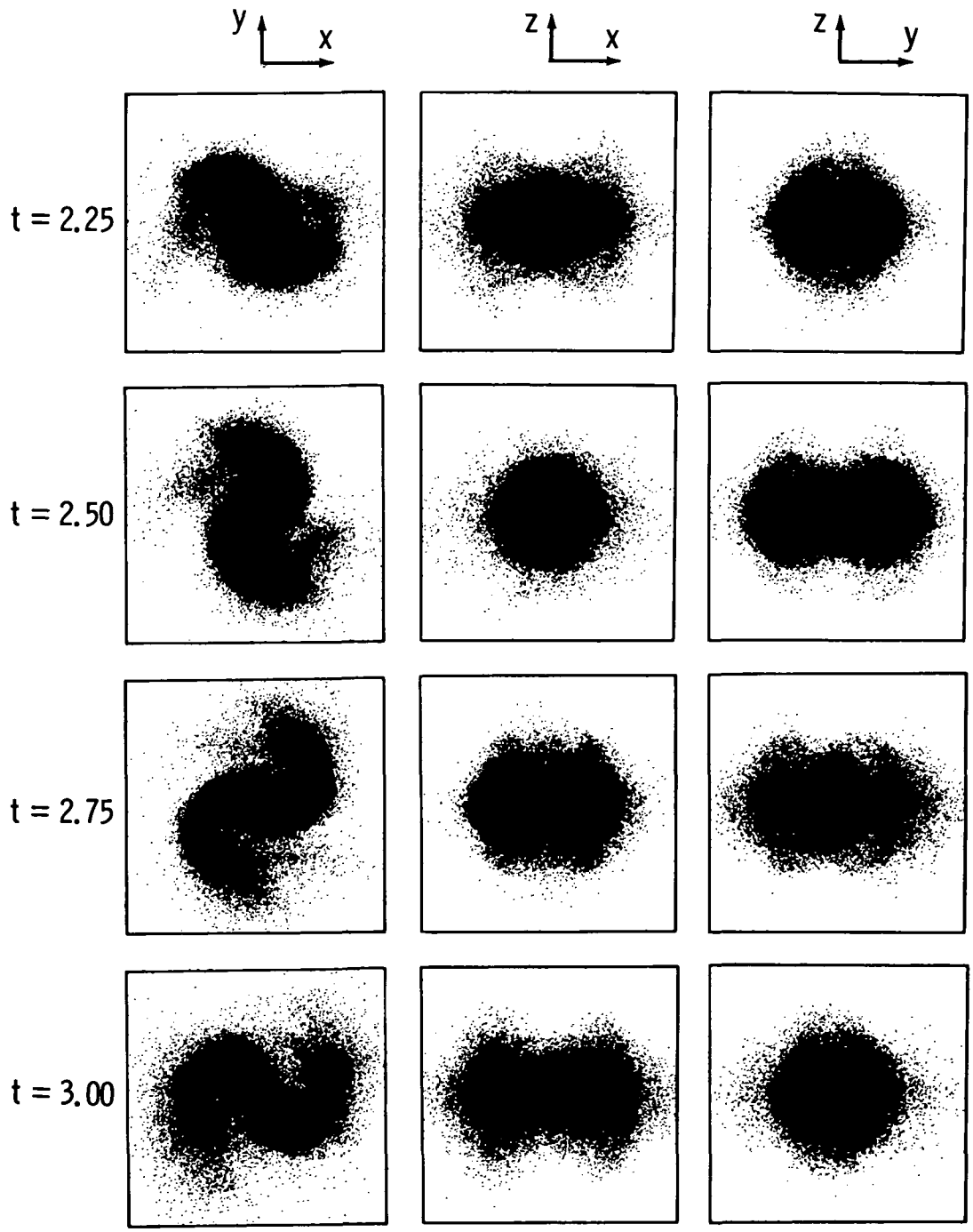

(a) Concluded.

Figure 43.- Continued.

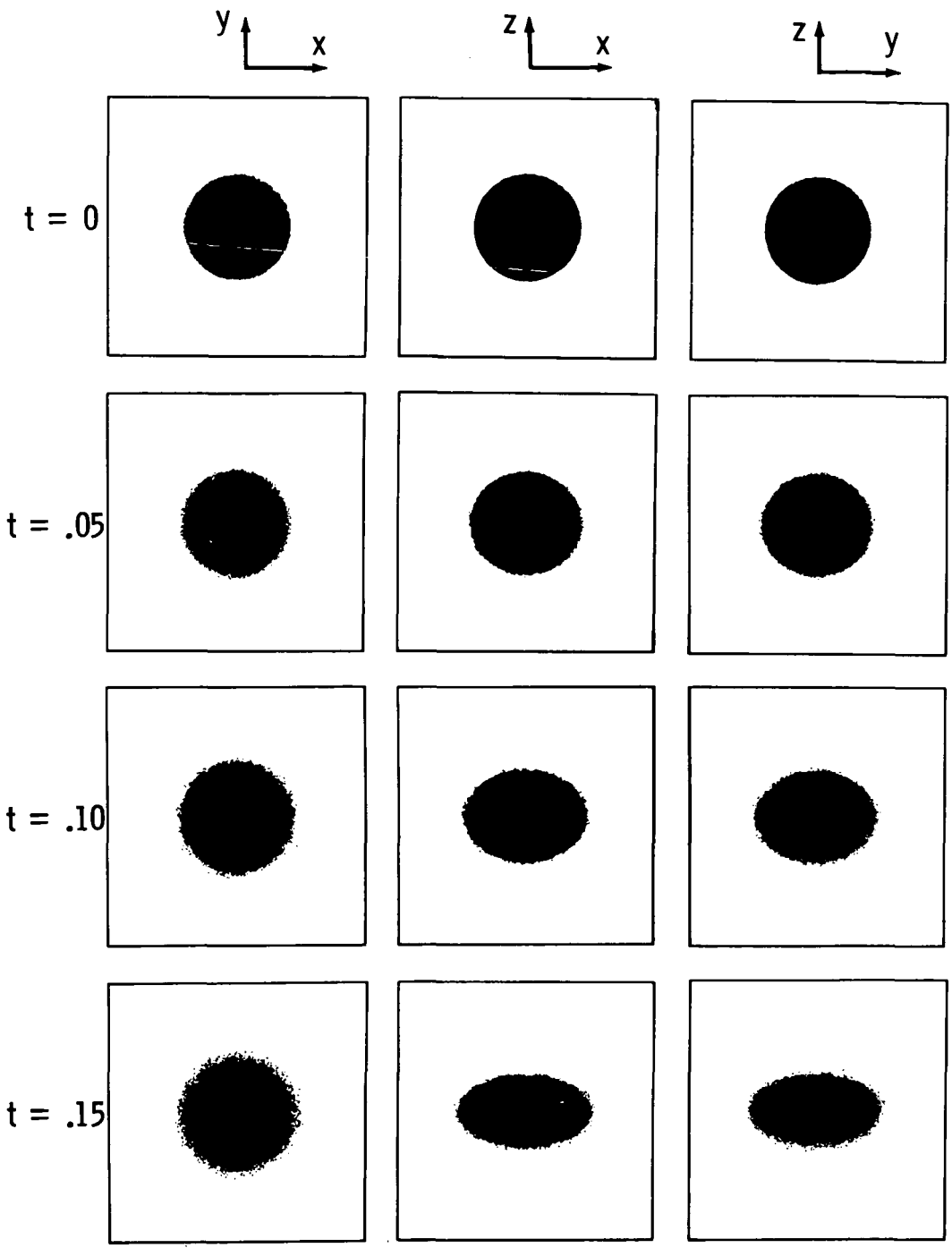

(b) Evolution with x-y projection containing 50 000 stars.

Figure 43.- Continued.

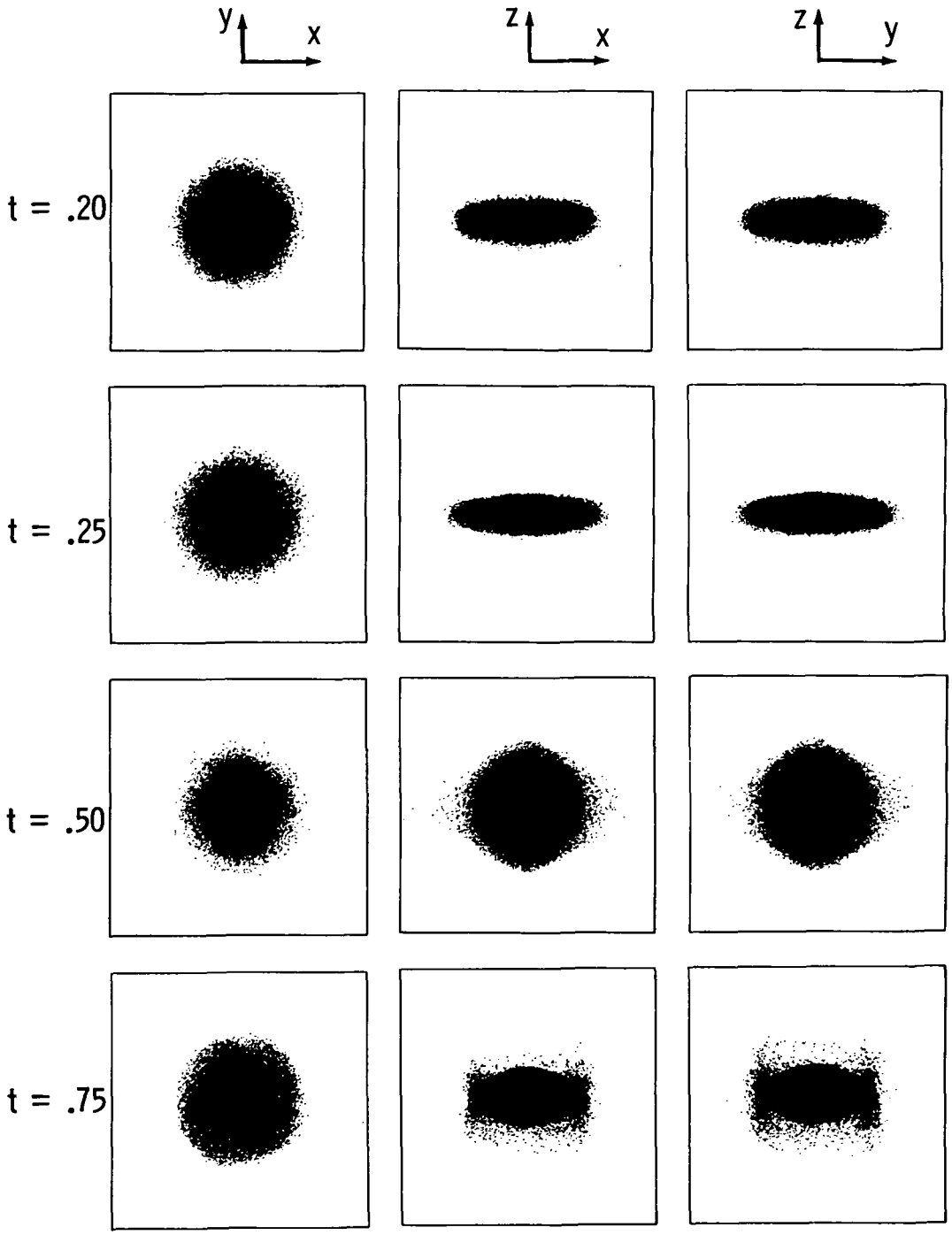

(b) Continued.

Figure 43.- Continued.

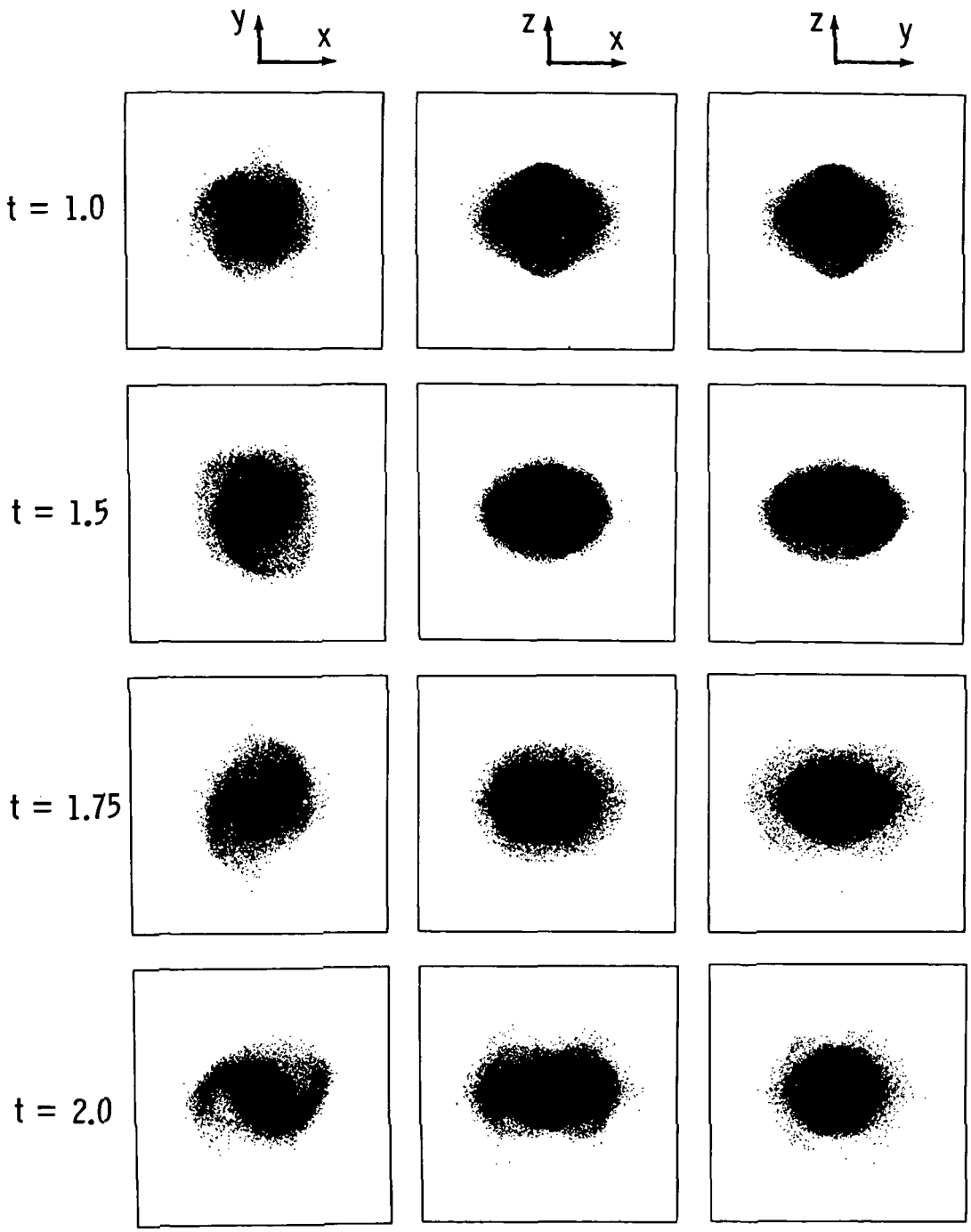

(b) Continued.

Figure 43.- Continued.

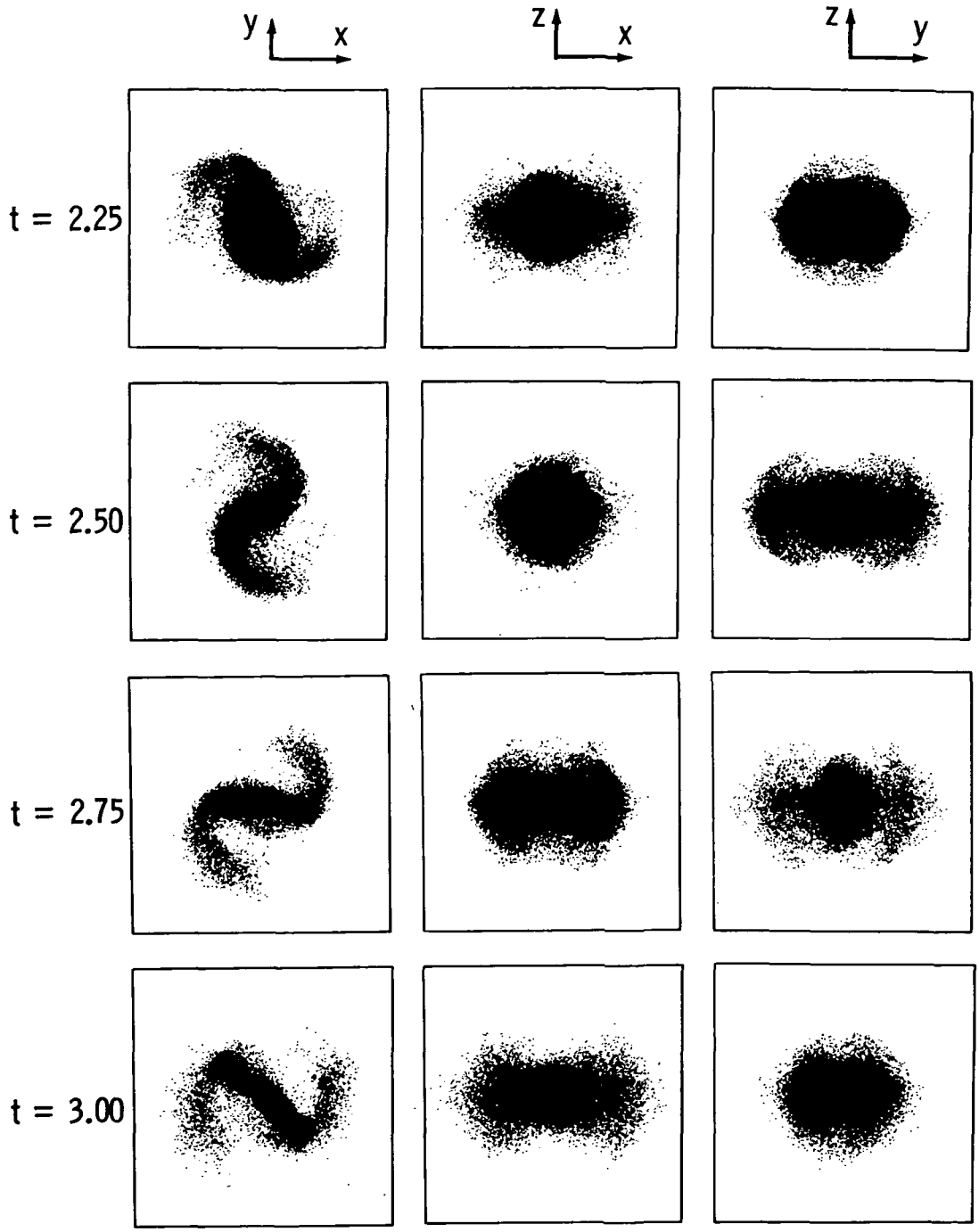

(b) Concluded.

Figure 43.- Concluded.

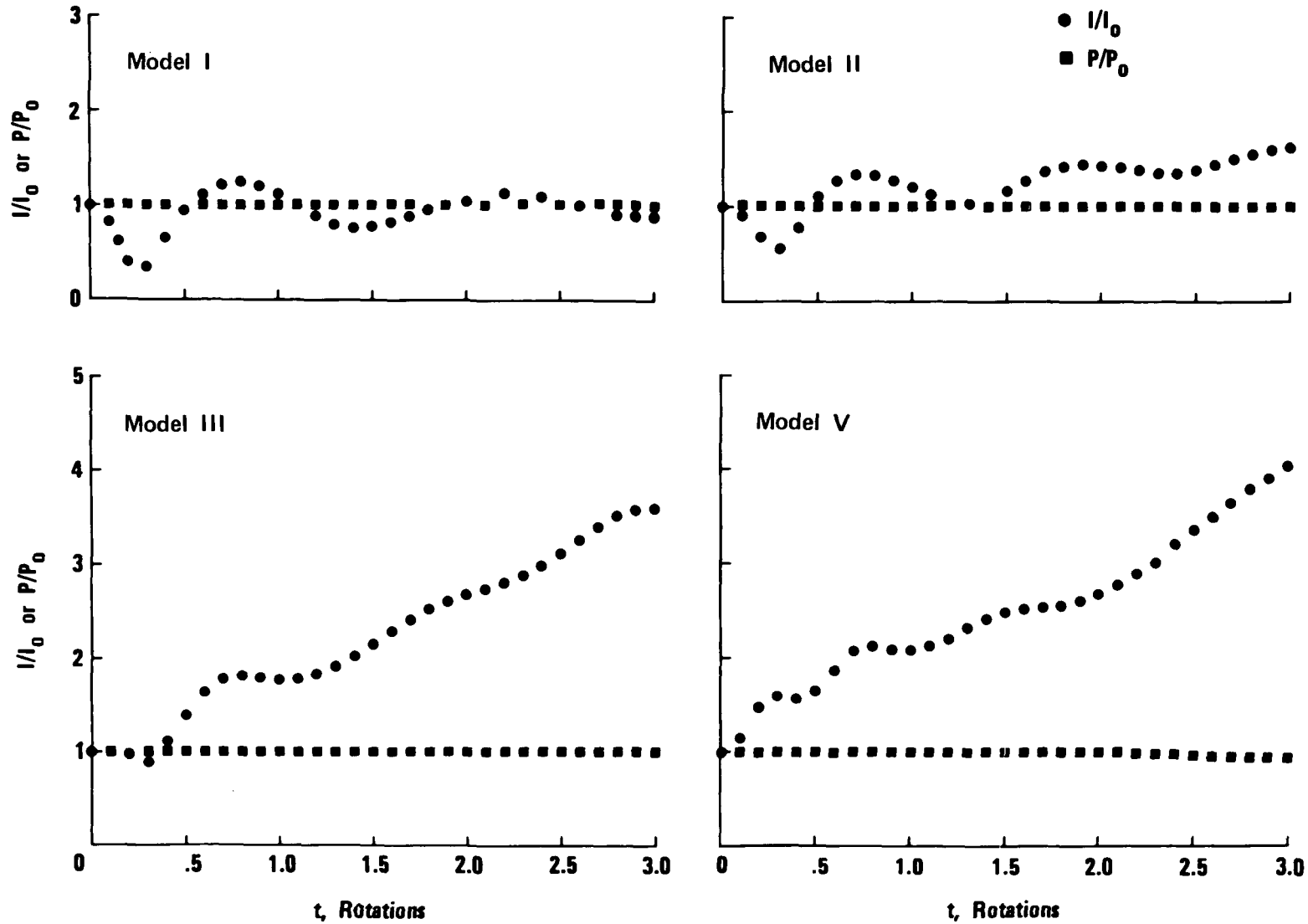

Figure 44.- Evolution of the moment of inertia I and the angular momentum P (divided by their initial values) for models I, II, III, and V.

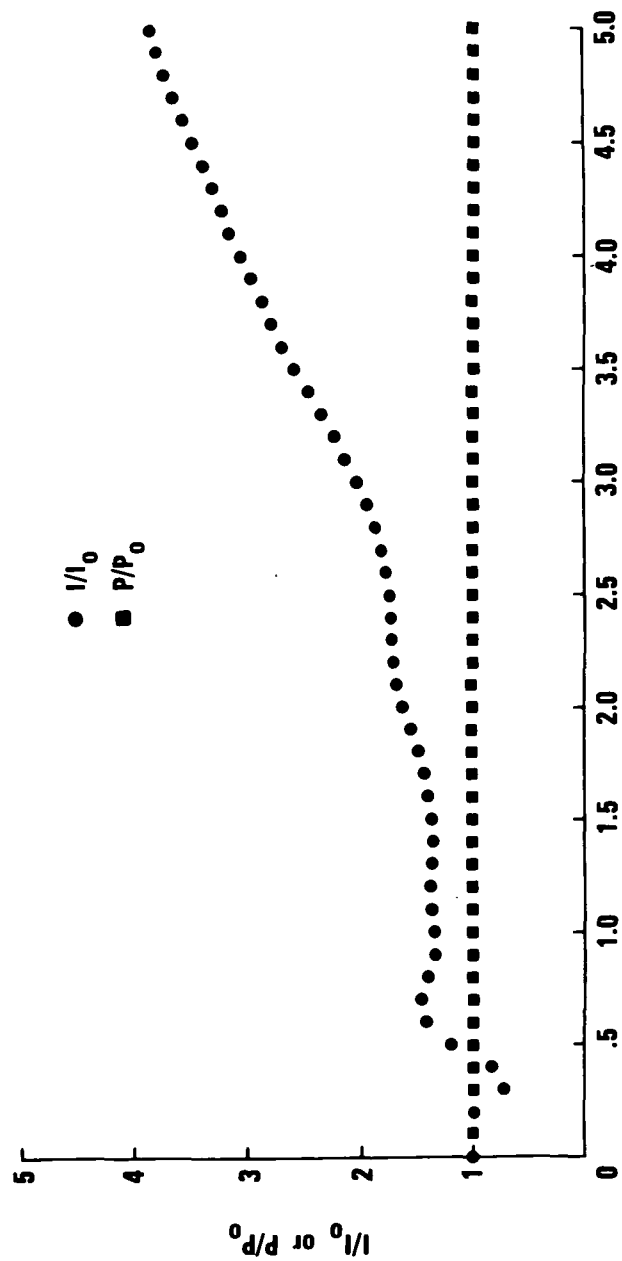

Figure 45.- Evolution of the moment of inertia I and the angular momentum P (divided by their initial values) for model IV.

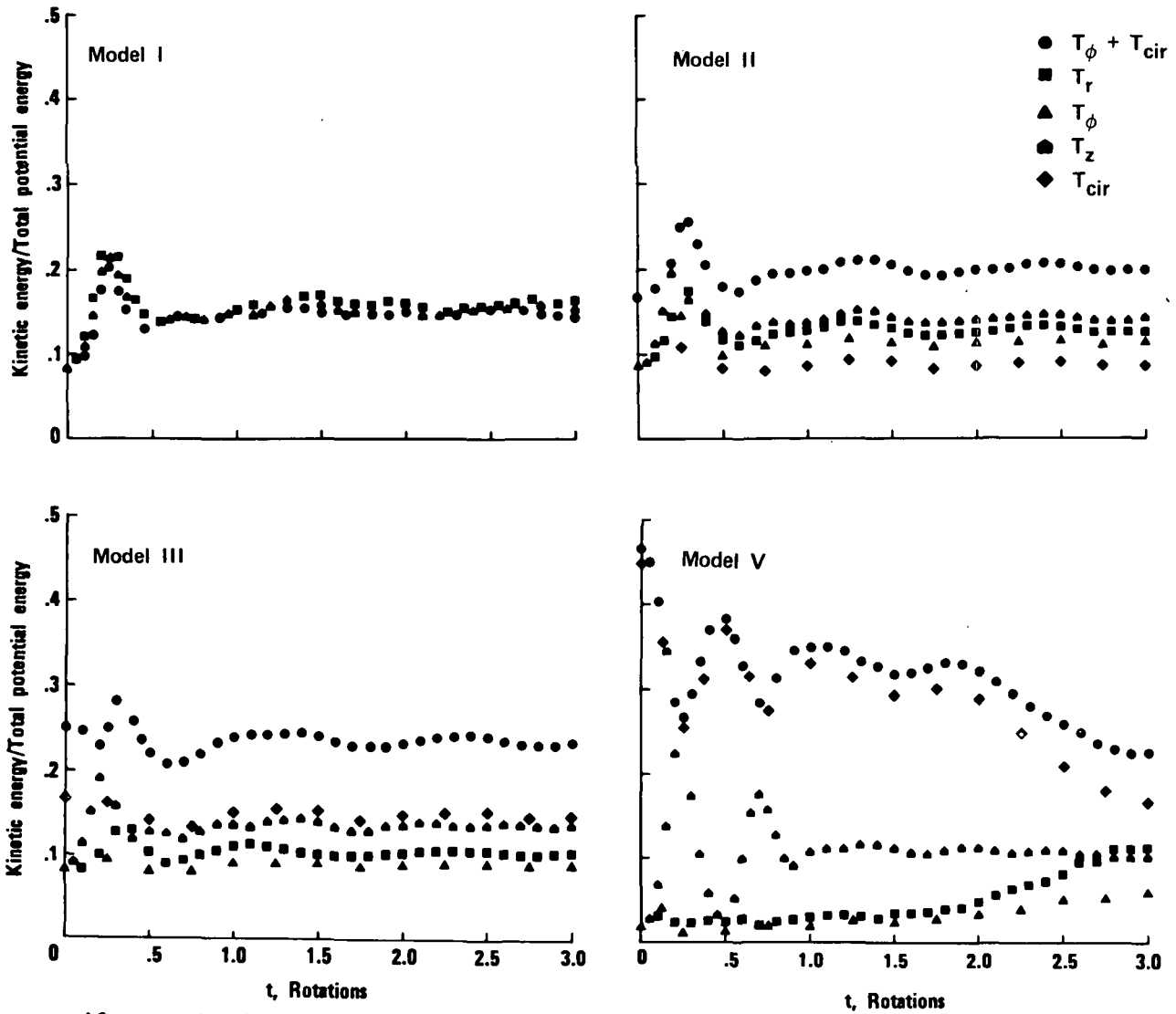

Figure 46.- Evolution of various ratios of kinetic energy to total potential energy for models I, II, III, and V.

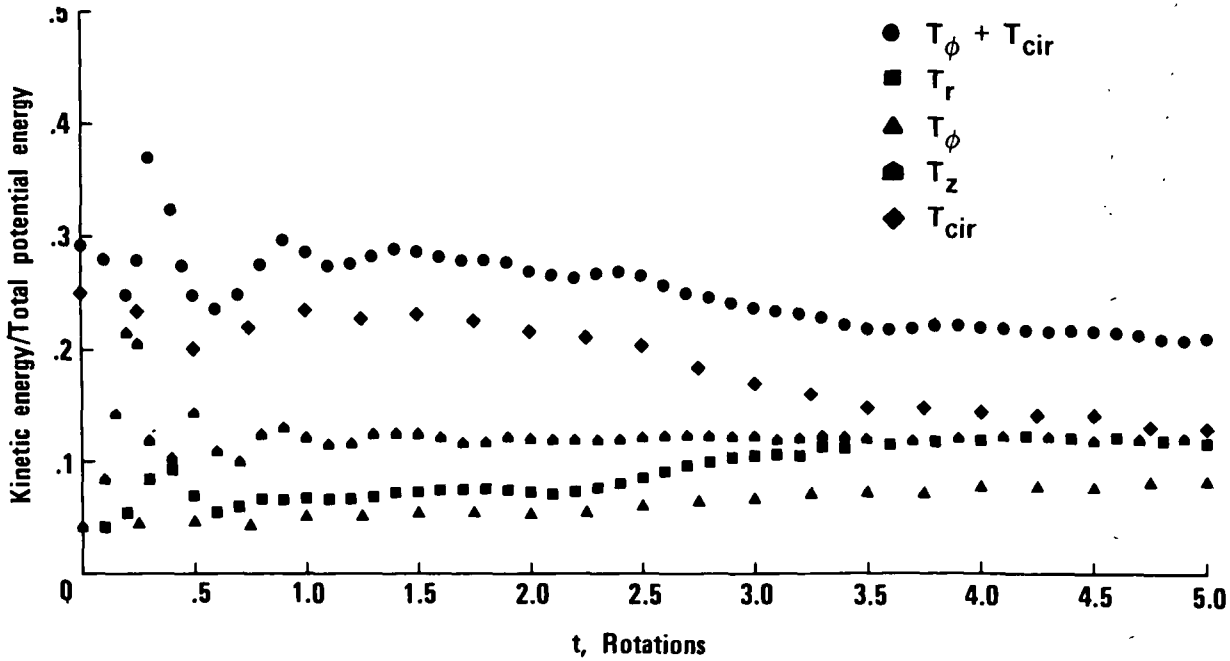

Figure 47.- Evolution of various ratios of kinetic energy to total potential energy for model IV.

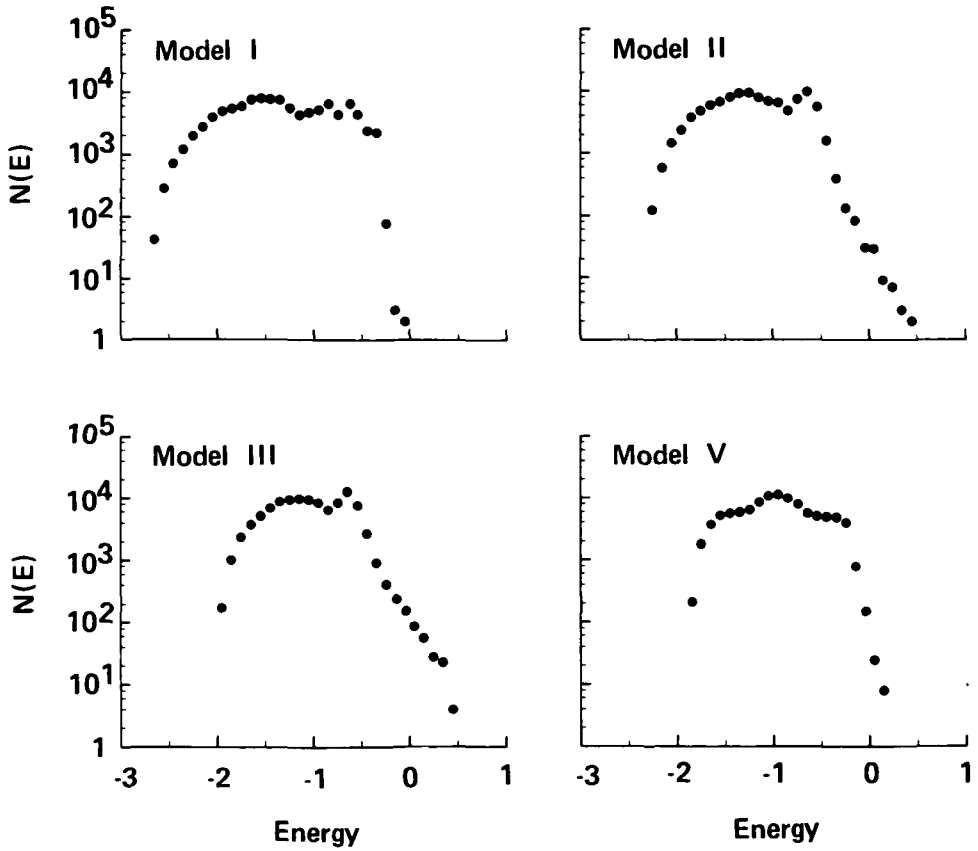

Figure 48.- Final energy histograms for models I, II, III, and V. The abscissa is the energy of a star in units of GM_g/R and the ordinate is the number of stars in an energy interval of width $0.05GM_g/R$.

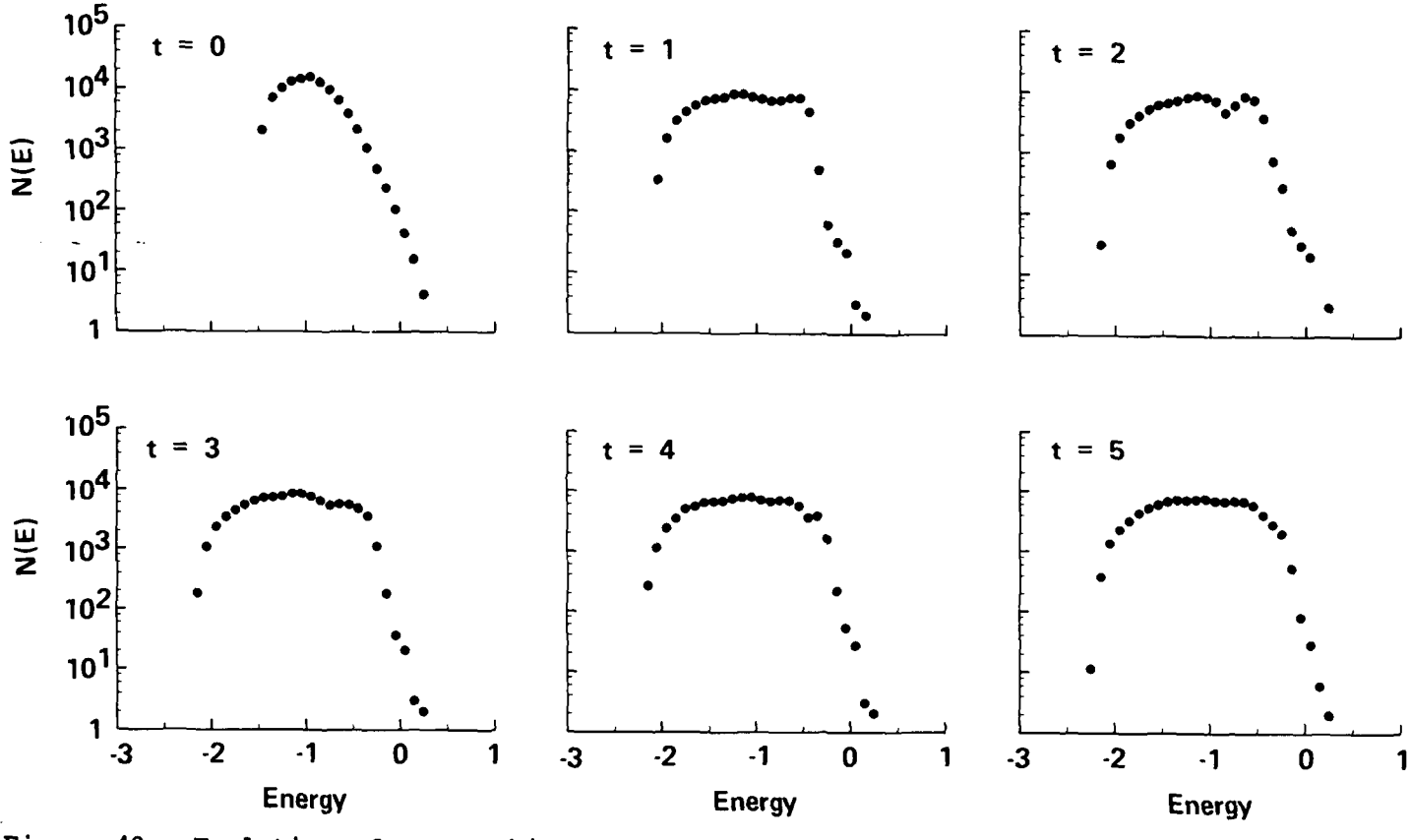

Figure 49.- Evolution of energy histograms for model IV. The abscissa is the energy of a star in units of GM_g/R and the ordinate is the number of stars in an energy interval of width $0.05GM_g/R$.

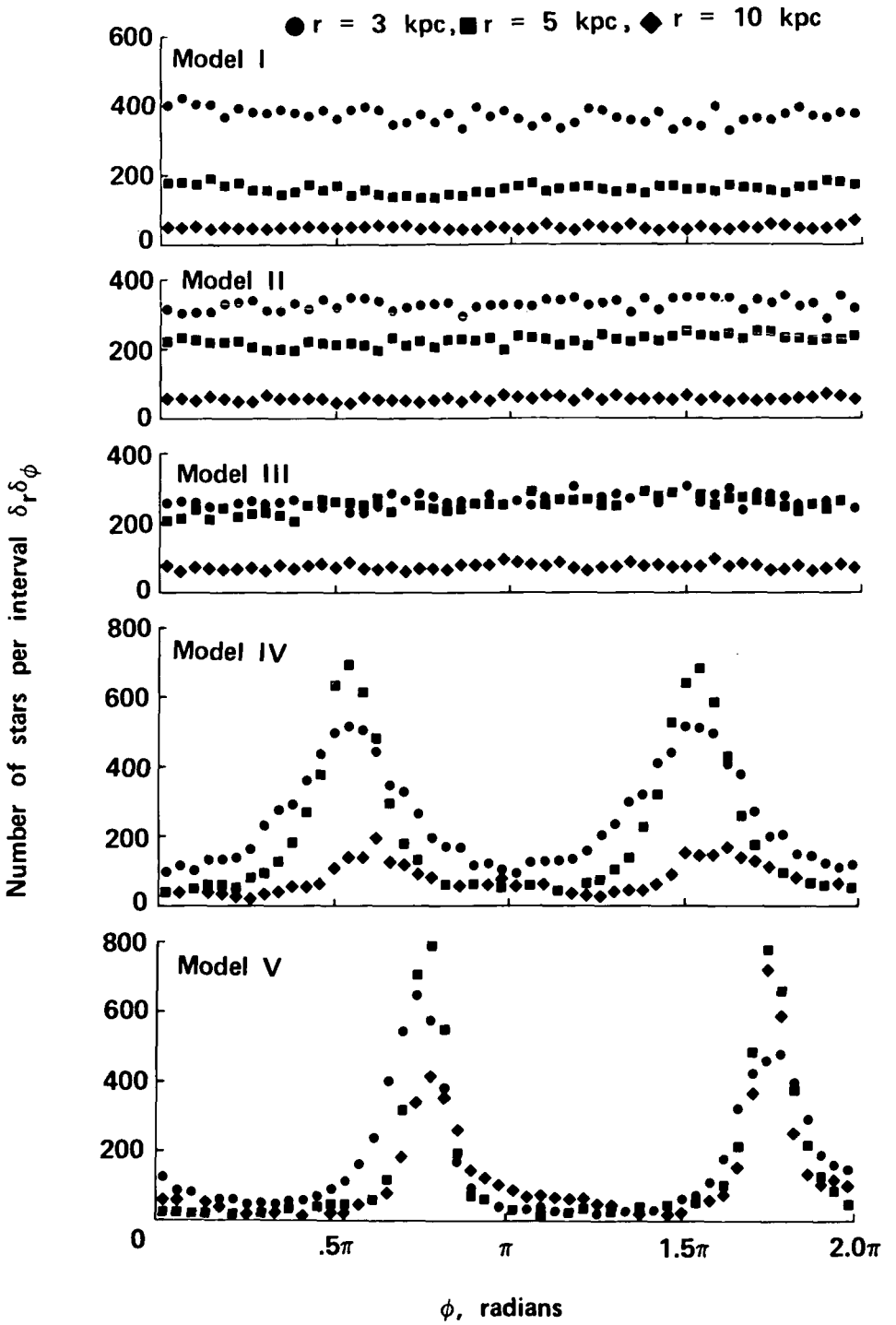

Figure 50.- Azimuthal variation of projected star density at t = 3 taken at three cylindrical radii.

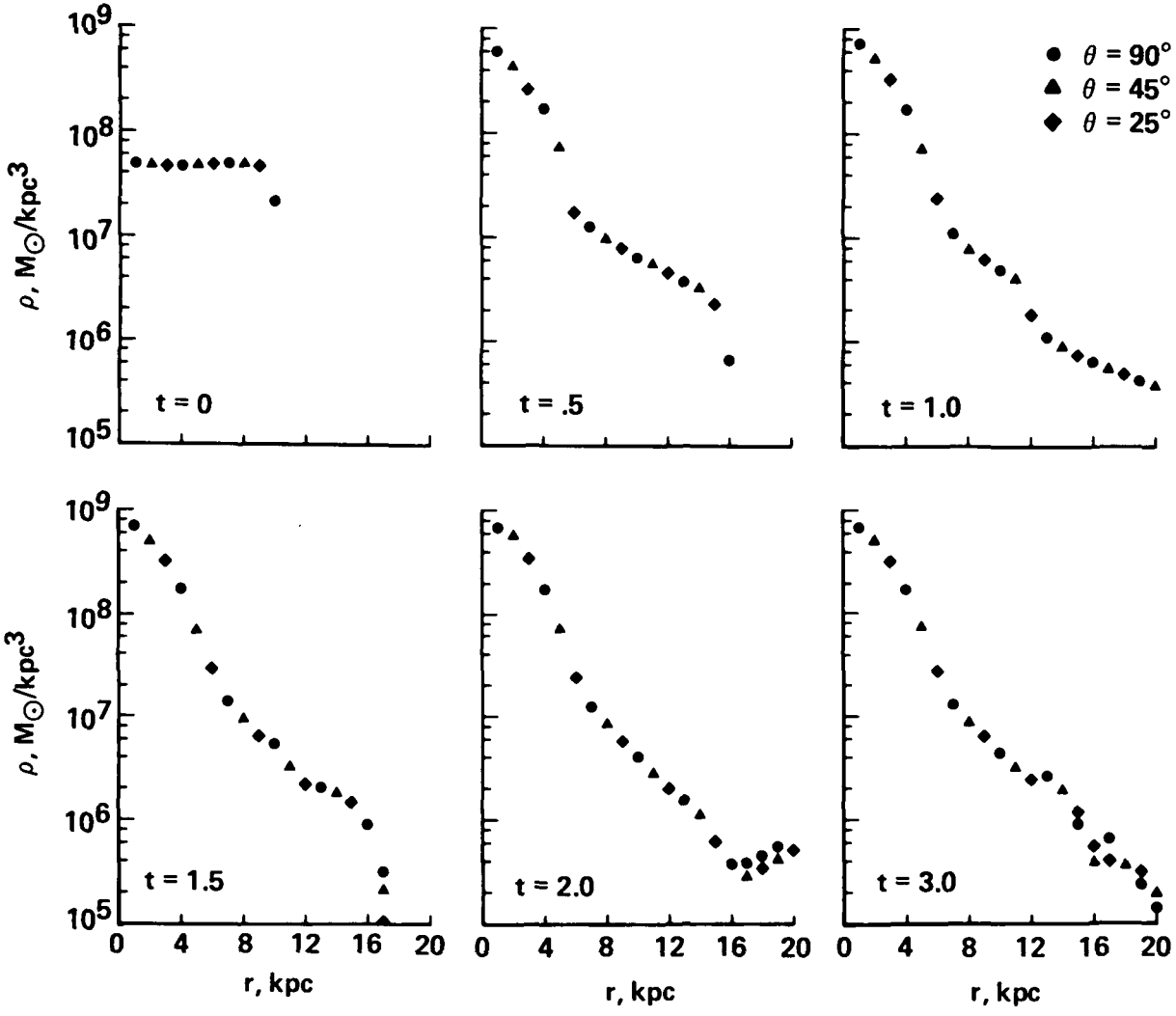

(a) Model I.

Figure 51.- Evolution of the radial volume mass density as a function of the spherical radius r.

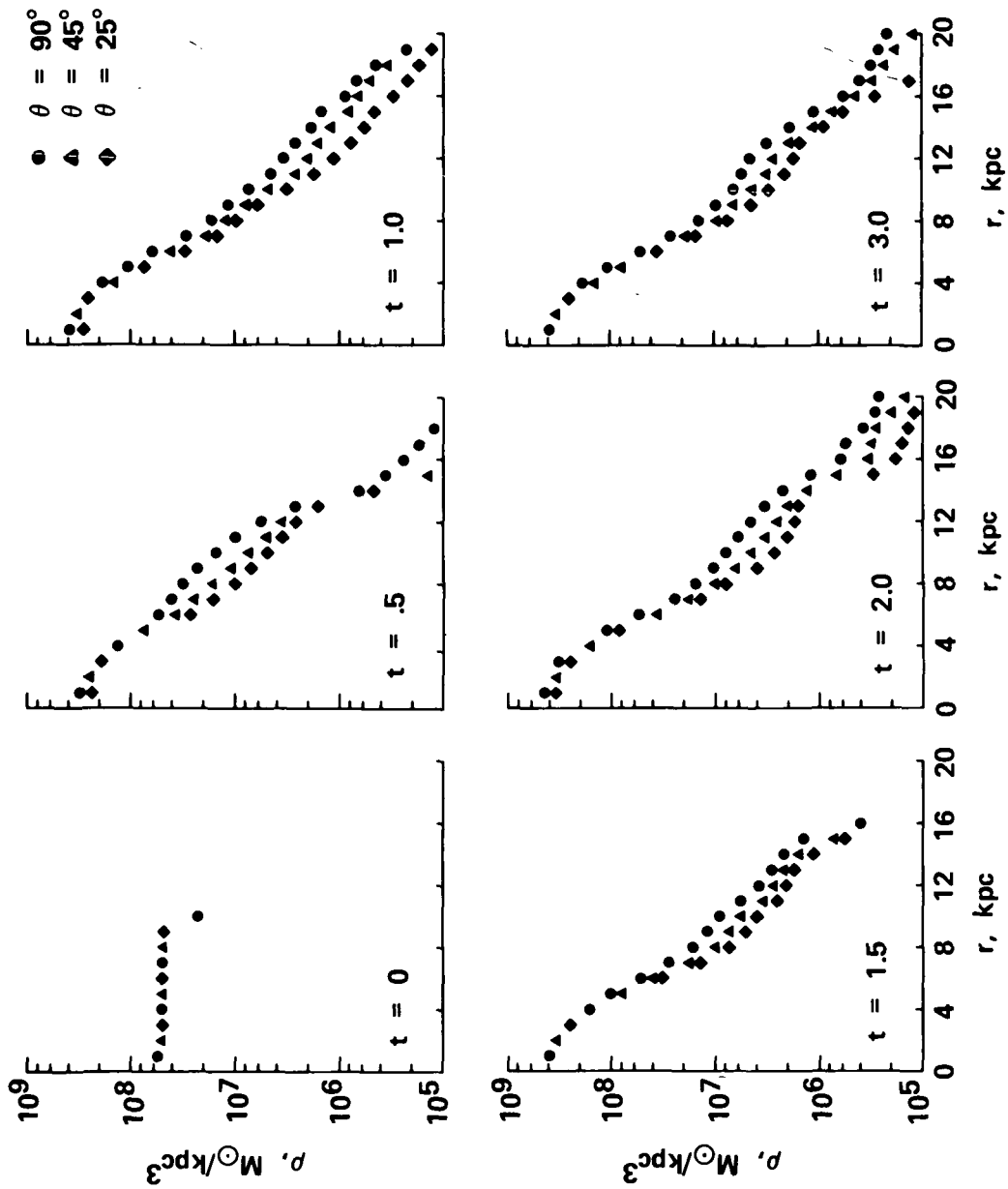

(b) Model II.

Figure 51.- Continued.

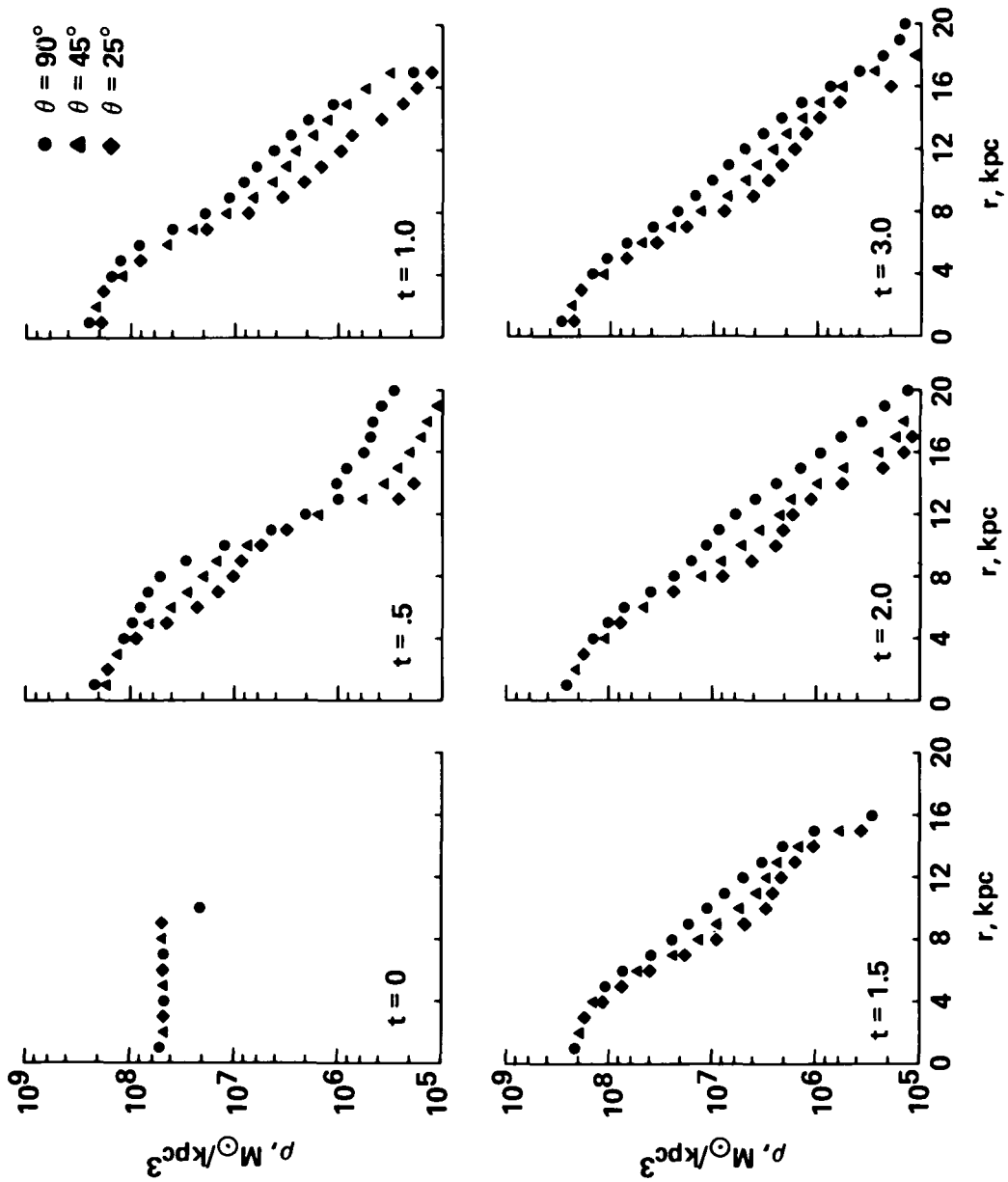

Figure 51.- Continued.

(c) Model III.

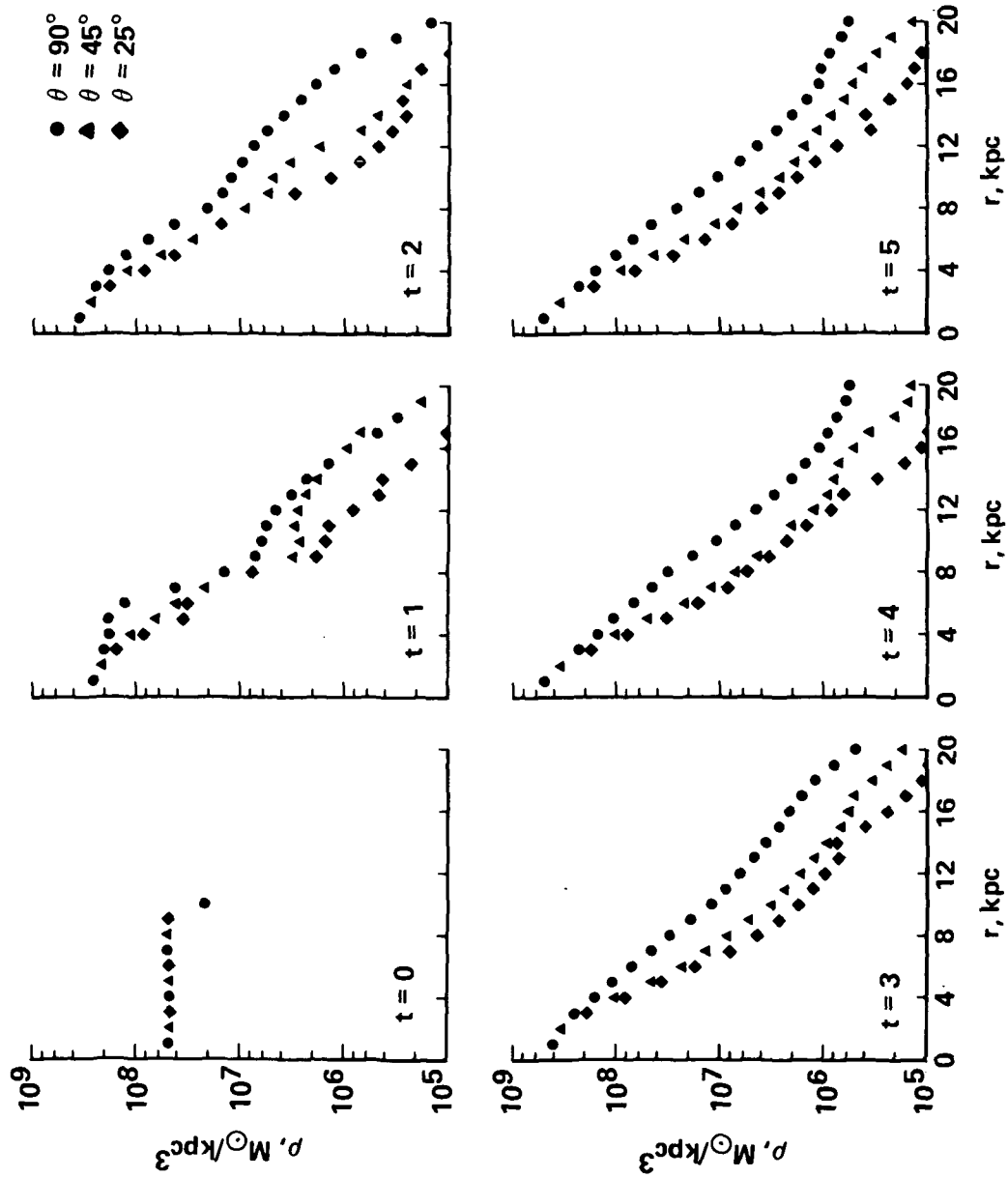

(d) Model IV.

Figure 51.- Continued.

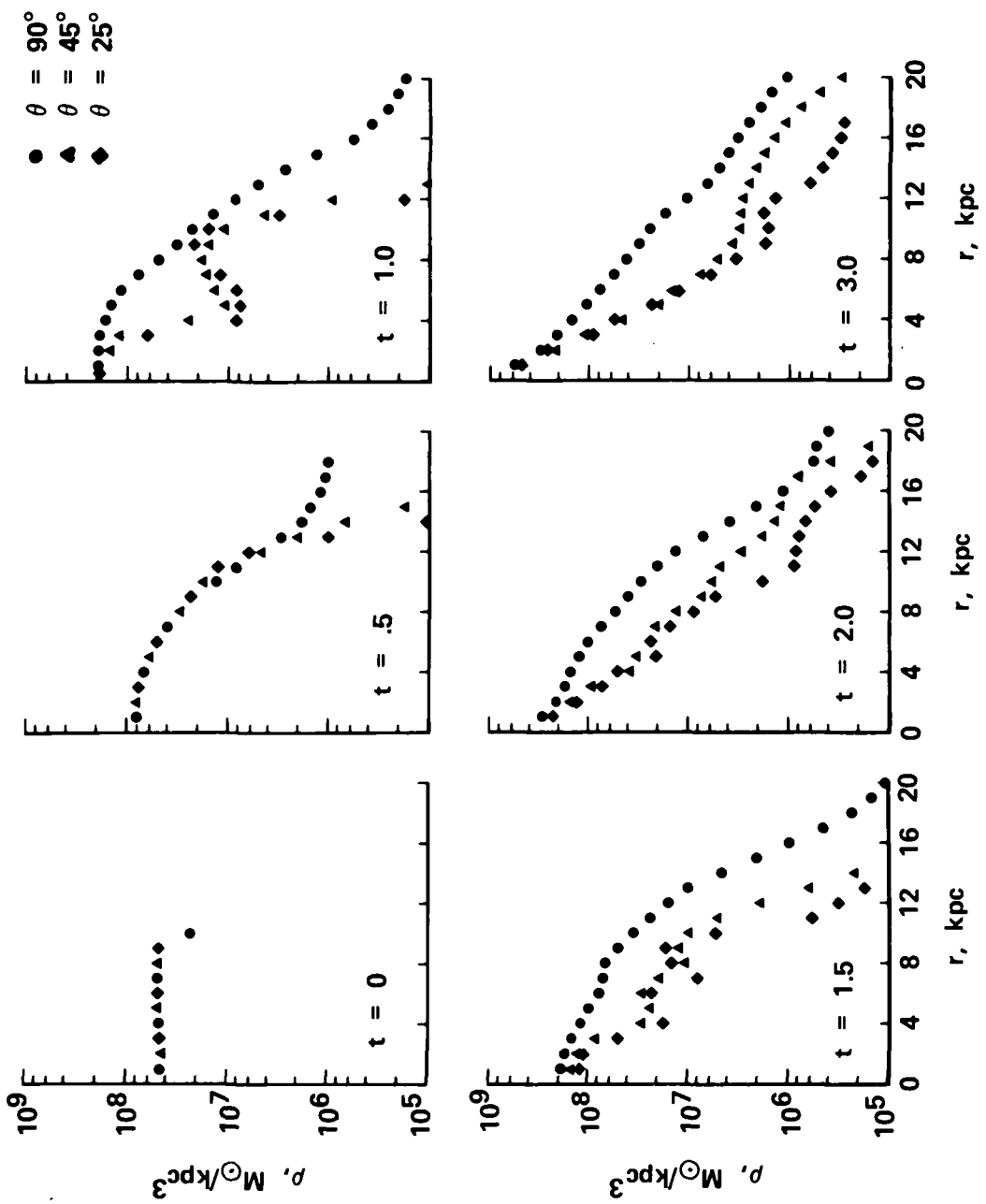

(e) Model V.

Figure 51.- Concluded.

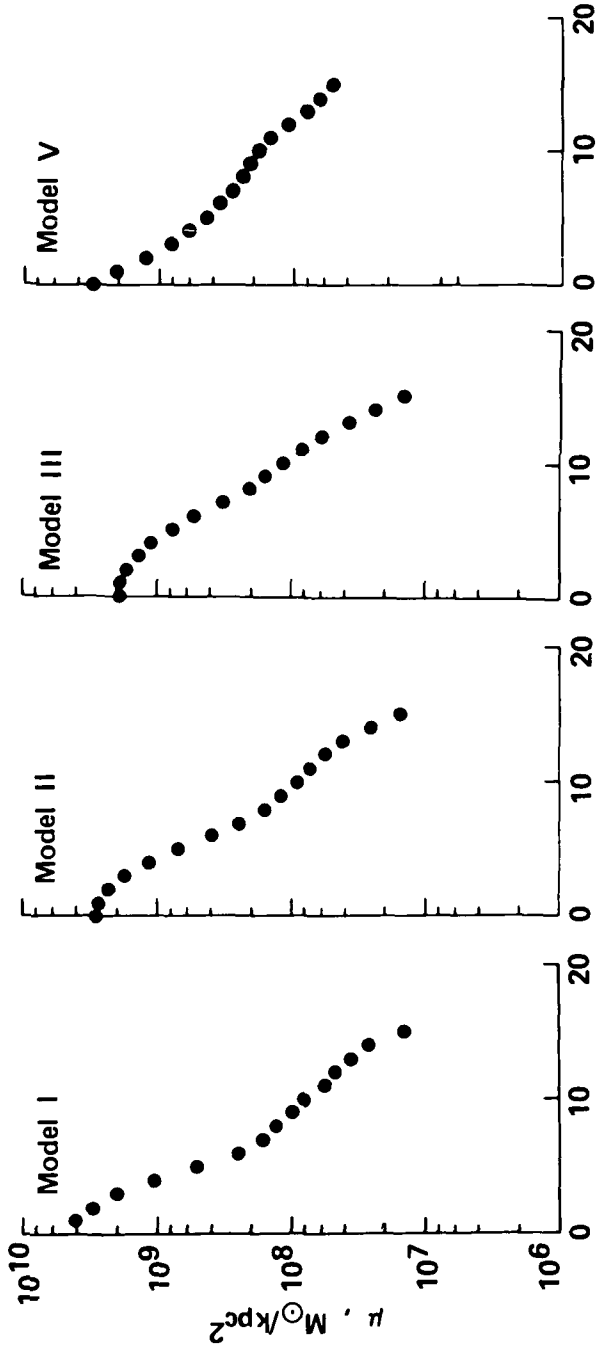

Figure 52.- Final azimuthally averaged, projected surface mass density for models I, II, III, and V.

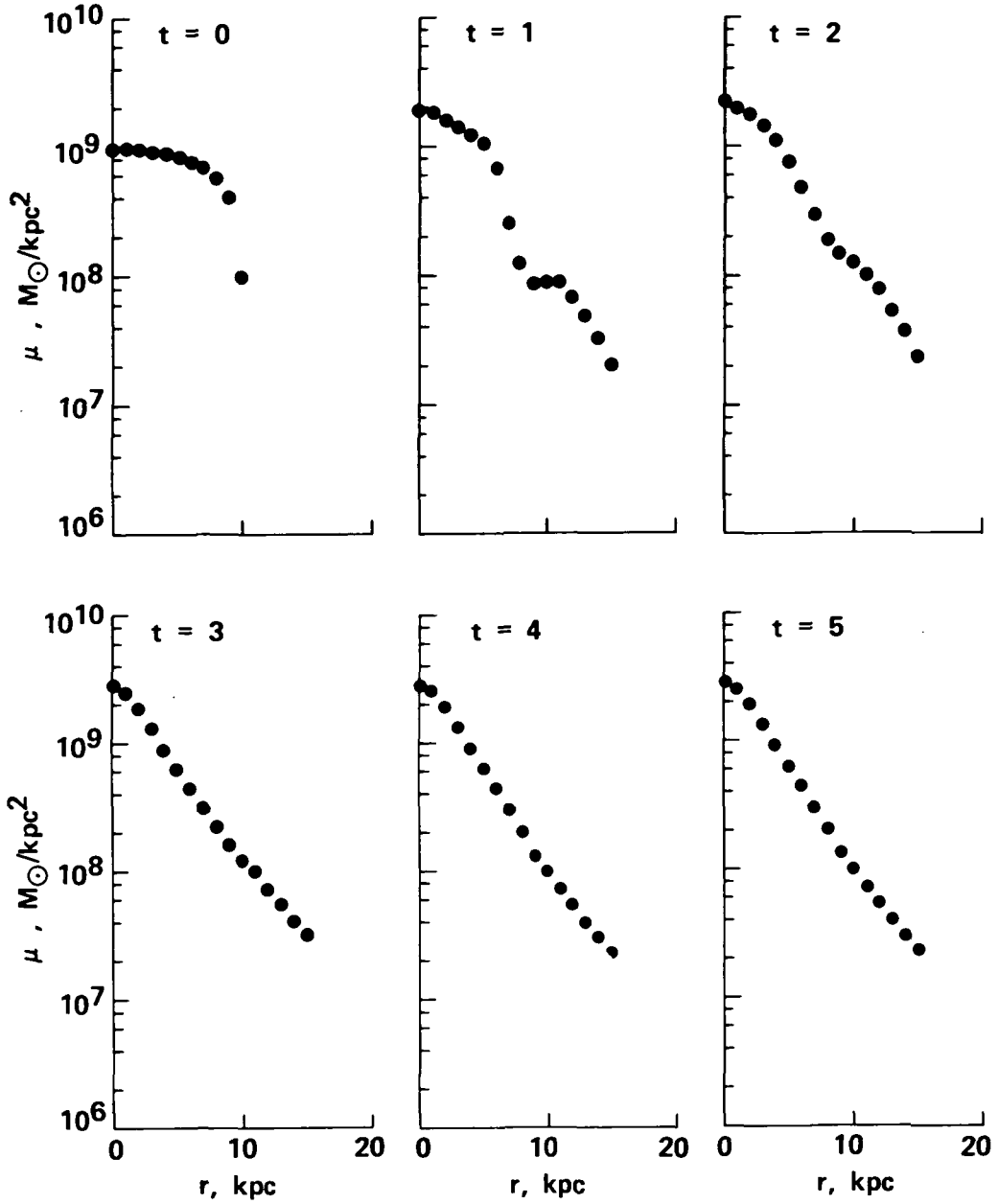

Figure 53.- Evolution of the azimuthally averaged projected surface mass density for model IV.

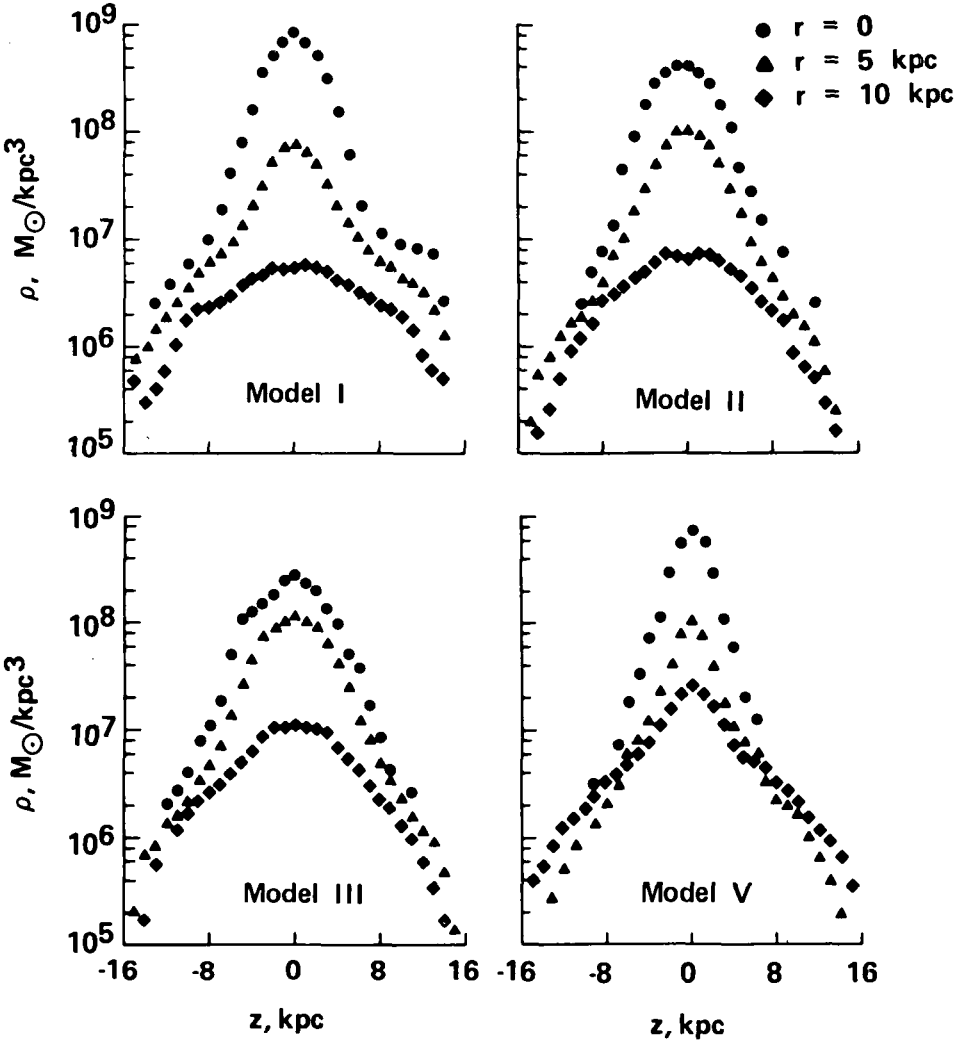

Figure 54.- Final volume mass density variation in the axial direction at three cylindrical radii for models I, II, III, and V.

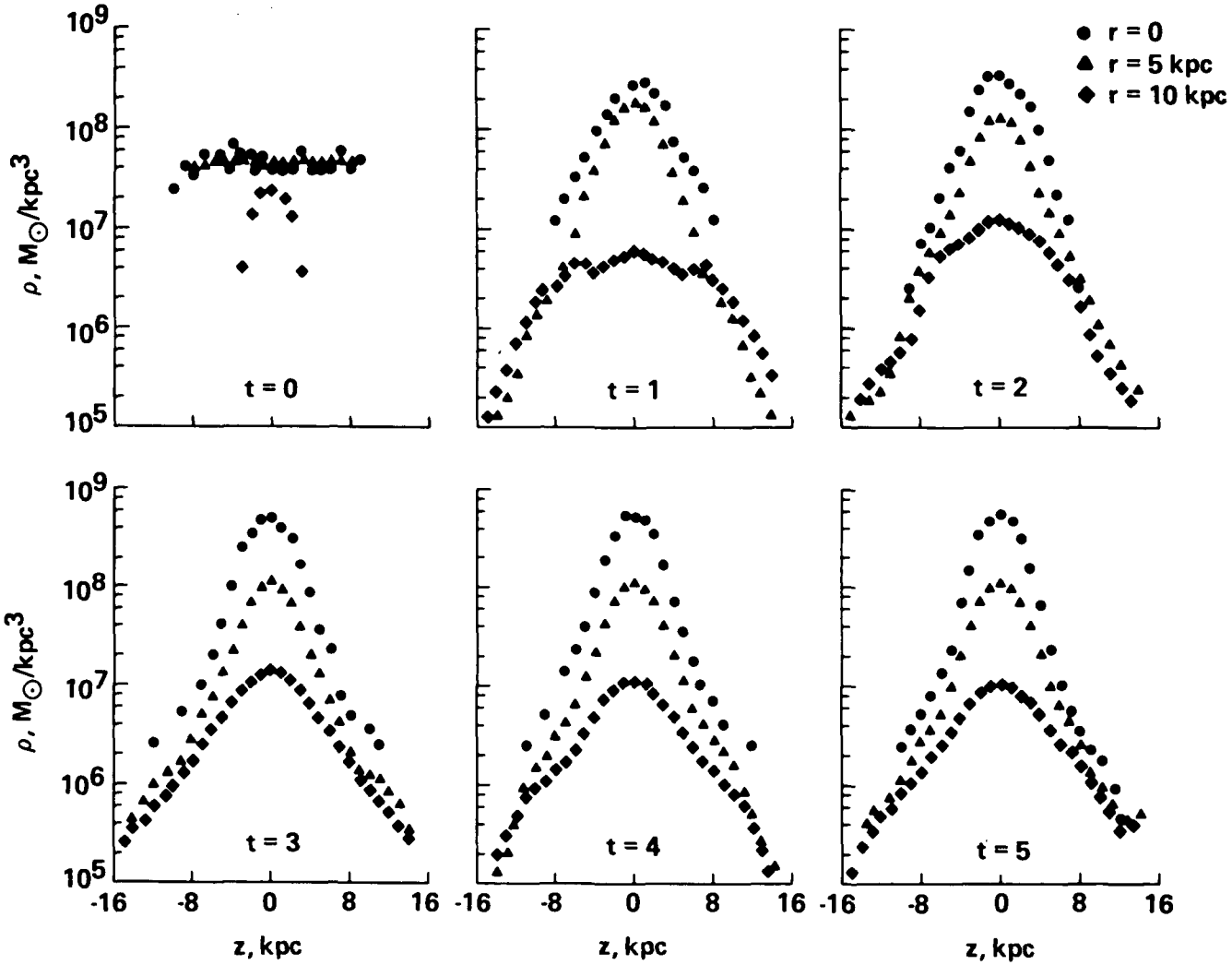

Figure 55.- Evolution of the volume mass density variation in the axial direction at three cylindrical radii for model IV.

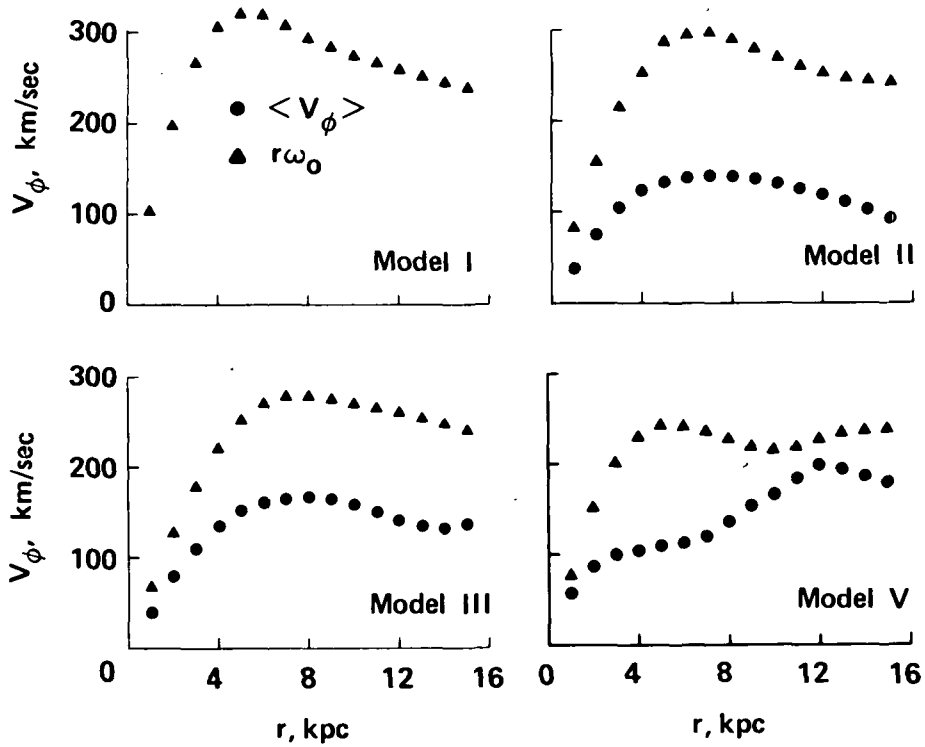

Figure 56.- Comparison of the final circular velocity $r\omega_o = \sqrt{K_r(z=0)\,r}$ with the mean azimuthal velocity $\langle V_\phi \rangle$ for models I, II, III, and V.

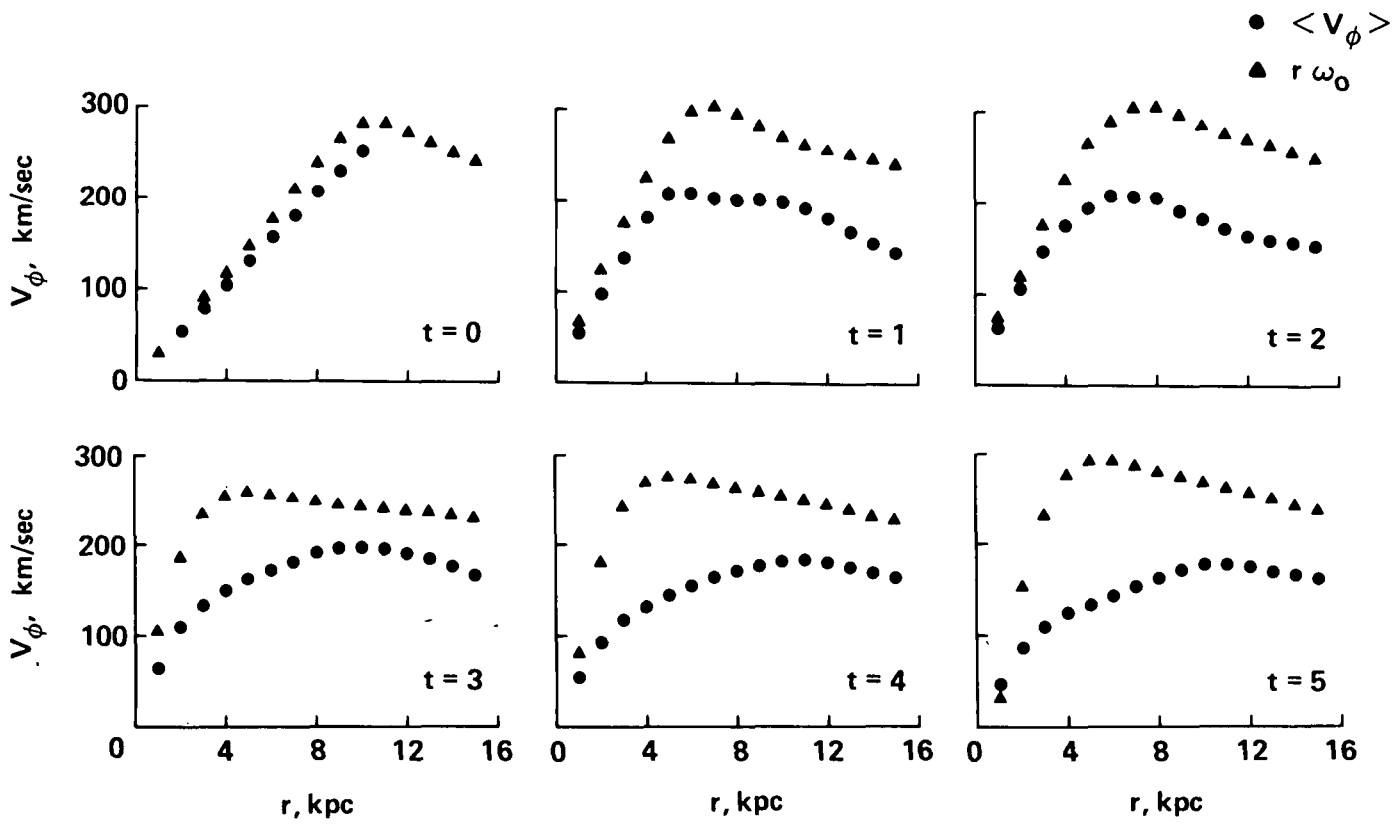

Figure 57.- Evolution of the circular velocity $r\omega_o = \sqrt{K_r(z=0)r}$ and the mean azimuthal velocity $<V_\phi>$ for model IV.

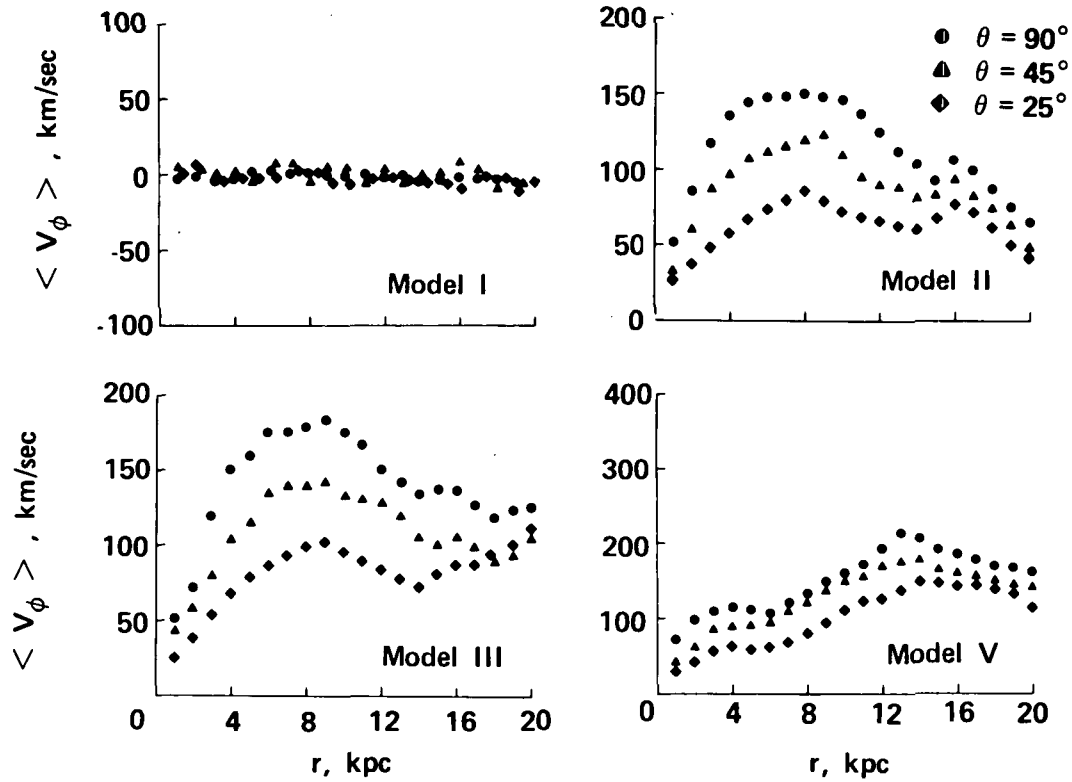

Figure 58.- Final mean azimuthal velocity as a function of the spherical radius r for models I, II, III, and V. Note the reduced region of solid body rotation for the bar-forming model V.

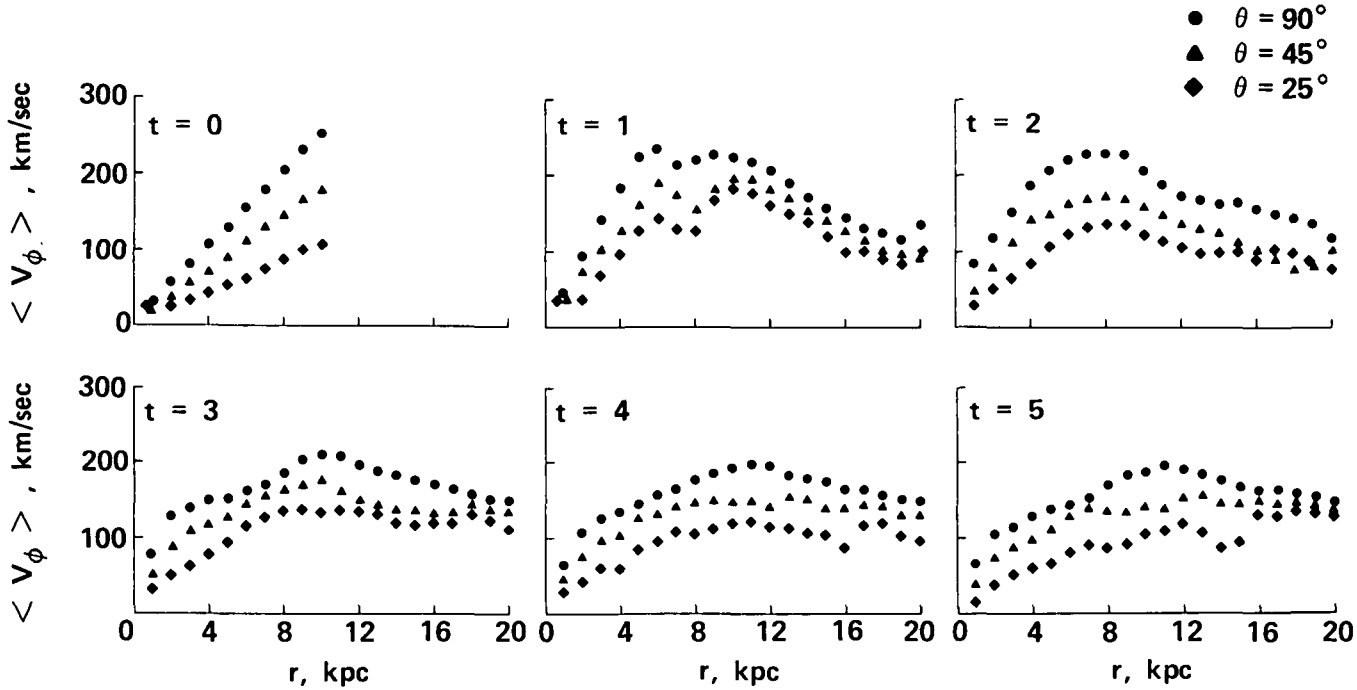

Figure 59.- Evolution of the mean azimuthal velocity as a function of the spherical radius r for model IV. Again this bar-forming model shows only a small central region with solid body rotation.

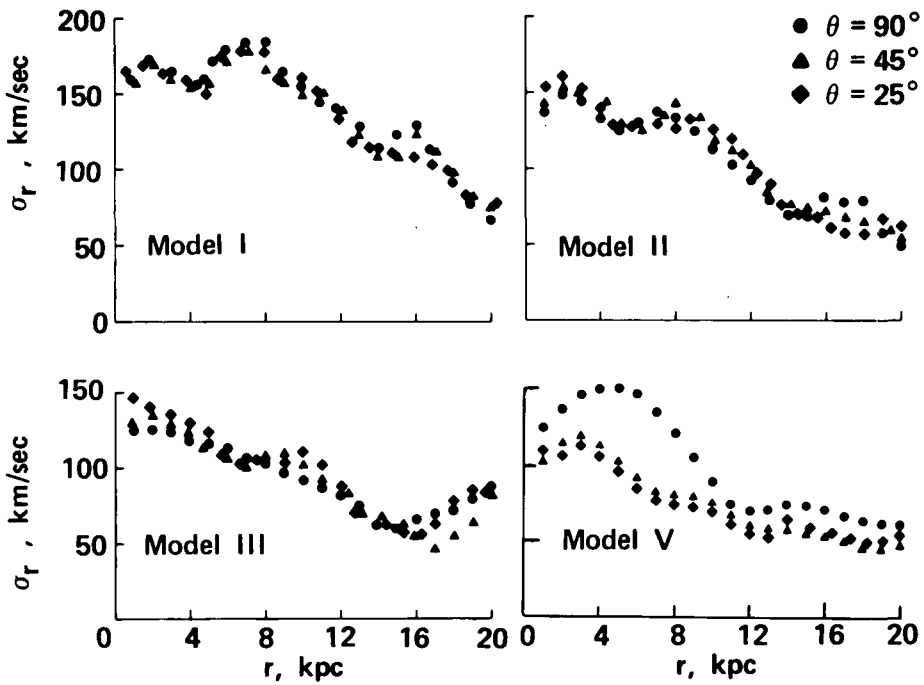

Figure 60.- Final radial velocity dispersion as a function of the spherical radius r for models I, II, III, and V.

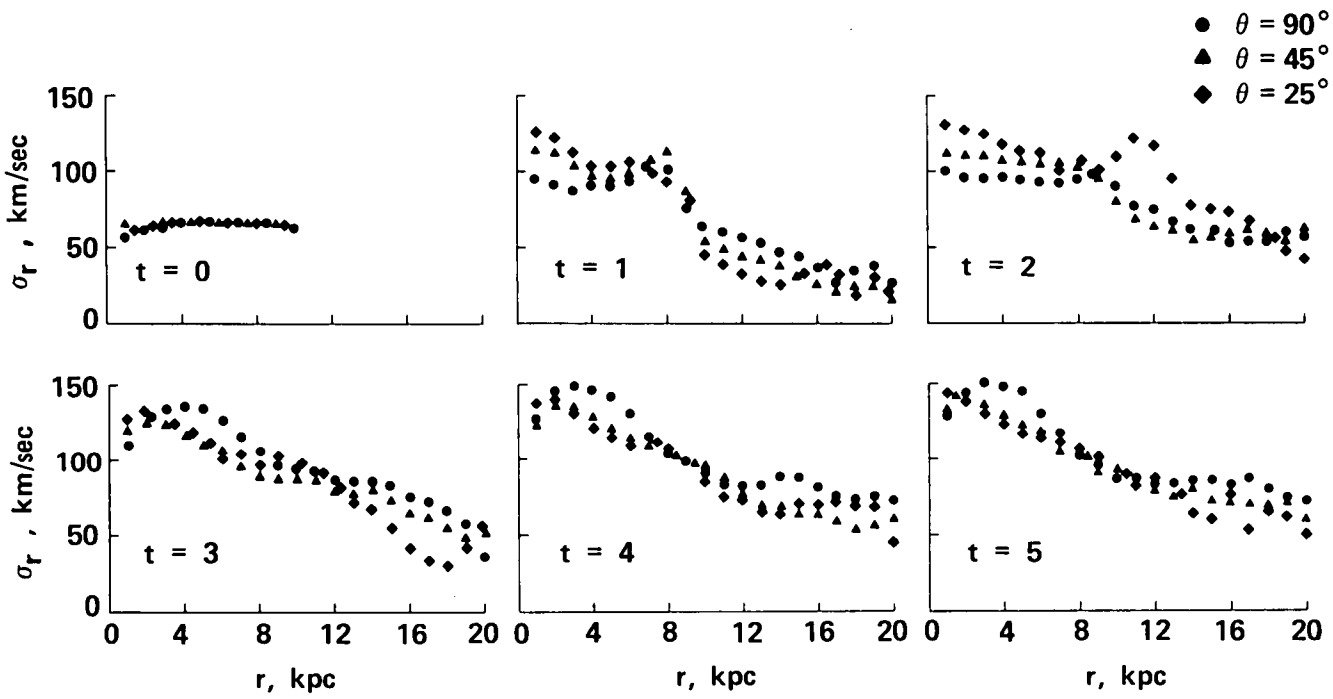

Figure 61.- Evolution of the radial velocity dispersion as a function of the spherical radius r for model IV. Note the nearly equal values for different colatitudes.

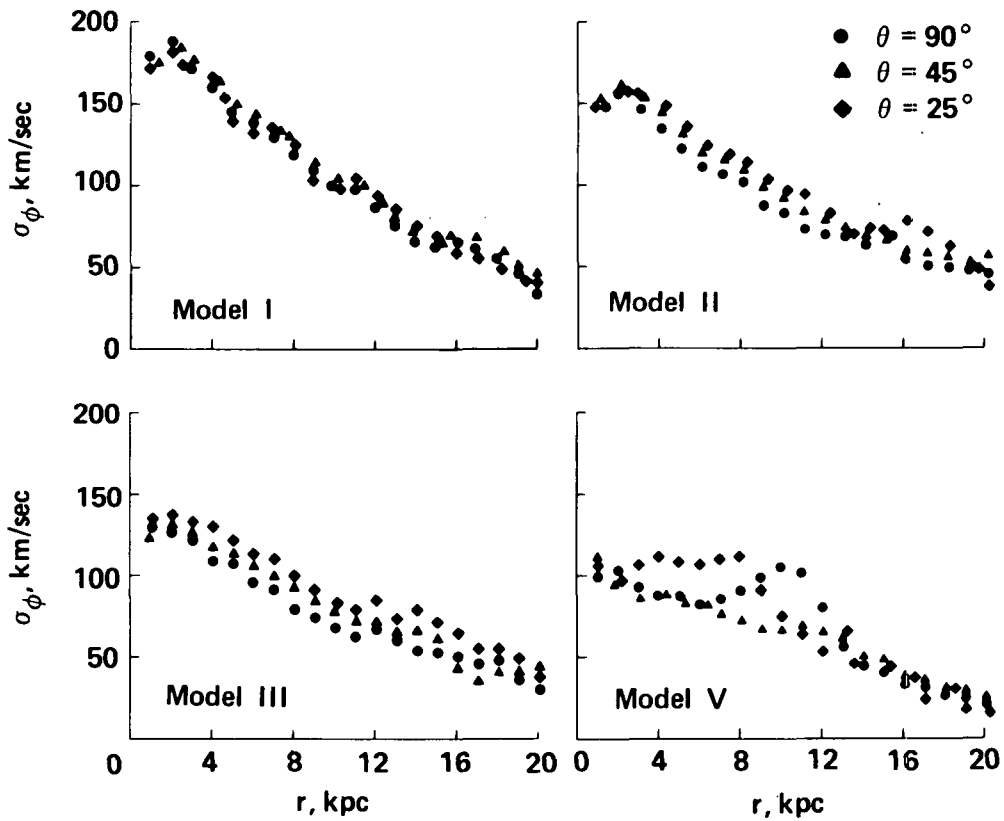

Figure 62.- Final azimuthal velocity dispersion as a function of the spherical radius r for models I, II, III, and V.

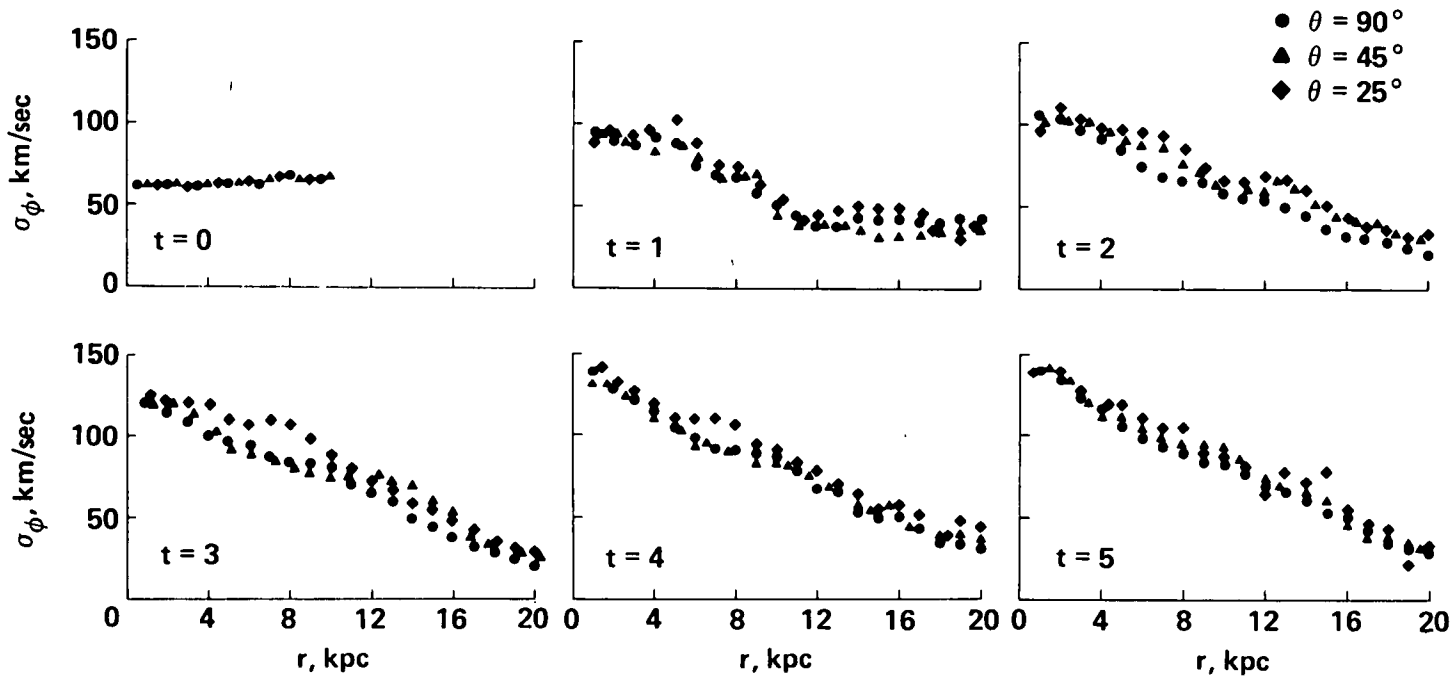

Figure 63.- Evolution of the azimuthal velocity dispersion as a function of the spherical radius r for model IV.

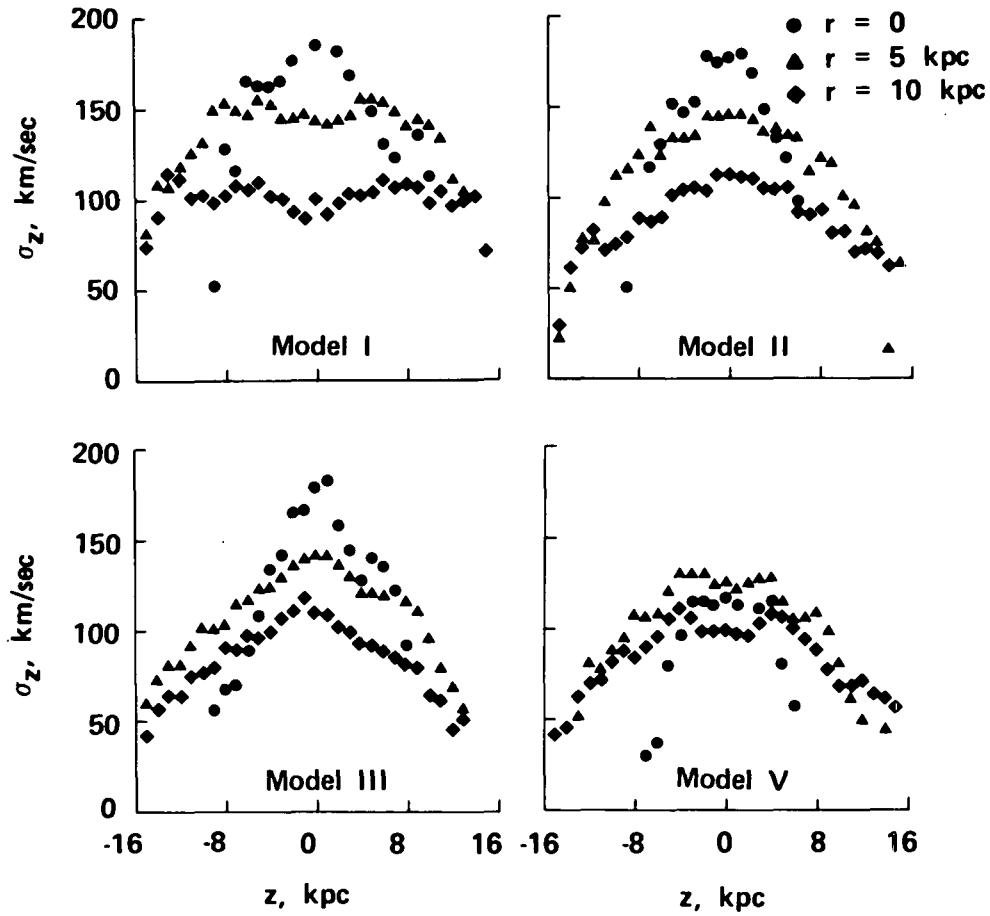

Figure 64.- Final axial velocity dispersion as a function of the spherical radius r for models I, II, III, and V.

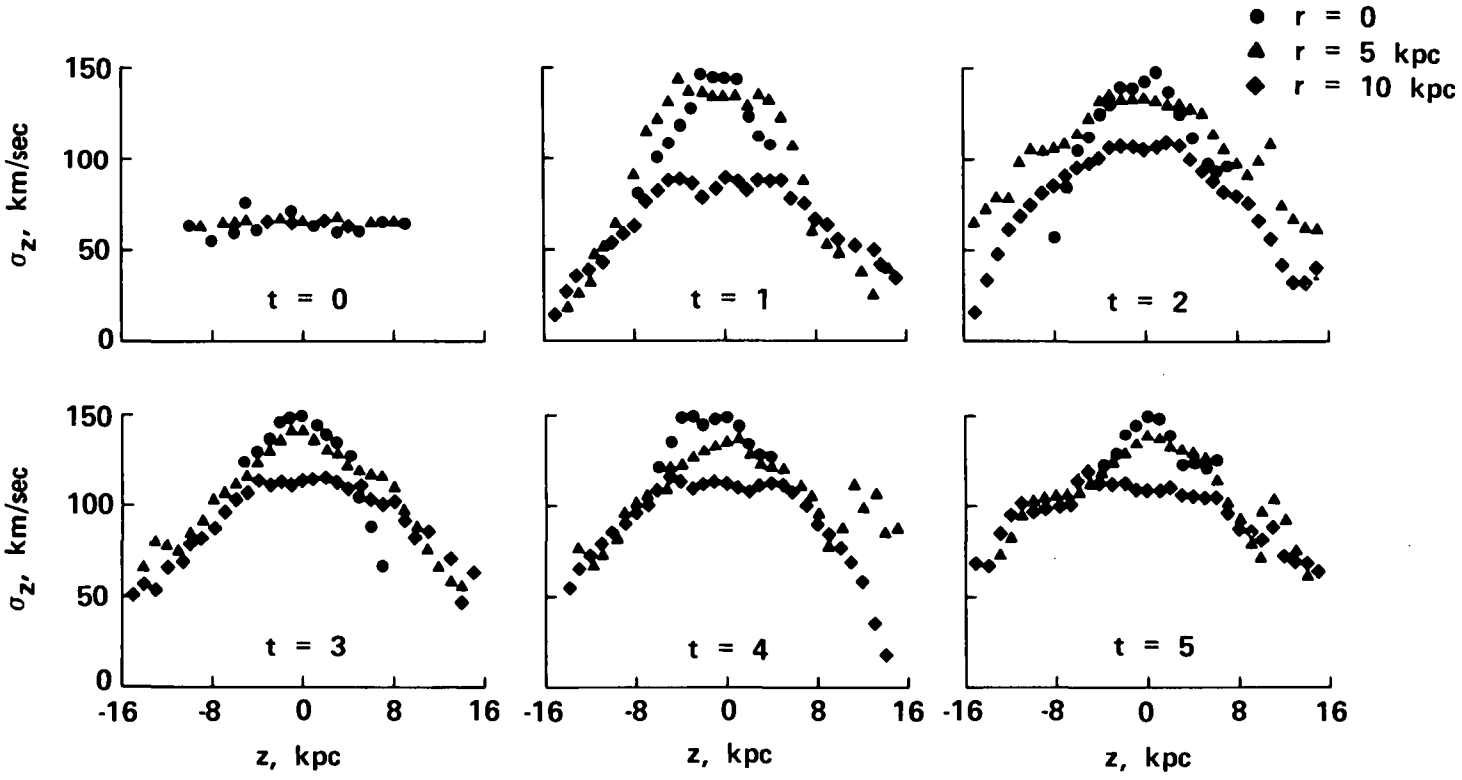

Figure 65.- Evolution of the axial velocity dispersion as a function of the spherical radius r for model IV.

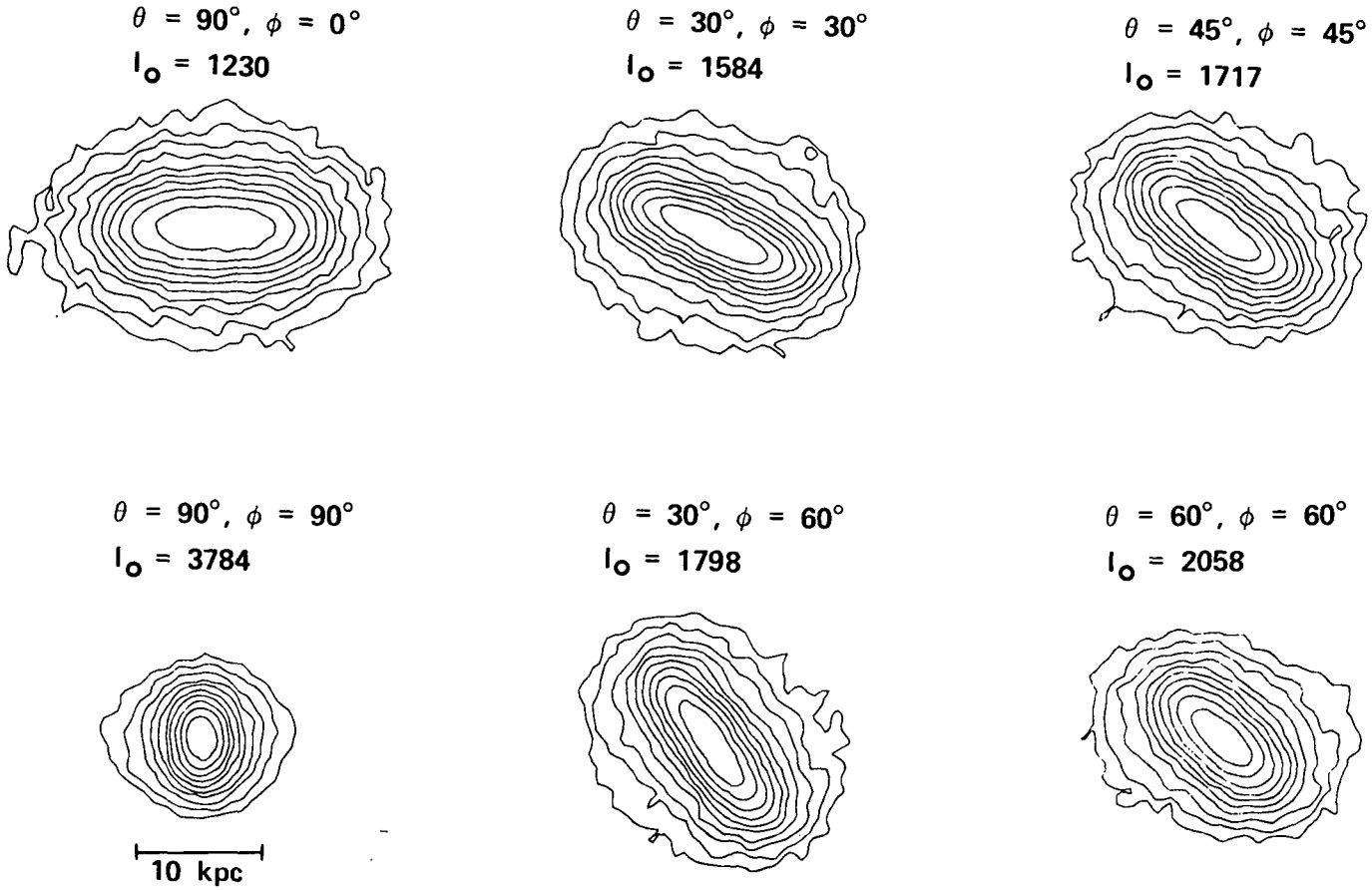

Figure 66.- Projected isodensity contours for various viewing directions of model IV at t = 5. I_o represents the peak in the projected number density of stars per kpc^2. The contours are evenly spaced in the logarithm of the projected density. There are 6 contour levels per factor of 10 with the innermost contour level at $0.68I_o$.

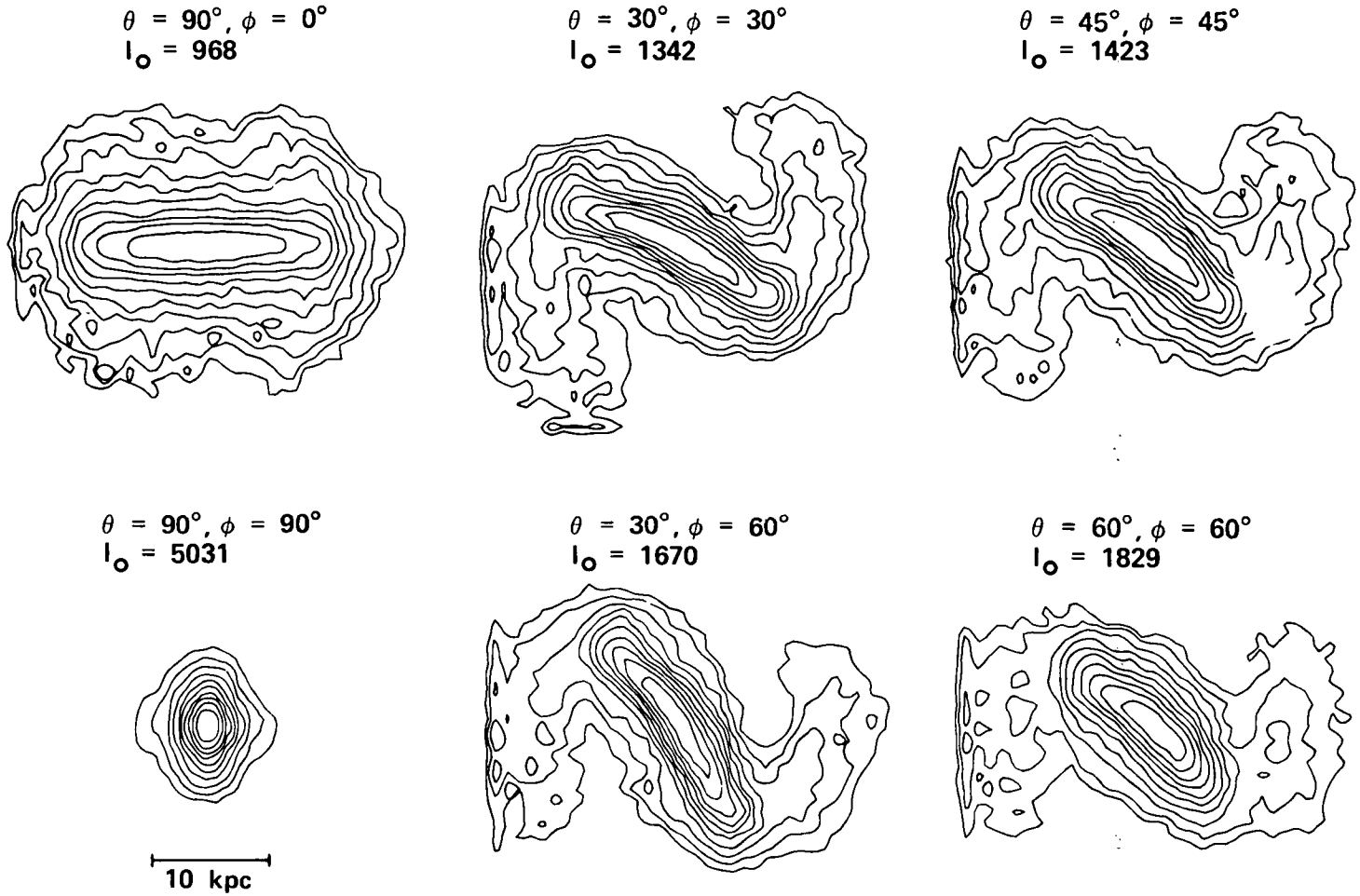

Figure 67.- Projected isodensity contours for various viewing directions of model V at $t = 3$. I_o represents the peak in the projected number density of stars per kpc^2. The contour levels have the same meaning as in the preceding figure.

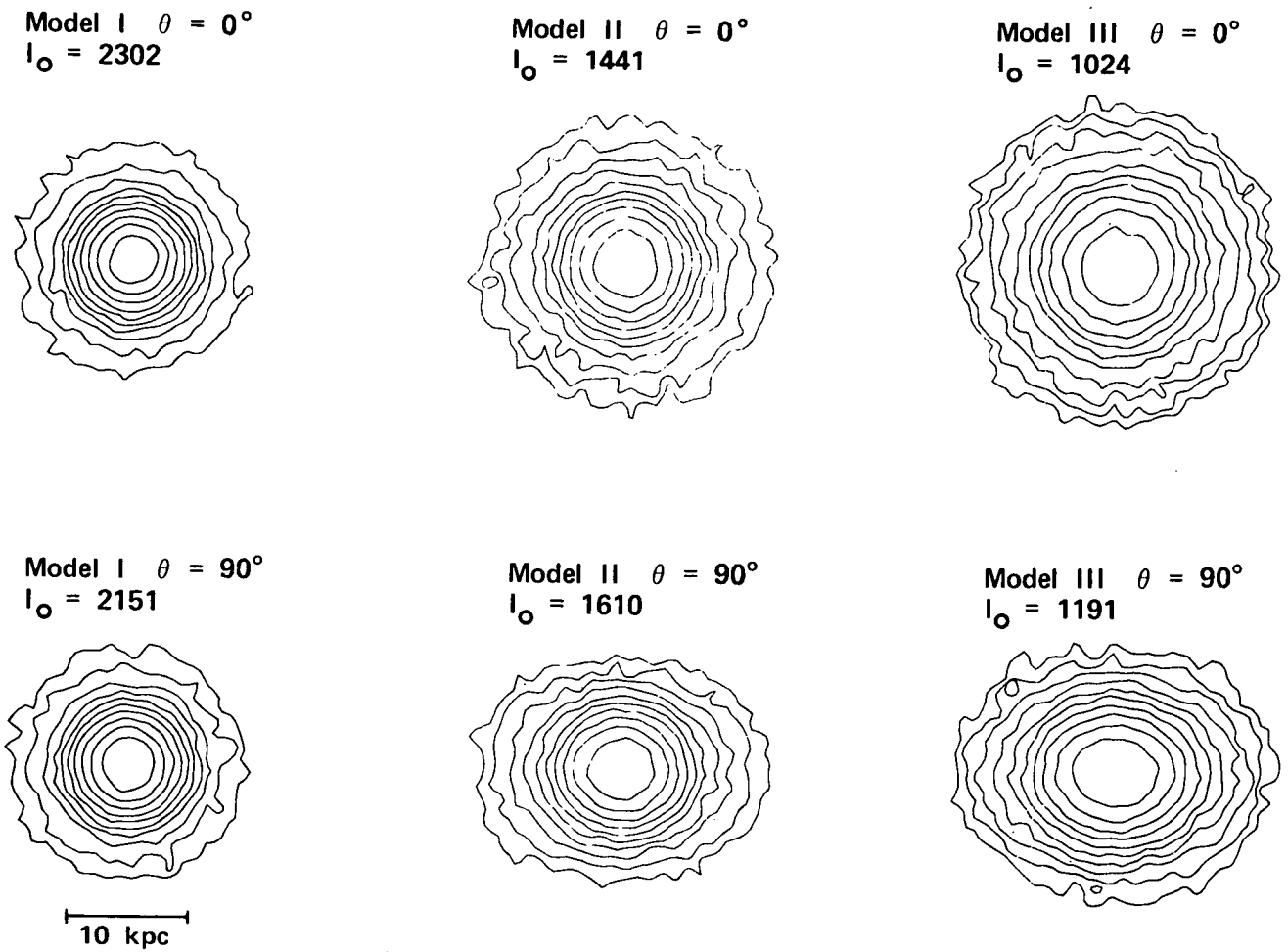

Figure 68.- Projected isodensity contours for both polar (θ = 0) and equatorial (θ = 90) viewing directions of models I to III at t = 3. The contour levels have the same meaning as in the two preceding figures.

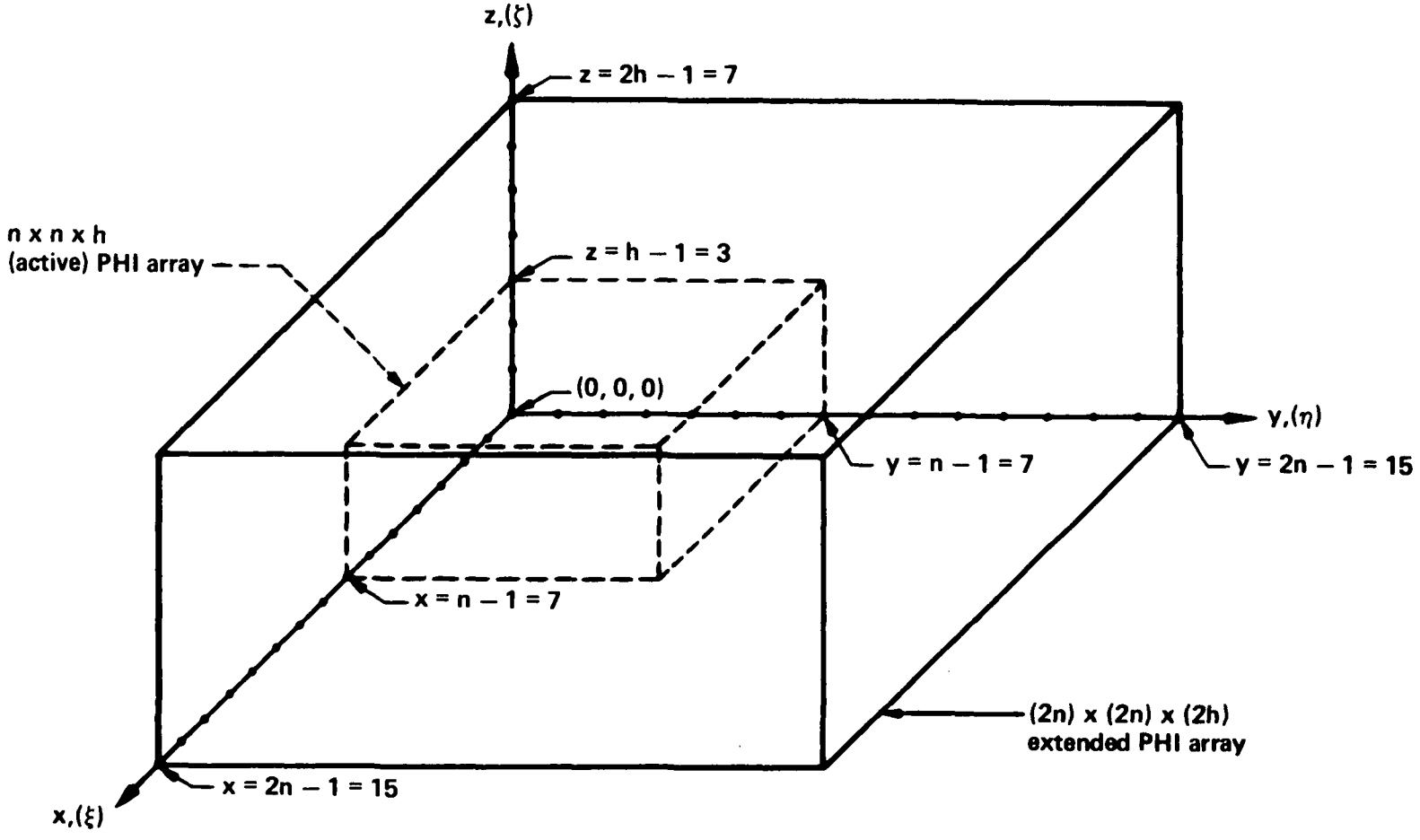

Figure 69.- PHI array (active), which contains the galactic density/potential mesh, and the extended PHI array, which is required for the Fourier potential solution of an isolated galaxy. Each x-, y-, or z-axis represents the following: (1) the x-, y-, or z-spatial direction, (2) the untransformed array subscript x, y, or z, and (3) the x-, y-, or z-direction transformed array subscript ξ, η, or ζ. For clarity in this and the following figures, the PHI array is dimensioned $n \times n \times h = 8 \times 8 \times 4$ while the program (listing I), as actually run, is dimensioned $64 \times 64 \times 16$ (table V).

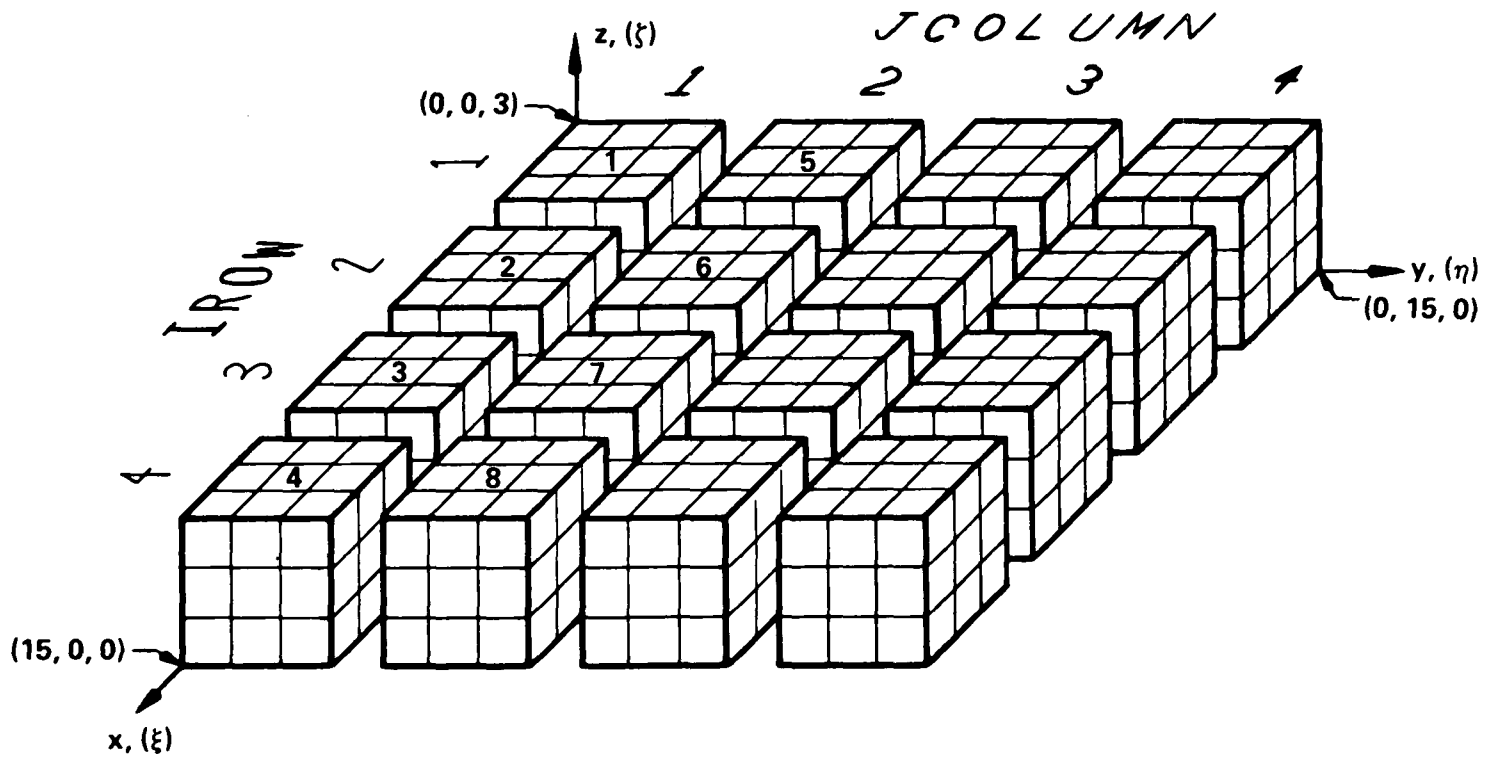

Figure 70.- Lower half (0 < z < h - 1 = 3) of the extended PHI array showing row and column designations of "chunks," (program of listing II). IROW 1 and 2 of JCOLUMN 1 and 2 constitute the active PHI array. The numbers on "chunks" of JCOLUMN 1 and 2 indicate the numbers of the disk files on which those chunks are stored. The "chunks" of JCOLUMN 3 and 4 do not require disk file storage.

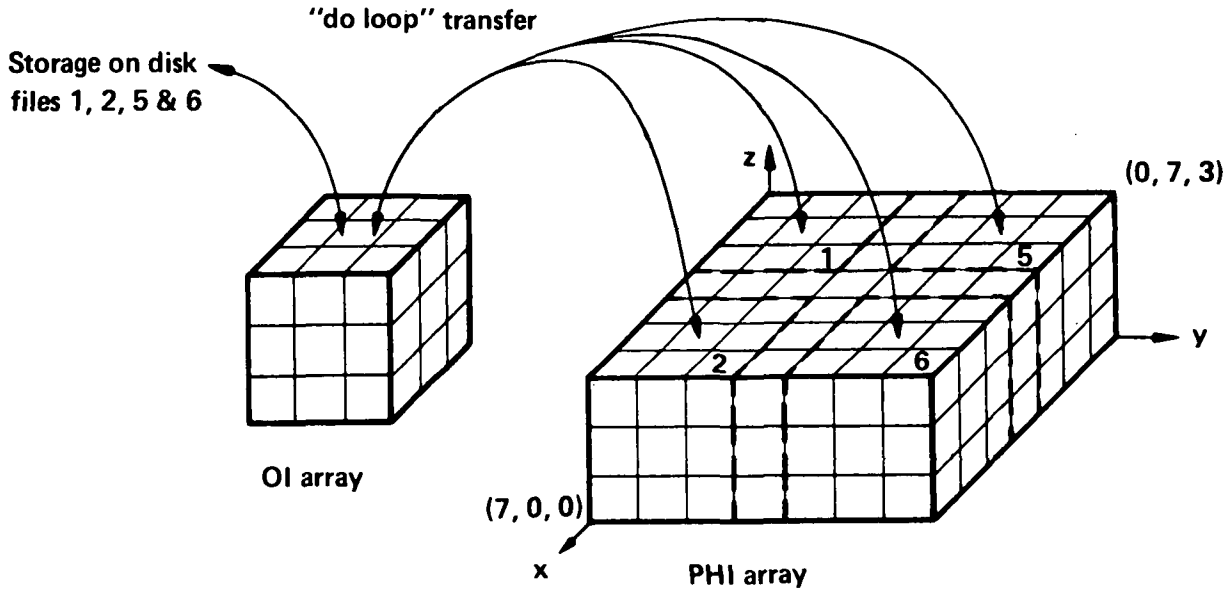

Figure 71.- Arrays dimensioned in the initializing and star advancing overlays (program of listing II). The numbers on the "chunks" indicate the disk files on which they are stored.

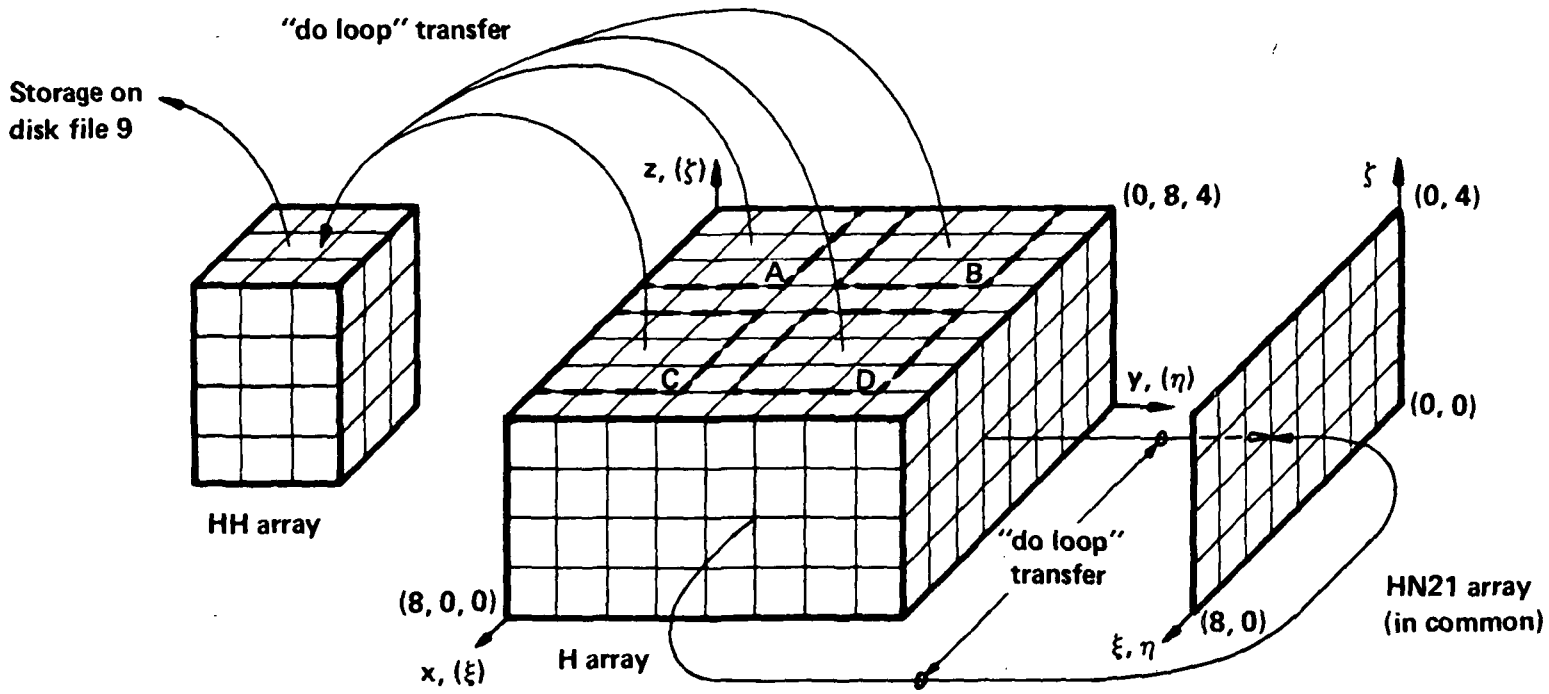

Figure 72.- Arrays dimensioned in GETH overlay, which performs a Fourier transform of the Green's function $H_{x,y,z}$ and stores the resulting $H_{\xi,\eta,\zeta}$ (program of listing II). (Letters A, B, C, and D are referenced by table IV.)

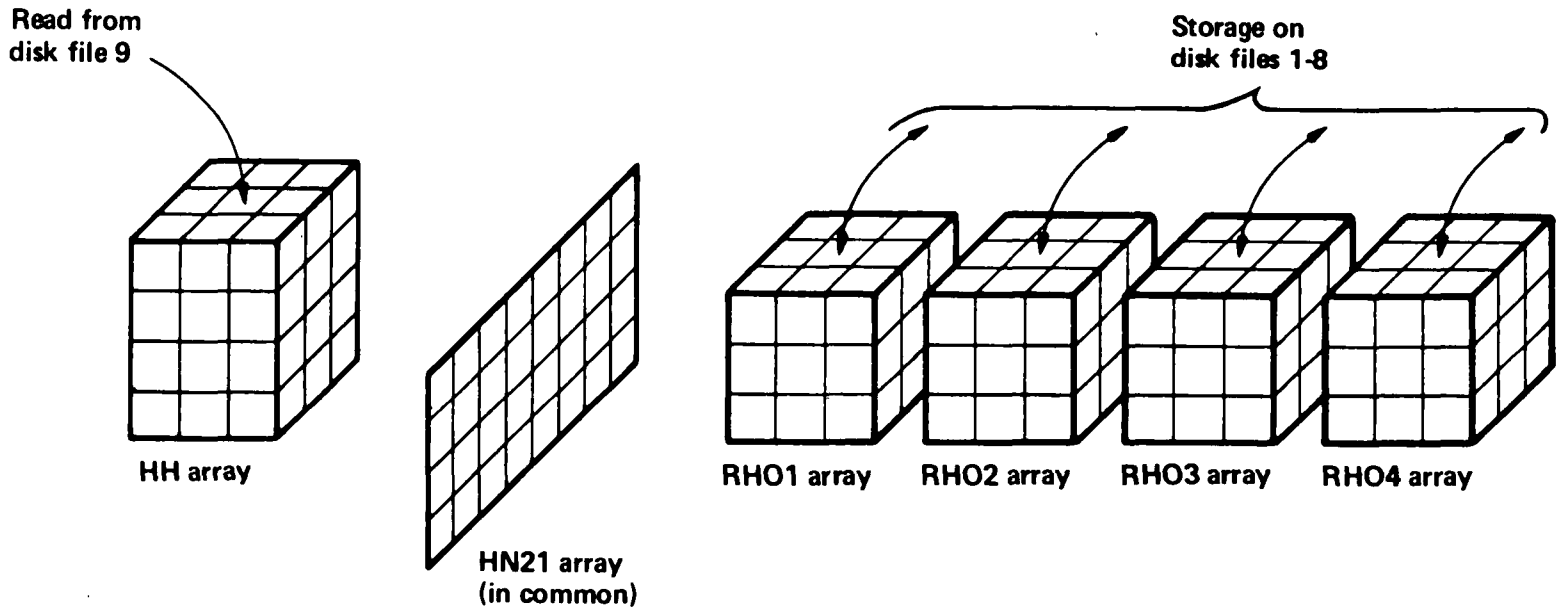

Figure 73.- Arrays dimensioned in the GETPHI overlay, which solves for the potential of an isolated galaxy (program of listing II).

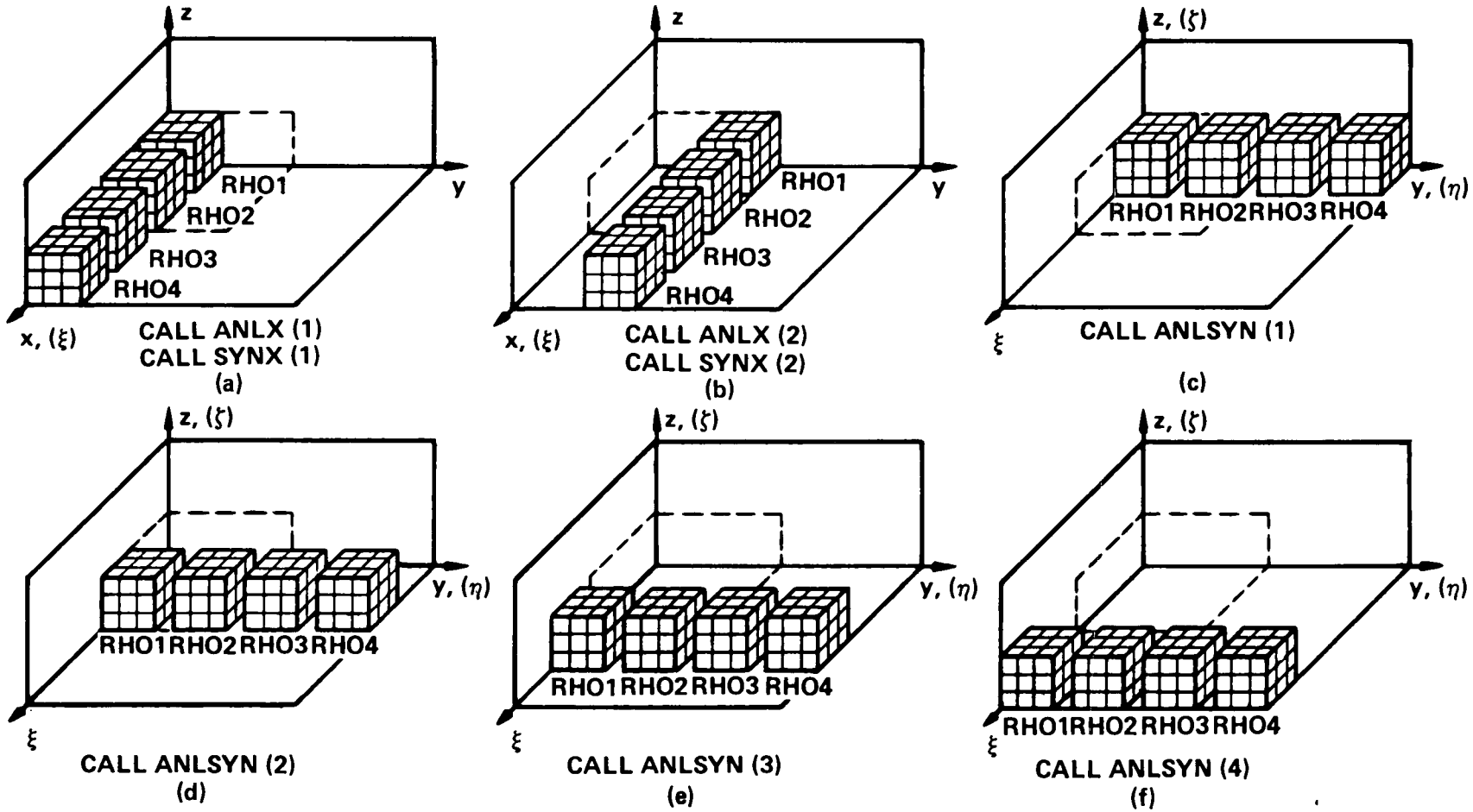

Figure 74.- Alignment of arrays RHO1, RHO2, RHO3, and RHO4 during calls by the GETPHI overlay to its subroutines (program of listing II). Although they are not dimensioned with the GETPHI overlay, the active PHI array and the extended PHI array projections on the planes $x = 0$, $y = 0$, and $z = 0$ are represented by dashed and solid lines, respectively. Axes labels represent subscripts of array elements which are untransformed (x,y,z), transformed (ξ,η,ζ), or either, as appropriate.

1. Report No.	2. Government Accession No.	3. Recipient's Catalog No.
NASA RP-1037		

4. Title and Subtitle	5. Report Date
COLLISIONLESS GALAXY SIMULATIONS	April 1979
	6. Performing Organization Code

7. Author(s)	8. Performing Organization Report No.
Frank Hohl, Thomas A. Zang, and John B. Miller	L-12730
	10. Work Unit No.
9. Performing Organization Name and Address	506-25-33-04
NASA Langley Research Center Hampton, VA 23665	11. Contract or Grant No.
	13. Type of Report and Period Covered
12. Sponsoring Agency Name and Address	Reference Publication
National Aeronautics and Space Administration Washington, DC 20546	14. Sponsoring Agency Code

15. Supplementary Notes

Frank Hohl: Langley Research Center, Hampton, Virginia.
Thomas A. Zang: The College of William and Mary, Williamsburg, Virginia.
John B. Miller: Old Dominion University, Norfolk, Virginia.

16. Abstract

Three-dimensional fully self-consistent computer models were used to determine the evolution of galaxies consisting of 100 000 simulation stars. One series of computer experiments used initially balanced flattened galaxies with an exponential radial density variation. Comparison of two-dimensional (infinitesimally thin disk) simulations with three-dimensional (disk with finite thickness) simulations showed only a very slight stabilizing effect due to the additional degree of freedom. The addition of a fully self-consistent, nonrotating, exponential core/halo component resulted in considerable stabilization. The most pronounced instabilities present were those due to the Jeans' instability in the outer regions of the disk, while at the same time a relatively slowly growing bar instability appeared. A second series of computer experiments was performed to determine the collapse and relaxation of initially spherical, uniform density and uniform velocity dispersion stellar systems. The evolution of the system was followed for various amounts of angular momentum in solid body rotation. For initially low values of the angular momentum satisfying the Ostriker-Peebles stability criterion, the systems quickly relax to an axisymmetric shape and resemble elliptical galaxies in appearance. The maximum flattening for these systems is equivalent only to an E2 system. For larger values of the initial angular momentum bars develop and the systems undergo a much more drastic evolution. The apparent rotational and random velocities of the bar systems are very sensitive to the viewing direction. An additional complication is the frequent misalignment of the apparent major axis with the direction that reflects the maximum rotation.

17. Key Words (Suggested by Author(s))	18. Distribution Statement
Galactic dynamics Spiral structure Computer experiments	Unclassified - Unlimited Subject Category 89

19. Security Classif. (of this report)	20. Security Classif. (of this page)	21. No. of Pages	22. Price*
Unclassified	Unclassified	147	$7.25

* For sale by the National Technical Information Service, Springfield, Virginia 22161

NASA-Langley, 1979

National Aeronautics and
Space Administration

Washington, D.C.
20546

Official Business
Penalty for Private Use, $300

THIRD-CLASS BULK RATE

Postage and Fees Paid
National Aeronautics and
Space Administration
NASA-451

NASA

POSTMASTER: If Undeliverable (Section 158
Postal Manual) Do Not Return